

Optical Spectroscopy on Organic-Inorganic Hybrid Structures

Dissertation
zur
Erlangung des Doktorgrades
der Naturwissenschaften
(Dr. rer. nat.)

dem

Fachbereich Physik
der Philipps-Universität Marburg

vorgelegt von

Ingo Meyenburg

aus

Kiel

Marburg/Lahn, 2020

Vom Fachbereich Physik der Philipps-Universität als Dissertation
angenommen am: 16.2.2021
Erstgutachter: Prof. Dr. Wolfram Heimbrod
Zweitgutachter: Prof. Dr. Gregor Witte
Tag der mündlichen Prüfung: 12.3.2021
Hochschulkenziffer 1180

Originaldokument gespeichert auf dem Publikationsserver der
Philipps-Universität Marburg
<http://archiv.ub.uni-marburg.de>



Dieses Werk bzw. Inhalt steht unter einer
Creative Commons
Namensnennung
Keine kommerzielle Nutzung
Weitergabe unter gleichen Bedingungen
3.0 Deutschland Lizenz.

Die vollständige Lizenz finden Sie unter:
<http://creativecommons.org/licenses/by-nc-sa/3.0/de/>

Meinen Eltern

-

Meinen Großeltern

Professor für Astronomie Volker Weidemann und
Mathematiklehrerin Helga Weidemann aus Kiel
Danke für die faszinierenden Einblicke in die Wissenschaft

-

Meinen Vorfahren

Contents

1. Summary	1
1.1. Abstract	1
1.2. Kurzfassung	2
2. Introduction	4
2.1. Functionalization of Semiconductors and Structure and Dynamics of Internal Interfaces	4
2.2. Application: Dye Sensitized Solar Cells	5
3. Fundamentals of Organic and Inorganic Semiconductors	9
3.1. Organic Molecules	9
3.2. Organic Semiconductors	16
4. Experimental: Optical Spectroscopy	20
4.1. Linear Absorption Spectroscopy	20
4.1.1. Basic Absorption Spectroscopy on Organic Materials	22
Chemical Shift	22
Tilt Experiments	23
4.2. Photoluminescence	25
4.2.1. Continuous Wave Photoluminescence	25
4.2.2. Time-Resolved Photoluminescence from 15 to 3000ps	27
4.3. Reflection and Straylight	30
4.3.1. Examples: Specular and Diffuse Reflection	31
4.4. Raman Spectroscopy	34
4.4.1. Theory	34
4.4.2. Experimental Setup	38
4.5. Electrooptical Measurements: Applied electrical bias on DSSCs	40
5. Excitons in Organic Layers on Inorganic Substrates	43
5.1. Pentacene	43
5.1.1. Preparation and characterization	44
5.1.2. Absorption Spectroscopy: Polarization Resolved Measurements of Single Crystals	45
5.1.3. Absorption Spectroscopy - The 2S Excitonic State	52
5.1.4. Absorption Spectroscopy: Evaluation of Davydov Components	57
Accessing the interface	59
5.1.5. Linear Reflection Spectroscopy	65
5.1.6. Raman Spectroscopy	67
5.1.7. Photoluminescence Spectroscopy	70

5.2.	Phthalocyanine	73
5.2.1.	Introduction	73
5.2.2.	Preparation and XRD characterization	73
5.2.3.	Cu-Phthalocyanine: Substrate Dependence	74
	Solid formation: polymorphism and exciton formation	74
	Standing and lying CuPc - different relation of intensities in split- ted excitonic Peaks	76
5.2.4.	TiO-Phthalocyanine	77
	Solid formation: exciton formation	78
	Excitonic Photoluminescence	82
	Reflection measurements	86
5.3.	Anthraquinone dyes	88
5.3.1.	Introduction	88
5.3.2.	Absorption and Photoluminescence Spectroscopy: Anthraphenol	89
6.	Charge Transfer in Organic-Inorganic Hybrid Structures - Accessing the Level Alignment at the Interface	93
6.1.	Charge Transfer in Organic-Inorganic Hybrid Structures: Indoline dye	93
6.1.1.	Sample Preparation and Experimental Details	94
6.1.2.	Absorption and Photoluminescence Spectroscopy	95
6.1.3.	Time-Resolved Photoluminescence Spectroscopy	96
	Dynamics of D149 on ZnO, TiO ₂ and glass	96
	Influence of Anchor Groups	100
	Charge Transfer Dependence of Layer Thickness - ZnO (0001)	102
6.1.4.	Conclusion	104
6.2.	Accessing the Level Alignment at the Interface	105
6.2.1.	Optical Determination of Charge Transfer Times from Indoline Dyes to ZnO in Solid State Dye-Sensitized Solar Cells	105
	Introduction	106
	Sample preparation and experimental Details	107
	Results and Discussion - Level Alignment	108
	Conclusion	112
6.2.2.	Variation of Substrates: Determining the Level Alignment of Sub- strates and Dyes relative to each other	113
	CdS with D149 - excited by 517 nm below CdS bandgap	114
	ZnSe with D149 - excited by 517 nm below ZnSe bandgap	114
	TiO ₂ and ZnO with indoline dyes D131 and D149	115
	Deduced Level Alignment scheme for D149 and D131 and differ- ent substrates	117
	Förster Transfer - CdS and ZnSe with indoline dye D149	118
6.3.	Suitability for organic solar cells	119
6.3.1.	Variations of Phthalocyanine dyes	121
	Zinc- and H ₂ -Phthalocyanine*(OH) ₂ : catecholate binding	124
	SubPcBOH	128
	Unsubstituted ZnPc - anchor variation - TRPL and IPCE results	132
6.3.2.	RK1 dye - reaching 10% efficiency with a fully organic dye	133

7. Conclusion	138
7.0.1. Proof of innovative ps-TRPL method	139
7.0.2. DSSC optimization	140
7.0.3. Additional measurement methods in DSSCs	140
7.0.4. Type II transition	142
Appendices	145
A. Phthalocyanine	146
A.1. Pc*OH ₂ - catechol anchor - PL results	146
B. Anthraquinone variations	147
B.1. Absorption and Photoluminescence Spectroscopy: Comparison of Alizarin, Phenoxazin, Anthraphen, Anthraphenol	147
B.2. Charge Transfer: ps-TRPL measurements	151
C. Indoline dyes	156
C.1. Absorption and Photoluminescence of Indoline dyes in solution . .	156
C.2. Photoluminescence spectroscopy - Trap formation for solid Indo- line dyes	156
C.2.1. Charge Transfer Dependence of Layer Thickness - D131 on TiO ₂ .	161
C.2.2. Influence of anatase Mesoporous TiO ₂ on Charge Transfer of dif- ferent Indoline dyes	161
D. Accessing the level alignment at the interface	163
D.1. Variation of Substrates	163
D.1.1. CdS and glass + D149 - reaching PL without substrate influence .	163
D.2. Electrooptical Characterization of D149 DSSC	164
D.3. Influence of Electrolyte on Level Alignment	166
E. ps-TRPL method applied in processed solar cells	167
E.0.1. Monochromatic Sensitized Solar Cells	167
E.0.2. Panchromatic Sensitized Solar Cells	169
F. Ruthenium dyes	173
F.1. Ruthenium dyes	173
F.1.1. Solid formation for Ruthenium dye N719	174
F.2. Ruthenium dyes in DSSC - TRPL	178
G. Type II Absorption for Catechol on TiO ₂ (meso) revealed by IPCE - also for RK1?	182
Bibliography and Notes	202
List of Figures	212
List of Tables	213
Scientific Contributions	214
Danksagung	217

1. Summary

1.1. Abstract

Organic Functionalization of Inorganic Substrates: Exciton Formation in Organic Layers on Inorganic Substrates

The organic molecules pentacene and phthalocyanine both are widely used for functionalization of semiconductors. Different phases form up when growing thin layers at the interface which have to be considered when discussing organic-inorganic hybrids. There remain open questions about exciton formation and optical properties. A thorough investigation of the influence of the substrate on the organic properties is necessary. Different crystalline phases of pentacene and phthalocyanines with an axial anchor including a metal atom (Cu-Pc, TiO-Pc) have been prepared and studied by X-ray diffraction and atomic force microscopy (Group Witte). Optical absorption spectroscopy and photoluminescence spectroscopy as a function of temperature between room temperature and 10 K have been performed. Peculiarities by growing pentacene on inorganic substrates are discussed.

Accessing the Interface - Pentacene on Different Inorganic Substrates

The polarization-resolved absorption spectra are determined for different pentacene polymorphs, both, for thin films grown on ZnO as well as for free-standing single crystals. A clear interrelation between the Davydov splitting of the lowest-energy singlet-exciton type transitions and the herringbone angle of the molecules in the unit cell is found, by this the herringbone angles can be determined by optical means. The variation in oscillator strength of the individual excitonic Davydov components with temperature is explained by a variation of this herringbone angle. The extraordinarily strong variation of the herringbone angle for Campbell phase pentacene films grown on ZnO substrates is attributed to interface-mediated strain due to the different thermal expansion coefficients of the organic and inorganic constituents.

Charge Transfer in Organic-Inorganic Hybrid Structures

We studied the electron transfer from excitons in adsorbed indoline dye layers across the organic-inorganic interface. The hybrids consist of indoline derivatives on the one hand and different inorganic substrates (TiO₂, ZnO, SiO₂(0001), fused silica) on the other. We reveal the electron transfer times from excitons in dye layers to the organic-inorganic interface by analyzing the photoluminescence transients of the dye layers after femtosecond excitation and applying kinetic model calculations. A correlation between the transfer times and four parameters have been found: (i) the number of anchoring groups, (ii) the distance between the dye and the organic-inorganic interface, which was

varied by the alkyl-chain lengths between the carboxylate anchoring group and the dye, (iii) the thickness of the adsorbed dye layer, and (iv) the level alignment between the excited dye (π^* -level) and the conduction band minimum of the inorganic semiconductor.

Optimization of Solar Cells: Revealing Level Alignment and Cluster-Formation

An efficient charge transfer from absorbing dye across the organic-inorganic interface into the semiconductor is crucial for high external quantum efficiencies in dye sensitized solar cells (DSSC). We use voltage dependent time-resolved photoluminescence in order to determine independently the charge transfer time from relaxed excited dye states into the conductive band minimum of the semiconductor, in consequence giving access to the level-alignment between dye and semiconductor. We can distinguish between excitons reaching the interface and excitons recombining due to quenching in the dye layers, which is especially important to detect unwanted agglomeration in DSSC. The advantages and disadvantages of panchromatic cells will be discussed.

1.2. Kurzfassung

Organische Funktionalisierung von anorganischen Substraten: Exzitonbildung in Organisch-anorganischen Hybridsystemen

Die organischen Moleküle Pentacen und Phthalocyanin sind weit verbreitet im Gebiet der Funktionalisierung von Halbleitern. Beim Aufwachsen von dünnen Schichten an der Grenzfläche entstehen unterschiedliche Phasen, welche bei der Untersuchung der organisch-anorganischen Hybride berücksichtigt werden müssen. Es bleiben offene Fragen zur Exzitonbildung und den optischen Eigenschaften. Eine gründliche Untersuchung des Einflusses des Substrats auf die organischen Eigenschaften ist notwendig. Verschiedene kristalline Phasen von Pentacen sowie von Phthalocyaninen mit einem axialen Anker, welcher ein Metallatom beinhaltet (Cu-Pc, TiO-Pc), wurden hergestellt und mittels Röntgendiffraktion und Rasterkraftmikroskopie untersucht (Arbeitsgruppe Witte, Universität Marburg). Absorptions- und Photolumineszenz-Spektroskopie wurden als Funktion der Temperatur zwischen Raumtemperatur und 10 K durchgeführt. Die Besonderheiten bei wachsenden Pentacen Schichten auf anorganischen Substraten werden diskutiert.

Zugang zur Grenzfläche - Pentacen

Polarisationsaufgelöste Absorptionsspektren wurden für verschiedene Pentacen-Polymorphe für dünne Schichten auf ZnO sowie für freistehende Einzelkristalle aufgenommen. Es wurde ein klarer Zusammenhang zwischen der Davydov-Aufspaltung des Singulett-Exziton-Zustands niedrigster Energie und des Herringbone Winkels der Moleküle in der Elementarzelle aufgezeigt. Der Herringbone-Winkel kann also über optische Spektroskopie ermittelt werden. Die Variation der Oszillatorstärke der einzelnen exzitonischen Davydov-Komponenten mit der Temperatur erklärt sich durch eine Variation des Herringbone-Winkels. Für die Campbell-Phase von Pentacen aufgewachsen auf ZnO-

Substraten tritt eine außerordentlich starke Variation des Herringbone-Winkels auf. Dies wird den unterschiedlichen thermischen Ausdehnungskoeffizienten der organischen und anorganischen Bestandteile zugeschrieben, welche an der Grenzfläche zu Verspannung führen.

Ladungstransfer in organisch-anorganischen Hybridsystemen

Hybridsysteme bestehend aus organischen Indolin-Derivaten und aus verschiedenen anorganischen Substraten (TiO_2 , ZnO , $\text{SiO}_2(0001)$, Quarzglas) wurden hergestellt. Dazu wurden Schichten aus Indolin-Farbstoff auf den anorganischen Substraten adsorbiert. Wir ermitteln die Elektronentransferzeiten von Exzitonen in Farbstoffschichten bis zur organisch-anorganischen Grenzfläche durch Analysieren der Photolumineszenz-Transienten der Farbstoffschichten nach Femtosekunden-Anregung und Anwendung kinetischer Modellrechnungen. Eine Korrelation zwischen den Übertragungszeiten und vier Parametern wurde gefunden: (i) die Anzahl der Ankergruppen, (ii) der Abstand zwischen dem Farbstoff und der organisch-anorganischen Grenzfläche, welcher durch die Alkylkettenlängen zwischen Carboxylat-Anker und Indolin-Zentrum des Farbstoffs variiert wurde, (iii) die Dicke der adsorbierten Farbstoffschicht, und (iv) die Höhe des Zustands-Niveaus des angeregten Farbstoff (π^* -Ebene) im Vergleich zum Leitungsbandminimum des anorganischen Halbleiters.

Optimierung von Solarzellen

Ein effizienter Ladungstransfer von absorbierendem Farbstoff über die organisch-anorganische Grenzfläche in den Halbleiter ist entscheidend für hohe externe Quantenwirkungsgrade in farbstoffsensibilisierten Solarzellen (DSSC). Wir unterscheiden zwischen Exzitonen, die die Grenzfläche erreichen, und Exzitonen, die aufgrund von Quenching in den Farbstoffschichten rekombinieren. Durch den Nachweis von Quenching mittels optischer Spektroskopie lassen sich unerwünschte Agglomerationen in DSSC detektieren und somit auch Solarzellen optimieren. Die Vor- und Nachteile von panchromatischen Zellen werden diskutiert. Wir verwenden spannungsabhängige zeitaufgelöste Photolumineszenz um die Ladungstransfer-Zeit von relaxierten angeregten Farbstoffzuständen in das Leitungsband-Minimum des Halbleiters zu bestimmen. Hierdurch erhalten wir Erkenntnisse über die Levelausrichtung zwischen Farbstoff und Halbleiter.

2. Introduction

2.1. Functionalization of Semiconductors and Structure and Dynamics of Internal Interfaces

Organic materials such as pentacene and phthalocyanine have optical and structural properties which are optimal for a deeper understanding of the functionalization of semiconductors. They form precisely defined phases, which can be distinguished by optical spectroscopy (see chapter 5). The solid-state excitons which form in the case of organic semiconductor layers are very well characterizable, as can be seen in the following picture of pentacene excitons, explained in detail in the chapter 5.1. Func-

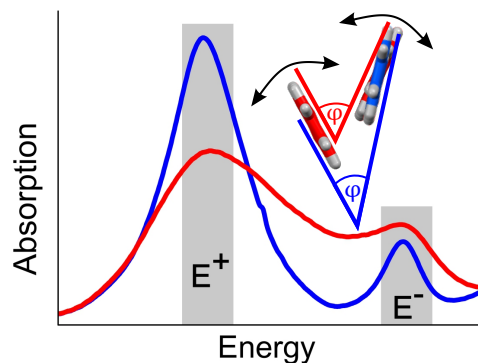


Fig. 2.1.: Pentacene exciton is splitted into E^+ and E^- , revealing the angle between the molecules (see section 5.1)

tionalization of semiconductors by means of organic materials is used in OLEDs and OFETs, photodiodes and solar cells[21]. The charge carrier mobility is not as high as in inorganic semiconductors, but organic materials can be advantageous for certain systems due to their high diversity and variability. This is particularly clear for the example of optimization of dye sensitized solar cells (DSSC). The size of the π -system in the dye changes the bandgap and the level alignment of the excited dye. Different functional anchoring groups vary the injection probability of the excitons. The absorption and thus the luminescence of the dyes can be controlled by chemical synthesis, which is particularly important for OLED systems.

This dissertation has been developed within the framework of two projects in which the Department of Physics is decisively involved. While questions concerning the "Functionalization of Semiconductors" fall within the scope of the Graduate School 1782, the Sonderforschungsbereich SFB 1083 "Structure and Dynamics of Internal Interfaces" explicitly deals with the processes at interfaces. Concerning the SFB, this study in-

investigates the electron transfer in organic-inorganic hybrid systems. A more detailed understanding of processes and charge transfer at the interface is important for further optimization of hybrid systems.

2.2. Application: Dye Sensitized Solar Cells

Principle of DSSCs

Grätzel cells are examples of organic-inorganic systems. In Grätzel cells a mesoporous network of tiny inorganic semiconductor corns exists which are sintered in order to create an electron conducting layer. These nanocrystalline corns are sensitized by a light absorbing dye, that means dye molecules or aggregates are attached to the wide band gap TiO_2 or ZnO semiconductor oxide by soaking. The surface and therefore the organic-inorganic interface of the mesoporous structure is greatly enlarged by up to a 1000-fold for a $10\ \mu\text{m}$ thick film in comparison with a two dimensional smooth layer. The basic concept of the dye solar cell is shown in the following scheme (Fig. 2.2).

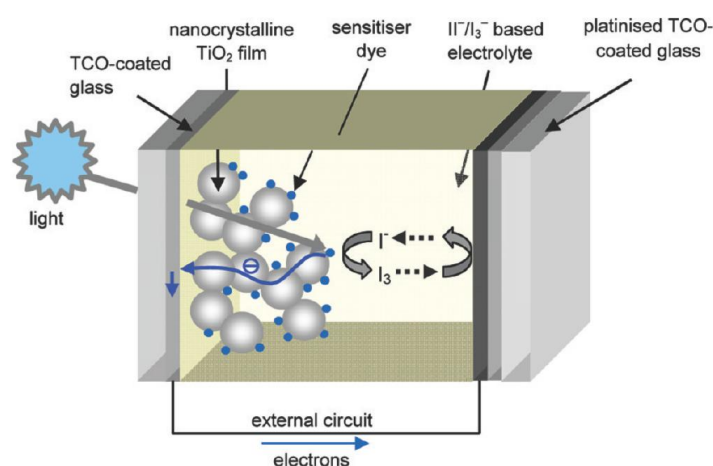


Fig. 2.2.: Schematic of a liquid electrolyte dye-sensitized solar cell. Photoexcitation of the sensitizer dye is followed by electron injection into the conduction band of the mesoporous oxide semiconductor, and electron transport through the metal oxide film to the TCO-coated glass working electrode. The dye molecule is regenerated by the electrolyte redox system, which is itself regenerated at the platinised counter electrode by electrons passed through the external circuit. Caption and picture are taken from Listorti [119]

After photoexcitation of the dye, a bound electron-hole pair is formed in the dye, an exciton. This is separated at the dye-inorganic semiconductor interface by injection of the excited electron into the inorganic semiconductor. With optimal soaking, only a monolayer of dye is attached to the mesoporous inorganic network. Then injection without diffusion of the exciton through a thicker dye layer is possible, thereby reducing quenching losses. The oxidized dye is reduced by a redox system; an iodide electrolyte is often used, but also different concepts including a solid state hole conductor ([59], [24]) are currently in focus. On the counter-electrode, a thin catalytic layer of platinum

on a conducting glass substrate enables the reduction of the oxidized redox system. The successfully injected electrons reach the transparent conductive oxide layer after diffusion through the mesoporous network driven by a concentration gradient. The electrical circuit is completed via electron migration through the external load.

Processes in DSSC's and Organic-Inorganic Hybrid Structures

The exact processes of injection, charge separation, recombination, reduction and electron transport in the cell are still under discussion. In particular, the charge transfer from the dye to the inorganic semiconductor is of interest, which can also be considered as a consequence of an energy scheme in the solar cell, shown schematically from Listorti et al. in Fig. 2.3 by a TiO₂meso DSSC.

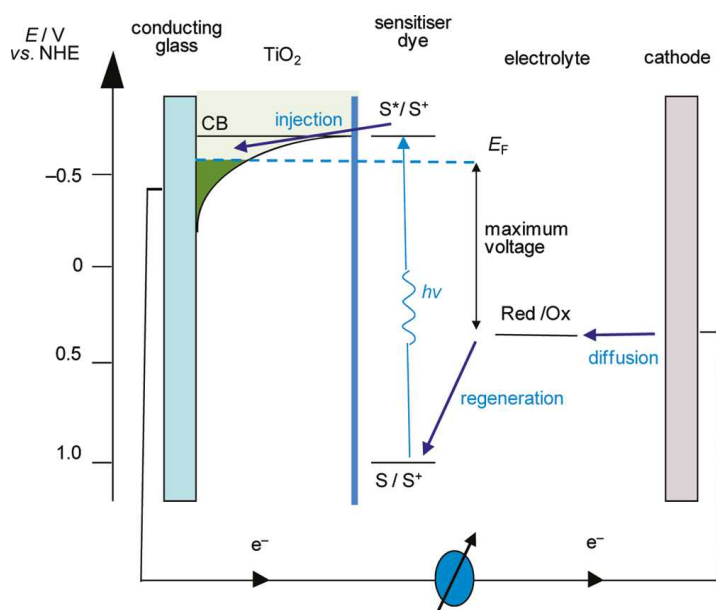


Fig. 2.3.: Energetics of operation of DSSCs. The primary free-energy losses are associated with electron injection from the excited sensitizer into the TiO₂ conduction band and regeneration of the dye by the redox couple. The voltage output of the device is approximately given by the splitting between the TiO₂ Fermi level (dashed line) and the chemical potential of the redox electrolyte. (Caption and picture are taken from Listorti [119])

The tapped cell voltage is much lower than the primary absorbed energy in the dye, it is ultimately the difference of the two Fermi levels of anode and cathode. The maximum cell voltage of a DSSC is usually less than 1 V, typically 0.5-0.8 V and thus typically less than half the energy absorbed in the dye. This is approximately indicated in the energy scheme with the resulting maximum voltage between the blue dashed line and the redox level of the electrolyte. The reduction of the cell voltage occurs through various loss processes in the cell, for example by the required driving force for the injection of the dye into the inorganic semiconductor [228, 71] and in the reduction of the oxidized dye by the redox system. Loss by excess energy upon absorption is a general problem with solar cells and can be reduced by multi-cell systems with different stacked dyes having top to bottom from larger to smaller bandgaps. In addition, transport losses

occur in the mesoporous inorganic semiconductor and down to the electrodes. In this work, time resolved photoluminescence measurements (see section 4.2.2) are used to retrieve informations about the level alignments and injection times of the organic-inorganic interface as illustrated in Fig. 2.3 with injection from sensitizer dye into the conductive transparent oxide. The energy levels without illumination are determined, for example, from cyclic voltammetry measurements. Yet, the energy level alignment at the interface especially during illumination is often not clear [71]. The introduced time resolved photoluminescence technique in this dissertation can be used as an additional diagnostic option for the level alignment on the interface and the injection times. The results of ps-TRPL can, in the end, help optimizing charge transfer and can therefore contribute to a higher solar cell efficiency and a deeper understanding of processes in solar cells.

Economical Situation

Grätzel cell dye solar cells have achieved efficiencies of over 10% when using only one dye. This applies both to purely organic dyes such as RK1 ([95] and section 6.3.2) and to metal-substituted organic dyes such as ruthenium dyes (chapter F.1 and [145, 60, 27]) or porphyrin-based dyes (chapter 6.3.1 and [222]). By stacking several cells one over the other and switching them in series, sunlight can be harvested more effectively. However, the companies Konarka, G24 and Dyesol were not successful in the implementation in the cost-covering production of DSSCs, also because of low stability and low efficiencies of the modules.

With another organic multi-solar cell concept with donor and acceptor molecules in organic layers absorbing in different color ranges Heliatek situated in Dresden achieved efficiencies of 13.2% in 2016 (see <https://www.heliatek.com/de/>) in the laboratory (see picture 2.4). According to Heliatek, the power input is comparable to conventional cells with 16 to 17% efficiency due to the good performance in low light and high temperatures. In the future, a cell efficiency of 15% is desired. The lifetime of this type of organic solar cell is with 25 years no longer an obstacle to success. Unfortunately, the total cell efficiency in production is still only 7-8 %, so organic solar cells can only serve niche markets due to their low efficiencies. Due to the high absorption coefficients of the organic materials, very thin layers of a few 100 nm are sufficient to effectively collect sunlight. The thin absorber layers together with the possibility of producing cells on flexible and lightweight substrates open up the market for modules on building facades and on textiles. To mention in this context are the many possibilities of colors and transparency. Also rollable, portable modules are conceivable or applications on car and mobile phone. Heliatek successfully completed an 80 million euro financing round in 2016, in total 115 million euro were invested until 2019.

The only a few years ago discovered perovskite solar cells, which consist partly of an organic hole conductor, should also be mentioned here. The company Oxford PV in Brandenburg an der Havel is researching to maintain the very high laboratory cell efficiency of more than 20% in one product line. An initially expected rapid displacement of the DSSCs and organic photovoltaic has not occurred. Stability was first the main problem of perovskite solar cells but this seems to be solved now, but the toxic material lead is still a problem, research is going on for tin as replacement.

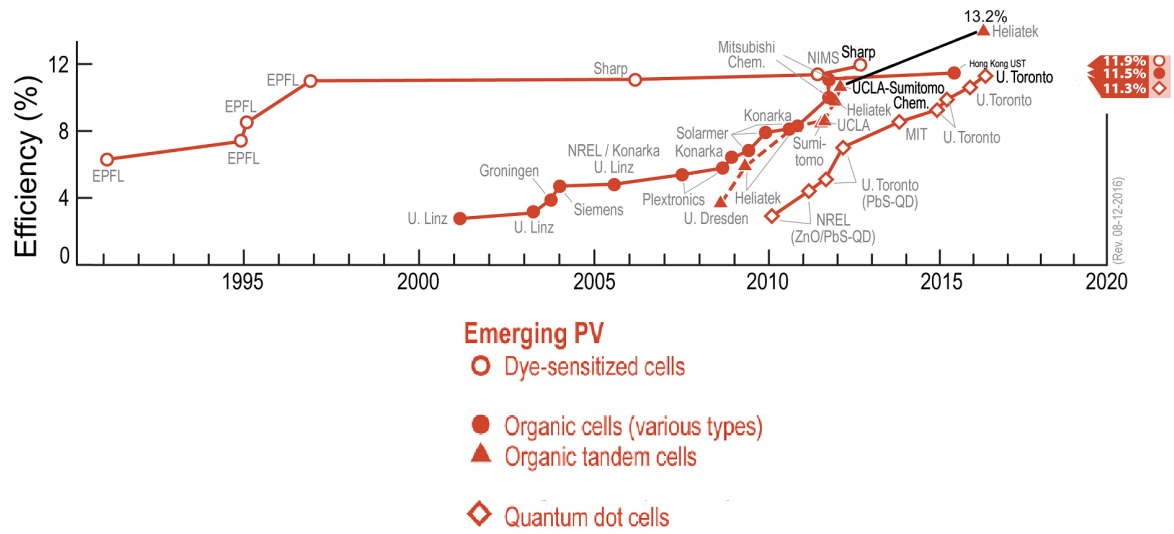


Fig. 2.4.: Best Research Cell Efficiencies (taken from NREL) for organic-based solar cells; the development of dye-sensitized solar cells (Grätzel type) in open dots

3. Fundamentals of Organic and Inorganic Semiconductors

In this dissertation molecular materials and its combinations with crystalline semiconductors are investigated. In order to understand the properties of the organic compound part, first the properties of organic molecules are described and then the consequences for solid formation of organic molecules. Depending on the molecule chosen and of the method of solid preparation, amorphous structures up to organic crystals are possible.

3.1. Organic Molecules

The entire chemistry of organic molecules is based on covalent bonds between carbon atoms. Carbon has an electron configuration of $1s^2 2s^2 2p^2$ with a total of four electrons in the $n=2$ atomic shell. Fig. 3.1 shows the forming volumes with electron distribution probabilities of higher than 90%.

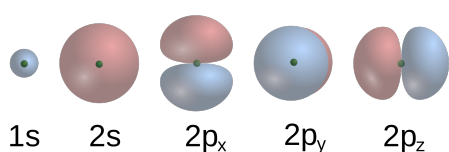


Fig. 3.1.: Shown are the isosurfaces, so that an electron with a probability of 90% is in the enclosed volume. The s orbitals are spherical while p orbital dumbbell-shaped. Figure taken from S-p-Orbitals, wikimedia.

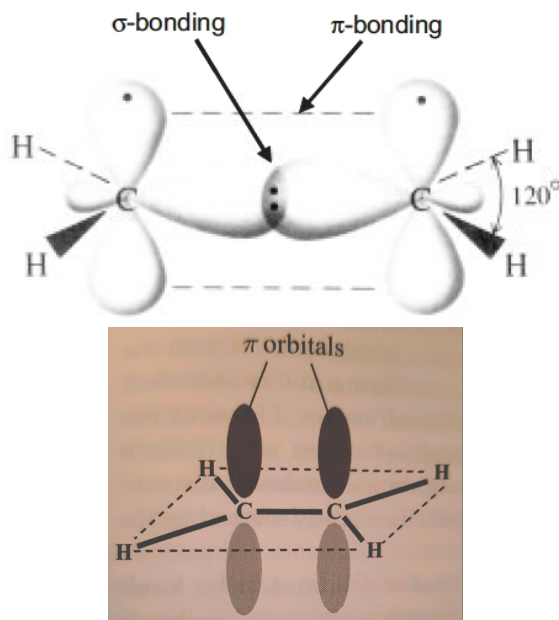


Fig. 3.2.: Ethylene as an example for the simplest conjugated π -electron system. Illustrated with its σ and π bonds (upper part, taken from Fig 1 of book [21]) and illustrated with the π bonds in a clearer planar view (lower part, taken from Fig. 8.1a of book [58])

For ethylene (see Fig. 3.2), each carbon atom is connected to two hydrogen atoms and has a double bond with the other carbon atom. One of the two 2s electrons is promoted into the empty $2p_z$ orbital, allowing the remaining 2s electron to hybridize with the $2p_x$ and $2p_y$ orbitals into three sp^2 compounds. The 2p electron which is not involved in the hybridization forms a π orbital in the z-direction, perpendicular to the plane.

The π -electrons of the p_z orbitals of the carbon form large delocalized π orbitals extending over the entire molecule. For benzen (Fig. 3.3), the overlap of the π orbitals yields a ring-like π orbital above and below the plane of the carbon and water atoms.

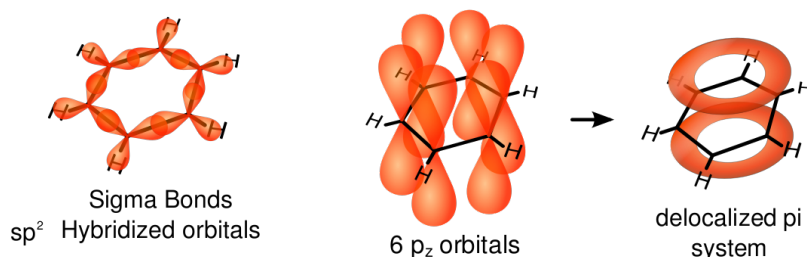


Fig. 3.3.: The benzene molecule (C_6H_6) with its two bond types. The hybridized $2sp^2$ orbitals of the carbons bind to each other and with the 1s orbitals of hydrogen. The $2p_z$ orbitals form the π -electron system. (Figure taken from Benzene_Representations, wikimedia) .

Organic molecules can be classified into saturated and conjugated systems, depending on the type of binding. Organic molecules such as benzene with alternating multiple and single bonds are called cyclic conjugates. Conjugated molecules are relevant to hybrid structures because they have very variable optical properties and many absorb in the visible.

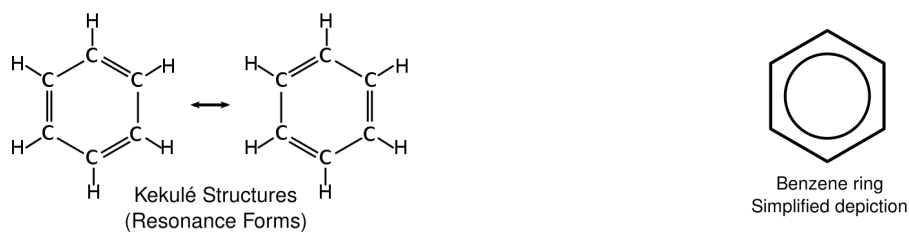


Fig. 3.4.: Alternating multiple and single bonds for organic molecules, here benzene (C_6H_6). Both descriptions exist. Often the description is therefore given as Fig. 3.5 with the Robinson ring symbol. Figure taken from Benzene_Representations, wikimedia.

Fig. 3.5.: Simplified description of Benzene without showing the H-atoms and with the ring inside instead of the varying multiple and single bonds. Often even the ring is omitted. Figure taken from Benzene_Representations, wikimedia.

π electrons are less strongly bound than electrons in saturated molecules. While in benzene the absorption edge is UV light, it is visible light for larger molecules such as pentacene; see Fig. 3.6 with detailed absorption bandgaps and Fig. 3.7 showing the redshift in the absorption spectra with increasing amount of acene size.

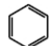
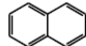
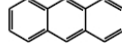
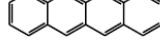
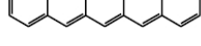
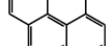
Molecule		Absorption
Benzene		254 nm
Naphthalene		311 nm
Anthracene		375 nm
Tetracene		471 nm
Pentacene		582 nm
Pyrene		352 nm

Fig. 3.6.: Relationship between Acene size and absorption bandgap. Figure taken from [183]

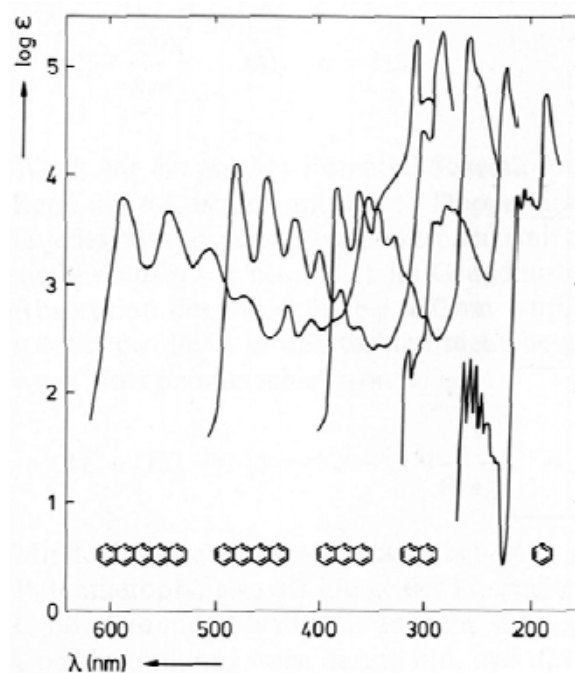


Fig. 3.7.: With increasing acene size the absorption spectra redshift, here shown in solution for benzene to pentacene from UV to visible absorption. (Figure taken from [73])

The electrons fill up the unoccupied ground states in one molecule. The highest state that can still be occupied is the HOMO (highest occupied molecular orbital) level. In the case of a conjugated molecule, this is a π orbital, since all σ bonds are very tightly bound and higher energies would be needed to break up the σ bonds.

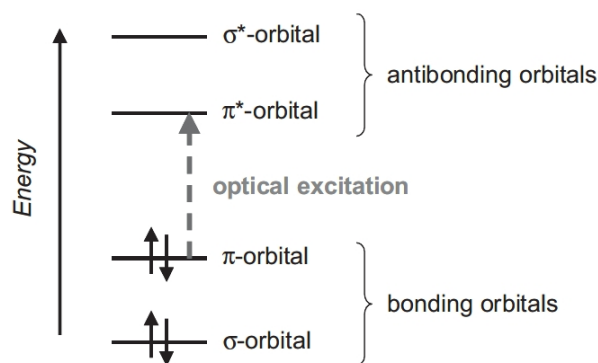


Fig. 3.8.: The viewgraph shows the energy levels of a π -conjugated molecule. The lowest electronic excitation is between the bonding π -orbital and the antibonding π^* -orbital (adopted from [21], originally from [207]).

Due to delocalization, the energy levels of such a system are no longer strictly discrete, but slightly widened, so that the transitions are broadened.

The first level above the HOMO is the LUMO (lowest unoccupied molecular orbital) level and is for organic molecules characterized by an excited π orbital, π^* . This is also called π - π^* transition.

It has to be noticed that there is still a discussion about the right definition of the levels. While the HOMO and LUMO levels are accepted for organic molecules as π to π^* transition, it is not clear if the excitation of the electron into the LUMO takes into account the decreased energy level of the electron due to formation of an intramolecular exciton (Frenkel type) with the produced hole in the HOMO state. Coulomb forces between excited electron and hole lead to decreased energy of the electron due to the exciton binding energy.

If the Frenkel exciton formation has a relevant influence on the energy of the LUMO by the Coulomb force, the calculated LUMO or π^* level is not equal to the lowest absorption state. But, since a direct absorption of a photon with the same energy as the exciton is possible and would show up in absorption spectra as the lowest lying absorption, the resulting measured spectra of absorption and photoluminescence do not change. Only the definition of the lowest energy peak should be changed in that way, that the π^* level already takes into account the exciton binding energy. Also, for the following theory part with energy level scheme, Stokes shift and Franck-Condon principle, this exciton binding energy would not change the discussed basic principles.

When considering energy levels, for optical spectroscopy it is relevant which transitions are considered (see as an overview Fig. 3.9 with the electron spins indicated at the side). While in the ground state, the electrons of a molecule align their spins antiparallel in pairs and therefore no resulting spin arises ($S=0$, singlet, ground state S_0), the first excited state may either have a singlet state $S_1=0$ or may have a total spin of $S=1$, with parallel alignment of the spin of the separated electron pair (first excited triplet state T_1). In case of T_1 , the multiplicity of the spin results in $2S+1$ triplet states, which usually have lower energies than singlet states.

Since photons do not have a spin, it is only possible to optically excite to higher states where the spin remains the same, i.e. in singlet states. The fluorescence studied in this work is emitted from the singlet-singlet transition between S_1 and S_0 and has lifetimes in the ns range. In contrast, a transition from the lowest triplet state T_1 to the ground state S_0 would have much longer decay times due to the actually forbidden transition, this luminescence is called phosphorescence.

The electrons and its states remain close to the respective organic molecules and the electronic states are therefore localized, in contrast to strongly delocalized states in band formation in inorganic solids. In consequence, the most important vibrational states are also localized. This may result in clearly visible vibronic replica in organic solutions spectra. In Fig. 3.7 this can be seen as the clearly distinct following replica after the main HOMO-LUMO absorption peak. The first replica peak is built by the main vibrational states. Multiple peaks occur due to combinations and doubling of vibrations. Organic spectra show that the optical transitions have a vibronic character, which is due to the strong coupling between electronic and vibronic states. In Fig. 3.9 the vibronic states are indicated as thinner lines above the thick lines of the main states. Those vibronic states are due to vibrations of the molecule about their bonds

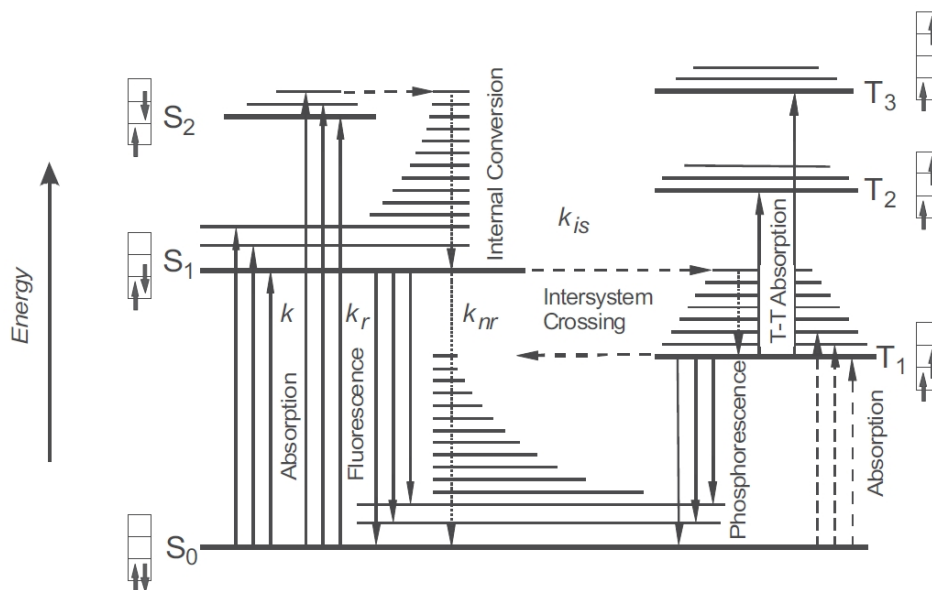


Fig. 3.9.: Energy level scheme of an organic molecule (left: singlet manifold, right: triplet manifold). Arrows with solid lines indicate radiative transitions, those with broken lines nonradiative transitions (taken from [154]). Typical lifetimes of the S_1 state are in the range 1...10 ns. Triplet lifetimes are usually in the ms range for pure aromatic hydrocarbons. Caption taken from [21].

which means additional vibrational energy. The vibrational-electronic process causes the electron to jump to the excited electronic state while creating vibrations simultaneously. The quantum-mechanically allowed discrete states depending on vibrational oscillation frequencies are often broadened into a continuum.

After excitation from ground state S_0 into a vibrational state of a higher singlet state the vibrational energy is transferred into thermal energy. The electron ends up at a singlet state and emits a photon when recombining with the ground state. This emitted photon has a lower energy as the exciting photon since energy was lost by non-radiative relaxation or because the recombination is with a vibrational state of the ground state. The occurring energy difference between absorption and emission spectra is called Stokes-shift (see Fig. 3.10).

In order to understand the Stokes shift in more detail, molecular configuration diagrams and the Franck-Condon principle are necessary (see Fig. 3.11, 3.12 and 3.13). The indicated coordinates r as the core distance and q as a length (q is generalized for more complicated molecules), have the same meaning of configuration coordinates. Figure 3.11 shows the excitation of a diatomic molecule with only one vibrational stretching mode between the atoms. With excitation the radius of the excited atom increases and consequently the internuclear separation increases, getting the configuration coordinate larger. r_1 indicates the minimal energy of the bound atoms in the ground state. If the distance gets smaller, electron-electron and proton-proton repulsion occurs, so energy increases. r_2 indicates the minimal energy of the system after excitation, when the molecule is in the excited electronic state. The given dumb-bell schemes show the

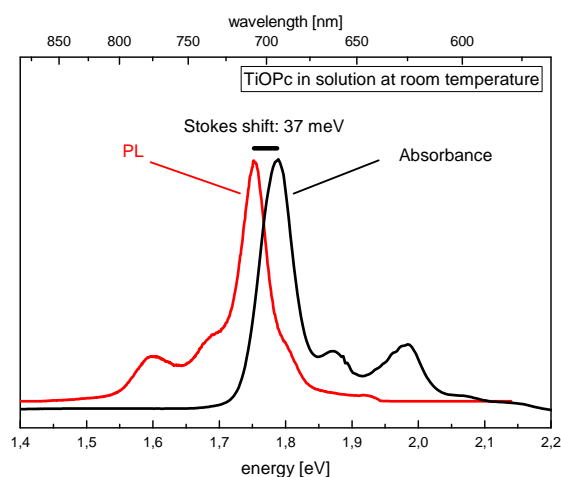


Fig. 3.10.: Comparing the absorbance with the photoluminescence spectrum of Titanyl-Phthalocyanine (TiOPc) in solution, a mirror-symmetry is apparent. If a mirror is placed in the overlap of both spectra, it acts like the symmetry axis. The Stokes shift of 37 meV is indicated between the absorbance main peak (1.789 eV) and the photoluminescence main peak (1.752 eV).

enlargement of the distance of the nuclei after excitation.

The vibronic process can be divided into different steps. At first, the absorption of a photon occurs into the excited state without altering r , in consequence the excited state has still the configuration coordinate of the ground state, r_1 . Secondly, the nuclei relax to the distance r_2 , still being in the excited state. At third the photon gets emitted with relaxation of the electron into the ground state while the distance r_2 between the nuclei is maintained. Finally, the nuclei relax again to the beginning ground state.

The Franck-Condon principle in detail describes the optical transitions between coupled vibrational-electronic levels of a molecule. The principle can be seen in Fig. 3.13, with vertical arrows in configuration diagrams representing the most probable transition. As can be seen, the nuclear coordinate does not change during absorption (blue arrow), but afterwards during relaxation of the excited vibronic states from $v'=2$ to $v'=0$. The green arrow indicates the favored emission transition. The resulting absorption and emission depending on the energy are shown on the right side in the lower part of Fig. 3.12.

The molecule transition from one electronic state to another can be described regarding the probability densities for the involved vibrational levels in the absorption transition. The more the vibrational wave functions of the two states are compatible with each other (i.e., as similar as possible to the original nuclear coordinate), the more likely this transition is. Some vibronic transitions are more likely than others, namely those that do not change core distance. Considering matrix elements for an electric-dipole transition and vibrational wave functions the Franck-Condon factor is calculable as the square of the vibrational overlap integral. The factor is a measure for the overlap of probability densities. For Fig. 3.12 with the maximal absorption and emission at vibronic level 2 the factor would be expected $n_2=2$.

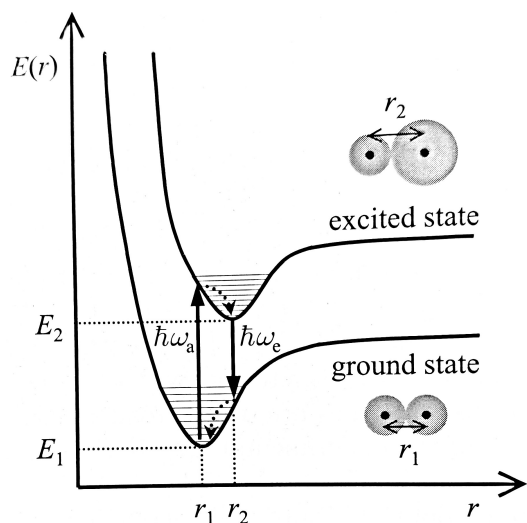


Fig. 3.11.: Energy-level diagram for the ground state and an excited state of a simple diatomic molecule, as a function of the separation r between the two nuclei. Vibrational-electronic absorption and emission transitions at energies of $\hbar\omega_a$ and $\hbar\omega_e$ are indicated. The schematic 'dumb-bell' diagrams of the molecule, with the radius of one of the atoms increasing in the excited state, illustrate the point that the equilibrium separations of the nuclei in the two electronic states are different. (Figure and caption taken from [58])

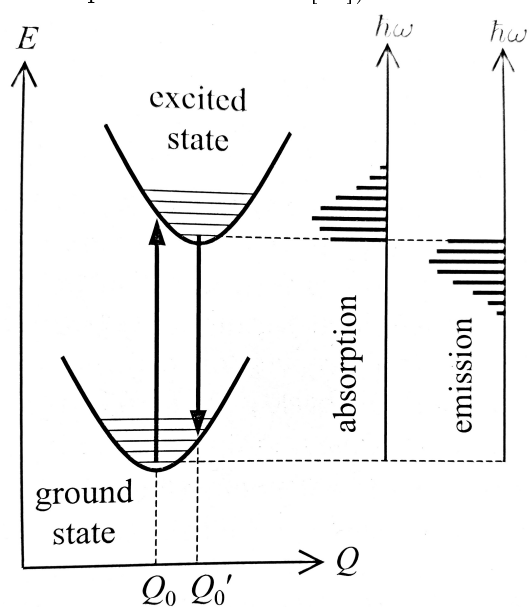


Fig. 3.12.: Configuration diagram for two electronic states in a molecule. Vibrational-electronic transitions are indicated by the vertical arrows, together with a schematic representation of the absorption and emission spectra. (Figure and caption taken from [58])

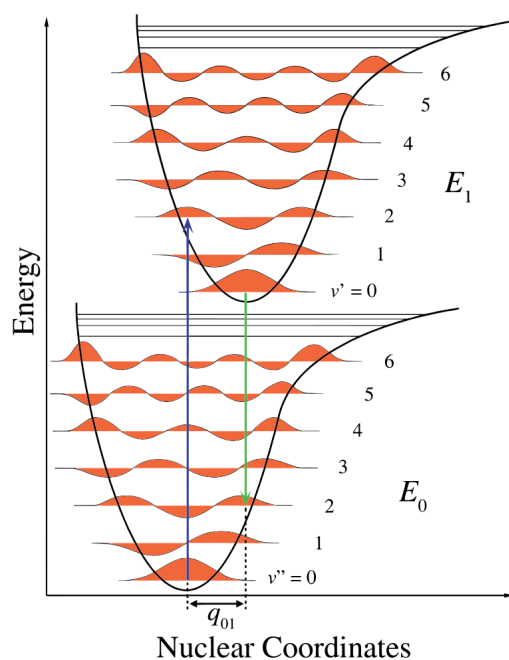


Fig. 3.13.: Franck-Condon principle energy diagram. Since electronic transitions are very fast compared with nuclear motions, vibrational levels are favored when they correspond to a minimal change in the nuclear coordinates. The potential wells are shown favoring absorption transitions between the vibronic states $v''=0$ and $v'=2$ and emission transitions between the vibronic states $v'=0$ and $v''=2$. (Figure and caption taken from FranckCondonDiagram, wikipedia)

3.2. Organic Semiconductors

A solid is a periodic arrangement of atoms that can be continued indefinitely. Depending on the type of bonding between the atoms, the outer electrons may be delocalized throughout the solid. This leads to a considerable widening and overlapping of the energy levels, so that bands are forming which cover a broad energy spectrum. The initially discrete levels of atoms have become broad bands.

Solids based on conjugated molecules are held together only by Van der Waal's forces. These forces are relatively weak compared to the forces within the molecule that result from the strong covalent bonds between the atoms. As a result, the electronic structure remains tightly bound to the respective molecule, resulting in localized electron states. It is important to take into account the structure of the solid. While for amorphous solids the electron transport can be described by a hopping model with very low conductivity (10^{-3} cm²/Vs [21]), for highly purified organic crystals band-like transport is occurring. Due to quenching in traps room temperature mobilities in molecular crystals reach only values in the range from 1 to 10 cm²/Vs [101]. The band in molecular crystals is smaller than for inorganic semiconductors. Different band widths are given in literature: Brütting [21] gives a value of typically a few kT at room temperature while Schwörer specifies values for both HOMO and LUMO of up to 738 meV (pentacene) for acene crystals ([183] table 8.3). Schwörer indicates in contrast to Brütting that overall bandwidths are thus larger than kT for all the acene crystals.

The band like formation in crystalline organic semiconductors is due to delocalized exciton formation called charge-transfer excitons, this will be explained in the following paragraph.

As discussed before, tightly bound Frenkel type exciton formation for a single molecule should occur. For organic solids with stronger interacting molecules a new type of exciton appears which has characteristics just between the tightly bound Frenkel exciton and the free Wannier-Mott excitons existing in inorganic semiconductors. The so called charge transfer exciton extends over two different molecules with the hole on one molecule and the electron on the other.

Charge-Transfer excitons can occur between two different types of molecules, this is strongly discussed in the organic solar cell community [10, 63, 12, 20]. To mention is also that charge transfer excitons between organic materials and a solid may occur, as shown for example by Piersimoni et al. [153]. This phenomenon is also called type-II exciton.

In this work charge transfer states between two equivalent types of molecules are discussed, see chapter 5. Regarding for example pentacene (see Fig. 5.11a), the low-energy excitonic states form only in a solid and not in a solution with DMF. If the new appearing low-energy exciton was a molecular singlet exciton, it would indicate a shift of the molecular singlet exciton from spectra in solution to the spectra of solids, and this would not imply the emergence of new excitons in solids. Although some papers still discuss the new excitonic peaks as shifted peaks from solution to solid, a shift does not seem to be the right interpretation, since many organic spectra form new solid excitons instead of a shift of the solution singlet exciton. TiO-Phthalocyanine (Fig. 3.15) and Cu-Phthalocyanine (Fig. 5.35) are shown as examples, an overview of exciton formation

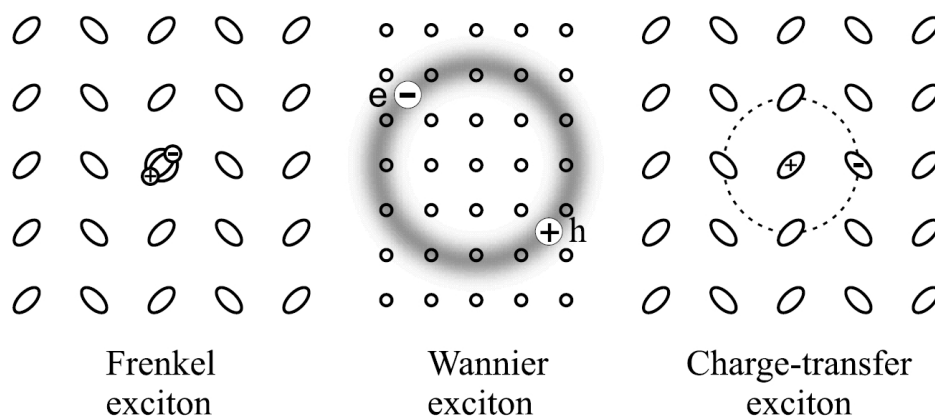


Fig. 3.14.: Excitons with different radii: diagram of a Frenkel exciton, a Wannier exciton, and a charge-transfer (CT) exciton. Wannier excitons have not been observed in organic crystals. Figure and caption taken from Schwörer ([183] Fig. 6.13).

with both Phthalocyanines can be seen in Fig. 5.41. This exciton formation can also be interpreted from photoluminescence spectra, for example for TiOPc in Fig. 3.10 with a low energy exciton peak emerging for solid structure.

The exciton formation in phthalocyanine is discussed contrarily in literature as can be seen for Zn-Phthalocyanine, which is similar to CuPc regarding spectra formation [47, 78, 125, 114]. The most plausible explanation is by Wojdyla et al., they discuss ZnPc spectra in [216] and [217] and define in Fig. 2 of [217] the lowest energy band as exciton and the second peak as $\pi-\pi^*$, the same would be the interpretation for CuPc (for experimental results, see chapter 5.2).

Regarding pentacene, recent results using different theoretical approaches have challenged the conventional interpretation of the lowest energy bands as pure Frenkel type and instead propose a more delocalized exciton [201, 186, 38].

In this dissertation the formed low-energy exciton is discussed as more Frenkel type singlet exciton forming in solids, which allows us to adapt a simple dipole-dipole interaction model fitting surprisingly well, but we also discuss it as charge transfer exciton (see pentacene section 5.1.3).

Summed up, this might be more of a definition discussion. From definition of charge transfer excitons as interacting over two molecules, these new Frenkel type singlet excitons emerging in solid structures can also be named as charge transfer excitons.

In solid-state layer formation, different crystalline phases with different properties depending on production process can be formed, see for example chapter pentacene 5.1.4 Fig. 5.16. Also amorphous layers with very unordered amount of tiny crystals can be formed. Solid formation results in solid-state excitons in the spectrum, which cause in relation to the solution a red shift of the absorption / reflection and of the PL. In Fig. 3.17 TiOPc is shown, green and red curves are red-shifted compared to the black ones of the solution spectra (see chapter 5.2 for more informations on exciton formation in phthalocyanines). If not a layer but powder of an organic material is examined, dis-

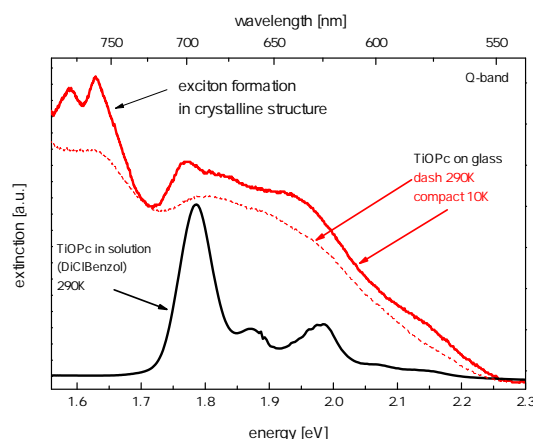


Fig. 3.15.: Comparison of absorption of TiOPc in solution (black curve) with TiOPc as crystalline structure. Clearly new peaks emerge at lower energy than peaks in solution. They are indicated as excitons which only emerge in solid structures of TiOPc.

ordered structures with many defects occur. Therefore, the PL of powder (green thick curve) is again red-shifted from the PL on the crystal (red thick curve) to a deeper lying defect PL. Further figures showing the differences in optical spectra from molecular to powder PL can be found in chapter Anthraquinone 5.3.2, Fig. 5.58 and 5.59.

In conclusion, it is possible to identify the phase and quality of organic materials by linear optical spectroscopy.

In order to verify the different forms of solids also time resolved photoluminescence can be used. Spectra are relevant if comparing times of TRPL, but in general it can be observed that from molecule to solid a faster decay occurs. Regarding powder, deep trap formation leads to a PL decay different from molecular and solid layer PL. Regarding Anthraphenol, no charge transfer was shown on semiconducting metal oxides, see appendix B.2 in Fig. B.8, and results on those substrates can therefore be used as a general study material. It can be seen that solid formation leads to faster decay, see Fig. 3.17. Higher crystallinity leads to faster decay of the PL as can be seen on SiO_2 , molecular components lead to slightly slower decay as can be seen on $\text{TiO}_2(100)$. The PL of deep trap of powder shows a different shape of the decay curve, a single exponential decay occurs at the beginning, clearly distinguishable from the exciton PL curves.

Looking at charge transfer at hybrid structures, a resulting decay of a mixture of non-transferring cluster PL induced by defects, internal photoluminescence and decay due to charge carrier loss by charge transfer into the accepting part can be analyzed. In consequence, the important charge transfer times of electrons into the inorganic solid can be calculated, see chapter 6 for more informations, for example in Fig. 6.7.

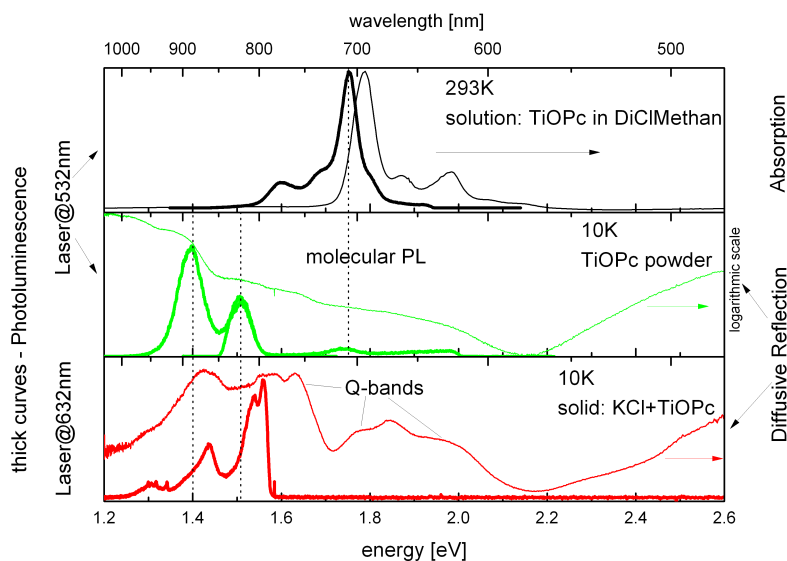


Fig. 3.16.: Comparison of TiOPc in solution, in powder form and as crystal regarding absorbance and photoluminescence spectra.

The upper part shows TiOPc in solution, as already shown before in Fig. 3.10. Thick curves belong to PL and thin curves to absorption. The middle graph shows TiOPc powder, interestingly also a tiny peak of molecular PL can still be seen. The main PL stems from deep traps and is therefore redshifted strongly against PL in solution. Powder-PL is also redshifted against crystals of TiOPc on KCL (lower part), crystalline PL shows no clear peaks of deep traps, so it seems to be produced without defects as occurring in powder.

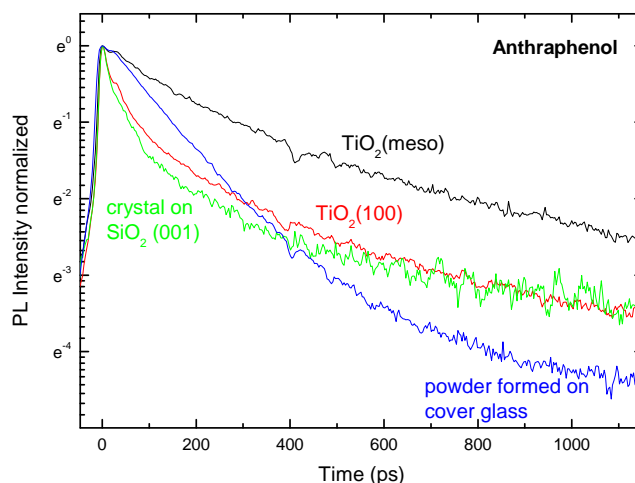


Fig. 3.17.: Connection between ps-TRPL curves and organic material state. A non transferring dye Anthraphenol is used for demonstrating general correlations. From quasi-molecular PL on $\text{TiO}_2(\text{meso})$ to crystalline layer a faster TRPL can be observed. Powder formation leads to a different decay to molecular and layer PL.

4. Experimental: Optical Spectroscopy

In this section, the optical spectroscopy methods used for this work are explained and schematic structures are shown. The basic measuring methods absorption and photoluminescence supplemented by reflection and Raman spectroscopy enable a clear identification of the examined material, a 'fingerprint'. Absorption and luminescence are related, as demonstrated by the Franck-Condon principle (see Fig. 3.13). Time-resolved luminescence gives additional information in which time the excited states decay. This allows identification of a loss channel such as by charge transfer.

4.1. Linear Absorption Spectroscopy

The following figure shows an example of a structure for the absorbance measurement of solutions in cuvettes. Also solid samples can be measured placed instead of the cuvette with a sample holder. The light source used for the UV range is a deuterium lamp (190 to approx. 800 nm); a tungsten incandescent lamp is used for the visible and near infrared wavelength range (370 nm to 1100 nm). The image of the spiral of the tungsten lamp is focused from behind onto the aperture of the deuterium lamp. As a result, both light sources can be optically bundled. The light rays from both lamps are collimated by a converging lens. The parallel light beam passes through the sample and is subsequently focused onto the entrance slit of a spectrograph. A concave, holographic diffraction grating spectrally splits the light beam onto the photodiode array shown. The array consists of a row of 1024 individual photocells, with a wavelength range of 190 nm to 1100 nm. The read-out interval corresponds to 0.9 nm per photocell.

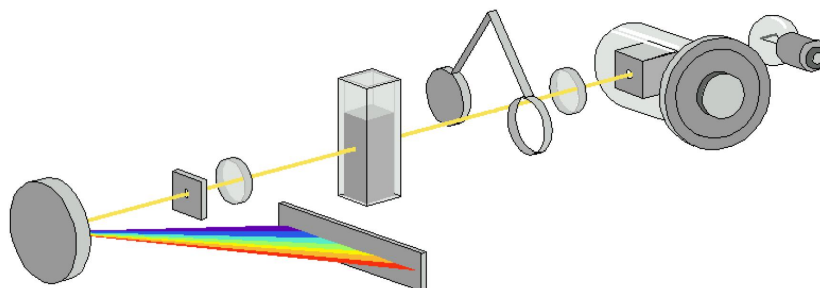


Fig. 4.1.: Schematic drawing of Agilent 8453 UV-VIS spectroscopy system (taken from User Guide)

A more detailed picture of a spectrograph exemplifies Ocean Optics HR4000CG UV-VIS, which has been used in many absorption and photoluminescence experiments. The light is either focussed on the entrance slit (2), or coupled in a glass fiber connected to

an SMA connector (1). The light then reflects off the collimating mirror (4) onto the grating (5), where it is diffracted. Afterwards, a second mirror (6) focuses the light on the CCD detector (8).

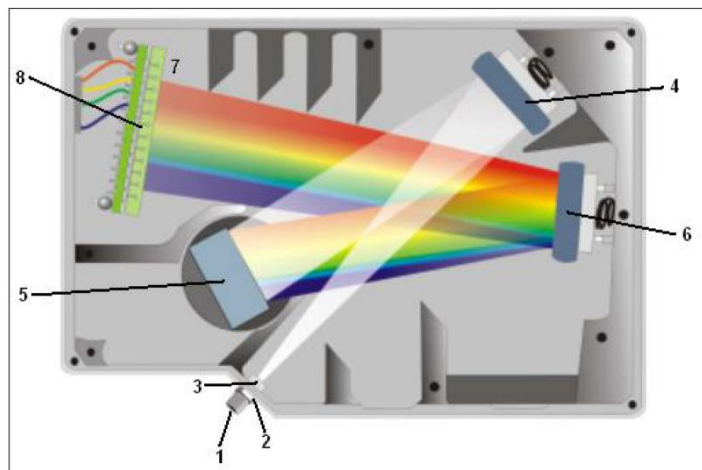


Fig. 4.2.: Schematic drawing of Agilent 8453 UV-VIS spectroscopy system (taken from User Guide)

In order to measure the absorbance, one measures against the reference (i.e. the substrate or air). The result is the absorbance $-\log_{10} \frac{I}{I_0}$ or absorption $-\ln \frac{I}{I_0}$ with I_0 as the blank measurement, I is the transmission. If one wishes to measure the absorption of a material in solution without the solvent absorption, I_0 is accordingly the transmission through pure solution. Lambert-Beer holds $I = I_0 * \exp(-\alpha \cdot d)$, in consequence $\alpha \cdot d = -\ln \frac{I}{I_0}$. With knowledge of the extinction coefficient α the thickness of the layer can be determined by the absorption measurement. However, one must remember that reflection and scattering also appear as absorption, these would have to be extrapolated separately for a clean absorption measurement.

In the absorption study of microscopic structures, a microscope setup must be used. The magnification can be either achieved by magnifying objectives close to the specimen, see for example the modified microscopic Raman stage in Fig. 4.23 with white light coupled in for transmission. Or it can be realized by a magnifying lens system according to the lens equations

$$\frac{1}{f} = \frac{1}{g} + \frac{1}{b}; \quad \frac{B}{G} = \frac{-b}{g}$$

With the latter described method the enlarged image arises at the entrance slit of the spectrometer. By means of generating an intermediate image via a lens system with both concepts it is also possible to measure microscopic absorption in inaccessible places within larger cryostats; cryostats are cooling devices that can be cooled down to 4 – 10 K by helium, thus allowing temperature-dependent measurements. The intermediate image generated by the transmitting sample site is generated by means of a lens system in the case of such an inaccessible sample site. In the intermediate image, an area can now be selected by means of an aperture or pinhole of variable size. The chosen

area can then be enlarged by means of a magnifying lens and is then focused on a spectrometer entrance slit via a focussing lens. If one uses the concept of magnification via lens systems after the intermediate image, then usually no pinhole is needed, since the magnification of the desired object is often greater than the entrance slit. Then only the light transmitted through the microscopic object reaches the entrance slit. The entrance slit thus serves as a selection of the desired image area. If a piece of paper is held in place of the entrance slit, then you can see the enlarged sample image in color. In all concepts, skilful decoupling of the beam path on a camera, for example via a folding mirror just in front of the spectrometer, allows real color images of the enlarged sample to be recorded. The camera acts as the optical control for the area chosen by the pinhole or aperture. For example, if the intermediate image is four times magnified, a 20 μm pinhole positioned in the intermediate image corresponds to a 5 μm area on the sample. Polarization-dependent absorption studies can be realized for all magnifying systems by inserting a polarizer into the beam path.

4.1.1. Basic Absorption Spectroscopy on Organic Materials

In order to investigate an organic material, at first basic measurements should be performed to get to know the basic optical properties of the material. The solvability in different solutions should be investigated and the effect of solvent on the energy level of the absorption spectra.

Absorption spectra of prepared films should be compared with spectra in solution whether solid effects occur (see discussion in theory part about organic semiconductors 3.2, Fig. 4.8, 3.15 and 3.17). The features of organic spectra both of solids and in solution should be identified.

New prepared films should be investigated in an optical microscope. Structures, homogenous or inhomogenous areas can be identified and measured in absorption. Microscopic pictures and microscopical absorption should be performed in order to reveal monocrystalline regions and reveal absorption effects when using a polarizer (see section 5.1.2).

Regarding prepared films with a supposed or revealed crystalline structure and equivalent aligned molecules on a flat surface, tilting and turning the substrate during absorption measurements might give insight into the crystalline structure.

Chemical Shift

Solvents with high polarity (high permittivity) are good solvents for ionic and other polar compounds, solvents with lower polarity (low permittivity) are better solvents for non-polar compounds.

The different polarity of the solvent or the environment also leads to a change in the optical spectra, this is referred to as solvatochromism and is a subject for chromophores. With higher solvent polarity, a blue shift is hypsochromic, a redshift is bathochromic. Which form is present depends on the polarity of the ground state and the excited state of the molecule, since the solvent polarity also alters the orientation and shape of the molecules and thus the energy of the levels.

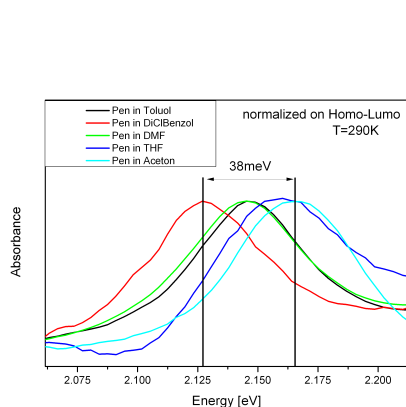


Fig. 4.3.: Pentacene in solution: $\pi - \pi^*$ absorbance spectra. Chemical shift due to changed solvents.

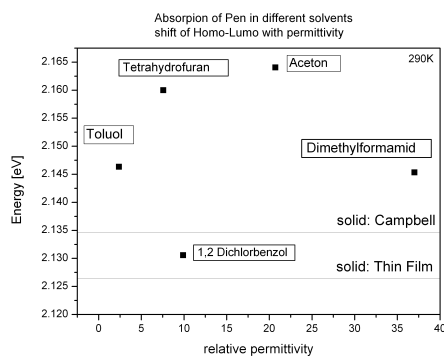


Fig. 4.4.: Pentacene in solution: Energy of the main $\pi - \pi^*$ absorption peak in dependence of the solvent permittivity. No clear correlation can be found. The energy levels of the $\pi - \pi^*$ absorption of two solids are shown for comparison.

For organic molecules such as pentacene and phthalocyanine a correlation is expected. Fig. 4.3 shows a clear shift of up to 38 meV for pentacene due to different solvents. No clear correlation to the permittivity can be seen for pentacene (Fig. 4.4).

Regarding Cu-phthalocyanine (see detailed discussion about Cu-Pc spectra in Chapter 5.2.3) a similar behavior as for pentacene can be seen. A shift of about 20 meV between solvent dichlorobenzene and DMF can be seen (Fig. 4.5). Comparing the energy shift over relative permittivity of CuPc (Fig. 4.6) and pentacene (Fig. 4.4) the trend is about the same as for pentacene. Although the correlation between energy and solvent properties can't be resolved, an analogy seems to exist for different organic materials.

In literature, detailed investigations on solvent shift of D149 were performed by Lohse et al. [122]. They show that the Stokes shift is correlated with solvent polarity and that more protic solvents have faster PL decay than aprotic solvents.

As a result of this consideration of chemical shift, we have to formulate more generally for organic molecules: Strong energy shifts of spectra may be due to the different polarizability of the different solvents or by the combined effect of solvent polarizability and molecular properties. This has to be taken in account when comparing organic molecules with each other or when comparing solutions with solids.

Tilt Experiments

Looking at Fig. 5.1 and 4.22 it is clear that the Thin-Film phase of pentacene is nearly standing upright on the substrate. Therefore, tilting the sample should allow more absorption by the long part of the molecule. After tilting the Thin-Film sample (on sapphire) by 45 degrees, more should be absorbed by the long axis than when keeping the sample perpendicular to the beam path. In Fig. 4.7 absorption of the long axis actually increases a bit, but not as relevant as expected. With normal incidence of light, there

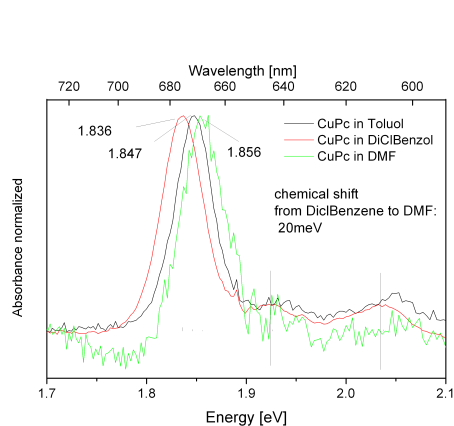


Fig. 4.5.: Cu-phthalocyanine in solution: $\pi - \pi^*$ absorbance spectra. Chemical shift due to changed solvents.

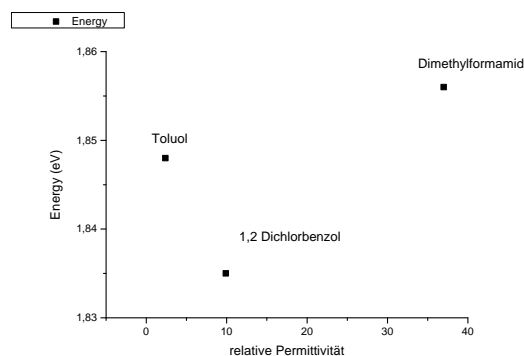


Fig. 4.6.: Cu-phthalocyanine in solution: Energy of the main $\pi - \pi^*$ absorption peak in dependence of the solvent permittivity. No clear correlation can be found, but the trend is similar as for pentacene (see Fig. 4.4).

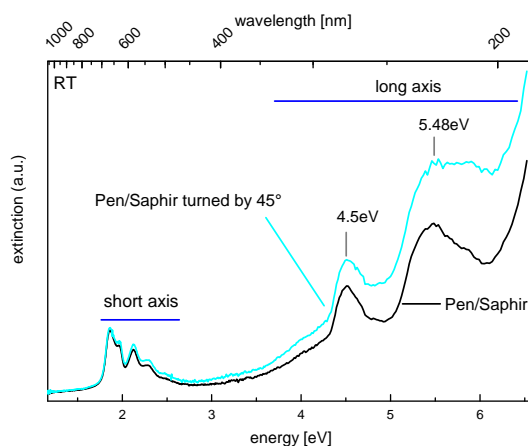


Fig. 4.7.: Absorbance measurements of thin film phase pentacene on sapphire. Short and long axis absorptions are indicated, as discussed for example in detail by Anger et al. [4].

is already absorption of the long axis, since the molecules are not completely upright. If absorption of pentacene crystals is compared with pentacene in solution (see Fig. 4.8), a much stronger effect can be seen for the long axis absorption. Due to the chaotic order of the pentacene molecules and therefore equal distribution of long and short axis the long axis absorbs much stronger. After Anger et al. [4] long axis states were determined for 3.73 eV and 4.40 eV. Those states can be found also in the solution spectra shown here, but the detailed higher vibronic states in the solution spectra questionate the energies of Anger et al. since some kind of replica are at higher energies of the stated states instead of at lower energies.

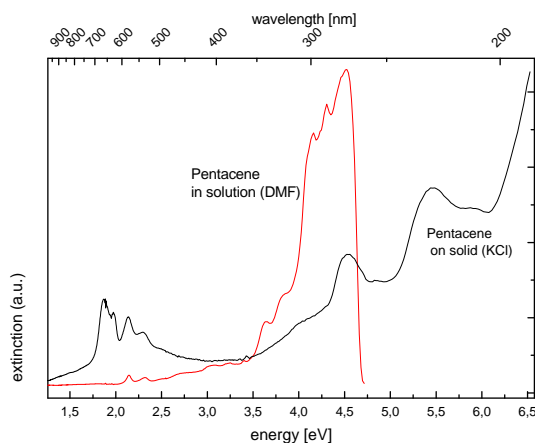


Fig. 4.8.: Comparison of absorption of pentacene in solution (red curve) with pentacene as crystalline structure on KCl.

The long axis absorption is much stronger viewable in solution.

4.2. Photoluminescence

Excitation of a photoluminescent sample by a suitable laser yields the photoluminescence (PL) which is correlated with the absorption. The PL identifies the examined material like a fingerprint, the emission therefore gives a detailed insight into the material properties (see sections 3.1 and 3.2). The molecules with visible absorption often emit strongly in the visible and thus become interesting for optical applications.

The temporal decay dynamics of the PL gives insight to internal processes like transfer times or loss channels. In time resolved PL (TRPL) excitation is realized by a very short light pulse instead of continuous wave excitation for continuous wave PL. A triggered detecting system records the PL emission as a function of time. Time resolution for interest in this thesis down to ps is possible with streak cameras. The experimental stages of PL and TRPL are described in the following subsections in more detail.

4.2.1. Continuous Wave Photoluminescence

The following scheme illustrates the principle experimental stage for photoluminescence.

Different lasers can be used as excitation sources. Plasma laser based on the light emission of excited ions in ionized gas deliver 325 and 442 nm (He-Cd), 514 nm (Ar) and 632 nm (He-Ne). Modern diode lasers are available for the range from UV to NIR, in this lab 405, 442 and 632 nm are available. The frequency-doubled Nd-YAG laser with a strong green emission at 532 nm is pumped by a 808 nm laser diode.

The sample is hit by laser light either entering the optical path between sample and spectrometer by a semi-transparent mirror or entering from the side as shown in Fig.4.9. The laser light can be focussed or widened if a lens system is used between laser and sample. A powermeter gives the opportunity to determine the laser power, i.e. the delivered energy per second. If the photon energy of the laser is able to excite electrons of the sample in higher states the laser energy gets absorbed. If photoluminescence

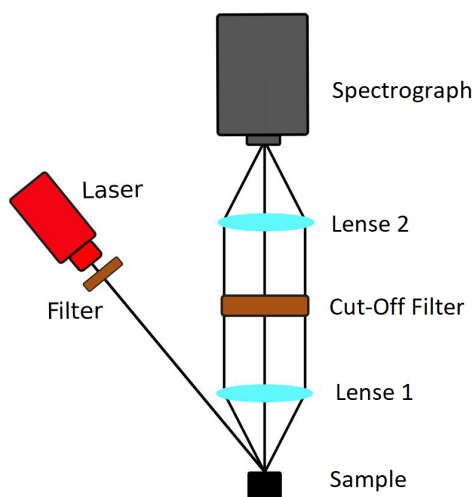


Fig. 4.9.: Outlined is the schematic structure of a photoluminescence measuring station. A laser excites electrons in the sample (optionally positioned in a cryostate), the emerging PL is imaged via a lens system on the entrance slit of a spectrograph. (Scheme taken from Examensarbeit of Luise Rost [168])

follows, the radiation is isotropic in space. The room angle part of the radiation is collected by the collimating lens.

The image of the generated PL may be 1:1 at the entrance slit of the spectrometer, or again include magnifying optics as described above in the absorption stage. A magnification enables the optical control of the sample part hit by the light, in this way for example a small organic crystal of the size of some μm or a special layer region can be hit very defined. Suitable long pass filter are chosen in order to filter out possible laser light reflected from the sample but in same time transmitting the photoluminescence emission at lower photon energies.

For sufficient photoluminescence light a compact spectrometer as usually also used for absorption measurements can be used, for example the Optics HR4000 UV-VIS with a fixed entrance slit of $5\ \mu\text{m}$. It detects the whole spectrum at once using an array of detectors such as a charge-couple device (CCD). Alternatively and especially useful for low photoluminescence intensity a less compact but more variable spectrograph system can be used to detect the PL spectra. The spectrum is recorded by scanning the wavelength region by turning the built in dispersive element of the spectrometer, either prism or grating, and in the same time measuring the intensity of the light at each scanned wavelength with a sensitive detector such as a multiplier tube. The slit width of the entrance slit can be varied up to mm size. Even very low photoluminescence intensities can be detected with such a variable spectrograph setup.

Like in absorption spectroscopy a helium cryostate can be used for the sample to cool down to 4 K. This is useful especially for charge transfer excitonic transitions in organic materials, which are often not luminescent at room temperature. (Excitons in organic materials often have a very low binding energy, so at room temperature the exciton is separated and only deeper traps can be seen in luminescence (see for example Phthalocyanine, Fig. 5.45).)

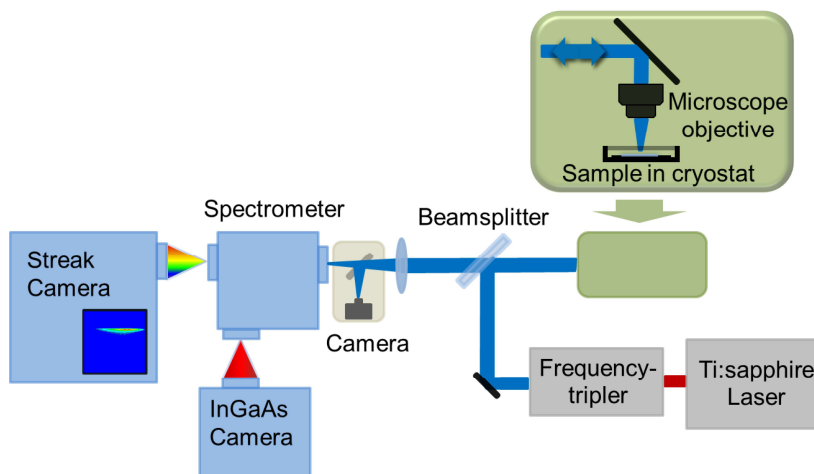


Fig. 4.10.: Schematic drawing of the confocal ps-TRPL setup. A microscope objective is used to focus the laser light on the sample surface. Only photoluminescence coming exactly from the focal plane will be detected from the streak camera. An optical control enables precise positioning of the sample site. Figure is taken with permission of Nils Rosemann from [166].

4.2.2. Time-Resolved Photoluminescence from 15 to 3000ps

A schematic sketch of the setup used for most TRPL measurements is given in Fig. 4.10. Mainly, it is a PL stage with a streak camera as detector. The laser is coupled in the beam path by a beamsplitter and is focussed by a microscope objective onto the sample surface. The stage is very sensitive to the focal plane of the objective, only PL from the focal plane will reach the streak camera. Optionally the light can be decoupled from the spectrometer onto a ccd array or a infrared sensitive InGaAs Camera, but this option was not used for the results shown here. As an optical control a camera is installed which can be activated by an optional mirror in the beam path right in front of the entrance slit. This confocal optical system including the optical control allows a very precise sample investigation with high PL sensitivity and good reproducibility of the measurement results. The programmed labview software of Nils Rosemann allows a fast and clear evaluation of the TRPL decay curves and spectra.

The method of time resolved photoluminescence with a streak camera and the used experimental stage including technical data are described in the following paragraph. It is based on the more detailed description in [166, 32]. A standard titanium-sapphire laser (Ti:Sa) emitting ~ 100 fs long pulses in the wavelength range of 700 - 1100 nm (1.12 - 1.77 eV) with a repetition rate of 78 MHz is used as a light source. The Ti:Sa is pumped by a neodymium-doped yttrium aluminium garnet (Nd:YAG) laser that is intra-cavity frequency doubled emitting a wavelength of 532 nm. The desired wavelength is pulsed by optimizing the mirror system and two prisms at a particular resonance of the laser modes in the cavity. The power of the Ti:Sa is up to 2.8 W at about 800 nm and decreases to lower and higher energies. The outgoing laser energy can be doubled or tripled afterwards by a frequency doppler or tripler, so that pulses in the visible or UV range are possible (235-550 nm). However, the ideal conversion efficiency is 22

and 1% for doubler and tripler, respectively, so the resulting power is correspondingly lower. For the wavelength of about 410 nm usually used in this thesis a maximum of about 400 mW is possible after good optimization of the lasing system. Due to the focussing of the laser radiation, much lower power is sufficient to achieve a good PL. For the organic samples investigated in this thesis including organic solar cells it is important not to destroy the samples by too high power inputs, in consequence the laser power is attenuated. Even for organic samples with very low photoluminescence it is better to integrate over longer times with a high gain than to use very high laser power.

The monochromator in the spectrometer with a chosen grating of 40 slits per mm results in a wavelength dispersion of 250 nm. The photons of the selected wavelength range hit the photocathode of GaAs which has a sensitivity in the region of 250-850 nm. The generated electrons are then directed into the streak camera.

The electrons are accelerated in the directly connected 2D photomultiplier. In this array of many small tubes a higher current is generated, the strength of amplification is regulated by the gain. The electrons are accelerated through two capacitors in vacuum and thereby deflected in the z-axis by an applied AC voltage. Then they encounter a luminous material, which converts the stream back into photons. These photons hit the CCD directly behind. The sine AC voltage across the capacitors gives the time resolution by vertical deflection of the electrons, but not every part of the sine period is usable. A full sine period of the AC voltage is 12.5 ns resulting from about 80 MHz of the laser pulse frequency. The sine is linear in the middle part, nonlinear in the curvatures. The linear part around the zero crossing (1.5 ns) can be used well for reliable time resolution. The alternating voltage deflects the electrons more or less depending on the voltage in the z-plane. One can read off the 1.5 ns time window just by reading the z-axis with a Si diode array, at this chosen time resolution 512 pixels are equivalent to 1500 ps which results in about 3 ps per pixel time resolution (see resulting image of the ps-stage 4.11, y-axis). By accumulating the measurement at many sine passages, a reliable time course is created. Depending on the delay against the trigger point one can access to different times after the laser pulse, up to 5 ns are still possible. The trigger point defines the time difference from laser pulse generation to laser pulse detection which is depending on the electronic system and optical pathway of the light, the delay defines the time difference to the beginning time of laser pulse detection.

The result of this ps-stage software is as shown and explained in Fig. 4.11.

The decay of the laser pulse is shown in Fig. 4.12. The time resolution is limited by the response time of the detector. Measured decay times of samples equal to the laser decay time of 15 ps show a decay faster than the response time of the detector which cannot be evaluated by this chosen time resolution. A higher time resolution can be chosen in order to avoid this problem, for example 512 pixel are then equivalent to 500 ps. For an evaluation of times close to the response time of the detector an unfolding of the response function and the sample decay curve would be necessary. In this thesis neither a higher time resolution nor an unfolding of functions was necessary.

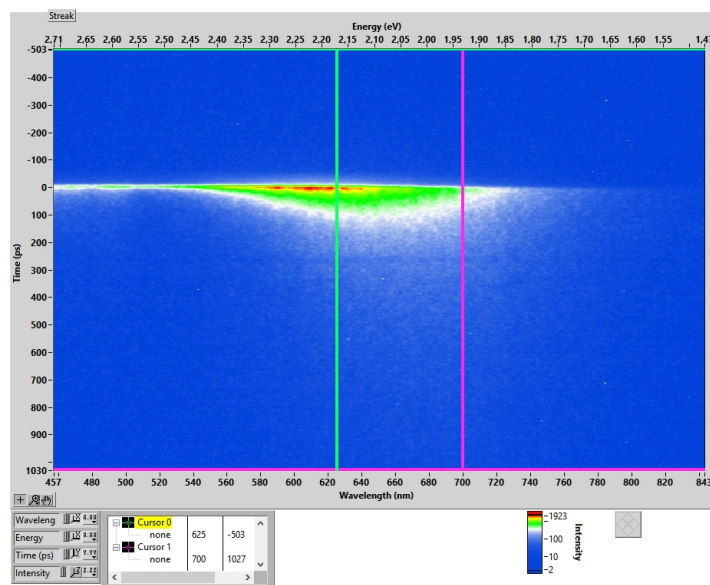


Fig. 4.11.: Example for ps-Stage software HPDTA result which is used to evaluate the decay times. The x-axis is the calibrated wavelength in nm and energy scale in eV and shows the spectra over the wavelength, the coloured scale explained below the image indicates the intensity. The y-axis corresponds to the time resolution in ps. Integrating the spectrum region as chosen by the two vertical lines for every given time data point, the time resolved photoluminescence of the chosen spectral region is calculated. An example is shown in Fig. 4.12, when the laser signal decay is evaluated. An additional evaluation software was used. The resulting decay curve for this image can be seen in Fig. 6.25, green curve.

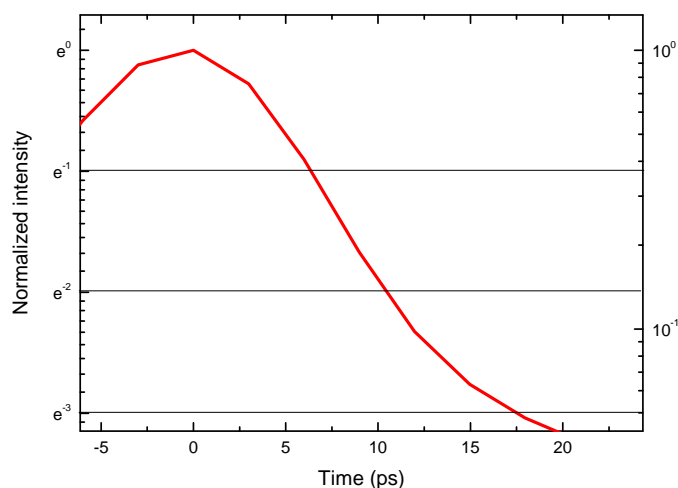


Fig. 4.12.: Laser decay of laser at 443 nm, shown as integrated spectrum of 415 nm to 490 nm over time. After about 10 ps the laser intensity decreases by e^2 to a percentage of about 13.5%, after about 17 ps the laser intensity decreases by e^3 to a percentage of about 5%.

4.3. Reflection and Straylight

A reflection measurement is a useful supplement or even an alternative to absorption measurements under certain conditions. Specular and diffuse reflection measurements can help to obtain a meaningful spectrum similar to the absorption spectrum. Scattering effects in the absorption spectrum can be identified by reflection measurements (see examples in 4.3.1). Clearly, a reflection measurement gives the opportunity to retrieve informations of layers on opaque substrates, for example on a silicon wafer. Reflection was successfully used in this work for organic molecules pentacene (5.1.5) and phthalocyanine (5.2).

In principle the experimental stage is similar to an absorption measurement. For a reflection measurement a light source must illuminate the sample and the reflected light of the illuminated area is imaged onto the entrance slit of a spectrograph. As described in the section of the linear absorption measurement, various magnifications of the sample site via objectives or lens systems can also be achieved here, even in the case of poorly accessible sample sites, for example with the sample positioned in a larger cryostat. In addition, a polarizer can be installed at any location of the beam path in order to be able to perform polarization-dependent reflection measurements. For each measurement, a reference measurement must be performed. When measuring a transmissive layer on an opaque substrate, the substrate should be measured as a reference. If the influence of the substrate is negligible, for example with a very thick layer, then the reference is the specular reflection of a mirror or the scattering reflex of a diffusely scattering aluminum plate, depending on whether specular or diffuse reflection is measured.

If a sample is illuminated in an angle from the side, the spectrograph can be used to detect either the specular reflection or the diffuse reflection, depending on the angle of rotation of the sample between the light source and the reflection beam path. In the case of diffuse reflection, one only collects the scattered light of the sample and does not allow the specular reflex to reach the entrance slit.

In some cases, it is important at which angle the light hits the sample. For example, standing molecules on the substrate might absorb differently from tilted or lying molecules, in consequence more lateral instead of vertical light incidence would reflect differently. Therefore, for a vertical light coupling to a sample surface which is lying at right angles to the light beam, the light source is coupled to the sample via a semitransparent mirror in the vertical light path; the mirror reflects the light on the sample, from there the reflected light can pass the semitransparent mirror on the return path again and is then forwarded to a spectrograph. The same stage as for Raman measurements was used, but with white light instead of a laser as the light source (see Fig. 4.23). In the section on reflection on pentacene (section 5.1.5), this construction was used to perform the specular reflection measurement. Angle-dependent diffuse reflection measurements can also be carried out in such a structure if the sample is not aligned perpendicular to the beam path but is tilted.

If photoluminescence occurs when the sample is illuminated, it overlaps the reflection signal, which leads to changes of the reflection spectrum. This effect must be taken into account in the analysis, for example regarding Titanyl-Phthalocyanine in 5.2.4.

Calculation of absorption from reflection, three cases:

- Thin little absorbing layer with structures smaller than the wavelength of light: specular reflection measurement through a low absorbing layer with negligible scattering corresponds to an absorption measurement through approximately the double layer thickness of the layer with the substrate acting as a mirror. The calculation stays the same as with absorption measurements: $Abs = -\ln(\frac{I}{I_0})$
- A thick absorbing crystal with little scattering: If no light transmitted through the sample leaves the sample, that means only reflected light is leaving the sample which was directly reflected at the interface by the reflection law, the calculation is $Refl = +\ln(\frac{I}{I_0})$. The sign is changed in comparison to an absorption measurement, since only reflected light from the interface will reach the detector which is not reduced in intensity by absorption in the layer.
- A scattering sample with structures in the range of the wavelength of light: the diffusive reflection is measured instead of the specular reflection, in consequence the scattered light from the surface or from scattering centers beneath it reaches the detector, without being reduced in intensity by absorption inside the layer. Again the calculation is $Refl = +\ln(\frac{I}{I_0})$. This method is very effective with samples having scattering problems in absorption measurements but may also be useful for all other samples.
- Mixture: a mixture of absorbing and reflecting properties is usually difficult to interpret, since transmission is superimposed with reflection. But yet strong structures might show in the spectra which can be useful for interpretation.

To sum up, reflection measurements can help in order to gather spectroscopic informations from opaque samples like thick crystals or layers on opaque substrates. Scattering errors in absorption spectra due to roughness or small structures can be detected and avoided. The similarity between transmission and reflection (see Fig. 4.13) and the resulting absorption is shown for example by Wojdyła et al. [217] for the case of Zinc-Phthalocyanine thin films on quartz (and further phthalocyanines). In that paper it is also discussed how to achieve the complex refractive index and dielectric constants directly from spectral data. In Fig. 4.14 the resulting spectra for n and k reveal the similarity between the inverse transmission and the extinction coefficient k , in consequence reflection spectra can give useful spectra and reliable insights into the possible absorption structure.

4.3.1. Examples: Specular and Diffuse Reflection

Pentacene

In chapter 5.1 pentacene is investigated thoroughly, see also section 4.4 and Fig. 4.22 for more introductive informations. Large monocrystalline crystals in Siegrist phase were grown by Andrea Karthäuser, group Witte. The specular reflection of a very thick hardly transmitting crystal is compared with the absorption measured on a very thin crystal on glass, see Fig. 4.15. As a result, one can see comparable curves when using $Refl = +\ln(\frac{I}{I_0})$ for reflection and $Abs = -\ln(\frac{I}{I_0})$ for absorption as calculations.

In section 5.1.5 polarization dependent reflection measurements on different pentacene phases are shown, including the thick Siegrist crystal.

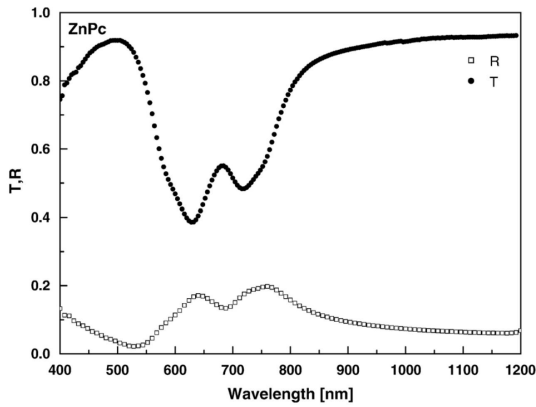


Fig. 4.13.: The similarity between transmission and reflection is shown for thin layers of ZnPc on quartz (Fig. from[217])

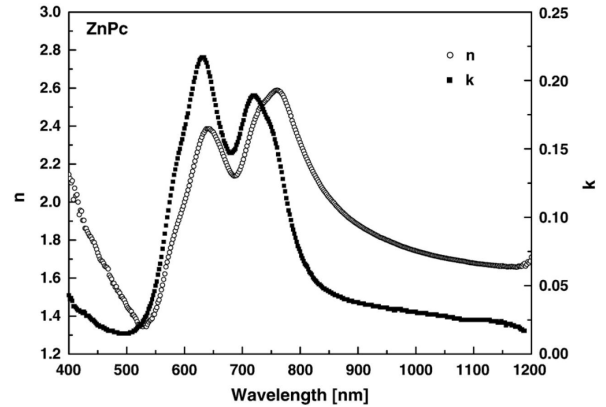


Fig. 4.14.: Refractive index n and extinction coefficient k as a function of wavelength (Fig. from[217]).

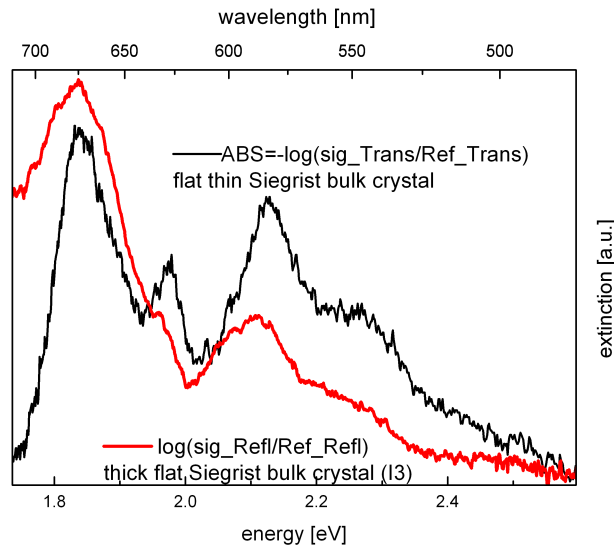


Fig. 4.15.: Comparison of Absorption and Reflection for monocrystalline pentacene Siegrist phase crystals. A thick crystal was used for the reflection measurement while a thin crystal was used for the absorption measurement. Both spectra look similar, although calculated differently.

CuPc

In section 5.2.3 Copper-Phthalocyanine (CuPc) is introduced. For standing CuPc on glass (Fig. 4.16) the layer is homogeneous with no larger crystal structures and the absorption measurement shows no scattering effects. Measurements in specular reflection have to be calculated with $Abs = -\ln(\frac{I}{I_0})$, that means that here the upper discussed case of an absorption measurement through approximately the double layer thickness is present, the glass acting as the mirror substrate. In contrast to that, the absorption of lying CuPc in Fig. 4.16 shows strong crystal formation. This leads to scattering effects in the absorption spectrum. Unfortunately, absorption spectra under 100x mag-

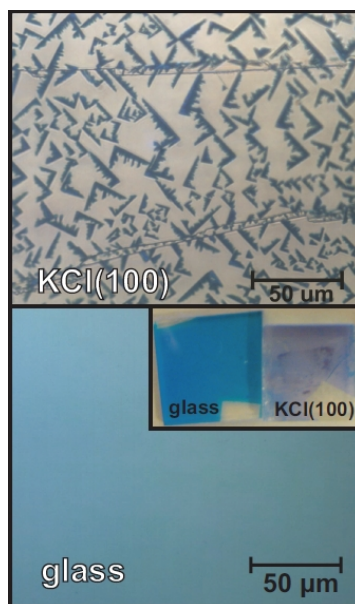


Fig. 4.16.: Microscopic pictures of standing CuPc on glass and lying CuPc on KCl taken from Jan Kuhnert, Group Heimbrodt, Marburg [111]

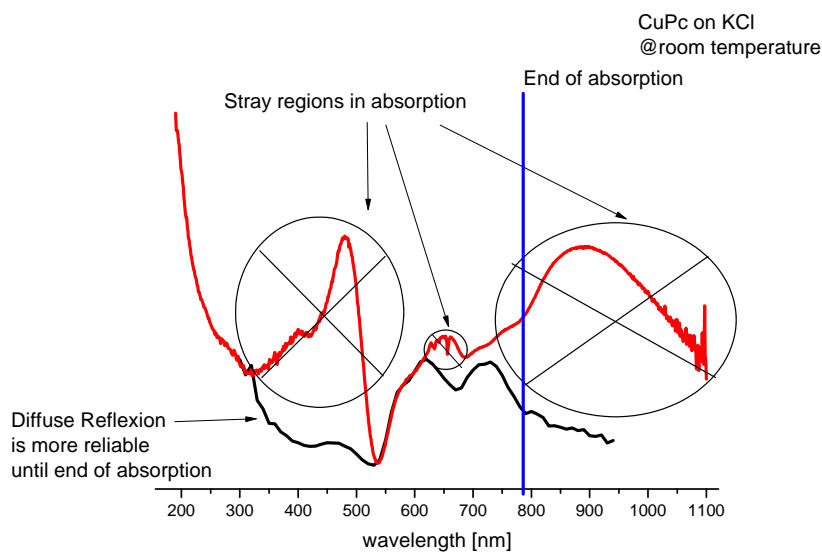


Fig. 4.17.: KCl+CuPc - comparison of diffusive reflection and absorbance identifies stray effects

nification on one single crystal are difficult to achieve due to partial transmission limit, only some main features can be detected. In consequence, the sample is measured in diffuse reflection which minimizes the scattering effects (see Fig. 4.17). The reflection formula $Abs = +ln(\frac{I}{I_0})$ is used. The clear identification of straylight is one advantage of diffusive reflection measurements. The calculated reflection spectra are reasonable for a first estimation, since they roughly confirm the main features in the absorption spectra.

TiOPc

Titanyl-phthalocyanine (TiOPc) will be introduced in section 5.2.4. Absorbance measurements on standing TiOPc on glass and lying TiOPc on KCl (Fig. 5.42) show spectra different to literature due to scattering effects in the red part of the spectrum. Considering only the absorption spectra, a first indication of stray light is the variation of the lower energy spectral part depending on the chosen sample area or method of measurement (parallel light, focused light, ulbricht sphere, see Fig. 5.43a and 5.43b). A next indication for straylight is the photoluminescence (PL) region: since TiOPc shows photoluminescence in contrast to CuPc, especially at 10 K, in the far red PL region no absorption should be present, except a mixture of phases occurs showing different PL in one focus point. In consequence, for single phase samples, absorbance region can be identified roughly by identifying the photoluminescence region. A detailed discussion for TiOPc can be found in section 5.2.4.

Interestingly, the photoluminescence region is connected with the scattering region. Reflection spectra are superimposed by the PL (see Fig. 5.50 and 5.51).

Diffuse and specular reflection measurements can support to verify stray light. In addition, reflection measurements provide a high level of spectral detail. TiOPc reflection spectra are discussed in section 5.2.4.

4.4. Raman Spectroscopy

Inelastic scattering of light by molecular vibrations was first reported by Raman[158] who got the Nobel prize in 1930 for his discovery. Today Raman scattering have become standard spectroscopic tools in the study of semiconductors and the method is developing strongly as analysis tool and optical process control in industry. A deeper insight into Raman theory can be found in Yu Cardona [225], a compact overview in [73]. A review about Raman measurements on organic semiconductors based on conjugated molecules is published recently [218]. This short theoretical introduction is based on both books and the review and is further leaned on the bachelor thesis of Matthias Weber [211] and Mikko Wilhelm [212]. The experimental part is based on the diploma thesis of Andreas Schneider [180].

4.4.1. Theory

Although most of the light travelling through a medium is either transmitted or absorbed following the standard laws of reflection and refraction, a very tiny fraction is scattered in all directions by inhomogeneities inside the medium. These inhomogeneities may be static or dynamic. Defects such as dislocations in a crystal are static scatterers and scatter the light elastically without frequency change, the Rayleigh scattering. Fluctuations in the density of the medium that are associated with atomic vibrations are examples of dynamic scatterers. Some scatterers relax to a different vibrational state, which is Raman scattering. The scattered photon can either have less energy than the initial one (Stokes) or gain energy in comparison to the initial photon energy (Antistokes), see Fig. 4.18. Antistokes Raman depends on the initial populations of ground vibrational states and is therefore typically weaker than Stokes scattering,

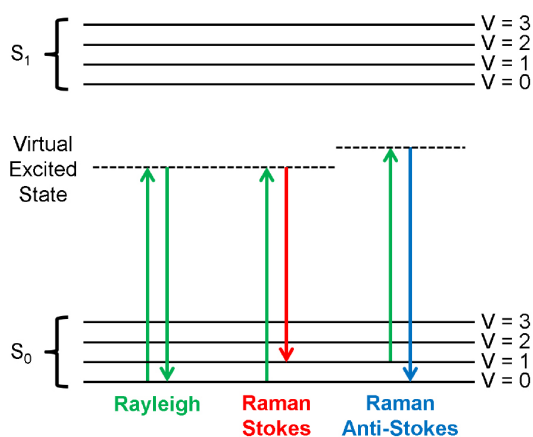


Fig. 4.18.: Figure and capture taken from [218]: Diagram comparing energy level transitions for Rayleigh and Raman scattering with respect to the ground and first excited electronic states (S_0 and S_1), and vibrational energy levels with index V .

$$A_g = \begin{pmatrix} a & 0 & 0 \\ 0 & b & 0 \\ 0 & 0 & c \end{pmatrix} \quad B_{3g} = \begin{pmatrix} 0 & 0 & 0 \\ 0 & 0 & f \\ 0 & f & 0 \end{pmatrix}$$

Table 4.1.: Raman tensors of pentacene

especially at not hot temperature like room temperature. In this work, only Stokes scattering will be discussed. Since the Raman signal is weak, an intense light source such as a laser is needed. While the Rayleigh scattered light is filtered out, Raman scattered light is reaching the detector (experimental setup in subsection 4.4.2).

In this work, pentacene is investigated due to its model character as simple planar aromatic system. [30] estimated Raman modes by DFT/B3LYP/6-31G(d) calculations and compared the theoretical values with experimental results.

Two examples of vibrations in pentacene are shown in Fig. 4.19. The band at 1178 cm^{-1} (A_g) is related to strongest C–H in-plane bending modes, it is related to the symmetric motion of H-atoms located on both sides of the pentacene molecule. The 1378 cm^{-1} (B_{3g}) band belongs to the aromatic C–C stretching modes, its asymmetric vibration lies also in the molecular plane [30].

A_g and B_{3g} are Raman tensors. Mathematically, a Raman tensor describes a depiction that maps the electric field vector onto the polarization vector.

In order to be able to specify Raman tensors for the individual vibrations, the molecule must be provided with a coordinate system, see Fig. 4.20.

Under these assumptions, the considered Raman tensors then have the following form in table 4.1:

The intensity I of a mode is, as in equation (4.1), proportional to the magnitude square of the product of incident light \vec{e}_{in} , Raman tensor of the mode \hat{R} and stray light \vec{e}_{out} .

$$I \propto |\vec{e}_{in} \hat{R} \vec{e}_{out}|^2 \quad (4.1)$$

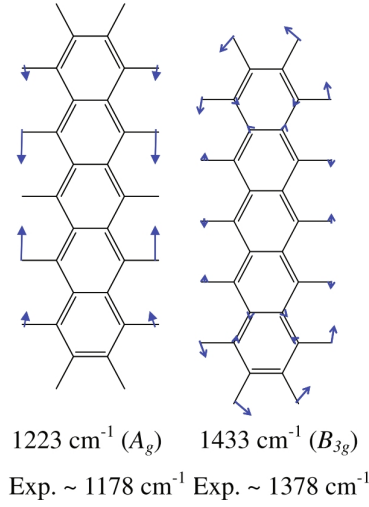


Fig. 4.19.: Figure and caption taken from [30]: Shows a representation of two A_g and B_{3g} vibrational modes of pentacene as determined by a DFT/B3LYP at 6-31G(d) calculation of an isolated pentacene. The vectors representing the atom displacements in the Cartesian coordinates are multiplied by a factor of three.

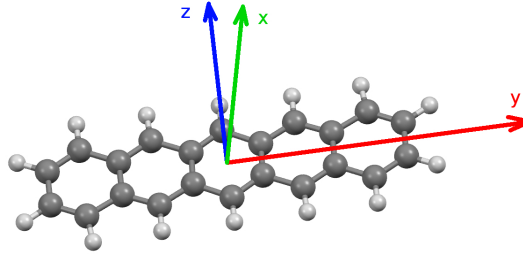


Fig. 4.20.: Choice of an orthogonal coordinate system to specify the Raman tensors of the pentacene molecule. The x-axis protrudes vertically from the molecular plane. Figure and capture taken from [211].

In the case of B_{3g} symmetry, the equation then results in equation (4.2).

$$I \propto |\vec{e}_{in} \widehat{B}_{3g} \vec{e}_{out}|^2 = f^2 * |y_{in} z_{out} + z_{in} y_{out}|^2 \quad (4.2)$$

The mode intensity I is therefore maximal when the incident and scattered light is polarized in the y - z plane of the molecular system. Since the electric field of the light is polarized perpendicular to the direction of propagation, it follows that the intensity I is maximum, as long as the light is irradiated into the molecular system from the x -direction. The light would then impinge perpendicular on the flat side of the pentacene molecule. If the light does not hit the flat side perpendicularly by not coming directly from the x -direction, the intensity I is lower.

For the A_g -mode follows accordingly

$$I \propto |\vec{e}_{in} \widehat{A}_g \vec{e}_{out}|^2 = |x_{in} a x_{out} + y_{in} b y_{out} + z_{in} c z_{out}|^2. \quad (4.3)$$

Since a , b , c are not known and may be different for each A_g mode, this is not evaluable in our case. As a consequence, the intensity of a B_{3g} mode reveals lying pentacene

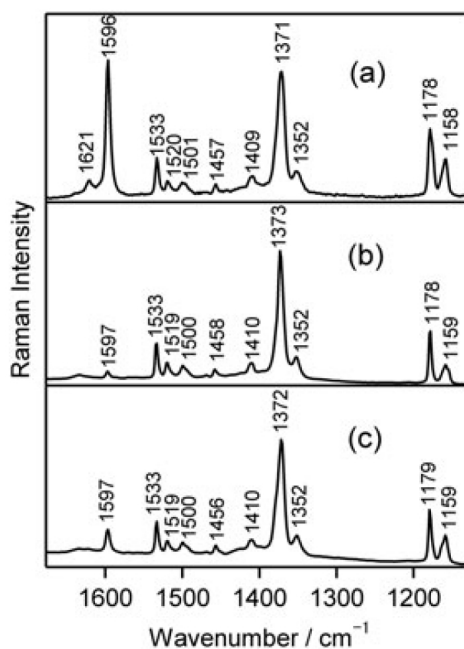


Fig. 4.21.: Raman spectra of pentacene: (a) crystalline powder, (b) 1.54-nm phase film (thickness, 20 nm, ThinFilm), and (c) 1.44-nm phase film (thickness, 100 nm, Campbell). Figure and capture taken from [184]

while an A_g mode should be stable for every possible pentacene orientation against the incoming light. The ratio of a B_{3g} and a A_g mode is correlated to the tilt angle of the molecules. This idea is discussed for example in [184] and [134]. Hosoi et al. [88] demonstrated that the relative intensity of the band at 1596 cm^{-1} (B_{3g}) against the intensity of the 1533 cm^{-1} (A_g) band is sensitive to the tilt angle of the pentacene molecule. The same intensity ratio was chosen by [220]. It has to be taken into account that the mode 1378 cm^{-1} (B_{3g}) shown in Fig. 4.19 is overlaid by the mode 1371 cm^{-1} (A_g) [30, 220] and is therefore not reliable for evaluation. Fig. 4.21 by [184] gives insight to Raman spectra of pentacene powder, pentacene ThinFilm phase and pentacene Campbell phase. A strong variation at 1596 cm^{-1} (B_{3g}) is obvious. The more isotropic distribution of molecules in pentacene powder results in a stronger signal for lying pentacene at 1596 cm^{-1} (B_{3g}). At the same mode Campbell is a bit stronger than ThinFilm, this can be interpreted as stronger tilted molecules for Campbell.

We chose 1596 cm^{-1} (B_{3g}) as the B_{3g} mode in our measurements. Since the mode around 1175 cm^{-1} (A_g) is relatively stable in all our measurements, we chose it as the A_g mode. We verify and complete the literature results by studying the Raman spectra on three pentacene phases Campbell, Siegrist and ThinFilm. It is again shown that we can detect lying and standing molecules clearly with Raman (Fig. 5.26 in results). We can even draw conclusions about the phases of the molecules from the peak relation (see results in section 5.1.6). However, a relationship between the tilt angle of the phase and the B_{3g} mode is not trivial since two molecules in the unit cell exist for crystallized pentacene (Fig. 4.22). Due to their different tilt angles to the substrate as well as different herringbone angles, both unit cell molecules have individual projection

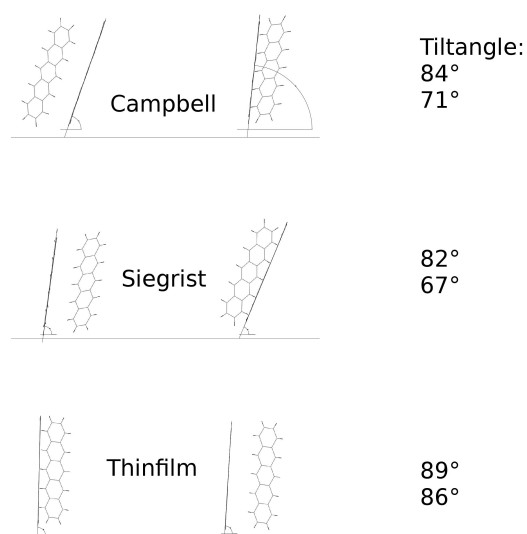


Fig. 4.22.: Representation of the tilt angle of the different pentacene phases Campbell, Siegrist and ThinFilm

surfaces in the y-z plane (for light impinging on the sample from above in x-direction) and thus different relevance for the B_{3g} signal.

4.4.2. Experimental Setup

The experimental setup is shown schematically in Fig. 4.23. The excitation light source is an argon-ion laser (Melles Griot 543) with a wavelength of 514.5 nm which is circularly polarized by a $\lambda/4$ plate. The laser light is guided through a glass fiber G_1 into a microscope (Olympus BX41 with an extension of Jobin Yvon), where it is spectrally filtered with a bandpass filter IF to remove interfering plasma lines. The excitation light is unpolarized but can be polarized horizontally or vertically with a polarizer P_2 . It encounters a holographic notch filter NF. This is a narrow-band filter which has a reflectivity of 99.9999% around the laser line but is almost transparent in the other wavelength ranges. The flanks of the reflection band are very steep, the reflection band region is -100 cm^{-1} to 200 cm^{-1} , corresponding to about $\pm 5 \text{ nm}$.

The notch filter reflects the incoming laser light (green) through the optical pathway into the objective of the microscope, which focuses it on the sample. The sample is attached to an X-Y translation stage. The scattered light is again collected in the objective lens. A half transmitting mirror (HM) can be put into the beam path which enables an optical control of the sample surface and the right focus by a CCD camera, therefore white light (blue) has to be coupled in with the optional HM either in transmission from downside the sample or in reflection from upside. The backscattered light reaches again the notch filter which filters out the elastic (Rayleigh) scattered component and the specular laser reflex, while the Raman scattered light is imaged by a lens onto the confocal diaphragm (BL) (intermediate image plane). With a subsequent optional polarizer P_3 , a horizontal or vertical polarization direction of the scattered light can be selected. While the optical control sees a larger sample area depending on the objective (10x, 50x or 100x) serving

as an overview, the confocal diaphragm BL chooses a variably smaller area in the intermediate image plane which afterwards is focused in the entrance of the glass-fiber G_2 . In consequence, a customized area size can be selected from the enlarged sample from which the Raman signal is to be collected. In principle, resolutions down to $1\ \mu\text{m}$ are possible with the $100\times$ magnification, providing a strong Raman signal. The light is conducted via a glass fiber G_2 and focused by a lens system L to the entrance slit of the spectrometer (Acton SpectraPro 500). The spectrally dispersed light is detected with a nitrogen-cooled CCD (Princeton Instruments Spec-10:100B/LN). This has a chip size of 1380×100 pixels, which are binned vertically in the spectroscopy to 1380 superpixels.

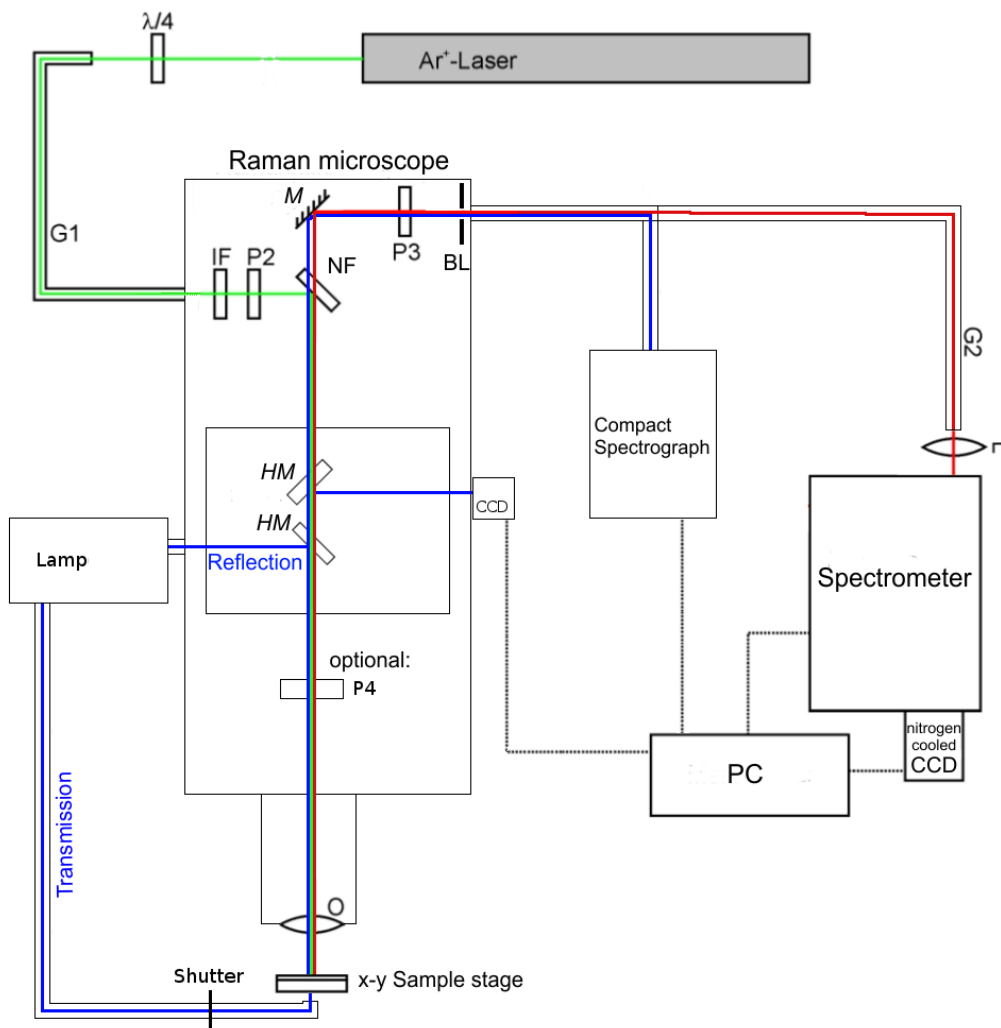


Fig. 4.23.: Scheme of the experimental setup for Raman spectroscopy. With the same stage slightly modified, transmission, reflection and photoluminescence measurements are possible, also polarization dependent. For polarized photoluminescence, a linear polarizer has to be positioned between P_3 and the image blend BL . For polarized absorption and reflection measurements, a polarizer P_4 can also be positioned in the beam path between lamp HM and objective O .

4.5. Electrooptical Measurements: Applied electrical bias on DSSCs

In order to determine the electric behaviour of a solar cell the current-vs-voltage characteristic is measured. The device built-up for this purpose can provide a voltage and in the same time can measure the currents through the device itself. This measured current flows between the two electrodes of the solar cell.

During illumination of the solar cell either by suitable light or laser, short circuit current flows if both electrodes are shortcut by a cable or by the device with a bias voltage of 0 V.

In Fig. 4.24 spectra of a DSSC with sensitizer indoline dye D149 is shown with (cell at 0 V) and without shortcut electrodes (cell at V_{OC}). In order to see the open circuit voltage according to the impinging light, the contacts between the electrodes can be removed or the applied reverse bias between the electrodes is changed until no current flows through the device anymore.

A slightly lower PL indicates that more charge transfer and less intrinsic recombination of D149 occurs in a shortcut cell. The little increase of charge transfer with shortcut electrodes results in a slightly faster PL decay, see Fig. 4.25. Those changes are not prominent but can prove already the method without the use of a I-U-device, just by connecting the two electrodes.

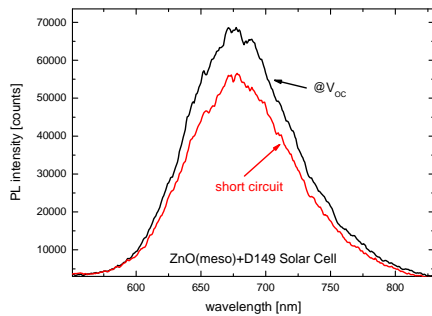


Fig. 4.24.: PL of D149 in DSSC of a shortcut cell (at 0 V) and without connected electrodes at open circuit voltage V_{OC} . The PL of D149 is slightly lower if the cell is shortcut due to production of current instead of intrinsic PL production.

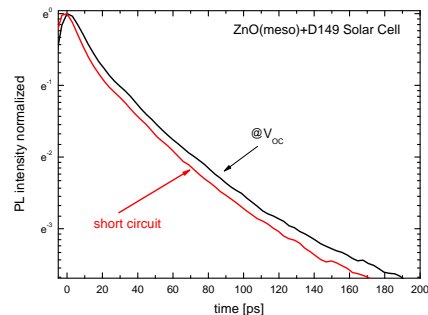


Fig. 4.25.: ps-TRPL of D149 in DSSC of a shortcut cell (at 0 V) and without connected electrodes at open circuit voltage V_{OC} . The decay of D149 PL is slightly faster if the cell is shortcut due to production of current instead of intrinsic PL production. A current production by charge transfer of electrons is an added loss channel of the intrinsic D149 PL.

By changing the applied bias, a current-voltage curve can be recorded. This can be done either manually or with a labview program programmed by Nico Hofeditz who wrote his

bachelor thesis about "Electrooptical Investigation of Dye Sensitized Solar Cells" (see [84]). At every set voltage, one can measure the photoluminescence automatically by the program or manually. For time resolved photoluminescence measurements, manual changes of the applied voltage are necessary.

In Fig. 4.26 the indoline dye D131 processed in a DSSC is measured in ps-TRPL at different applied electrical bias, the experimental method is explained in 4.2.2. An astonishingly strong dynamic of PL intensity can be seen, as shown also in the resulting decay curves of Fig. 4.27.

As can be seen by comparison of D131 DSSC (section 6.2.1, Fig. 6.10 and Fig. 6.12) and D149 DSSC (in appendix E.0.1) a cell with fast charge transfer is showing stronger dynamics in TRPL decay curves for different applied bias. In general, in order to achieve clear results with the TRPL method, the preparation conditions and cell status are relevant: agglomerations of dye lead to less dominant effect by charge transfer; also, an evaporated electrolyte is important, see discussion in appendix D.3.

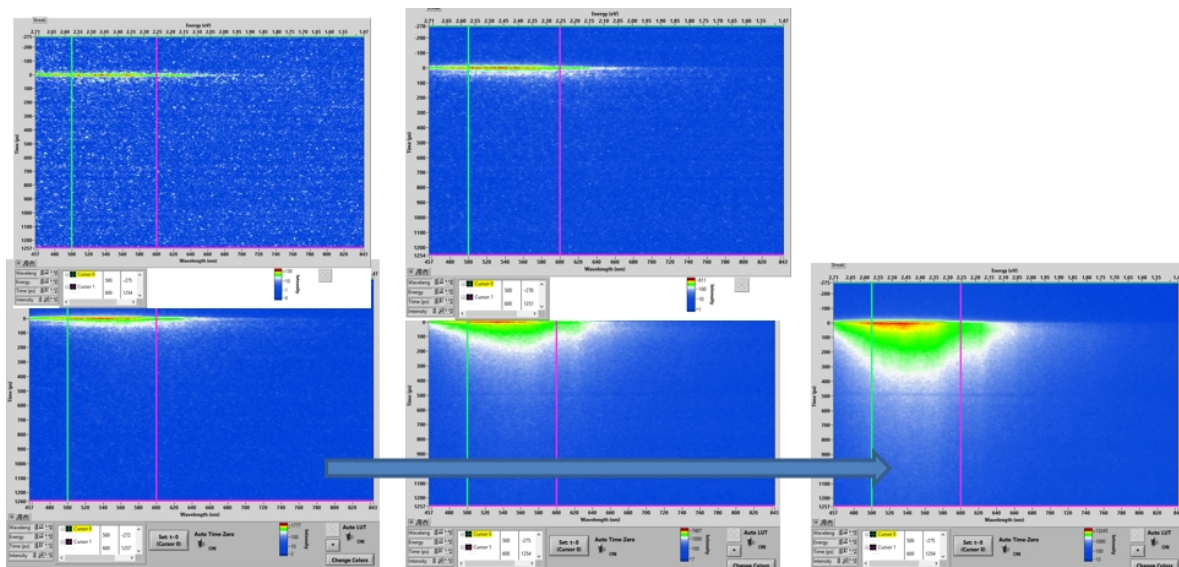


Fig. 4.26.: Applied electrical bias on DSSC sensitized with indoline dye D131 under laser light at bias voltage of -600 mV, 0 mV, $V_{oc}(508$ mV), 700 mV, 800 mV. A longer decay of the spectra can be seen in this bias order.

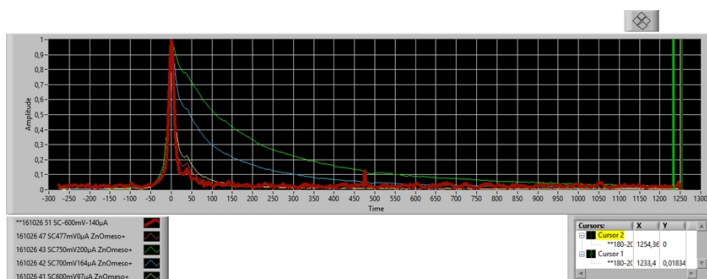


Fig. 4.27.: Resulting ps-TRPL decay curve for the ps-TRPL images of Fig. 4.26 in linear scale. The data of this software result is processed and fitted afterwards.

General correlations can be stated:

- with higher applied electrical bias the PL is reduced and the decay is slower, the injection of electrons into the semiconductor is reduced
- with decreased applied electrical bias the PL is increased and the decay is faster, the injection of electrons into the semiconductor is increased
- at a specific applied electrical bias the PL does not increase anymore, the injection into the semiconductor is not occurring. While increasing the bias to this point, the injection into the semiconductor may be reduced significantly in the final bias increase steps, resulting in lower PL increase and a slower deceleration as known for lower bias steps.

5. Excitons in Organic Layers on Inorganic Substrates

5.1. Pentacene

This chapter includes text parts and results of the publication "Temperature-resolved optical spectroscopy of pentacene polymorphs: variation of herringbone angles in single-crystals and interface-controlled thin films" [130] which was published in collaboration with Tobias Breuer, Andrea Karthäuser, Sangam Chatterjee, Gregor Witte and Wolfram Heimbrodt.

Their large structural and optoelectronic variability in combination with the possibility for low temperature processing and high mechanical flexibility render organic semiconductors and molecular dyes promising materials for the fabrication of future optoelectronic devices such as, e.g., organic light emitting diodes [188, 177] or organic photovoltaic cells [159, 51]. Among the vast variety of organic semiconductors, polyacenes such as pentacene are extensively studied model systems because they form highly ordered crystals and films [171]. They exhibit remarkably high, yet distinctly directionally dependent charge carrier mobilities [100] as well as anisotropic optical properties [55, 43, 83, 107] which are related to the molecular packing motifs in the crystalline phases. Conceptually, the optoelectronic properties of the molecular entities can be controlled either by the size of the polyacenes (i.e., the number of fused rings)[6, 137] or by chemical substitutions [102, 182]. Intriguingly, pentacene molecules in solution show significant and distinct photoluminescence emission while it is strongly quenched in the solid state[97] (see photoluminescence details in section 5.1.7). This may be attributed to efficient and fast singlet exciton fission in pentacene, the conversion of a bright singlet-type exciton into a pair of deep lying dark triplet states; a mechanism suggested for pentacene already in 1995 by Jundt et al.[97, 191]. This particular research interest has been rekindled by the opportunity to use singlet fission as carrier multiplication technique to enhance the efficiency of organic solar cells [191, 26, 214].

Several polymorphs have been reported for pentacene, adding enhanced complexity to the microscopic characterization of these processes. The single-crystal bulk structure was initially reported by Campbell et al. (C-phase (bulk))[23] which was later followed by a second bulk phase identified by Holmes et al. [85] and Siegrist et al.[189] (S-phase (bulk)). Moreover, an interface stabilized thin film (TF) phase is formed upon pentacene growth on inert substrates (like SiO₂) [171, 19, 178]. The latter transforms into the Campbell bulk phase with increasing film thickness or growth temperature[19]. Previous studies reported slightly different excitation energies for the low-energy excitons of the various phases [55, 2]. However, no integral systematic experimental study

has been reported hitherto. This is particularly unfortunate since detailed theoretical analyses have recently become available for the various crystalline phases of pentacene [15, 82]. The present incompleteness of experimental optical absorption data is mainly caused by the lack of polymorph-specific crystals or films that are suited for precise optical measurements. Due to the large absorbance of organic semiconductor materials optical data are frequently derived from ellipsometric reflection measurements of single crystals [43]. Previously, we have demonstrated that the use of optically transparent substrates with ultra-flat surfaces such as ZnO single crystals enables a straightforward way to determine the optical properties of (poly-)crystalline pentacene films by means of absorption measurements in transmission geometry [81]. Moreover, we have observed temperature dependent shifts of the Davydov splitting and energetic position of the singlet exciton which are attributed to strain at the molecule/substrate interface[81]. Here, we extend our study to all known crystalline phases of pentacene, determine the energy of the respective excitonic excitations and reveal the influence of the interface between inorganic substrate and organic semiconductor. Semitransparent pentacene crystallites of the bulk phase were prepared either as thin films at elevated temperature [19] or by employing liquid mediated growth[200] using ionic liquids. Correlating the exciton energies with the known molecular packing motif in the various crystalline phases allows furthermore to determine a temperature dependent change of the herringbone angle upon cooling of the films and crystals.

5.1.1. Preparation and characterization

Pentacene (Sigma Aldrich, purity > 99.9%) films are prepared on oxygen-terminated ZnO(000 $\bar{1}$) single-crystals (Crystec) by organic molecular beam deposition under high vacuum conditions. The ZnO surfaces are prepared by Ar⁺-ion bombardment 800 eV followed by annealing at 1200 eV (60 min) in a furnace under ambient conditions to avoid oxygen depletion of the substrates that occurs upon extensive heating in vacuum. This substrate preparation procedure yields highly ordered surfaces as confirmed by sharp (1 x 1) low energy electron diffraction patterns. Typically, one finds atomically flat terraces extending over more than 500 nm separated by monoatomic steps [65]. The sample is transferred into the vacuum chamber for film preparation. Here, the substrate temperature during film-deposition is controlled via a thermocouple directly attached to the sample surface. By appropriately tuning the substrate temperature during film deposition, pentacene films exclusively crystallizing in the TF-phase ($T = 295$ K) and C-phase ($T = 350$ K) are grown on ZnO at rates of about 6 Å/min to a nominal thickness of $d = 50$ nm. Both adopt the crystalline (001)-orientation corresponding to uprightly-oriented molecules (cf. Fig. 5.1). Single-crystals are grown onto transparent substrates (glass) by ionic-liquid-assisted molecular beam deposition. In that process, a supersaturated solution of pentacene is maintained in the ionic liquid 1-methyl-3-octylimidazolium bis(trifluoromethylsulfonyl)amide (Alfa Aesar) at elevated temperatures by continuously evaporating pentacene molecules into the solution. Upon appropriate choice of growth parameters, (001)-oriented single-crystals of large size (thickness of crystals ~ 600 nm, diameter of up to 500 μ m, cf. inset in Fig.5.17d) and high quality can be prepared[200] on top of optically transparent supporting substrates. Furthermore, the preparation conditions can be chosen to favor crystallization

of either the C-phase (bulk) by preparation at high molecular flux (7 nm/min) or the S-phase (bulk) by preparation at reduced molecular flux, which can be precisely discriminated by means of X-ray diffraction (XRD, cf. Fig. 5.1). These measurements have been performed with a Bruker D8 Discover diffractometer using Cu K_{α} radiation ($\lambda = 1.54056 \text{ \AA}$) and a silicon strip detector (LynxEye). The XRD spectra confirm that

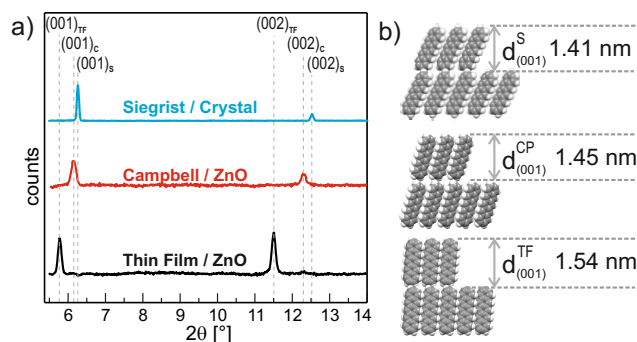


Fig. 5.1.: a) XRD data of different pentacene phases in upright orientation showing first and second order reflexes of the $(00l)$ plane. b) Schematic representation of the resulting different phases.

all the crystals and layers were prepared as pure polymorphs allowing for their precise optical analysis.

Furthermore, the influence of the substrate on the optical characteristics can be studied since crystals in the C-phase can be produced either by ionic-liquid assisted deposition or thin film growth. Optical absorption measurements are performed by using a white light lamp and a high-resolution grating spectrometer (Ocean Optics HR 4000 CG-UV-NIR, 3648px CCD row, entrance slit width $5 \mu\text{m}$) in the temperature range between $T = 10 \text{ K}$ and room temperature (RT, $T = 290 \text{ K}$).

5.1.2. Absorption Spectroscopy: Polarization Resolved Measurements of Single Crystals

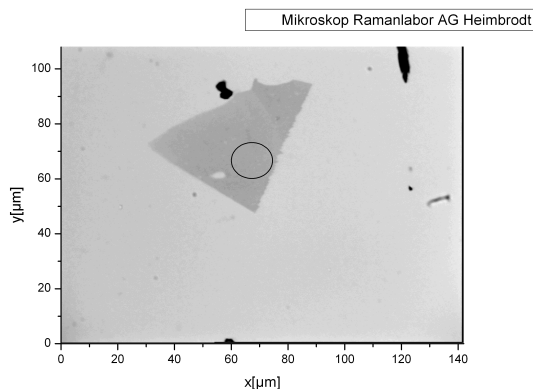
Pentacene shows a Davydov splitting of electronic states resulting in two polarization depending Davydov components especially visible for the lowest exciton in the absorption spectra. Regarding one single pentacene monocrystal, the different Davydov components lead to effects in polarized absorption spectra and polarization depending transmission microscopic images.

Turning a polarizer in conjunction with transmission microscopic images leads to different contrast on the images which helps to identify monocrystalline areas, see detailed absorption spectra when turning a polarizer and the effect on the two Davydov components in Fig. 5.3 and 5.4. On suitable identified areas, polarized absorption measurements can be performed down to 10 K in a cryostate. While for large monocrystalline bulk crystals this can be done principally (with some complications, see Fig. 5.5 a) and b)), for pentacene layers with a big number of tiny monocrystalline crystals on transparent substrates (see paragraph 5.1.2, 'layers of tiny monocrystalline crystals') it is more difficult to achieve the polarized absorption spectra of one tiny single crystal,

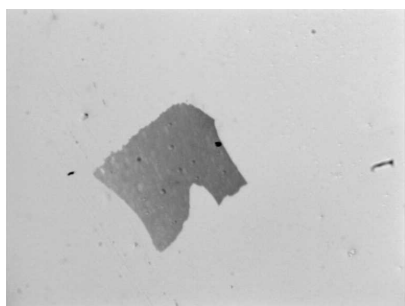
especially at 10 K. For an amount of tiny crystals it is more convenient to measure the absorption over an area of several tiny crystals without a polarizer. This results in an integral spectrum not resolving the two polarized Davydov components explicitly, yet the polarization effects can be evaluated by fit algorithm as explained later. With this integral method even samples with a crystal size below the smallest possible crystal size for microscopical absorption can be evaluated.

Monocrystalline bulk crystals

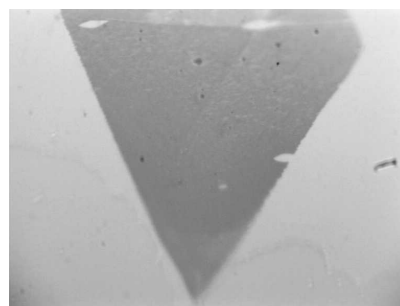
Crystals grown by liquid mediated growth are transferred on optically transparent substrates, see Fig. 5.2. Thin and homogeneous areas are identified with a microscope. This is important since slopes complicate polarization resolved measurements. A small grading can be seen already with the eye due to darker and lighter parts at figures 5.2 (b) and (c). The investigated samples must be thin enough to allow a detailed absorption spectrum without overabsorption of light.



(a) Pentacene in Siegrist phase including scale and measurement area; this very thin sample resolves into the oil after some days



(b) Pentacene in Siegrist phase, second sample, used for low temperature measurements down to 10 K



(c) Pentacene in Campbell phase, used for measurements from room temperature down to low temperatures of 10 K

Fig. 5.2.: Microscopic images of thin pentacene crystals grown by the liquid mediated growth using ionic liquids (grown by A. Karthaeuser, group "molecular solid-state physics", Prof. Witte, university of Marburg). The upper image includes the scale of the three shown images and the used measurement area (circle), the microscope magnification is 50 x.

Those monocrystalline polymorphs of Campbell and Siegrist phase can be investigated by polarized absorption spectroscopy after identifying its positions on the transparent substrate and of the homogenous areas on the samples with an optical microscope, see Fig. 5.3 and 5.4. Trends can be detected with turning the polarizer. The main Davydov components are marked with E+ and E-.

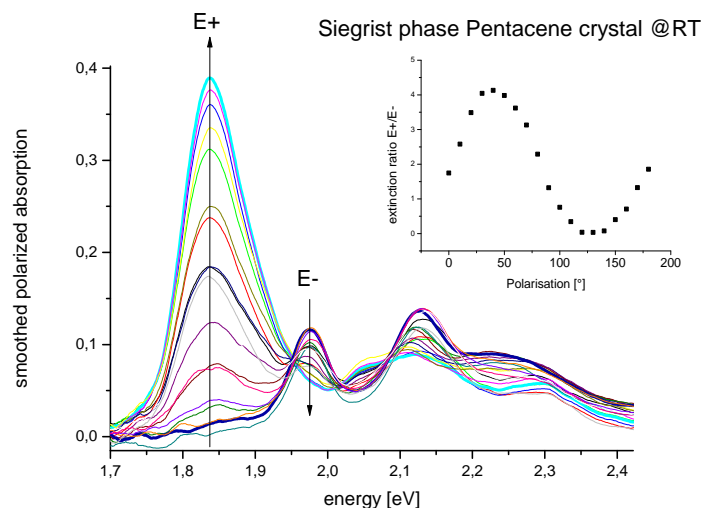


Fig. 5.3.: Absorption of sample Fig. 5.2 (a) measured polarization dependent; The Davydov splitting of the exciton can be clearly seen indicated by E+ and E-. The inset shows the ratio of the two Davydov components E+/E- against the polarization angle. A Sinus like curve shows the expected behavior of the two excitonic Davydov components.

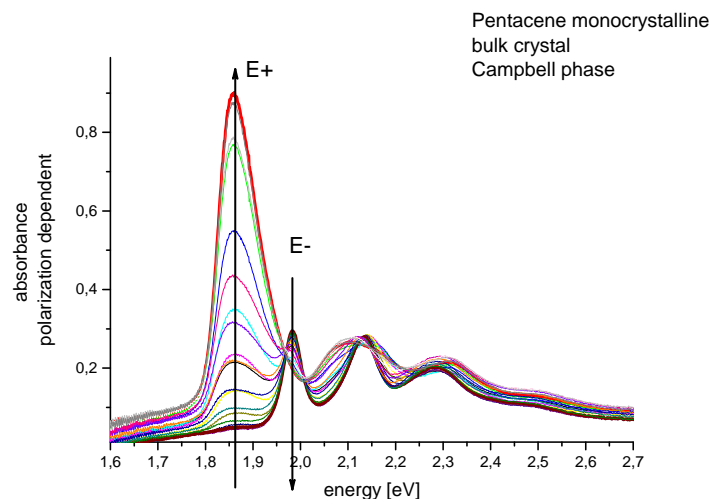


Fig. 5.4.: Polarization dependent absorption of Campbell bulk crystal (see Fig. 5.2 (c)) at room temperature measured integral over the full crystal with a 100 μm pinhole stage. As in Fig. 5.3, the Davydov components E+ and E- of the exciton are indicated. With the polarizer parallel to E+, the microscopic image of the crystal nearly is not viewable anymore on the camera screen due to low absorption for E- and therefore low contrast.

The RT measurements of the bulk crystals (Siegrist and Campbell) are compared with measurements at 10K in Fig. 5.5 a) and b). Only the polarizations parallel to E+ and E- are shown. When looking at the lower energy part of the spectra, the Siegrist phase shows a small interference at 10K and the Campbell phase shows a not totally diminishing lowest absorption, but in principle the spectra show the same effect as for room temperature, namely the deminishing of the Davydov components depending of the polarizer position. Regarding the Campbell crystal, the sharp peak at 10 K should possibly be due to experimental errors and not due to the sample, since the investigated area is proven to be completely monocrystalline at room temperature (proven by completely deminishing exciton components with one defined polarizer position). Unfortunately, this error could not be resolved. It is therefore generally more reliable to compare peak energies of the unpolarized spectra of both bulk crystals than to compare the energies of the polarized spectra, also regarding comparisons of RT to 10K. Yet, tiny shifts can be seen already in these graphs.

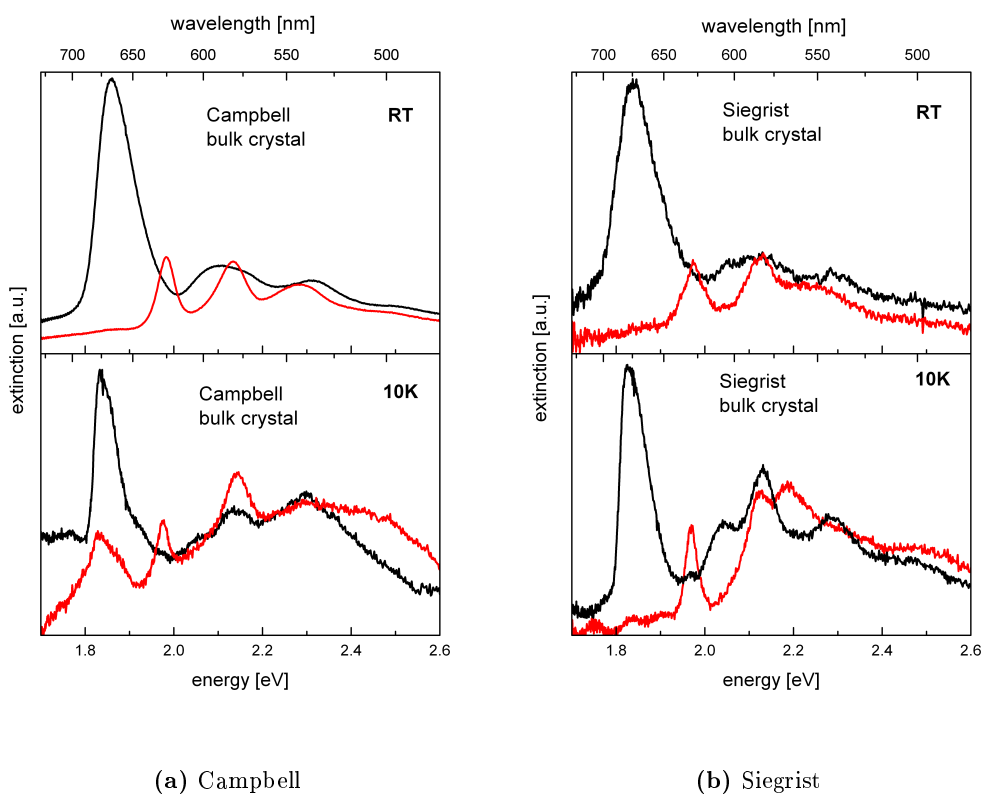


Fig. 5.5.: Siegrist and Campbell bulk crystals measured in polarization dependent absorption at room temperature and 10K.

Layers of tiny monocrystalline crystals

Layers of pentacene evolve in different phases according to deposition parameters during OMBD, explicitly the deposition temperature of the substrate is relevant. The different phases can be attributed to an unordered amorphous phase, a highly ordered ThinFilm

phase forming dendrites, Siegrist phase and Campbell phase. The different crystalline structures were investigated by AFM measurements (Fig. 5.6)

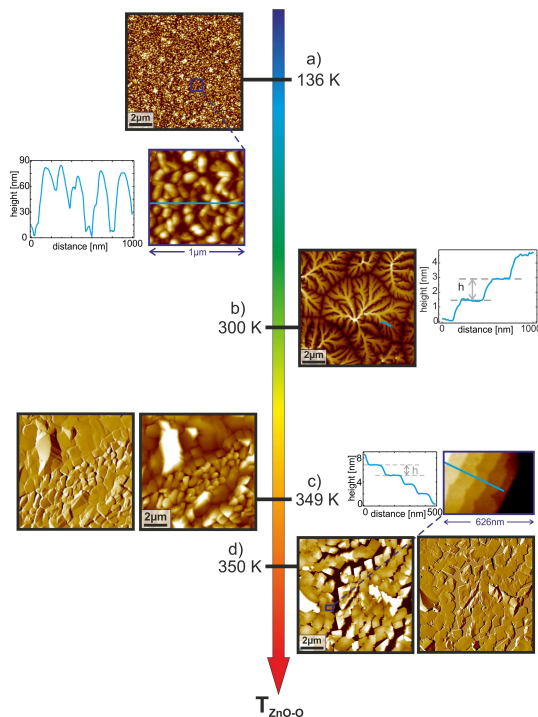


Fig. 5.6.: AFM images of group Witte: with increasing substrate temperature during crystal growth from amorphous phase (nanocrystalline) to Campbell phase. At 300 K thin film phase evolves with dendrites forming.

Dendrites can also form in Campbell phase, not shown here.

The difference between the pentacene phases is the different angle of the two molecules of the unit cell to each other (see Fig. 4.22) and the different lattice structure (Fig. 5.1). See Fig. 4.20 for an illustration of the molecule axes and Fig. 5.17 for a top view illustration. The effect of different polarizations on the transmission microscope image of the thin film phase dendrite crystals is shown in Fig. 5.7.

It is possible to choose by personal estimation one defined suitable microcrystalline crystal and to perform absorption measurements on it with the help of an image blend. Another method is to perform an absorption mapping of a predefined area. The experimental stage and software was built by the Chatterjee group (University of Marburg, physics department, group for optical spectroscopy). With a polarized absorption measurement homogenous crystal areas can be identified. This is shown in the colour image in Fig. 5.8. The suitable area position can be measured afterwards with a detailed polarization dependent absorption measurement, that means turning the polarizer for polarization dependent absorption spectra in sufficient steps.

When displaying the belonging absorption spectra of a line scan with a fixed polarization, the different alignment of the tiny crystal areas gets revealed, see Fig. 5.9. The Davydov components change in intensity due to different alignment of the crystal axes

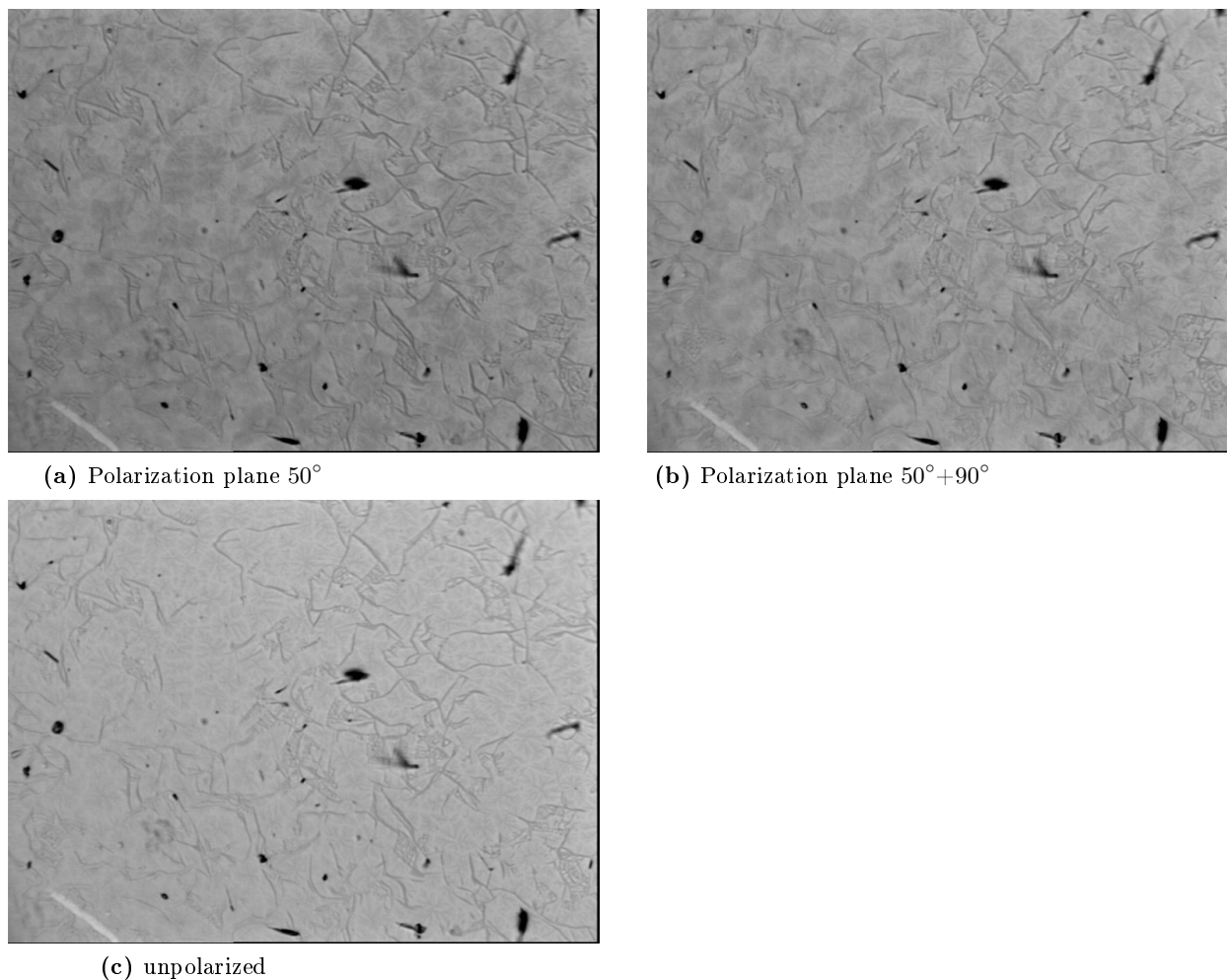


Fig. 5.7.: Polarized transmission microscope images: The polarizer is turned by 90 deg, the effect is like a negative image. The dendrites which at one polarization plane seem darker turn whiter when the polarizer is turned by 90 degrees. The size of the pictures is with 50 x magnification of the microscope $144 \mu\text{m} \times 108 \mu\text{m}$. Detailed explanations about the relation to the crystallic axis can be found in Fig. 5.17.

to the fixed polarization axis of the experimental stage.

Overview of polarized spectra of bulk crystals and layers and layers of tiny crystals

Comparing selection of crystals by mapping and by microscopic images, the selection by microscopic image with the human eye allows a larger area to be observed in-situ and has therefore time advantages. After selection of a suitable crystal with the human eye, the optical selection takes place with a changeable aperture blend situated in the intermediate image. In consequence, the microscopic image method with human eye is recommended. But in principle the same quality of polarization dependence is achieved

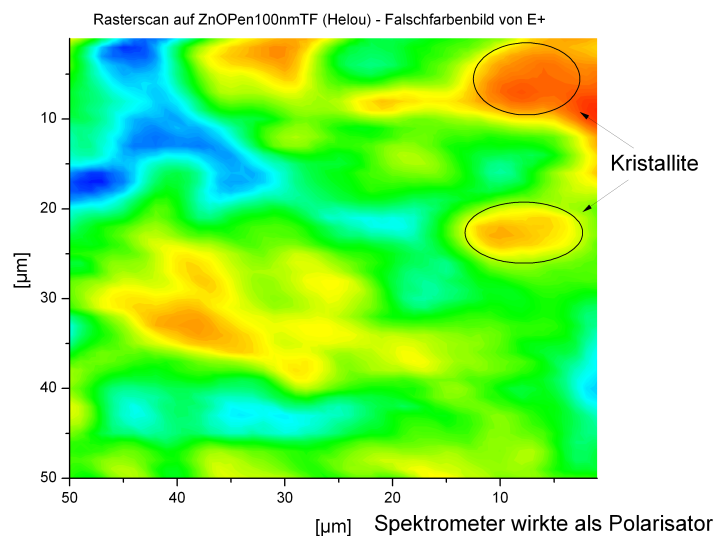


Fig. 5.8.: Finding equally aligned crystal surfaces by absorption mapping with fixed polarization. Suitable defined crystalline areas are marked with circles. 2-dimensional scan with one fixed polarization axis showing the E+ peak value.

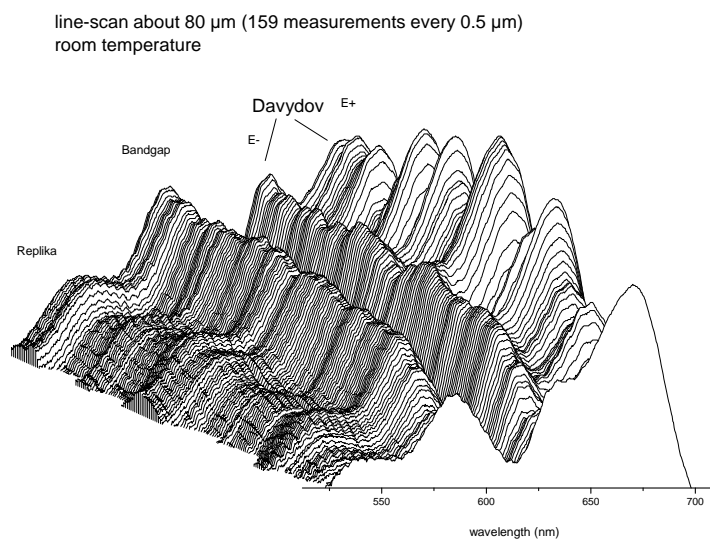


Fig. 5.9.: Absorption line scan with fixed polarization. 159 curves with 0.5 µm local distance between each curve. A line scan over several tiny crystals is shown. Line scan is 1-dimensional. Peaks remaining at equal height over some steps show larger homogeneous crystals, about seven homogeneous crystals are passed by this line-scan.

for both methods. For special samples or very tiny crystals such a polarized absorption mapping might be more appropriate and should be kept as an option for crystalline layers.

Although a lot of suitable crystals were measured, no ThinFilm crystal could be found with a perfect monocrystallinity since the crystals have not completely deminishing exciton components. This is due to experimental preparation reasons: very tiny dendrite crystals grow into each other and the resulting dendrites therefore are not fully monocrystalline. On one crystal often slightly different crystallization orientations can be seen already with the eye. Also, irritations at the crystal edges and on inner borders are possible. In Fig. 5.10 is an overview of polarized pentacene absorption spectra at room temperature. Layers on ZnO and bulk crystals are shown for comparison in the energy range of the short axis absorption. A detailed discussion of the excitonic part is done in chapter 5.1.4.

It can be concluded that polarization-resolved measurements on single crystalline pentacene are possible, but have its complications. It is therefore easier and faster to examine the unpolarized spectra and use fits to determine the herringbone angle.

5.1.3. Absorption Spectroscopy - The 2S Excitonic State

In Fig. 5.11a the extinction spectra in the energy range corresponding to excitonic transitions of pentacene in the different crystallographic phases S-, C- and TF-phase as bulk material and as film on ZnO at room temperature are presented. For comparison, the spectra of pentacene molecules in dimethylformamide are shown. The molecule absorption at about 2.14 eV is caused by the $S_0 \rightarrow S_1$ transition with transition dipole moment oriented along the short axis of the aromatic plane. The structures at higher energies can be ascribed to vibrational replica. Due to the van-der-Waals bonding induced band formation in solid pentacene crystals all absorption transitions exhibit noticeable broadening. Koch et al. [106] determined a dispersion of about 190 meV at room temperature for the bands derived from the HOMO. The weak van-der Waals coupling does not shift the transition maximum substantially from solution to solid pentacene. A chemical shift due to slightly different local dielectric constants is viewable in Fig. 4.3 and exhibits not more than 38 meV, another proof that the peaks evolving at lower energies are not due to a shift of the $S_0 \rightarrow S_1$ transition showing up in solution.

Therefore we ascribe the transitions at about 2.13 eV in the optical spectra of crystalline pentacene to the optical band gap E_g of crystalline pentacene and transitions at lower energies are due to exciton formation. Looking at Fig. 5.11a, the striking difference between the absorption spectra of molecules and crystalline pentacene is this appearance of the excitonic transitions below the band gap. In case of the single crystalline C-, S-, and TF-pentacene with two molecules per unit cell, two polarization depending absorption peaks for the exciton transition are expected as shown by Davydov [39]. Both Davydov-components can be well identified and are denoted E^+ and E^- , respectively. The Davydov components are shown in higher detail in Fig. 5.16.

In table 5.1 the energies of E_g and the Davydov components are presented for measure-

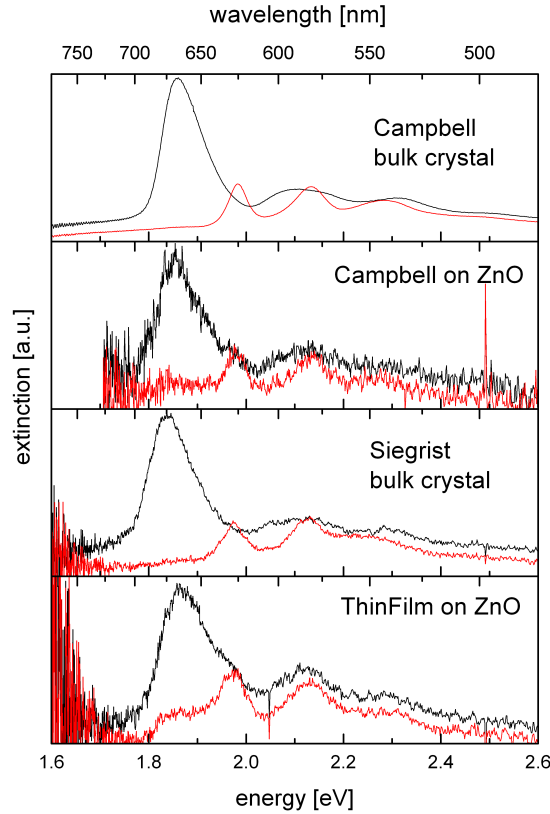
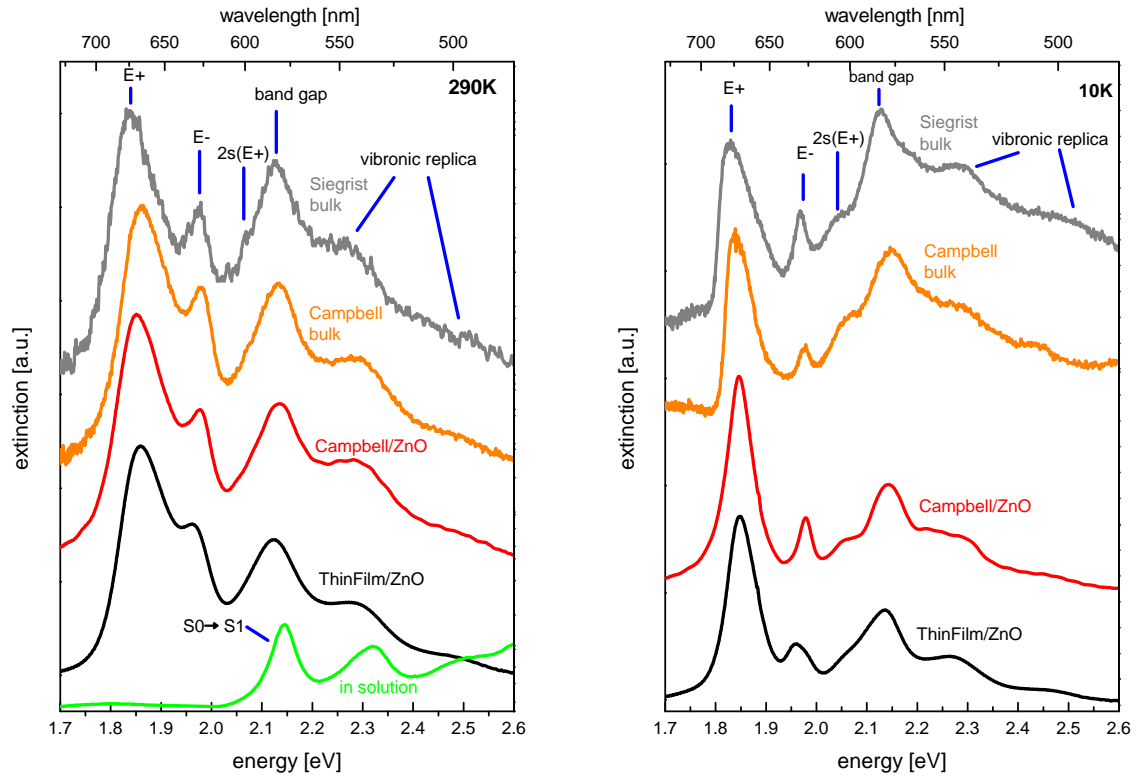


Fig. 5.10.: Microscopic polarized absorption spectra at room temperature with the polarizer parallel to the two maximal excitonic transition dipole moments which are perpendicular polarized to each other.

CB and Siegrist bulk crystals grown by OMBD assisted crystal growth in ionic liquid, the bulk crystals show fully deminishing exciton components and are completely monocrystalline. Campbell and ThinFilm layers (about 58nm and 100nm nominal thickness) grown by OMBD on ZnO:O.

ments at room temperature and $T = 10\text{ K}$. Actually, the spectra of all crystalline phases look rather similar, but small differences of the energy positions are found. Besides a chemical shift also different strain may cause different energy positions as has been shown earlier[81]. In Fig. 5.11b the extinction spectra are depicted for the various pentacene polymorphs measured at low temperature ($T=10\text{ K}$). The energy positions of the E_g as well as of the Davydov components are only slightly shifted (see table 5.1). More importantly, new transitions are observable now due to the strongly reduced linewidths of all bands, since the thermal broadening is reduced. This will be discussed in more detail later.

In Fig. 5.12 the polarized extinction spectra of the S-phase are shown as an example. The impinging light is polarized either along \mathbf{b} (\vec{D}_-) or perpendicularly to the \mathbf{b} direction (\vec{D}_+). Already at room temperature (see Fig. 5.12b) it can be seen, that both



(a) Optical extinction spectra at room temperature with different packing structure and of pentacene molecules in solution.

(b) Absorption spectra at $T=10$ K with different packing structure.

Fig. 5.11.: Optical extinction spectra of pentacene in the visible range with different packing structure (bulk Siegrist- and Campbell-phase and thin-film-phase and Campbell-phase on ZnO substrates) at different temperatures. A possible 2S state is indicated and discussed later.

Davydov-components are perfectly perpendicularly polarized. At a first glance the optical bandgap transition does not show any Davydov splitting at room temperature in Fig. 5.12b). Just a strong broadening can be seen for $\mathbf{E} \perp \mathbf{b}$. But looking at the different polarization resolved spectra of multiple polarization positions in Fig. 5.3 and Fig. 5.4, polarization dependent trends can be identified. In addition, at low temperature more absorption bands can be resolved due to the smaller linewidths (see Fig. 5.12a)). Beside the bandgap a new transition appears. Usually, those peaks at higher energies are ascribed to CT-excitons. We postulate a completely different explanation in the following discussion. Firstly we have to realize, that even the E_g transition exhibits a Davydov splitting, which is obviously smaller than the exciton splitting. This is discussed in [183]: "The Davydov splitting of vibronic levels in the ground state is however very small, because the resonance energy between an oscillating and a non-oscillating molecule in the ground state is very low." The new bands lying between the E^+ and the E_g^+ or between E^- and E_g^- , respectively, exhibit exactly the same polarization.

This congruence of the polarization between the occurring peaks indicated as 2s raises objections, however, to the CT-exciton model, since the dipole moment should not be coupled to the ground state exciton. The congruence rather indicates a correlation between the indicated 2s state and the ground state exciton. Assuming, the ground state exciton was not purely Frenkel-type but exhibits partially also Wannier-like character (this was already positively argued in the theory part, see 3.2), we thus can explain these transitions as 2s excitons. This is of particular interest, since a Rydberg-like series of excitons has so far never been observed for organic crystals. An estimation of the respective exciton binding energies, however, supports this interpretation. Using these assumptions, E_g is the optical transition from the conduction band to the valence band. The exciton binding energies can then be determined from the band position in Fig. 5.12a) as values of $\epsilon_b^+(1s) \cong 300 \text{ meV}$ and $\epsilon_b^-(1s) \cong 225 \text{ meV}$. For the 2s excitons $\epsilon_b^+(2s) \cong 92 \text{ meV}$ and $\epsilon_b^-(2s) \cong 72 \text{ meV}$ can be determined. Both 2s binding energies are about 15 meV higher than expected from a hydrogen-like series using Eq. (5.1) with Ry^* the exciton Rydberg energy and n being the principal quantum number.

$$E_{ex}(n) = E_g - Ry^* \cdot \frac{1}{n^2} \quad (5.1)$$

This deviation from a pure hydrogen-like Rydberg series is expected, however, since the excitons can not be described perfectly by Wannier-excitons but still exhibit a certain Frenkel-like character. Again, this explanation is in perfect agreement with recent DFT calculations and many-body perturbation to calculate the exciton energy of pentacene [186]. In this study it was reported that the exciton ground state is delocalized over several molecules and exhibits significant charge transfer character.

With these conclusions, the data of polarization resolved measurements at room temperature can now also be indicated including the 2s states, see Fig. 5.14 and 5.15. Because the Eg+ state in Fig. 5.14 and the 2s E- state in both figures is not clear at room temperature measurements, resulting energies are not as reliable as in Fig. 5.13 and 5.12. Interestingly, the Eg+ and Eg- polarization dependence is not the same as for E+ and E- anymore.

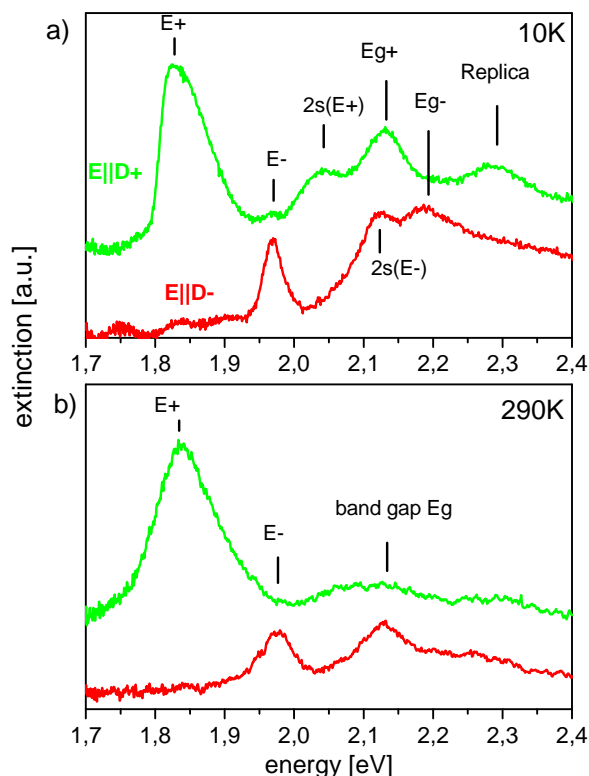


Fig. 5.12.: Absorption spectra of S-pentacene using linearly polarized light parallel to \mathbf{b} and perpendicularly to \mathbf{b} direction at $T = 10$ K and 290 K. see detailed explanation of crystallographic axes and dimer moments \vec{D}_{\pm} in Fig. 5.17.

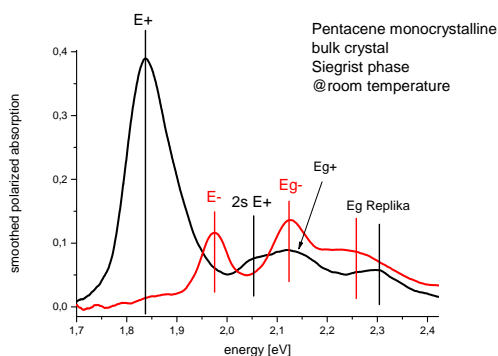


Fig. 5.14.: Absorption of sample Fig. 5.2 (a) measured polarization dependent. The lowest exciton state is indicated as in Fig. 5.3. The similar trends with turned polarizer are indicated including the postulated 2s states and the energy gap, both Davydov splitted. The 2s E- state is possibly included in the Eg- peak.

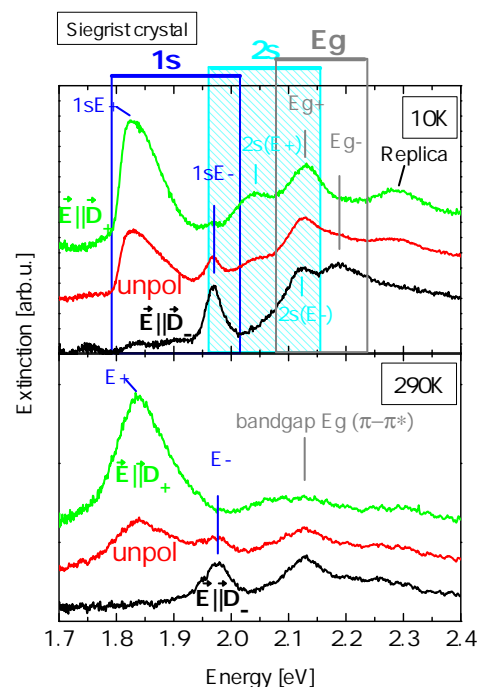


Fig. 5.13.: In addition to Fig. 5.12 the unpolarized absorption is added. The 1s and 2s excitonic state areas and the band gap region are indicated.

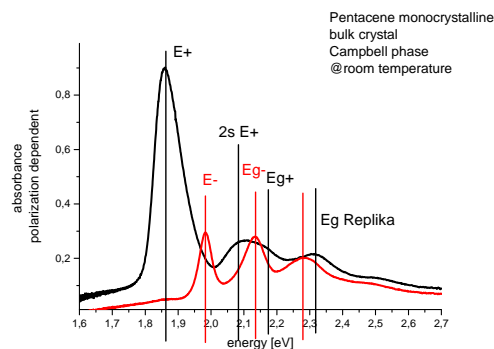


Fig. 5.15.: Absorption of sample Fig. 5.2 (c) measured polarization dependent. The lowest exciton state is indicated as in Fig. 5.4. The similar trends with turned polarizer are indicated including the postulated 2s states and the energy gap, both Davydov splitted. The 2s E- state is possibly included in the Eg- peak.

Additional evidence for a 2s state might be retrieved from reflection spectra, see 5.1.5, if measurements are performed at 10 K. This should be investigated in future.

Conclusions for the 2s exciton state

We have experimentally studied the exciton transitions in different phases of pentacene and could suggest a strong charge transfer or even Wannier-like character of the Davydov-split excitons. An excited exciton state could be revealed for all crystalline phases of pentacene, which can be explained as 2s exciton state on the basis of the polarization results. Deviations from the pure Rydberg series are caused by the still strong localization of the excitons and the respective partial Frenkel-like character.

5.1.4. Absorption Spectroscopy: Evaluation of Davydov Components

In this section, the Davydov Components of the lowest energetic electronic state are examined and evaluated in detail.

The absorption spectra of the different crystallographic phases of pentacene are presented in Fig. 5.16 at RT (dashed lines) and at $T = 10$ K (full lines). Both Davydov components[39] are clearly observed for the lowest exciton transitions and are denoted by E^+ and E^- , respectively. For sample temperatures of $T = 10$ K the bands are somewhat sharper due to a reduced electron-vibron coupling. Single crystals supported by optically transparent substrates of the bulk S- and C-phases are measured as well as thin films on ZnO-substrate in the TF-phase and the C-phase. Clearly, small yet distinct differences in the transition energies are found although all spectra may appear similar at first glance (cf. Table 5.1).

Table 5.1.: Energy positions of exciton Davydov components E^+ and E^- of different pentacene phases at $T = 290$ K and $T = 10$ K

Pentacene phase	E^+ [eV]		E^- [eV]	
	290 K	10 K	290 K	10 K
S-phase (bulk)	1.839	1.829	1.973	1.969
C-phase (on ZnO)	1.851	1.844	1.978	1.978
C-phase (bulk)	1.861	1.840	1.981	1.976
TF-phase (on ZnO)	1.859	1.848	1.966	1.961

The two exciton states E^+ and E^- also exhibit different polarization dependencies. Both components are linearly polarized and perpendicular to each other for normal incidence of light, e.g., the light impinges parallel to the \vec{c}^* -axis of the crystals. As an example, the absorption spectra for linearly polarized light parallel to the transition dipole moment of both Davydov components of the S-phase (bulk) are shown in Fig. 5.17d for both RT and $T = 10$ K. The light is polarized either along \vec{b} (\vec{D}_-) or perpendicularly to the \vec{b} (\vec{D}_+) direction (cf. Fig. 5.17a,c). In the simplistic Davydov-picture, the polarization of the dimer-transitions is explained by a quasi-classical vector summation of the respective monomer-dipole moments $\vec{D}_{1,2}$ as depicted schematically in Fig. 5.17c. As shown in Fig. 5.17a the monomer dipole moments are oriented along the short axis of the molecular plane [201].

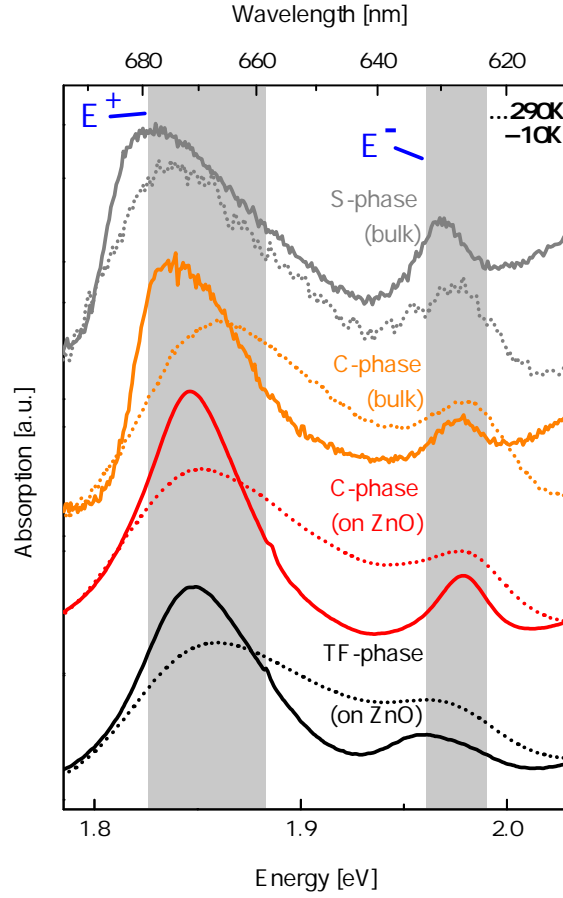


Fig. 5.16.: Optical absorption spectra (unpolarized) of pentacene in different polymorphs (S-phase (bulk), C-phase (bulk), C-phase (on ZnO) and TF-phase (on ZnO)) at $T = 290$ K and $T = 10$ K showing the region of 1.785 eV to 2.03 eV. The shaded areas denote the two lowest exciton transitions E^+ and E^- .

Here, the transition dipole moment for a molecular dimer amounts to

$$\vec{D}_{\pm} = \frac{1}{\sqrt{2}} [\langle \Psi_1 \Psi_2 | e\vec{r} | \Psi_1 \Psi_2^* \rangle \pm \langle \Psi_1 \Psi_2 | e\vec{r} | \Psi_1^* \Psi_2 \rangle], \quad (5.2)$$

if the electric transition dipole moments of the molecule are given by

$$\vec{D}_{1,2} = \langle \Psi_{1,2} | e\vec{r} | \Psi_{1,2}^* \rangle. \quad (5.3)$$

$\Psi_{1,2}$ are the ground-state wavefunctions of the two non-coupled molecules and the values \vec{D}_+ and \vec{D}_- correspond to the Davydov-components E^+ and E^- , respectively. The absorption coefficient α is determined by the quantum mechanical transition rate $W_{i \rightarrow f}$. According to Fermi's golden rule is $\alpha \propto W_{i \rightarrow f} \propto |\vec{D}|^2$.

Utilizing this simple model and applying it to both molecules in the unit cell of our crystals, we can determine the herringbone angle directly from the optical measurements by analyzing the intensity ratio of both Davydov-components. Evaluating the

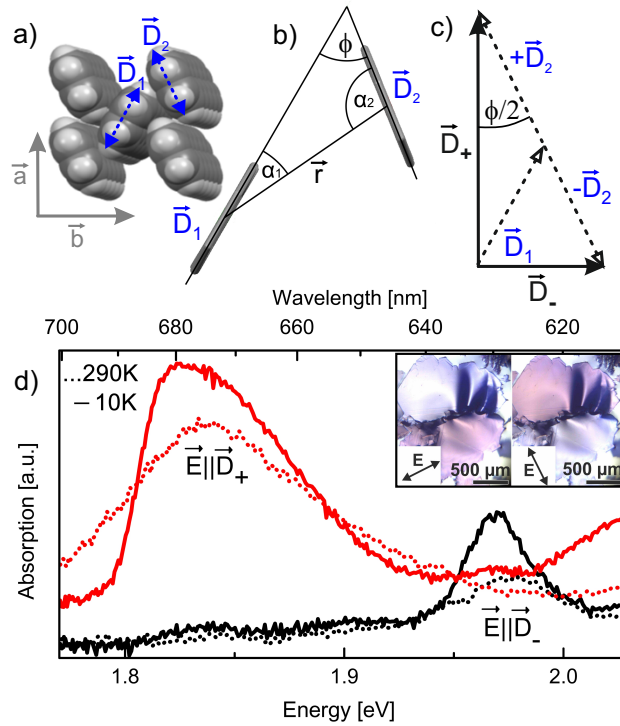


Fig. 5.17.: (a) Top view on pentacene molecules, $\vec{D}_{1,2}$ indicating the transition dipole moments of the molecules along the short axes of the molecular plane relative to the crystallographic axes (b) Schematic representation of orientation of both molecules in the unit cell and the herringbone angle Φ . (view along the long molecular axes)(c) Schematic vector summation of the monomer dipole moments forming the dimer moments \vec{D}_{\pm} . (d) Polarized absorption spectra of the pentacene S-phase (bulk) at $T = 290$ K and $T = 10$ K. The inset in d) shows typical optical micrographs with light polarization as indicated.

absorption A_{\pm} as integrated area of the respective bands, which is proportional to \vec{D}_{\pm}^2 , the herringbone angle Φ can be described by Eq. 5.4, deduced by a simple geometric relation (cf. Fig. 5.17c):

$$\Phi = 2 \cdot \arctan(\sqrt{A_-/A_+}). \quad (5.4)$$

Accessing the interface

Next, the temperature dependence is analyzed to study a potential influence of the substrates and the different thermal expansion coefficients on the herringbone angle and to reveal interface-specific effects. In Fig. 5.18 the temperature dependence of the absorption bands for pentacene films in the TF-phase (Fig.5.18a) and C-phase on ZnO (Fig. 5.18b) is compared. The absorption strength of the E^- band increases for both polymorphs with increasing temperature, whereas the height of the E^+ band decreases. Similar intensity variations of the Davydov components have already been reported for polycrystalline pentacene films and single crystals (cf. e.g. Refs. [55, 214]), however, the physical origin for this behaviour has not been explained so far.

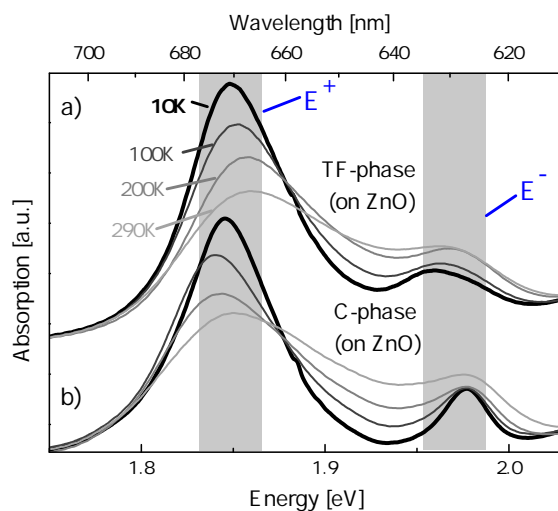


Fig. 5.18.: Absorption spectra (unpolarized) showing the region of 1.75eV to 2.03eV of pentacene films grown on ZnO in the (a) TF- and (b) C- phase at various temperatures.

Here, the aforementioned vector model is applied to explain this phenomenon by slight changes of the herringbone angle Φ with temperature. It is important to note that the intensity changes cannot be explained by broadening of the transitions due to enhanced electron-vibron coupling and respective increasing overlap of the absorption bands, since the intensities were determined by area fits of the deconvoluted entire bands. The increasing absorption of the E^- band in relation to the E^+ band is apparently caused by a redistribution of transition probability from E^+ to E^- . Due to the respective quantitative correlation described by Eq. 5.4, such an intensity variation corresponds to a variation of the angle between both molecules in the unit cell, i.e., the herringbone angle Φ . Obviously, pentacene films in C-phase and TF-phase on ZnO exhibit an increasing herringbone angle with increasing temperature.

In the following, these considerations are used to quantitatively determine the herringbone angles for the different pentacene phases at different temperatures. The angles are either obtained by spectral integration of the E^+ and E^- band intensities A_{\pm} from the polarized spectra shown in Fig. 5.17c for the S-phase (bulk) or from the unpolarized spectra in Fig. 5.16. In the latter case, however, both bands have to be evaluated separately by means of appropriate deconvolution fits. *We note that using unpolarized light, the extinction of both Davydov-components can be reliably determined, regardless of the lateral extension and alignment of the crystals in the analyzed region, since averaging of all relative orientations of the field vector and the crystalline island is automatically provided by the isotropic (unpolarized) light.*

In both cases, the respective analysis for the S-phase (bulk) yields a value of 52° at RT and 51° at $T = 10\text{ K}$ with an uncertainty of $\pm 0.5^\circ$. The value for $T = 290\text{ K}$ agrees well with the herringbone angle derived from a single crystal structural analysis by XRD[189]. Obviously, this angle is slightly reduced at $T = 10\text{ K}$ compared to RT. This finding is supported by an observed reduction of the herringbone angle of about $0.3^\circ - 0.6^\circ$ per 100 K during cooling determined by Haas et al. by means of X-ray structure analysis in the temperature range from $T = 413\text{ K}$ to $T = 120\text{ K}$ [69] and also

by Mattheus et al. for an analysis at $T = 90$ K[128].

Similarly, the temperature dependence of the herringbone angles is also deduced for pentacene films of the C- and TF-phases, both grown on ZnO substrates. The data are summarized in Fig. 5.19: angles of $\Phi_C \approx 53^\circ$ and $\Phi_{TF} \approx 58.5^\circ$ are determined for the C-phase and the TF-phase on ZnO at $T = 290$ K, respectively. Again, these values agree well with the angles derived from the corresponding XRD structure analysis [23, 143, 178]. We note, however, that Schiefer et al.[178] found different herringbone angles for the TF-phase in films prepared on different substrates, although they exhibit essentially the same lateral unit cell parameters. In particular, they reported a strong variation of Φ_{TF} between 54.3° on a-SiO₂ and 59.5° on Topas.

In our analysis we obtain for the TF-phase (on ZnO) a reduction of about 2.5° between RT and $T = 10$ K. This is only slightly larger than the observed reduction for the S-bulk crystal as discussed before. Surprisingly, a much stronger reduction by about 12° is found for the C-phase on ZnO substrates. We will come back to this point later.

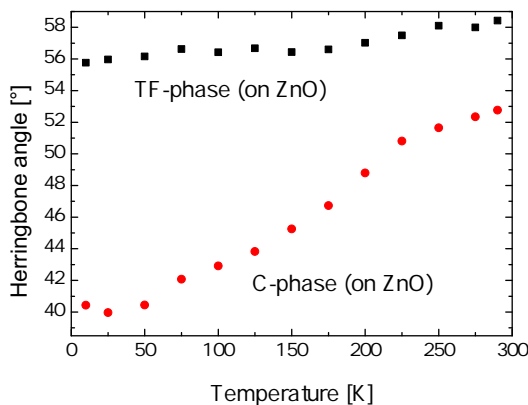


Fig. 5.19.: Evaluated values for the herringbone angle as function of temperature for pentacene films crystallized in the C-phase (on ZnO) (red) and TF-phase (on ZnO) (black), respectively.

Fig. 5.20a reveals an apparent correlation between the herringbone angles and Davydov splittings for the different pentacene phases at RT (indicated by filled red squares) and $T = 10$ K (indicated by filled black circles). Generally, an increasing Davydov splitting is found for decreasing herringbone angle. At RT, the herringbone angles slightly increase from the S-phase (bulk) to the TF-phase (on ZnO) while the Davydov splitting decreases (filled red squares). At low temperature the Davydov splitting is larger for all polymorphs, with the largest energetic splitting in the S-phase (bulk) and the smallest for the TF-phase (on ZnO). This is accompanied again by reduced herringbone angles.

In order to explain this observed correlation, the influence of the molecular interaction on the exciton formation should be taken into account. Recent results using different theoretical approaches have challenged the conventional interpretation of the lowest energy bands as pure Frenkel type and instead propose a more delocalized exciton[201, 186, 38].

Yet, we applied a simple dipole-dipole interaction model, which fits our data surprisingly well as shown in the following. By calculating the dipole-dipole interaction energy in such a model, the Davydov splitting can be described by

$$\Delta E = \frac{2}{4\pi\epsilon_0\epsilon} \left[\frac{\vec{D}_1 \cdot \vec{D}_2}{r^3} - 3 \frac{(\vec{D}_1 \cdot \vec{r})(\vec{D}_2 \cdot \vec{r})}{r^5} \right]. \quad (5.5)$$

For the crystallographic phases of pentacene, all containing two molecules per unit cell, we get Eq. (5.6) with $r = |\vec{r}|$ as the shortest center to center distance between the molecules (cf. Fig. 5.17b), with $\alpha_{1,2}$ as the angles between the transition dipole moments and the distance vector, and with $|\vec{D}|$ the effective optical transition matrix element

$$\Delta E = \frac{|\vec{D}|^2}{2\pi\epsilon_0\epsilon \cdot r^3} (\cos \phi - 3 \cos \alpha_1 \cdot \cos \alpha_2). \quad (5.6)$$

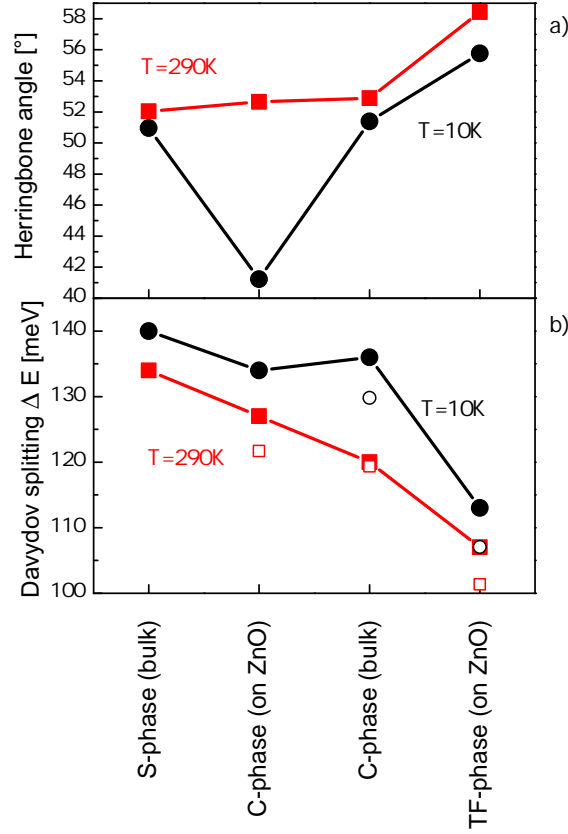


Fig. 5.20.: (a) The herringbone angle for the crystalline phases of pentacene and (b) the Davydov splitting at $T = 290$ K (red) and $T = 10$ K (black). The experimental points are filled red squares and black circles, respectively, while open red squares and black circles are estimated Davydov splittings from Eq. (5.6) (cf. text for details).

This enables us to apply this model to analyze the correlation between the herringbone angle ϕ and the Davydov splitting ΔE . For the S-phase (bulk), the angles ϕ ,

$\alpha_{1,2}$ (cf. Fig. 5.17) and the center distance r at RT are well known from X-ray structure analysis[189]. Using our experimentally determined Davydov splitting and the structural parameters of the Siegrist-phase[189] we can determine an effective optical transition matrix element using Eq. 5.6 as $|\vec{D}| = 1.639 \times 10^{-29}$ C m for a single pentacene molecule at $T = 290$ K. The dielectric constant was estimated from ellipsometric measurements[55, 43] as $\epsilon = 2.5$. Combining the same molecule matrix element and the known structural parameters of the C-phase (bulk)[23] at $T = 290$ K, we estimated the Davydov splitting for the C-phase (bulk) crystal (starting values at room temperature for Φ and $\alpha_{1,2}$ are known from X-ray structure analysis[23]) and the C-phase film (on ZnO) and find reasonable agreement with the experimentally determined values (open squares in Fig. 5.20b). Especially, the increasing Davydov splitting with reduced herringbone angle is well reproduced. As afore mentioned, the herringbone angles of the TF-phase films can be unequal for different substrates as shown by Schiefer et al.[178]. Interestingly, their data show a unique relation between Φ_{TF} and the respective values of $\alpha_{1,2}$ for the TF-phases on the different substrates. *A change of the herringbone angle in the TF-phase is symmetrically compensated by both alpha values, note that $180^\circ = \Phi + \alpha_1 + \alpha_2$.* Using this relation for our estimation, we deduce $\alpha_{1,2}$ from the experimentally determined Φ_{TF} for the present TF-phase film on ZnO. As shown in Fig. 5.20b also in this case the Davydov splitting which is calculated by Eq.(5.6) agrees quite well with the experimental value.

Even at $T = 10$ K, the interrelation between the herringbone angle and the experimentally determined Davydov splitting can be well described by Eq.(5.6) when taking the temperature dependence of the lattice parameters into account. Mattheus et al.[128] and Eiermann et al.[46] have performed temperature dependent structure analyses for the S-phase (bulk) and both found similar variations of the lattice parameters between RT and low temperatures. For a reduction of Φ the small inner angle α_1 is also reduced while α_2 is compensating both reductions by an increase; a change of the herringbone angle is therefore asymmetrically compensated. From their data we deduce the variations in the intermolecular distances r as well as the modification characteristics of $\alpha_{1,2}$ for different Φ (with an equal approach as for the TF-phase), which is asymmetric in contrast to the TF-phase. The asymmetric characteristics of the S-phase (bulk) is also used in our calculations for the evaluation of the temperature dependence of the other bulk crystal in the C-phase.

Using the measured Davydov splitting of the S-phase (bulk) at $T = 10$ K, we then determine a dipole matrix element $|\vec{D}| = 1.560 \times 10^{-29}$ C m of the monomer at $T = 10$ K which is only slightly smaller than the value obtained at RT. Using this matrix element and the measured herringbone angle determined at low temperature ($T = 10$ K), we calculated the Davydov splitting of the molecules in the C-phase (bulk) and of the TF-phase (on ZnO). The results are depicted by the open black circles in Fig. 5.20b. Again, the results are in good agreement with the experimentally determined values (filled black circles), which corroborates the present approach. Note, that for the S-phase (bulk) the calculated Davydov splittings are missing since the experimentally determined values serve as fitting points for the model.

Finally, we turn to the C-phase film on ZnO substrate. While at RT the calculated Davydov splitting is in sufficient agreement with the experimental value, the calculated

value strongly deviates from the experimentally observed splitting at $T = 10$ K. Here, the small herringbone angle combined with the asymmetric characteristic of $\alpha_{1,2}$ yields an extremely large Davydov splitting of $\Delta E_{calc} = 223$ meV (out of the depicted range in Fig. 5.20b) in our model. This unexpected behaviour can potentially be attributed to the substantial differences in the thermal expansion between molecular film and inorganic substrate, which leads to strain at the interface at lower temperatures.

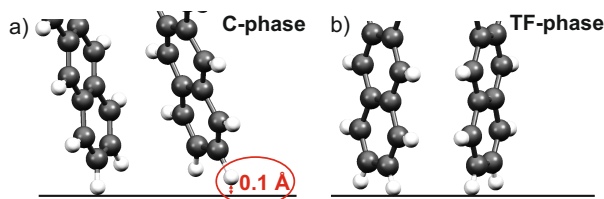


Fig. 5.21.: Detailed view of the arrangement of both molecules in the unit cell at $T = 290$ K for a) C-phase (bulk)[23] and b) TF-phase on amorphous silicon oxide[178]. The height of the lifted molecule in a) is amplified for clarification.

Closer inspection shows that only a single C-H unit of one of the molecules within the unit cell is in close proximity to the substrate while the other is elevated by about 0.1 \AA (cf. Fig.5.21a). The van-der-Waals bonding and the much smaller thermal expansion parameter of ZnO does not allow for a lateral reduction at the interface as known for the bulk material with decreasing temperature [81], which hinders the mobility of the molecule which is in direct contact with the surface. In contrast, an efficient rotation of the lifted and more weakly bound molecule appears reasonable. This assumption is perfectly in line with the determination of the individual molecular rotations in Eq.(5.6) by using the experimentally determined Davydov splitting: the strong change of the herringbone angle is performed by rotation of just one of both molecules about its long molecule axis, namely the slightly lifted molecule, while the position of the other molecule remained almost unchanged. *Note that for a given Φ the determination of $\alpha_{1,2}$ from Eq. (5.6) is not arbitrary. There exists only one pair of $\alpha_{1,2}$ which solves the equation.*

Under such circumstances, the herringbone angle is changed by a rotation of this molecule only. In our interpretation, this molecular rearrangement at the ZnO-pentacene interface is then transferred to the subsequent pentacene monolayers.

This scenario is clearly different from the other pentacene phases investigated in this study. In particular, it is also different from the C-phase (bulk), where always both molecules turn by certain and rather similar values. We emphasize that for the pentacene C-phase in bulk crystals such a strong variation of the herringbone angle as in films on ZnO is not found. This apparent difference may be attributed to the absence of interfacial thermal strain as in the case of films prepared on ZnO, since in the bulk crystals corresponding substrate-adsorbate strain is non-existent. It is worth mentioning, that one can not expect a similar interface behaviour for the TF-phase film on ZnO, since there both molecules are similarly in contact with the substrate and therefore exhibit an equivalent binding situation on the surface (Fig.5.21b).

Conclusions for evaluation of Davydov components of the excitonic state

A clear interrelation between the herringbone angle of the molecules in the unit cell of pentacene crystals and the respective Davydov splitting in the linear optical absorption spectra is found. The variation of the peak height of the individual excitonic Davydov components with temperature is explained by a variation of this herringbone angle. An extraordinarily strong variation of the herringbone angle for C-phase pentacene samples grown on ZnO substrates is observed, whereas it remains essentially constant for freestanding bulk C-phase crystals. This is attributed to the microscopic interface structure between the pentacene film and the ZnO substrate where the more weakly coupled molecule in the unit cell is capable of an efficient rotation about its elongated axis.

For the reliable analysis of optical spectra the microscopic structure has to be appropriately taken into account. This is particularly true, when interfacial strain and interface-induced effects are relevant, for example due to largely different thermal expansion coefficients of organic film and substrate. Hence, the exciton transition energies and microscopic interaction scenarios reported in this study for $T = 290$ K and $T = 10$ K may contribute to a detailed theoretical modelling of the different pentacene phases including interfacial strain.

5.1.5. Linear Reflection Spectroscopy

The results presented here were developed in collaboration with Matthias Weber (Bachelor thesis [211]). The experimental stage used can be seen in Fig. 4.23. The basics 4.3 show that the reflection and absorption of pentacene have similarities (section 4.3.1, Fig. 4.15). Thus, it is also possible to perform polarization-dependent measurements on monocrystalline pentacene crystals in reflection, similar to absorption (for example as in Fig. 5.12), and draw conclusions on differences between the pentacene phases. An explanation of the cause of the Davydov splitting of the excitons and the polarization dependence of the associated components can be found in section 5.1.4, illustrated in Fig. 5.17.

Fig. 5.22 shows the reflection spectra of a thick almost opaque Siegrist-pentacene bulk crystal (sample ID I3, grown by Andrea Karthäuser, group Witte, university of Marburg) with the polarizer turned from linearly polarized light impinging parallel to \mathbf{b} (blue) to perpendicularly to \mathbf{b} direction (red), from 0° to 90° . This measurement clearly shows the monocrystallinity of the considered crystal region, since the individual Davydov components E+ and E- would otherwise not disappear at a certain polarization of the light. It is therefore possible to show the purity of crystallinity of a pentacene crystal also by reflection measurements.

Comparing the polarized reflection spectra of Siegrist and Campbell phase retrieved from tiny bulk crystals (Fig. 5.23), a redshift for the Siegrist phase is observed. This is in congruence with the observation of a redshift in absorption: looking at the absorption values of table 5.1, a redshift of about 8 nm (from about 666 nm to about 674 nm) should occur for the E+ component and only a small redshift of about 2.5 nm should occur for the E- component (from about 626 nm to 628,5 nm). In fact, the reflection spectra

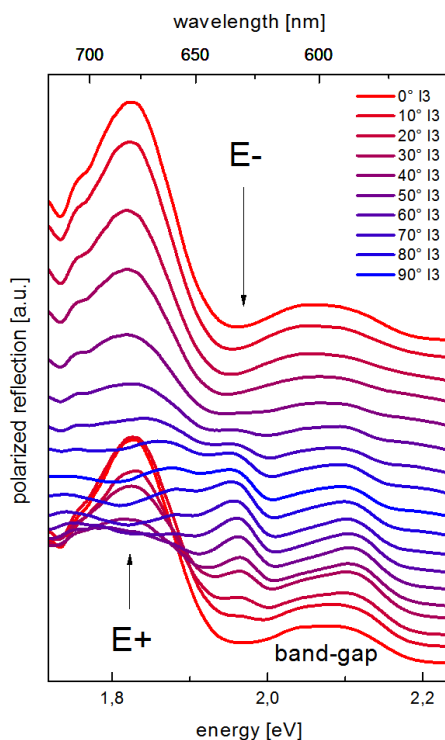


Fig. 5.22.: Reflection spectra of Siegrist-pentacene using linearly polarized light parallel to \mathbf{b} (blue) up to perpendicularly to \mathbf{b} direction (red) at $T=290$ K. Big Siegrist crystal (sample I3) is shown. Graph taken from Bachelor thesis of M. Weber[211].

lie both redshifted about some nanometers from the absolute absorption values. For $E+$, in consequence, reflection measurements are not able to determine absolute energy values directly, but a tendency can be retrieved also from reflection measurements. In addition to this problem, the sample should be thick enough not to allow light which transmitted the whole crystal back and forth to enter the detector. This reflected light will have absorption characteristics mixed with reflection characteristics and leads to an overlaid absorption spectrum as can be seen for the Campbell phase in Fig. 5.23. This mixture of absorption and reflection leads to a non deminishing $E+$ component (light green curve for Campbell in Fig. 5.23).

Yet, a reflection measurement is a useful tool to detect first trends and differences in optical properties of samples which do not enable transmission measurements.

For non-transmissive samples like pentacene on graphen, reflection measurements are the only option to retrieve absorption informations. Since pentacene on graphene develops a lying structure nearly with molecules parallel to the substrate, a non-splitting of the excitonic state is expected, since only the geometry of the short axis of the pentacene molecules contribute to the Davydov splitting of the lowest energy exciton. This is indeed shown, see Fig. 5.24. While for standing Siegrist phase the $E+$ component deminishes with turning the polarizer, this is not the case for lying Siegrist phase on

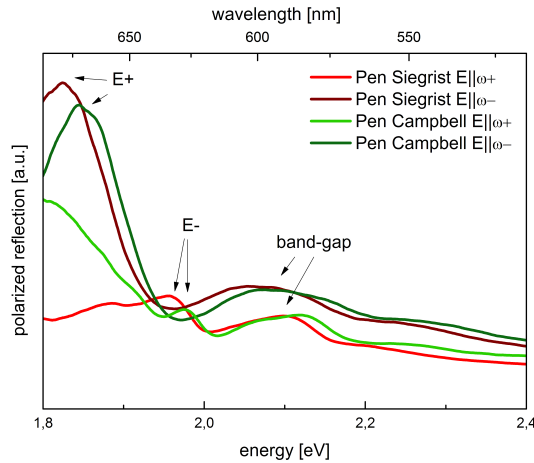


Fig. 5.23.: Comparison of reflection spectra of pentacene bulk crystals of Siegrist and Campbell phase at room temperature. Polarisation dependent measurement. Figure taken from M. Weber [211], $\omega+$ and $\omega-$ must be exchanged for each other in the legend and have the meaning of D_+ and D_- in Fig. 5.17.

graphene. As expected, no E- or E+ component occurs with turning the polarizer but only one component indicated as E. Reflection measurements can therefore prove if pentacene is lying or standing and even gives insights into the excitonic energies excluding Davydov effects.

5.1.6. Raman Spectroscopy

The results shown here were developed in cooperation with Matthias Weber (bachelor thesis [211]) and Mikko Wilhelm (bachelor thesis [212]), also measurements by Jonathan Helzel (master thesis [80]) are included in the discussion. The experimental stage used can be seen in the experimental part 4.4.

The study of pentacene crystals (produced by group Witte, University Marburg) shows that Raman spectroscopy measurements can be used to draw conclusions about the crystalline phase and the tilting angle of molecules in the unit cells through the relationship of two Raman modes. Based on the different tilt angles of the pentacene phases, the ratio of the 1175 cm^{-1} peak to the 1596 cm^{-1} peak is influenced. The mode at 1596 cm^{-1} has a B_{3g} -symmetry, so it is sensitive for the tilt angle. The mode at 1175 cm^{-1} (A_g -symmetry) is relatively stable in all measurements (for a more detailed theoretical introduction see 4.4.1). Besides the general underground due to filter luminescence and, if occurring, photoluminescence, Raman peaks of substrates have to be considered. For pentacene on graphite (Fig. 5.26) a strong graphite Raman peak near 1596 cm^{-1} might appear, here the influence on the pentacene spectrum is fortunately small. In case of pentacene on ZnO the underground has to be carefully subtracted for both relevant Raman lines (see Fig. 5.27 and 5.28).

The comparison between the intensity ratios of the lying (Fig. 5.26) and the standing

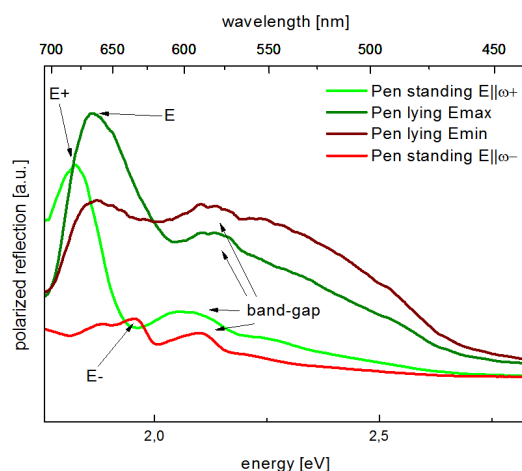


Fig. 5.24.: Comparison of polarization dependent reflection spectra of standing and lying Siegrist-pentacene. $\omega+$ and $\omega-$ have the meaning of D_+ and D_- illustrated in Fig. 5.17. For lying pentacene no Davydov splitting is viewable as expected since the light impinges not from above on the short axis geometry but on the long axis of the pentacene molecules. Figure taken from M. Weber[211].

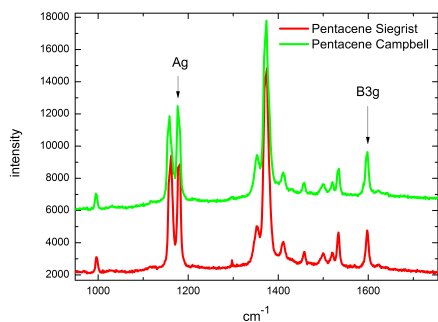


Fig. 5.25.: Raman peaks for the different pentacene crystal phases Campbell and Siegrist. The ratios between 1175 cm^{-1} and 1596 cm^{-1} are similar, yet distinguishable (see table 5.2)

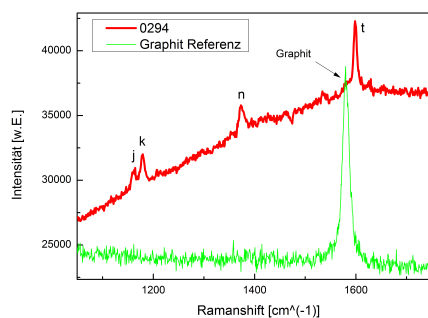


Fig. 5.26.: On graphite pentacene can grow in lying Siegrist phase, see red curve with sample 0294. The Graphite Raman peak around 1580 cm^{-1} has to be taken into account. The B_{3g} mode 1596 cm^{-1} is clearly the strongest line due to lying molecules.

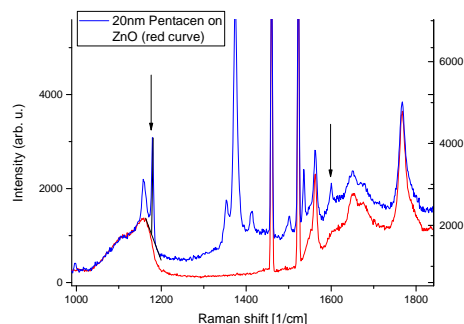


Fig. 5.27.: 20nm pentacene layer in Thin-Film phase is grown on ZnO-O. The underlying underground from the ZnO substrate has to be considered. The ratio between 1175 cm^{-1} and 1596 cm^{-1} is 4.8.

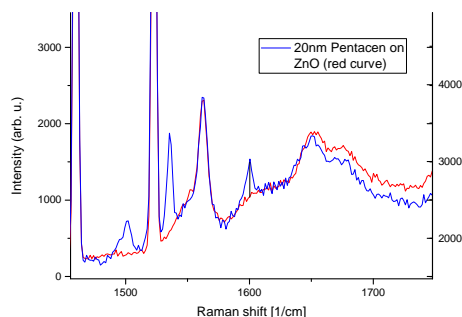


Fig. 5.28.: 20 nm pentacene layer in Thin-Film phase is grown on ZnO-O. The underground is adapted on the spectrum around the 1596 cm^{-1} mode in order to reveal the exact peak intensity.

Siegrist phase (Fig. 5.25) clearly shows the expected behaviour. For nearly horizontal pentacene molecules on graphite, the intensity of B_{3g} mode clearly dominates all other modes.

Table 5.2 shows the results from Raman measurements on different pentacene phases.

Table 5.2.: Overview of the determined peak ratios of the modes 1178 cm^{-1} (A_g -symmetry) and 1596 cm^{-1} (B_{3g} -symmetry). Determination of the phase of pentacene crystals.

phase	substrate	mode ratio A_g/B_{3g}
Thinfilm	ZnO	4 to 10
Thinfilm	SiO_2	>4
Thinfilm	KBr	3.6 to 4.2
Thinfilm	sapphire	3.7
Campbell (crystalline film)	ZnO	2,09 ($\pm 0,2$)
Campbell (crystal)	SiO_2	2,24 ($\pm 0,25$)
Siegrist (big crystal, standing)	Quarz	3,4 ($\pm 0,2$)
Siegrist (big crystal, standing)	SiO_2	2,98 ($\pm 0,46$)
Siegrist (lying)	graphite	0,45 ($\pm 0,05$)

As expected, the Campbell phase has a smaller intensity ratio than the Thinfilm phase. Similarly, the Siegrist phase is in line with expectations, it shows a smaller ratio than the Thinfilm phase. Only the fact is surprising that the Siegrist phase gives a larger ratio than the Campbell phase, despite smaller known tilt angles between the molecules and substrate (see Fig. 4.22 in experimental Raman part). Measurement errors are highly likely to be excluded, since the results were well reproduced on different crystals. However, with the determined reproducible mode ratios, the pentacene phases can basically be detected by Raman spectroscopy. On ThinFilm samples intensity ratios show a stronger variation than for Campbell and Siegrist phases, but yet the ratio is always 3.6 which is distinguishable from Campbell and Siegrist. Taking comparable substrates for all three phases like SiO_2 or ZnO, the ratio of the ThinFilm phase is with 4 even

more different from the other two phases. One reason for the higher variety is that the molecules are relatively upright on the substrate and small changes in the tilt angle of the molecules to the substrate therefore lead to large intensity differences of the B_{3g} mode. The only question is where the small changes in tilt angle originate from. One observation which might be an explanation is that small crystallites give a higher ratio than areas on the sample with larger crystals, this was proven for pentacene ThinFilm on ZnO. From this observation one can derive a presumption: the more the disorder in the crystalline layer and the higher the amorphicity at the grain boundaries, the more tilted molecules or small tilted grown crystals occur in relation to a standing homogenous single crystal. Conversely, the less overlap of the crystals at the grain boundaries, the larger the homogeneous crystals, the less tilted molecules are detected. This presumption is also supported by the difference in the Campbell phase between crystal and more film-like, crystalline structure. The amorphous-looking film structure has probably more tilted molecules than a large grown crystal. According to ThinFilm a small ratio is a measure for well-grown, homogenous crystallinity. But also for the other phases the crystal quality can be checked by the relationship of the modes. Tilt angle experiments were also performed on the most reliable sample (i.e. the big Siegrist crystal I3). As expected, a larger tilt resulted in a sinking ratio. Due to the problem of non-trivial projections of the molecules onto the y-z plane with light from above as the x-direction, discussed in the section 4.4.1, these tilting experiments are not completely unambiguous. However, the trend is proven (further studies can be found in the bachelor thesis of Matthias Weber [211]). This projection effect may also explain why the Campbell-Siegrist phase contradicts the mode-relation mentioned above; namely, the y-z projection surface could be smaller for Siegrist than for Campbell despite the stronger tilt angles of the Siegrist phase. To clarify this, the tilting experiments could be repeated with polarized laser light and a well-known crystal axis to establish a clear mathematical relationship between the tilt angle of the Siegrist crystal and the B_{3g} Raman mode.

5.1.7. Photoluminescence Spectroscopy

The Photoluminescence (PL) in solution shows no exciton formation as in solid crystals but only the PL of the π^* - π transition (see chapter 3 for a theoretical introduction). The additional seen peaks evolving in absorption at higher energies and at lower energy in the PL spectrum are due to vibronic replica.

While in solution a photoluminescence (Fig. 5.29) is easily detected, for crystalline pentacene the photoluminescence is strongly diminished (Fig. 5.30).

Jonathan Helzel [80] measured the photoluminescence of pentacene layers of different thickness at 10 K. The photoluminescence measurements show the free exciton PL which corresponds to the lower part of the Davydov splitted exciton shown in the extinction measurements. Furthermore two states of trapped excitons are shown that disappear very fast with increased temperature (not shown here). The assignment of the peaks is done in [80] referring to results of Rui He et al. [77] and Anger et al. [4].

As mentioned in the beginning of this chapter 5.1 the only very weak free exciton PL

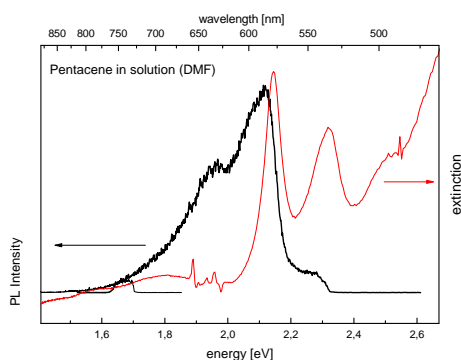


Fig. 5.29.: Photoluminescence and absorption in solution (DMF); the π - π^* transition is the peak with lowest lying energy in the shown absorption spectrum, apparently the PL belongs to this transition. A mirror symmetry of the PL regarding the absorption can be seen although strongly broadened in PL spectrum. The decay time of the PL is 8 ns/e (not shown here).

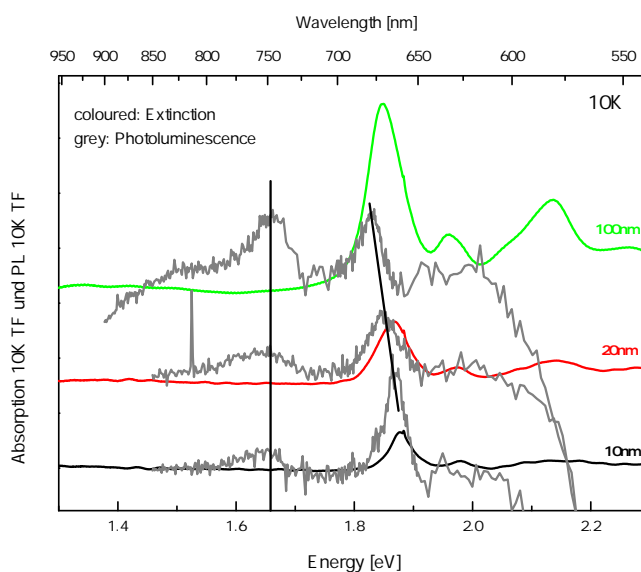


Fig. 5.30.: Photoluminescence of layers of 10, 20 and 100 nm pentacene ThinFilm on crystalline ZnO measured at 10 K; figure consists of measurements by J. Helzel [80]

The shift of the free exciton PL with increasing layer thickness is due to the different thermal expansion coefficients of pentacene and ZnO-O. The strain is reduced with increasing thickness, leading to lower energy of the free exciton PL. The trapped states (PL peak at lower energies) increase in intensity with thickness, possibly due to displacement or impurities.

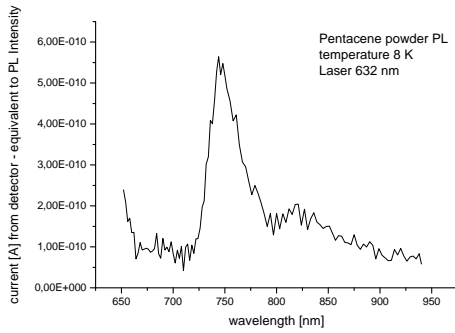


Fig. 5.31.: Photoluminescence of a pentacene powder at 8 K. No free exciton PL can be seen or the signal is smaller than the noise.

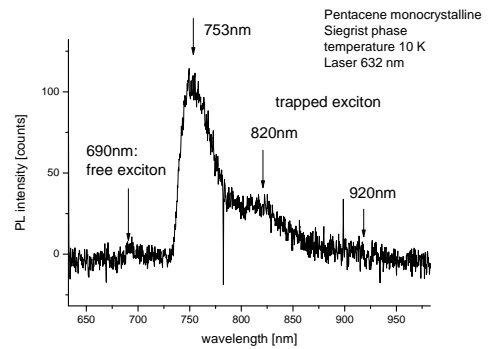


Fig. 5.32.: Photoluminescence of a pentacene Siegrist crystal at 10 K. The tiny free exciton PL is indicated at 690 nm.

may be attributed to efficient and fast singlet exciton fission in pentacene, which means a conversion of a bright singlet-type exciton into a pair of deep-lying dark triplet states; a mechanism suggested for pentacene already in 1995 by Jundt et al. [97, 191].

The same PL measurements performed on the Siegrist bulk crystal (Fig. 5.32) revealed only a very small peak of free exciton photoluminescence and a much more dominant deeper photoluminescence of the trapped exciton. For pentacene powder no free exciton PL can be identified or its signal is smaller than the noise amplitude (Fig. 5.31).

A measure for quality of pentacene crystals can be derived: at 10 K, free exciton PL appears only in pentacene crystals of high purity while trapped exciton PL occurs for crystals with more defects or disorder. It can be concluded that the quality of crystalline order is a lot higher for layers on ZnO than for bulk crystals.

The trapped exciton PL should be especially dominant for unordered pentacene powder. But looking at the powder PL of pentacene (Fig. 5.31) and the PL of a mono-crystalline Siegrist bulk crystal (Fig. 5.32), astonishingly, the PL is congruent. In addition, although measured at different measurement stages, it can be interpreted from the intensities that both trap PLs are similarly weak. Only the small occurrence of free exciton PL for the Siegrist crystal at 690 nm indicates a slightly better crystalline order. This means that the powder crystallinity is nearly as high as for the monocrystalline bulk crystal. And, looking at the nearly deminished free exciton PL, the crystalline quality of both powder and bulk Siegrist crystal is not as high as for layers built by OMBD.

With this knowledge of free exciton and trapped exciton PL another explanation for the strong deminished free exciton photoluminescence in pentacene crystals can be proposed. Quenching of free exciton PL also occurs due to deep traps acting as killer centers for free exciton PL and does not only occur by singlet exciton fission. Yet, the very weak deep trap PL in pentacene crystals which only occurs at strong cooling is not sufficient to explain the strong quenching of the pentacene free exciton photoluminescence. The internal fission process probably still remains the dominant quenching process.

5.2. Phthalocyanine

5.2.1. Introduction

The organic semiconductor Copper-Phthalocyanine (CuPc, see Fig. 5.33a and 5.33b) and other Metallic Phthalocyanines are used, for example, in solid-state dye sensitized solar cells [208]. They exhibit remarkable chemical stabilities and versatile functionalities due to the π -conjugated macrocycle. [224]. We investigate the influence of the substrate and preparation conditions on the resulting phase and crystal formation for CuPc and titanyl phthalocyanine (TiOPc). This short introduction refers to Morse-Boron et al.[138], where explanations of the chemical structure can be found in detail. Phthalocyanines are a class of common colorants, Cu-Phthalocyanine is for example used as colourant for blue paper tons. In addition, phthalocyanines have also been employed as functional materials in organic electronic devices [37]. The four central nitrogen atoms ligate the metal ion in the central cavity, see upper left picture of Fig. 5.34. Additional equatorial or axial ligands can be added, both asymmetric or symmetric (Fig. 5.33c and 5.34).

Copper phthalocyanine

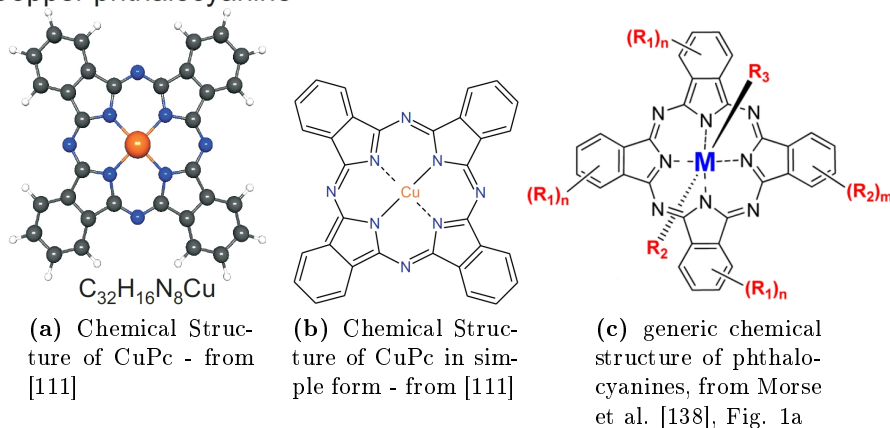


Fig. 5.33.: Chemical structure of phthalocyanine

Virtually all metal and metaloid atoms of the periodic table form phthalocyanines, the two exceptions are uranium and boron, which form uranyl superphthalocyanine and boron subphthalocyanine, which have five and three repeating isoindoline units instead of four in their ligand structure, respectively.

5.2.2. Preparation and XRD characterization

Phthalocyanine (CuPc and TiOPc, Sigma Aldrich) films are prepared by Witte group, Marburg (Michael Kothe) on glass or potassium chloride (KCl) by organic molecular beam deposition under high vacuum conditions. The sample is transferred into the vacuum chamber for film preparation. Here, the substrate temperature during film-deposition is controlled via a thermocouple directly attached to the sample surface. By appropriately tuning the substrate temperature during film deposition phthalocyanine

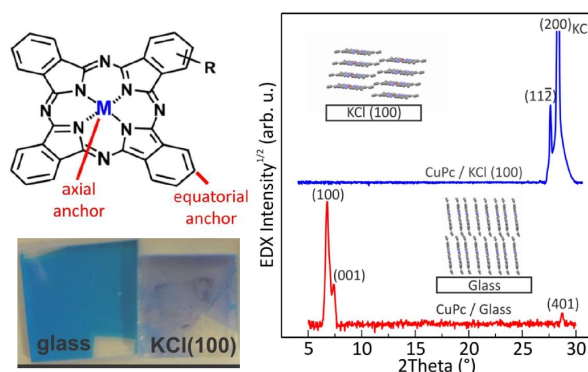


Fig. 5.34.: upper left: chemical structure of metal phthalocyanine indicating axial and equatorial anchors; lower left: outer colour appearance of phthalocyanine layers on glass and KCl; right: XRD measurements showing standing and lying alignment of CuPc layer depending on substrate.

films can be produced in different phases and different orientation. XRD measurements have been performed (Witte group, Marburg) with a Bruker D8 Discover diffractometer using Cu K_{α} radiation ($\lambda = 1.54056 \text{ \AA}$) and a silicon strip detector (LynxEye).

5.2.3. Cu-Phthalocyanine: Substrate Dependence

XRD measurements show the flat alignment of CuPc on KCl and the upright alignment on glass, see right part of Fig. 5.34. The lower left part of Fig. 5.34 shows the resulting colours of the layers. While on glass a layer with blue colour is formed, on KCl a more violet layer develops. This macroscopic effect suggests different absorption, reflection or light scattering properties of the samples.

In Fig. 4.16 microscopic pictures of standing and lying CuPc are shown. It can be seen that standing CuPc on glass is a homogeneous layer while for lying CuPc on KCl strong crystal formation occurs with distinct crystals which act as light scattering centers. The standing layer on glass consists of very small crystals that are not scattering light and have complete substrate interaction, i.e. do not point in all directions like amorphous Phthalocyanine would do.

Solid formation: polymorphism and exciton formation

Cu-Phthalocyanine shows polymorphism because planar metallic phthalocyanines can stack in different modes. The resulting phases reveal different solid state electronics and functionalities depending upon crystal structures [224]. For CuPc either an almost perfect α -phase (black) or a mixed α/β -phase (red curve) was found in case of upright standing molecules on glass, see Fig. 5.35 [203]. The phases can be also identified by XRD measurements [203, 87].

Differences in packing structure of the two phases are illustrated in Fig. 5.36.

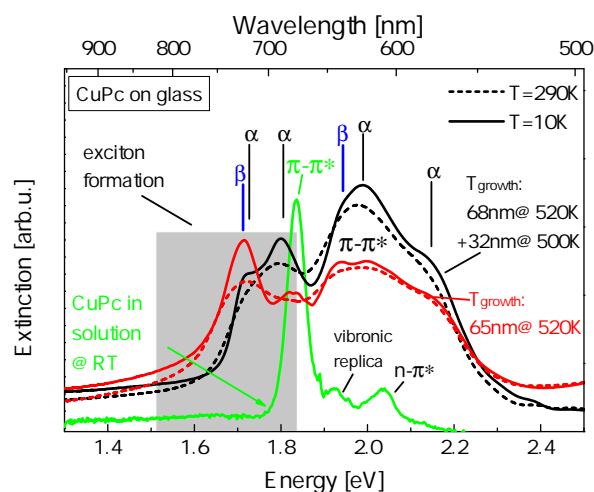


Fig. 5.35.: Comparison of 100 nm and 65 nm CuPc on glass prepared at different temperature conditions. The extinction is normalized on layer thickness. Shown are spectra with temperatures at RT and 10 K. Marked α and β phase.

In green CuPc in solution (DiClBenzol) is shown, the difference of spectra of solid CuPc in comparison to solution spectra is due to solid formation including exciton formation. The latter explained in chapter 3.2, for example regarding TiOPc in Fig. 3.15

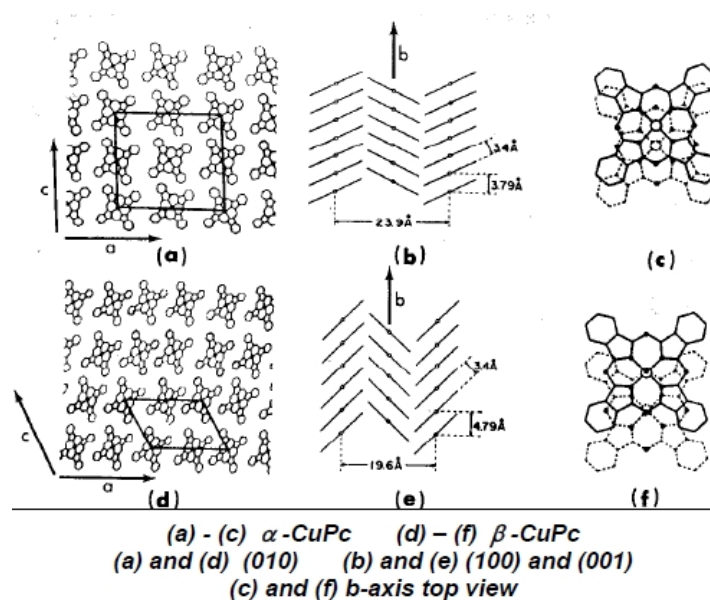


Fig. 5.36.: Molecular arrangements in α - and β -CuPc, taken from [116], further details discussed in [213].

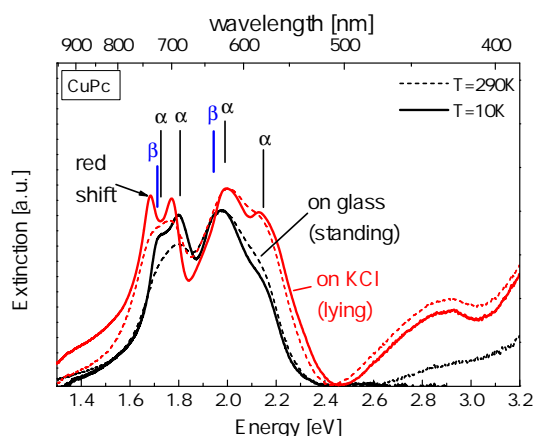


Fig. 5.37.: Comparison of extinction spectra of 50 nm CuPc on glass and 40 nm on KCl. Samples were prepared by Michael Kothe, Witte group, Marburg. Substrate temperature during OMBD were for standing molecules 460 K and for lying molecules 350 K, respectively. The spectra were measured by Jan Kuhnert, group Heimbrodt, Marburg.

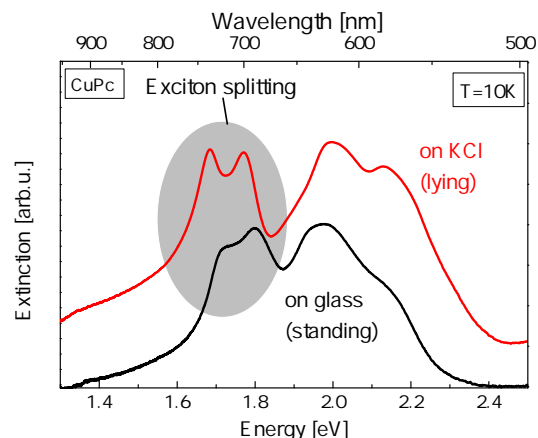


Fig. 5.38.: Comparison of lying CuPc on KCl and standing CuPc on glass at temperature of 10 K. Exciton splitting can be seen, but β phase exciton splitting is not clear enough to be distinguished from α splitting. The spectra were measured by Jan Kuhnert, group Heimbrodt, Marburg.

The π - π^* transitions of the films are broadened compared to the molecules in solution due to the van der Waals interaction (weak intermolecular coupling) [215]. In addition, exciton formation occurs, see grey shadowed region in Fig. 5.35. In theory chapter 3.2 more explanations are given about exciton formation in organic semiconductors.

Standing and lying CuPc - different relation of intensities in splitted excitonic Peaks

Regarding CuPc extinction spectra of upright alignment on glass compared to lying alignment on KCl, differences occur which get revealed in more detail at low temperature of 10 K (see Fig. 5.37), α and β phase are indicated with lines. The peaks of standing molecules on glass were identified in Fig. 5.35 by the known α and β phase peaks. For lying CuPc on KCl in π - π^* spectral region, a mixture of α and β phase occurs, interestingly the π - π^* absorbance peaks show a slight red shift compared to the absorbance peaks of standing molecules on glass. Regarding the exciton region, even at room temperature a clear blue shift of the α peaks occurs compared with α phase peaks of the standing molecules on glass. The lowest absorption peak is probably the sum of the red shifted α and β peaks of standing molecules on glass, but with a more pronounced peak.

Fig. 5.38 focuses on the differences of lying and standing CuPc at 10 K in the exciton spectral region. The higher detailed absorbance peaks for lying CuPc at 10 K indicate a higher crystallinity on KCl than on glass. Due to poorer crystallinity of the standing CuPc molecules on glass, the absorption peaks are slightly broadened. The different relation of intensities for the splitted excitonic peaks occur due to different

access to the dipole transitions and show a more pronounced β formation for lying molecules. If the splitted peaks in excitonic and π - π^* spectrum can be interpreted as splitting it should be clarified by further measurements if the β phase also shows a splitting.

The red shift of the excitonic peaks for lying molecules on KCl should be seen in combination with the blue shift of the π - π^* transition. This results in a stronger exciton binding energy for lying CuPc than for standing CuPc.

5.2.4. TiO-Phthalocyanine

Titanyl phthalocyanine (TiOPc) is a non-planar polar molecule, the chemical structure is shown in Fig. 5.39. It is one of the most efficient organic photoconductors in the near-IR region and used in laser printers and OLEDs[181]. Due to its absorption properties in the visible spectrum extended toward infrared, more optoelectronic applications for TiOPc are possible, as for example as active channel in OFETs [37].

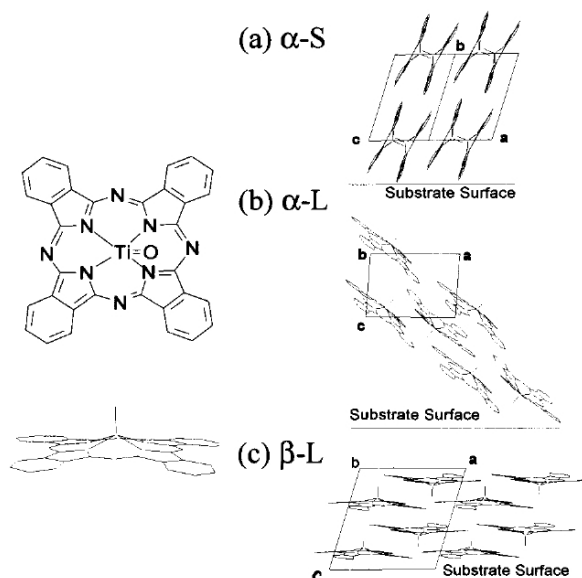


Fig. 5.39.: Figure and caption taken from [224]: Molecular structure of oxotitanium(IV) phthalocyanine (TiOPc) and molecular orientation models for (a) α -standing, (b) α -lying, and (c) β -lying.

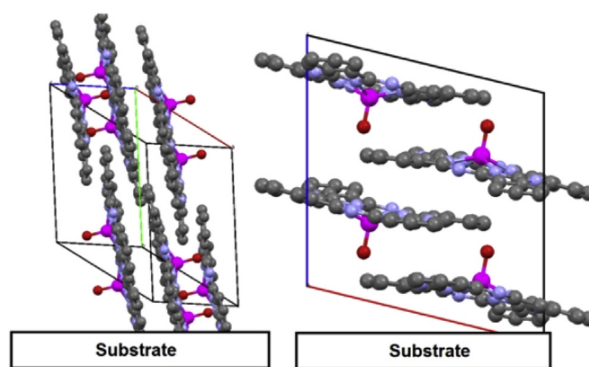


Fig. 5.40.: Figure and caption taken from [37], Fig. 4: Representation of the molecular arrangement of TiOPc with respect to the substrate in the α -phase (left) and β -phase (right). Remark: the angle of the molecules towards the substrates is different from the illustration of [224] in Fig. 5.39, which of the illustrations is the right one should be investigated in further experiments.

As illustrated in Fig. 5.39 TiOPc develops different crystalline phases in dependence of growth parameters during OMBD or single crystal growth by chemical vapor deposition, revealed by XRD measurements. See also [37] for detailed investigation of growth parameters on phase and alignment. Phase I is named the β phase and phase II the α phase. A phase with optical properties in between both phases is possible which is not discussed in this chapter, the Y-phase [135]. The different polymorphs have different electrical and optical properties, the latter can be seen for example in Fig. 5.44b.

For more details of chemical structure and molecular order see [40]. While the alignment of both α and β phase is influenced by substrate morphology, the phase, size and shape of the formed crystals depend on substrate temperature and further preparation conditions. A high kinetic beam energy and high substrate temperatures favor α phase. For lower substrate temperatures smaller crystals than with high substrate temperature form and an enlargement of grain size occurs with increasing beam kinetic energy due to increased diffusion time on the substrates. For higher substrate temperatures as 220°C needle like structures build up with larger crystal size and the effect of increasing beam kinetic energy is vice versa resulting in slightly smaller crystals [37]. In order to obtain both α and β phase crystal formation in coexistence or a β -predominant phase, high substrate temperatures of $400 - 500^\circ\text{C}$ are needed during OMBD.

Regarding the produced samples of Michael Kothe from Witte group, Marburg, used for the shown TiOPc thin film results of this work (both on glass and KCl), a mixture of α and β phase or a single β phase can be expected due to the very high substrate temperature of 500°C during OMBD.

Solid formation: exciton formation

Fig. 5.41 shows the absorption spectra of solid layers of TiOPc in comparison to molecules in solution. The spectra of CuPc are included in order to show the differences between both phthalocyanines. As for CuPc, TiOPc shows a broadened absorption in

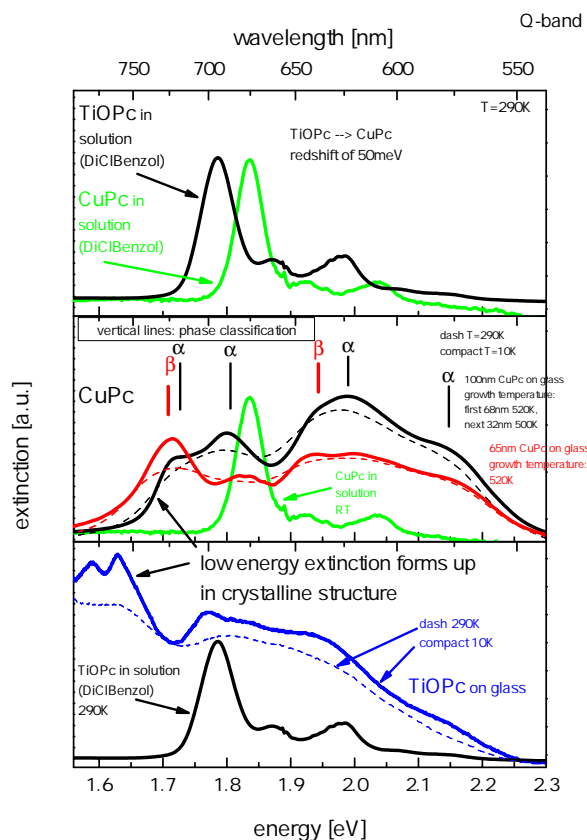


Fig. 5.41.: Absorption spectra of TiOPc in solution (upper part) and as solid (lower part). In the mid part and added as solution spectrum CuPc spectra are shown.

the visible range in comparison to absorption in solution. TiOPc spectra exhibit a red shift to CuPc spectra, both for solution and solids. From room temperature to low temperatures of 10 K a sharpening of absorption peaks can be seen (see lower part in Fig. 5.41), especially in the red spectral region of the lowest absorption peaks.

When comparing solid and solution absorption spectra, an indication that the new forming low energy absorption band in NIR spectral region can be interpreted as exciton formation is provided by a detected quasi molecular layer which does not show exciton absorption in NIR region, see green curve in Fig. 5.42. The exciton formation occurs only if molecules interact with each other in crystalline structures and develop charge-transfer excitons, see chapter theory 3.2.

In literature, detailed absorption spectra of the different phases can be seen in [172, 135, 224], in addition one β spectrum is shown in [181]. It is shown in [40] that an alpha spectrum evolves from amorphous spectrum by thermal annealing at 150°C. A total phase transition from amorphous to α phase can be realized by exposure of the film to EtOH solvent vapours [204, 40].

Fig. 5.44a and 5.44b show typical α and β phase spectra from literature. While the β phase of both authors seems to be equal, the α phase of both authors is not completely congruent. Yet the important main absorption peak in the NIR spectrum around 850 nm

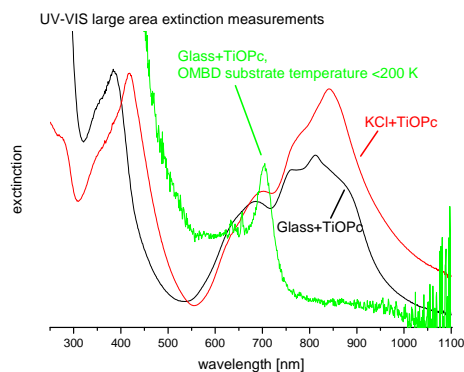
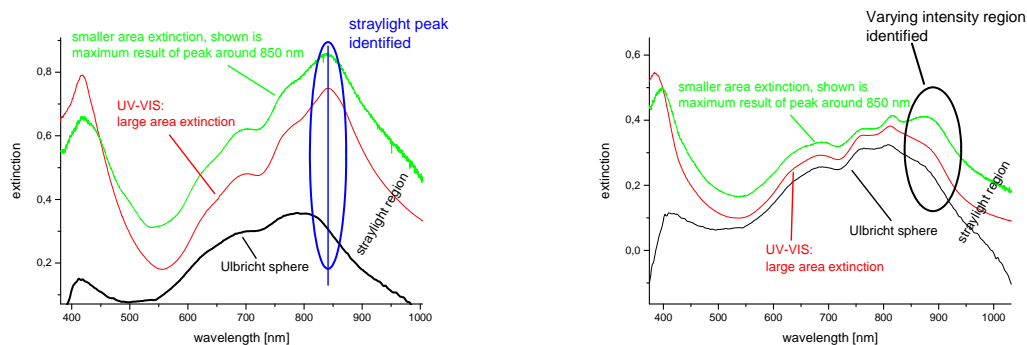


Fig. 5.42.: Absorption measurements: Comparison of TiOPc layer on glass @500 K with 50 nm thickness, 25nm amorph layer on glass @<200 K and 53 nm layer on KCl @500 K. The scale is set arbitrarily for best comparison. A slight redshift of TiOPc on KCl in comparison to on glass can be detected. The NIR peak on KCL indicates a possible stray light region which should be investigated by other optical methods (Ulbricht sphere and reflection measurements).



(a) TiOPc on KCl: Straylight region identified in NIR spectral region.

(b) TiOPc on glass: Extinction peak identified in NIR.

Fig. 5.43.: Investigation of TiOPc samples on glass and KCL with different measurement stages including Ulbricht sphere. This helps to identify straying phenomena and real absorption peaks. The NIR peak around 850 nm changes its strength, especially for TiOPc on KCl but also for TiOPc on glass. Ulbricht sphere measurements show a deminishing NIR peak on KCl but a remaining peak on glass, identifying straying on KCl and a real extinction on glass in NIR region.

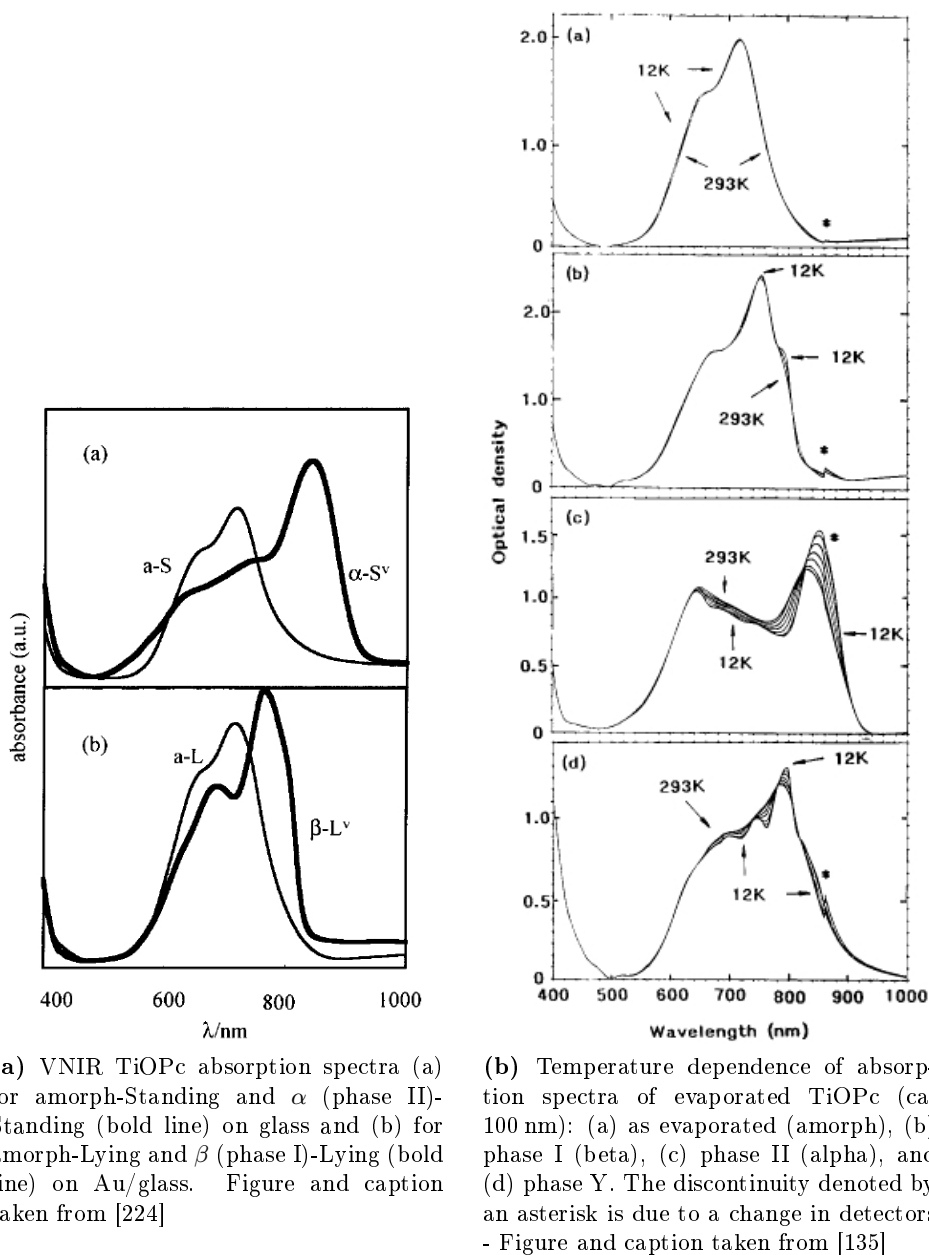


Fig. 5.44.: Absorption spectra of TiOPc from literature.

is shown for both authors and can be taken as indication for the α phase.

The Y-phase shown here from Mizuguchi et al. in Fig. 5.44b is different from Saito et al. [172] which indicate the lowest energy absorption peak at 830 nm. The Y-phase is left out from the discussion of optical spectra in this work, also because only α or β phase may occur with the OMBD settings used here.

The absorption spectra from literature do not show complete congruence with the measured spectra in this work, this is discussed in the following.

As can be seen, the peaks indicating the α phase around 850 nm occur both for TiOPc on glass and on KCl, see Fig. 5.42. But also β phase shows its main characteristic peak at around 810 nm of the absorption spectrum in both spectra of TiOPc on glass and KCl.

It has to be clarified if the spectra show mixtures of α and β phase or if pure β spectra for TiOPc on glass and KCl could be determined, if taking wavelengths greater than 800 nm in the red spectral region as an effect of scattering, see the indicated possible stray peaks in Fig. 5.42. As can be seen in Fig. 5.42, the peak in NIR is not as pronounced for TiOPc on glass as for TiOPc on KCl. Investigating the same samples with different absorption stages including Ulbricht sphere (see Fig. 5.43a and 5.43b), the NIR peak changes its strength, especially for TiOPc on KCl but also for TiOPc on glass. This reveals a scattering effect in NIR for TiOPc on KCl and the lowest energy peak around 850 nm can be therefore be interpreted as straying phenomenon for TiOPc on KCl. Probably pure β phase can be indicated for TiOPc on KCl.

Regarding TiOPc on glass, this corresponds with its remaining peak at around 850 nm also to the α spectrum, see Fig. 5.44a. TiOPc on glass can therefore probably indicated as mixture of α and β phase.

Due to the straying effect in NIR spectral region and additional α phase absorption in NIR, the exciton splitting is not as clear as for CuPc 5.38. Yet, this phenomenon is clearly revealed in Fig. 5.41 for TiOPc on glass at 10 K. At cold temperatures of 10 K for TiOPc both on glass and KCl show a splitting in absorption spectra at around 800 nm, see Fig. 5.48, with more pronounced splitting on glass. This exciton splitting is also shown in literature for β phase (phase I) at 77 K from Saito et al. [172], Fig.1b. Mizuguchi et al. discuss exciton splitting [135] by addressing the main absorption bands at 660 nm and 840 nm of the α phase II as result from reduction of molecular symmetry. A detailed discussion about exciton formation for TiOPc should be done in future including the exciton splitting detected in this work regarding the luminescence at around 800 nm.

Excitonic Photoluminescence

The PL of TiOPc on a substrate (KCl) is shifted in comparison to solved molecule PL (see Fig. 5.45). This red shift is due to the broader absorption forming in solid state and the consequently lower energy of the photoluminescence. In the consequence of crystal formation TiOPc can show charge-transfer exciton PL (see chapter theory 3.2 for more details on exciton formation) if highly ordered crystalline structures are grown. Lower bands in the PL spectra come from defect states of the crystal.

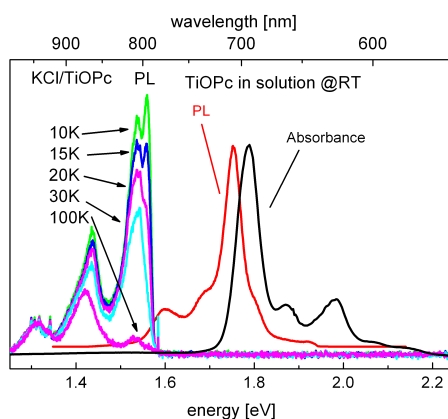


Fig. 5.45.: Comparison of the PL of TiOPc in solution with on potassium chloride. As shown in Fig. 3.10 a mirror-symmetry is apparent for PL in solution to absorption in solution. The PL of a solid layer of TiOPc on potassium chloride at different cool temperatures is shown with an increasing PL with decreasing temperature. The PL shows a strong redshift in comparison to the PL in solution due to exciton formation, explained later in chapter "Organic Semiconductors" 3.2

PL spectra can help to distinguish between the TiOPc phases because they are not influenced by absorption or scattering and reflection effects which might occur, especially on crystal formation as for TiOPc on KCl.

Literature shows Photoluminescence spectra as can be seen in Fig. 5.46 which are the PL spectra referring to absorption of Fig. 5.44a. In addition, a photoluminescence of 894 nm is discussed in [40] which stays spectrally equal for all spectra between amorphous and pure α phase. Since 894 nm is not congruent with the α -luminescence of Yonehara et al. [224], a clear proven photoluminescence is missing.

Regarding the spectral results of this work with examining TiOPc on different substrates KCl and glass, the photoluminescence spectra at 10 K show strong differences (see Fig. 5.47 and 5.48).

Both spectra of TiOPc on glass and KCl show a luminescence at around 800 nm. This indicates that both samples cannot be pure α phase, since a pure α phase should show luminescence at lower energy than the lowest absorption, i.e. at wavelengths larger than 850 nm. Literature does not show such a sharp and dominant photoluminescence peak at around 800 nm, not even at lower temperatures of 77 K (see Fig. 5.46). This shows that the built layers of Michael Kothe, Witte group, Marburg, are of higher crystalline quality than the layers investigated in literature and that the sharp and dominant PL around 800 nm is probably due to excitonic PL. If powder or drop casted TiOPc is investigated, sharp PL peaks do not occur, see lower part in Fig. 5.48.

Especially, the highest energy PL peak at around 800 nm of TiOPc on KCl is remarkable, since the peak does not form up on glass. This peak shows a strong temperature dependence (see Fig. 5.45), while the upper excitonic states show an extremely weak temperature dependence. The PL at around 800 nm evolves at lower temperatures and increases to a maximum at 10 K. For both TiOPc on glass and on KCl the PL peaks around 800 nm reveal excitonic PL, the strong temperature dependence at around

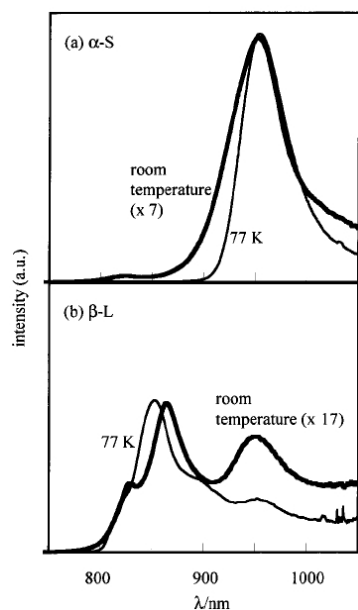


Fig. 5.46.: Normalized fluorescence spectra of (a) α (phase II)-Standing on Pt/glass and (b) β (phase II)-Lying on Au/glass. Figure and caption taken from [224]

800 nm on KCl might be an effect of the existing TiOPc phase.

Comparing the PL results of this work with literature excluding the sharp peaks around 800 nm, TiOPc on KCl shows strong similarities to β -Lying PL of Fig. 5.46. As already concluded for TiOPc on KCl as most probable phase deduced from the absorption spectra, PL measurements confirm this conclusion and identify the layer on KCl as probably pure β phase.

For TiOPc on glass a mixture of α and β phase is suggested deduced from absorption measurements. But the according PL is not showing the peaks of the PL on KCl except the strong peak at around 810 nm which occurs both for TiOPc on glass and on KCl, see Fig. 5.47 and 5.48. The mechanisms of exciton relaxation and deep traps should be clarified in further investigations in order to understand the PL on glass. It might be that a transfer from β -phase states to α -states occur and that the spectrum on glass is a pure α -state spectrum, except the strong PL at 810 nm which might stem from the β phase. The PL on glass around 915 nm might have the same origin as the PL shown in literature for the α phase at 894 nm [40] or at about 950 nm in Fig. 5.46[224]. It could be interpreted then as the resulting PL of the lowest energy absorption of the α phase. But as can be seen in the powder PL, also other deep traps might occur which show the given luminescences of the literature.

Time resolved photoluminescence TiOPc

As an outlook from this work, first results of time resolved photoluminescence measurements are shown. While in solution a long decay time of 12.4 ns occurs, the decay time shortens on KCl to about 3.4 ns in the first ns (see Fig. 5.49), which is therefore limited by the experimental stage. ps-TRPL measurements should be performed with solid TiOPc layer to reveal the decay times.

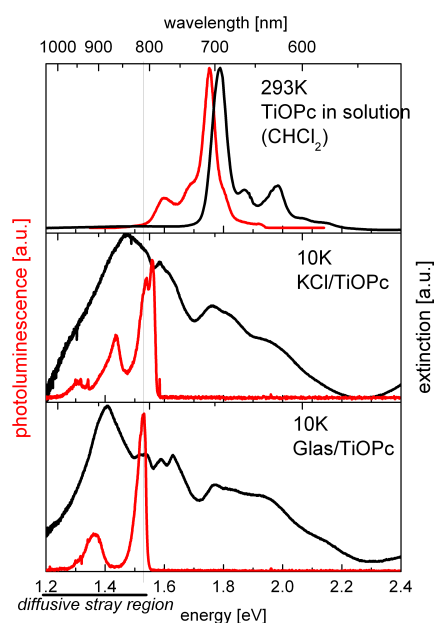


Fig. 5.47.: Photoluminescence spectra and absorption spectra are illustrated for TiOPc in solution and for layer on planar substrates. The solid PL at 10 K show strong differences comparing TiOPc on glass and on KCl.

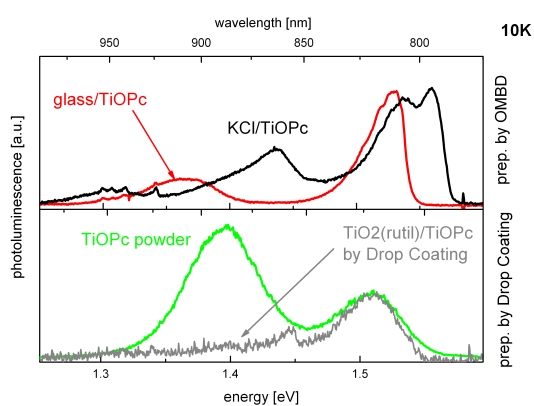


Fig. 5.48.: Photoluminescence spectra of TiOPc on different substrates and as powder. The sample on TiO_2 was prepared by drop casting.

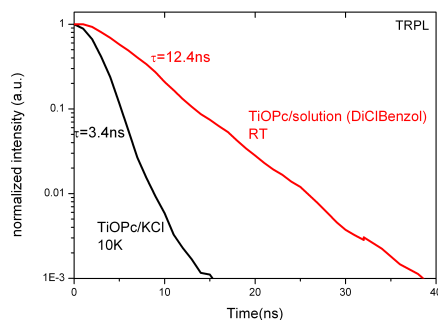


Fig. 5.49.: ns-TRPL results for TiOPc in solution at room temperature and for powder at 10 K.

Not shown in the graph is the decay curve of the small molecular peak shown in powder PL, see Fig. 3.17 around 700 nm. This quasi-molecular PL has a decay time of 6.7 ns at 10 K. Compared to 12.4 ns in solution for molecular PL at room temperature, the quasi-molecular PL decay is faster at 10 K. In literature TRPL is discussed in Yamaguchi et al. for Y-TiOPc [219] due to interest of Y-TiOPc for photoconductivity. Further TRPL measurements at room temperature and 10 K are necessary including investigation of exciton PL in order to give more insight into TiOPc decay mechanisms and allow a theoretical discussion.

The small PL peak at 850 nm shown in lower part of Fig. 5.48 for TiOPc drop casted on TiO₂ appears at the same position as for TiOPc drop casted on CdS. TiO₂ and CdS differ in level alignment. In consequence it seems to be not a type II charge transfer photoluminescence, i.e. the recombination of an exciton across the interfaces of TiO₂ and TiOPc. Charge Transfer from TiOPc to TiO₂ is discussed in [221] and [226] and should be also investigated in future in more detail, a layer of TiOPc on TiO₂ is a possible system to detect a type II PL.

Reflection measurements

As already discussed in the experimental part for TiOPc 4.3.1 specular and diffuse reflection measurements help to identify stray light in optical spectra.

In theory chapter 3.2 in Fig. 3.17 diffusive reflection spectra of TiOPc show that such spectra can help to achieve informations of samples with stray light spectral regions and absorption measurement difficulties.

In Fig. 5.50 and 5.51 temperature dependent diffusive reflection spectra of TiOPc on KCl and Powder are shown. As can be seen for TiOPc on KCl in Fig. 5.50, the photoluminescence adds to the diffusive reflection spectra as positive signal. Exactly in the stray-light spectral region a photoluminescence occurs, but this rather sharp peak at around 870 nm seems not to be the reason for the broad diffusive reflection peak around 870 nm. Regarding the diffusive reflection at longer wavelength up to 1000 nm, a scattering effect occurs. Yet it is not as pronounced as the scattering on TiOPc powder

in Fig. 5.51. It is therefore not clear from the diffusive reflection measurements if the sample TiOPc on KCl shows an α absorption peak at around 870 nm or if straylight and PL is the reason for that peak.

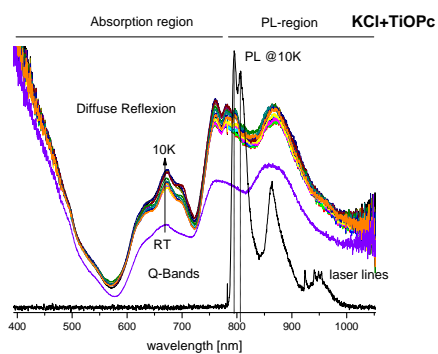


Fig. 5.50.: TiOPc on KCl: temperature dependent diffusive reflection measurements at varying temperatures, the photoluminescence at 10 K is added to show its influence on the diffusive reflection spectra.

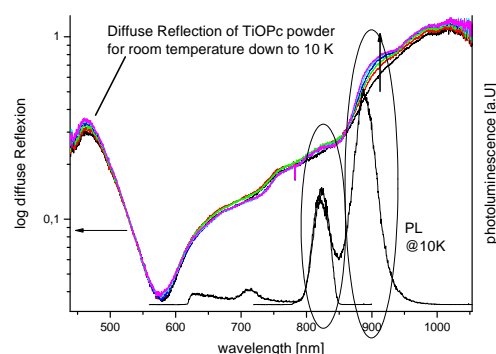


Fig. 5.51.: TiOPc powder: temperature dependent diffusive reflection measurements at varying temperatures, the photoluminescence at 10 K is added to show its influence on the diffusive reflection spectra.

Specular reflection measurements help to identify such spectral regions with diffusive reflection and scattering because in specular reflection the diffusive scattering signal should be much less pronounced than in diffuse reflection. For TiOPc on KCl, the diffuse reflection peak around 870 nm disappears, see Fig. 5.52. This indicates that the peak evolves from diffusive reflection and scattering effects.

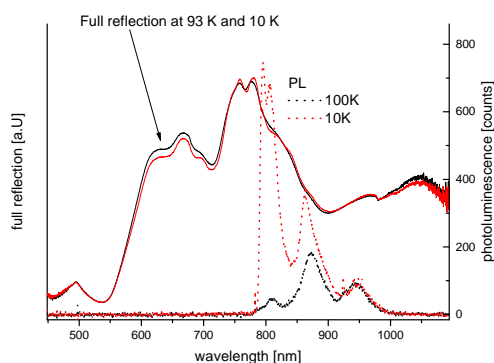


Fig. 5.52.: Specular reflection of TiOPc on KCl - no extinction peak at 870nm can be seen.

In addition to reflection measurements, stray light spectral regions can be indicated from Ulbricht sphere measurements, see Fig. 5.43a and 5.43b.

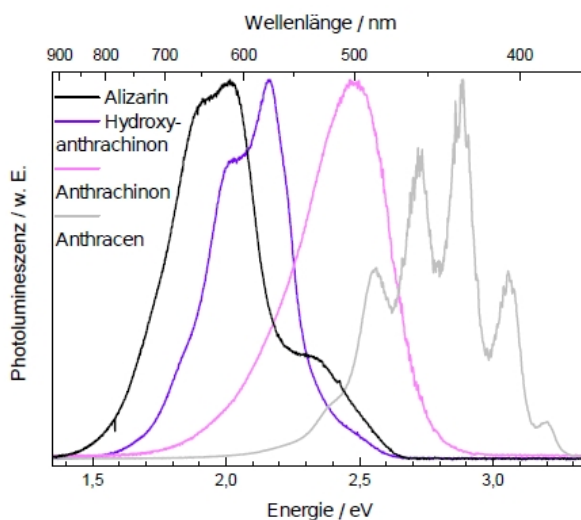


Fig. 5.54.: PL of Anthracene, Anthraquinone, Hydroxy-Anthraquinone, Alizarine in solution (Chloroform). Added Hydroxyl groups lead to a redshift. The picture is taken from bachelor thesis of Benjamin Heidelmeier [79].

5.3. Anthraquinone dyes

5.3.1. Introduction

Fig. 5.53 shows the chemical structures of pre steps of the Anthraquinone Alizarin. All Anthraquinones are based on Anthraquinone (see Fig. 5.53 b, Anthrachinon). Further modifications with one or two hydroxyl groups lead to Hydroxyanthraquinone and Alizarin, respectively. From definition, a catechol is an unsaturated six-carbon ring with two hydroxyl groups attached to adjacent carbons, which occurs here for Alizarin.

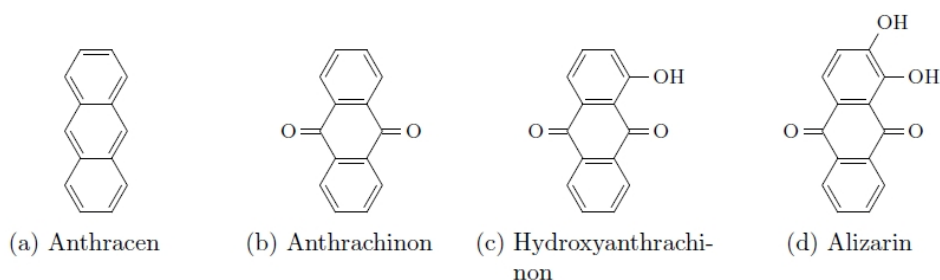


Fig. 5.53.: Chemical Structure of pre steps of Alizarin. Anthrachinon is the starting point of synthesis of all Anthraquinone modifications. The picture is taken from bachelor thesis of Benjamin Heidelmeier [79]. PL spectra of the molecules are shown in Fig. 5.54.

Anthraquinones usually have high molar extinction coefficients and strong absorption bands in the visible light range [68]. These properties make anthraquinone derivatives interesting for the use in dye-sensitized solar cells [66] so that alizarin and related compounds have already been investigated with efficiencies up to 2.17% [72]. The intention is to modify the anthraquinone backbone by substitution with amine and

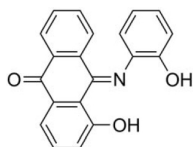


Fig. 5.55.: 9-(2-Hydroxyphenylamino)-1,10-anthraquinone with trivial name Anthraphenol

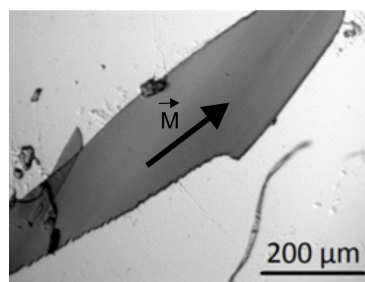


Fig. 5.56.: Microscopic picture of an anthraquinone imine Anthraphenol single crystal grown on a quartz substrate.

imine moieties to improve the absorption and electrochemical properties for the use in dye sensitized solar cells (DSSC).

Principles of DSSC are illustrated in Fig. 2.2 in chapter 2.2.

Further investigations of optical properties of different Anthraquinones were performed. Anthraquinones with trivial names Anthracen, Anthraquinon, Hydroxyanthraquinone and Alizarin and Anthraphenol were investigated by Benjamin Heidelmeier, group Heimbrodt, Marburg, in a bachelor thesis [79]. Important results of this thesis are also shown in this work in the appendix B.1, ps-TRPL measurements are included in appendix B.2.

Furthermore, different Anthraquinone based Zn-Phantron-complexes and its ligands were investigated which might be suitable for OLED applications due to its partially occurring extreme strong photoluminescence. Those ligands and complexes were investigated by absorption, reflection and photoluminescence measurements at different temperatures from room temperature to 10 K. The results are not shown in this work but can be found in the PhD thesis of Christian Prinzisky [155] including a detailed discussion about the resulting optical spectra.

5.3.2. Absorption and Photoluminescence Spectroscopy: Anthraphenol

This paragraph is overtaken in large parts from the publication [155] of Christian Prinzisky, group Sundermeyer, Marburg, chemistry department. Christian Prinzisky also synthesized the organic molecules and provided them in powder form for optical investigations in group Heimbrodt, Marburg, physics department. At this publication i contributed by optical measurements and provided the paper text shown in 5.3.2 in collaboration with Prof. Heimbrodt, Marburg, physics department.

The luminescence and absorption properties of anthraquinone imine Anthraphenol in the solid phase on substrates in the low-energy region are studied. Single crystals were prepared by dropcasting of Anthraphenol in chloroform onto rutile TiO₂ and quartz substrates. High-quality platelet-shaped crystals were obtained with dimensions of about 500 μm and a thickness of a few μm. A typical microscopic picture is given in Figure 5.56, the chemical structure is shown in Fig. 5.55.

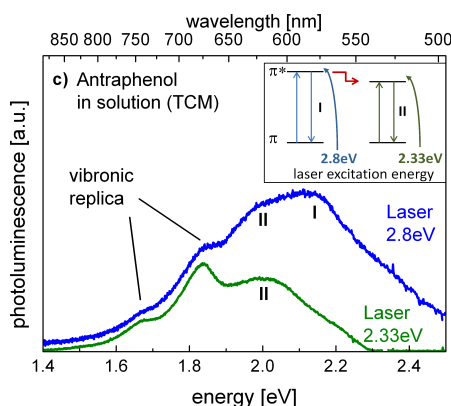


Fig. 5.57.: Luminescence spectra at room temperature of anthraquinone imine Anthraphenol in solution (chloroform) excited by different laser energies (2.33 and 2.8 eV).

Absorption measurements were performed by using a high-resolution grating spectrometer equipped with a CCD camera and a halogen lamp as light source. In the case of bulk crystals, the light was focused by a microscope objective before impinging onto a selected crystal. For photoluminescence (PL) spectroscopy, an argon ion gas laser of 2.41 eV (microscope PL in the case of bulk crystals), a laser diode of 2.8 eV, and a frequency-doubled diode-pumped solid-state laser of 2.33 eV were used as excitation sources.

The luminescence and extinction spectra of anthraquinone imine with trivial name Anthraphenol in solution (chloroform) recorded at room temperature are depicted in Figures 5.57 and 5.58a). It is interesting to note that the luminescence spectrum depends on the excitation wavelength. By exciting above the π - π^* molecule absorption two main peaks (denoted I and II in Figure 5.57) can be seen. By exciting below the π - π^* absorption only the peak II and vibronic replica can be seen. We ascribe band I to the π^* - π recombination and band II to an excitonic recombination. From the data obtained here we cannot determine whether it is a strongly localized Frenkel exciton or rather an exciton with charge-transfer character.

We compare now the luminescence and extinction spectra of anthraquinone imine Anthraphenol recorded in solution with the corresponding transitions in the solid phase. In Figure 5.58 b) the luminescence and extinction spectra recorded at room temperature are depicted for single crystals on a TiO_2 substrate. Remarkably, a strong polarization of the excitonic absorption spectra could be observed. The light-green curve was measured by using linear polarized light along the direction depicted by the arrow in Figure 5.56. The dark-green curve was recorded with the polarizer rotated by 90° about the normal axis of the plane. The crystals clearly exhibit a strong anisotropic absorption. Although the two transitions at around 2.8 and 2.6 eV do not show anisotropic behavior, the transition at 2.35 eV is caused by a dipole oriented solely along the elongated axis of the crystal. By measuring different spots on the TiO_2 substrate, it became clear that the bands at 2.8 and 2.6 eV originate from different layers. Whereas the unpolarized absorption at 2.6 eV as well as the polarized absorption band at 2.35 eV come from the crystal, the band at 2.8 eV most probably arises from an underlying thin amor-

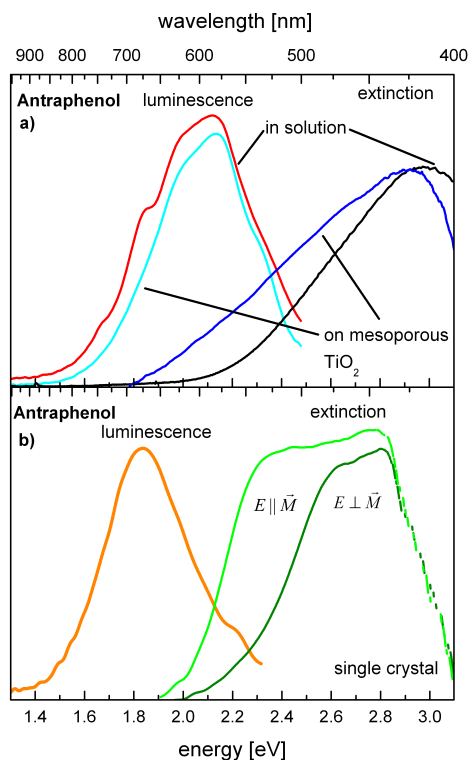


Fig. 5.58.: Extinction and luminescence spectra at room temperature of (a) anthraquinone imine with trivial name Anthraphenol in solution (chloroform) and on mesoporous TiO₂ sensitized by soaking, and (b) anthraquinone imine Anthraphenol single crystals grown on rutile TiO₂ substrates.

phous layer. The crystals exhibit a luminescence band at 1.83 eV (orange curve), which experiences a Stokes shift of about 500 meV. We ascribe this transition to delocalized excitons in the crystal. It is remarkable to note that the crystal emission is redshifted compared with the molecular Frenkel exciton.

It is very interesting to compare the spectra of the single crystals and molecules with those of solid anthraquinone imine Anthraphenol in mesoporous TiO₂, see Figure 5.58 a). Crystal formation is strongly suppressed in that case; a pure molecule PL spectrum can be seen and even the absorption band is dominated by the pi-pi* absorption at about 2.95 eV.

Figure 5.59 explains the contributions of different layer properties (upper part) to the shown crystal spectrum (lower part and Fig. 5.58 b)). The upper part shows the absorption spectra of an amorphous layer (in red) with an absorption maximum at about 2.8 eV and the spectrum of a tiny single bulk crystal (in grey) and the according PL.

For comparison, the PL spectrum of the anthraquinone imine Anthraphenol powder is shown in Figure 5.59 as a black curve in lower part. The small redshift to the

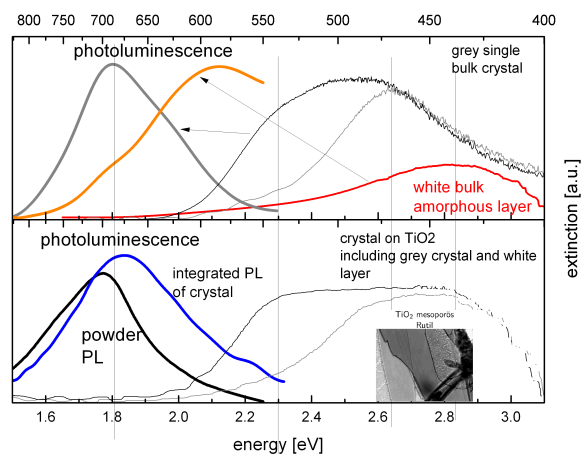


Fig. 5.59.: Contribution of Anthracene mono-crystalline and amorphous layer to crystal absorption and PL spectra. For comparison, powder PL is shown.

crystal PL may be caused by relaxation into defect states, which do not show up in the highly ordered single crystals. Furthermore, the small redshift of the crystal PL of the lower part in comparison to the crystal PL of the upper part can be explained by a contribution of the amorphous layer PL (in orange in upper part) to the PL spectrum, resulting in a small redshift of the pure crystal PL.

6. Charge Transfer in Organic-Inorganic Hybrid Structures - Accessing the Level Alignment at the Interface

This chapter includes text parts and results of the publications "Charge transfer at organic - inorganic interfaces - Indoline layers on semiconductor substrates" of the authors I. Meyenburg, J. Falgenhauer, N.W. Rosemann, S. Chatterjee, D. Schlettwein, and W. Heimbrodtt [131] and "Optical determination of charge transfer times from indoline dyes to ZnO in solid state dye-sensitized solar cells" of the authors Meyenburg, I., Breuer, T., Karthäuser, A., Chatterjee, S., Witte, G., and Heimbrodtt, W. [132].

6.1. Charge Transfer in Organic-Inorganic Hybrid Structures: Indoline dye

Organic-inorganic semiconductor hybrids are promising functional materials for advanced, optoelectronic devices. For example, dye-sensitized solar cells of the Grätzel type [148] are candidates for commercial photovoltaic applications. Despite the relatively low quantum efficiencies compared to silicon based solar cells and to the recently reported perovskite based solar cells [120], there is continuous interest in Grätzel type solar cells, as they are low cost devices and thus provide short energy payback times.

An important process in high efficient dye-sensitized solar cells is an optimized electron transfer, i.e., the electron injection yield from the dye into the conduction band of the semiconductor at the organic-inorganic interface[119]. Physically, a mandatory prerequisite is the best possible electronic coupling between the excited dye sensitizers and the conduction band of the semiconductor. The relevant parameters for injection

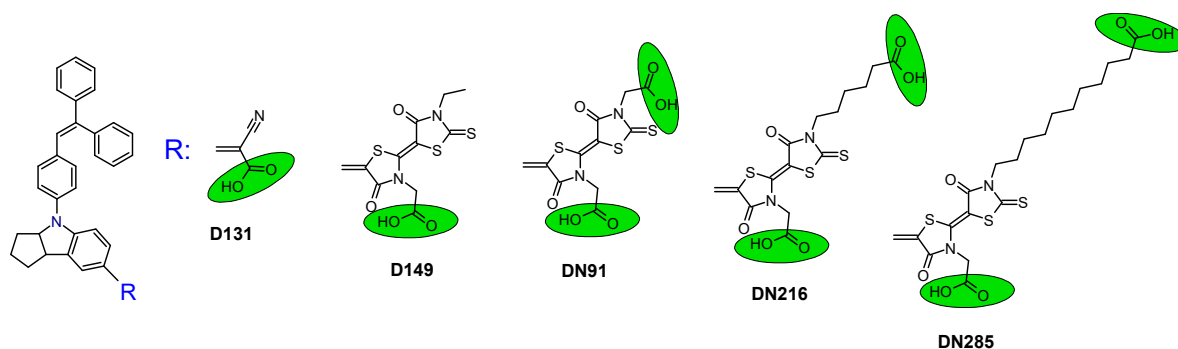


Fig. 6.1.: Schematic picture of the chemical structure of the various indoline derivatives.

consist in (i) the level alignment between the excited state of the dye and the conduction band minimum (CBM) of the semiconductor as well as (ii) the mean distance between the excited sensitizer molecules and the semiconductor surface.

To date, various different semiconductor materials and dyes were suggested as efficient organic-inorganic hybrids for solar cell application (see, e.g., [67] and the review by Ooyama and Harima [147]). Overall, TiO₂ is the prototypical n-type semiconductor. This material was already suggested in the original realization by O'Regan and Grätzel [148]. It is a wide bandgap material and therefore transparent for a sufficient spectral range of sunlight. A considered viable alternative is ZnO[54, 169, 165, 164]. The location and type of anchoring group also plays a key role for the electronic coupling to the substrate [119, 187]. The carboxylate anchoring group used in our studies have been shown to favor the electron injection into a metal oxide surface [119, 175].

Pump-probe transient absorption spectroscopy on the ps timescale is the most widely used method to study the excitation dynamics of dyes in solution [52, 122] and to determine electron transfer times [164, 193, 53, 150]. Such measurements typically use high-energy fs pulses for excitation. The depletion of the excited state is determined by the charge transfer (CT) but can be influenced also by the relaxation and formation of excitons as well as charge accumulation and respective screening effects. In this paper, we study the CT times for a variety of indoline dyes and semiconductor substrates by time-resolved photoluminescence (TRPL). In particular, we study the kinetics of the excitons in the dye layers after formation and relaxation from the primarily excited higher energy levels and determine the CT times from the exciton states to the interface at low excitation densities. We will show that the respective transfer times can differ substantially for physical reasons from times determined by pump-probe measurements.

The excitonic PL transients are a complicated interplay of various processes influencing the transition probability. On one hand, the effective medium or molecule-molecule interaction changes the lifetime; on the other hand, many loss and energy transfer channels influence the lifetime. The resulting non-exponential curves are commonly fitted by a sum of several exponential functions or even by stretched exponentials, leaving the interpretation of the resulting transients as a sophisticated complex challenge. Here, we apply kinetic model calculations to describe the decay curves in order to reveal the charge transfer times from the excitons to the interface. Experimentally, we vary the substrate and hence the energy level alignment. Additionally we vary the geometric alignment of the dyes relative to the organic-inorganic interface and study the influence of different anchor groups.

6.1.1. Sample Preparation and Experimental Details

We study a series of five different indoline derivatives. All share the identical indoline chromophore, while the anchor groups are varied. The schematic structures are depicted in Fig.6.1. D131 and D149 have only one carboxyl anchor group but differ in the distance between the carboxyl group and the indoline chromophore. All the other indoline derivatives have two carboxyl anchor groups and differ from each other in the length of the anchor chain of the second carboxyl group.

We prepared the sensitized mesoporous samples by immersing films of the mesoporous semiconductors into a solution of indoline dye and acetonitrile / tert. butanol (50%/50%). This "soaking" is the standard technique for Grätzel type dye sensitized solar cells. The substrates for soaking are mesoporous ZnO (ZnO(meso)) or mesoporous anatase TiO₂ (TiO₂(meso)). TiO₂(meso) samples consist of a 10 μm thick layer on fluorine-doped tin oxide (FTO) glass which is built up by ~20 nm thick particles of TiO₂. The layer is prepared by applying a TiO₂-gel and sintering at 450°C. Mesoporous ZnO was prepared by an electrochemical deposition of ZnO on FTO glass in the presence of a structure-directing agent, using KCl as electrolyte component. The deposited film was left overnight in an aqueous KOH solution to remove the structure-directing agent and dried before the sensitization (see [163] for experimental details).

Indoline dye layers were prepared by drop casting the same solution as used for soaking on flat substrates, i.e., on single crystals of ZnO(0001), rutile TiO₂(100), and SiO₂(0001) (Crystec) as well as on standard fused silica.

We performed photoluminescence (PL) and absorption measurements by means of a standard setup with a high-resolution grating spectrometer. For the steady-state PL, a laser diode of 442 nm (2.8 eV) and for the optical absorption measurements a white light lamp were used.

The time-resolved PL experiments were performed using a standard streak-camera setup. Details are given for example in [7]. The 100-fs pulses of the tunable Ti:Sapphire laser were frequency doubled to 2.8 eV (442 nm) for most experiments; a 475 nm color-glass edge filter was used in the detection to suppress scattered laser light. Sensitive measurements on thin layers of D149 and D131 samples were excited at 3.06 eV (405 nm) in combination with an edge filter at 2.76 eV (450 nm).

6.1.2. Absorption and Photoluminescence Spectroscopy

The PL spectra of all indoline derivatives in solution are summarized in Fig. 6.2a. The different lengths of the chains do not substantially influence the $\pi \rightarrow \pi^*$ transitions. The $S_1 \rightarrow S_0$ PL transition energy is very similar for D149 and DN285. However, it exhibits a slight redshift for the shorter anchor chains in DN216 and DN91.

(see appendix C.1 for a detailed comparison of absorption and corresponding photoluminescence in solution)

For comparison, a typical PL spectrum of a D149 layer deposited on ZnO(meso) is depicted in Fig. 6.2b. Compared to Fig. 6.2a, we find a typical red-shift of the emission due to molecule-molecule interactions. This red shift is observed for all different substrates (TiO₂(100), TiO₂(meso), ZnO(0001), ZnO(meso), fused silica), however, the substrates have no significant influence on the spectral width and shape. Comparing the extinction spectra in Fig. 6.2 of D149 in solution and of a D149 layer on ZnO(meso) reveals a broadening due to the weak van-der-Waals molecule-molecule interaction and the respective band formation and dispersion. The different energies of the PL and extinction transitions are caused by the Stokes shift expected according to the Franck-

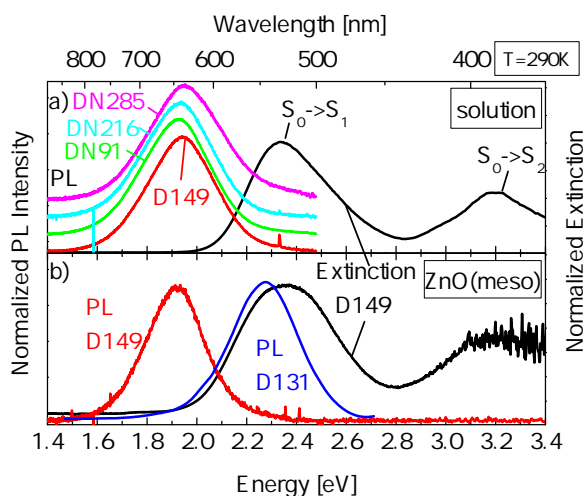


Fig. 6.2.: (a) Photoluminescence of indoline derivatives and extinction spectra of D149 in solution at room temperature. (b) Photoluminescence of D149 and D131 and extinction of D149 on mesoporous ZnO at room temperature.

Condon principle.

In Fig. 6.2b the PL of a D131 layer on ZnO(meso) is depicted for comparison. Clearly, the PL is strongly blue shifted compared to D149; this is typically for the smaller π electron system.

6.1.3. Time-Resolved Photoluminescence Spectroscopy

Dynamics of D149 on ZnO, TiO₂ and glass

In what follows we study the decay dynamics of D149 on ZnO and on TiO₂ in detail. For D149, a conversion efficiency of 6 to 9% on TiO₂(meso) substrates were reported earlier by Horiuchi[86] and Ito[93]. The PL decay transients for D149 films on different substrates are summarized in Fig. 6.3.

The solution data are given for reference. Here, the D149 molecules exhibit a long lifetime for the $S_1 \rightarrow S_0$ transition $\tau_{D149} = 500$ ps. The little deviation from the single exponential revealed by the bi-exponential fit (see Fig.3 and table I) is tentatively attributed to the so-called concentration quenching effect, i.e., the excitation energy is distributed through radiationless energy transfer between the dye molecules and eventually gets transferred to a nonradiative "killer" center.

The residual deviation from the single exponential is tentatively attributed to the so-called concentration quenching effect, i.e., the excitation energy is distributed through radiationless energy transfer between the dye molecules and eventually gets transferred to a nonradiative "killer" center. Even concentration dependent aggregation of D149 in solution leads to a reduction in lifetime [48], see Fig. 6.4.

The D149 on both mesoporous ZnO or TiO₂ exhibit very fast decays. Intriguingly, no substantial difference between the mesoporous substrates ZnO and TiO₂ is found.

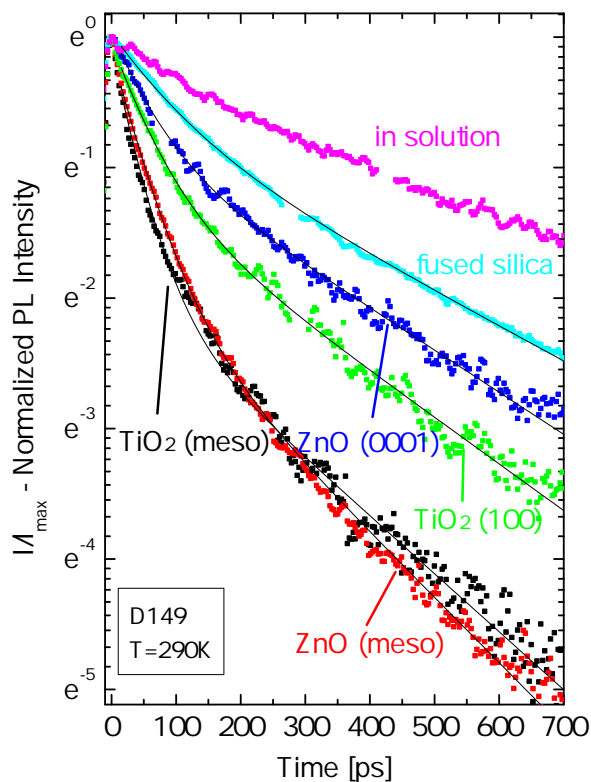


Fig. 6.3.: Photoluminescence transients of D149 in solution and on various substrates on a logarithmic scale.

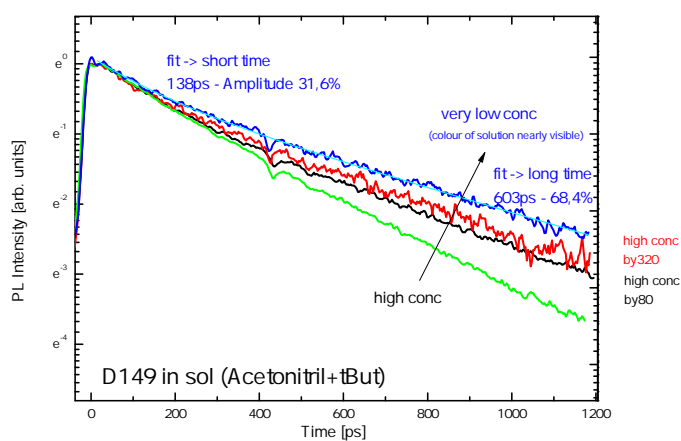


Fig. 6.4.: TRPL of indoline D149 in solution, measured concentration dependant. The lower the concentration, the slower is the decay of the photoluminescence.

Obviously, additional and much faster decay channels are involved now compared to solution. The dominant channel is the transfer of electrons to the interface between the organic layer and the inorganic semiconductor substrate. It should be noted that an alternative loss process, namely the radiationless energy transfer to the inorganic semiconductor, is not possible due to the wide bandgap of the oxide-substrates. Contrarily, a thin layer of D149 on a fused silica substrate does not show such a fast decay.

In general, we ascribe the PL of the dye films to an excitonic recombination with a lifetime τ_{exc} . It should be noted at this point that the exciton lifetime always comprises the radiative and nonradiative recombination probability as well as possible loss channels in the solid phase. Any additional loss channel changes the respective kinetic description such that it is described according to Eq. 6.1 with $w_{\text{trans}} = 1/\tau_{\text{trans}}$ being the electron transfer probability to the interface either to conduction band of the semiconductor or to interface trap states. Both extra channels reduce the number of radiative excitons. Hence, the effective exciton lifetime is then given by Eq. 6.2, which still results in a single exponential decay. However, all experimentally observed decay curves are clearly non-single exponential (cf. Fig. 6.3) inferring a more sophisticated analysis and additional states and channels need to be involved. It is quite clear that only those excitons close enough to the interface can contribute to the charge transfer. Excitons which are too far away from the interface and do not reach the interface during their lifetime cannot dissociate and lose electrons by CT. They will hence recombine with the time constant τ_{exc} . A detailed theoretical description for transients including the mobility of excitons by hopping or diffusion is beyond this paper. Hence, we straight-forwardly divide the excitons in those being close enough to the interface and contributing to the CT and those too far away for a CT to take place during their lifetime.

$$\frac{dn_{\text{exc}}}{dt} = -\frac{n_{\text{exc}}}{\tau_{\text{exc}}} - w_{\text{trans}} \cdot n_{\text{exc}} \quad (6.1)$$

$$1/\tau_{\text{eff}} = 1/\tau_{\text{exc}} + 1/\tau_{\text{trans}} \quad (6.2)$$

This separation yields bi-exponential decay curves given by Eq. 6.3. The weighting factor n_{a} gives the amount of excitons which are created close enough to the interface and can perform either a charge transfer or recombine radiatively. The factor n_{b} is the number of excitons which are too far away from the interface and will therefore recombine radiatively.

Fits of the experimental data using Eq. 6.3 are given as black lines in Fig. 6.3. The exciton lifetimes, the transfer times and the respective weighting factors are given in Table 6.1. Note that the electron transfer time from D149 to TiO_2 is little shorter compared to ZnO which basically agrees with experimental results of Sobuś et al.[193]. It should be mentioned that the transfer times are longer than the ones reported earlier for D149 on ZnO(meso) which have been determined by transient absorption measurements[164]. This difference is attributed to the fact that we measure the transfer time after the exciton formation and subsequent relaxation into the lowest excited states which allow for a charge transfer. It is commonly accepted that the mean transfer time becomes shorter when the electron is in a higher excited state[119, 228].

We should mention here other authors using also TRPL to determine charge transfer

Table 6.1.: Photoluminescence decay times and weighting factors of D149 determined by means of Eq. 6.3 (see text for details). The accuracy of all values is $\pm 5\%$.

D149	τ_{trans} [ps]	n_{a} [%]	τ_{exc} [ps]	n_{b} [%]
TiO ₂ (meso)	46	78	225	22
ZnO(meso)	61	77	200	23
TiO ₂ (100)	69	61	280	39
ZnO(0001)	69	51	310	49
fused silica	115	44	375	56
in solution	96	18	500	82

times reported substantially longer times than ours [31, 192]. Snaith et al. [192] found $\tau_{\text{trans}} = 330$ ps for D149 on TiO₂. We ascribe such discrepancies to an unavoidable effect caused by different interface to volume ratios. An example of this is evident when comparing the decay curves on mesoporous substrates with the decay curves on flat surfaces (see Fig. 6.3). The generally slower decay of the films on the smooth substrates is due to the reduced interface area and the corresponding higher amount of excitons which perform a radiative recombination. This is clearly revealed by the weighting factors (see Table 6.1). For the meso-structures we find n_{a} to be about 0.8, i.e. about 80% of the excitons lose the excited electron by transfer to the substrate, whereas this value is reduced to about 50% on flat substrates. The relative number of recombining excitons to the number of excitons performing a charge transfer is higher the thicker the organic film. Even the exciton lifetimes of D149 layers (see Table 6.1) is different for the meso and flat substrates. We will come back to this point later.

$$n_{\text{exc}}(t) = n_{\text{a}} \cdot \exp\left(-\frac{t}{\tau_{\text{eff}}}\right) + n_{\text{b}} \cdot \exp\left(-\frac{t}{\tau_{\text{exc}}}\right) \quad (6.3)$$

We now turn to the decay curve of the D149 thin solid film on fused silica in Fig. 6.3). It is known that no electron transfer into the silica is possible. Nevertheless, a perfect fit needs again a biexponential function. About 56% of the excitons recombine radiatively with an excitonic lifetime of about $\tau_{\text{exc}} = 375$ ps. About 44% of the excitons suffer from another loss channel. We ascribe the loss channel in that case to radiationless transitions, which are always present in the amorphous layers.

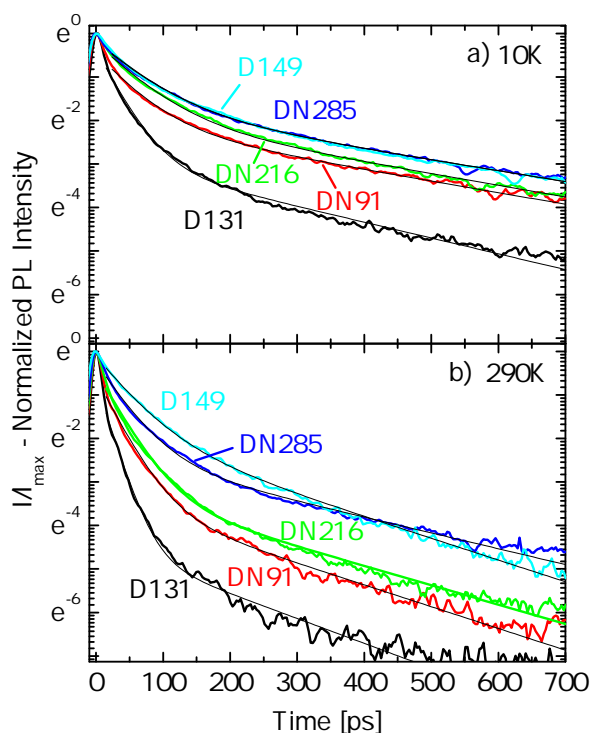


Fig. 6.5.: Photoluminescence decay of indoline dyes on mesoporous ZnO at temperatures of 10 K and 290 K on a logarithmic scale. The respective curves on a linear scale can be found in the SI.

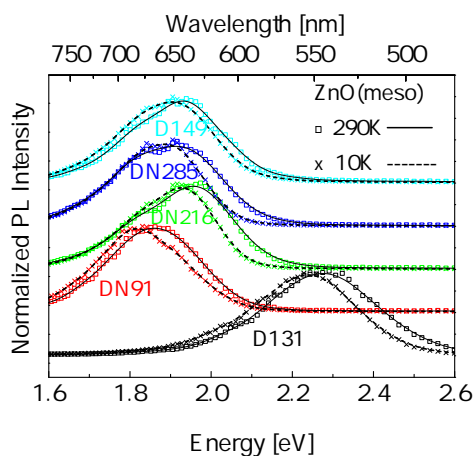


Fig. 6.6.: Photoluminescence of various dyes on ZnO(meso) at room temperature and $T = 10$ K.

Influence of Anchor Groups

Next, we study the influence of the anchor groups on the decay dynamics. Anchoring groups are expected to improve the energy or charge transfer to the organic-inorganic interface. The PL transient of the various dyes on ZnO(meso) are depicted in Fig. 6.5. The

Table 6.2.: Indoline dyes on mesoporous ZnO at temperatures of 290 K and 10 K. The accuracy of all values is $\pm 5\%$.

ZnO (meso)	τ_{trans} [ps]	n_{a} [%]	τ_{exc} [ps]	n_{b} [%]
D149 @290K	61	77	200	23
DN285 @290K	47	84	275	16
DN216 @290K	41	91	225	9
DN91 @290K	38	91	200	9
D131 @290K	23	95	175	5
D149 @10K	70	76	400	24
DN285 @10K	70	73	400	27
DN216 @10K	65	77	375	23
DN91 @10K	55	77	375	23
D131 @10K	37	88	275	11

results are shown for $T = 10$ K (Fig. 6.5a) and at room temperature (RT) (Fig. 6.5b). The thin black lines are the best fits using Eq. 6.3. All parameters are given in Table 6.2.

D131 and D149 have both only one carboxyl anchoring group. The charge transfer time is however much faster in case of D131. This is attributed to the fact that due to the blue shift the excited state of D131 is at higher energies above the ZnO-CBM than the corresponding excited state of D149. This interpretation is supported by cyclic voltammetry experiments [56, 96] and theoretical calculations [228, 104, 89, 127]. A higher energy of the excited state causes a faster charge transfer, in line with earlier findings. To further study this phenomenon we compare the transfer times at RT and $T = 10$ K. Whereas the band gap of ZnO increases by about 55 meV by cooling the semiconductor from RT (3,383 eV [91]) down to $T = 10$ K (3,438 eV at 4 K [202]) the indoline layers undergo a red shift (see Fig. 6.6). The energy difference between the excited electron state and the CBM of ZnO is hence reduced. This can lead to substantially reduced charge transfer probability and respective longer transfer times (see Table 6.2). It should be mentioned, however, that at low temperatures due to the reduced molecular motion even the exciton-phonon coupling is reduced. This leads on the one hand to longer exciton lifetimes but on the other hand even the phonon assisted electron transfer could be reduced. Unfortunately, it is not possible to distinguish between both processes on the basis of our experiments.

We now turn to the second COOH anchor group. Comparing DN91 and D149 reveals that the second anchor improves the CT although the level alignment is expected to be almost identical. Extending the alkyl chain lengths for the second anchor (DN91 \rightarrow DN216 \rightarrow DN285) increases the CT-time, in good agreement to earlier pump-probe transient absorption measurements at similar samples[164], and approaches the CT-time of D149 with just one COOH anchor.

Charge Transfer Dependence of Layer Thickness - ZnO (0001)

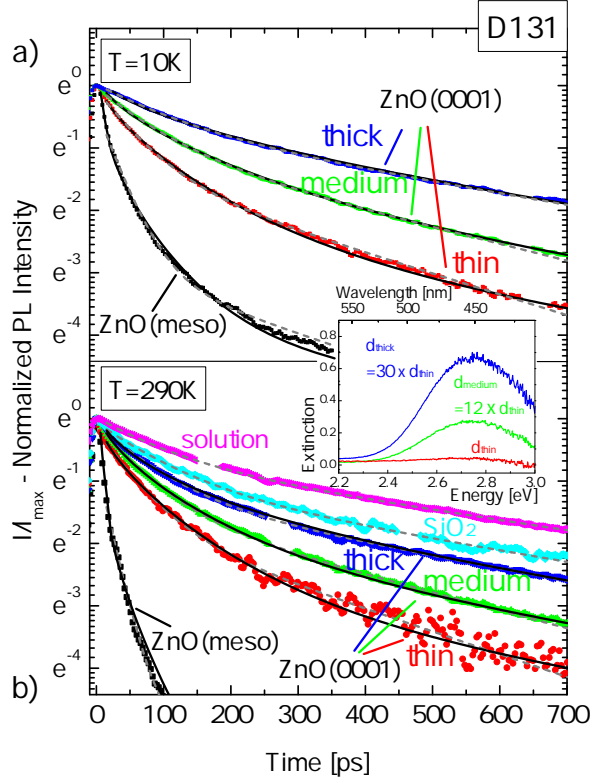


Fig. 6.7.: Photoluminescence decay of D131 on ZnO on a logarithmic scale. The respective curves on a linear scale can be found in the SI. Dashed line: Fit using Eq. 6.3; full lines: Fit using Eq. 6.6 (see text for details). Inset: Extinction of different layers on ZnO(0001).

Finally, we revisit the aforementioned difference between the transients in case of mesoporous and smooth interfaces. Therefore, we plot the PL transients for D131 on ZnO in Fig. 6.7. We prepared a series of different layer thicknesses on ZnO(0001). The absorption spectra of the thin, medium, and thick layers are depicted in the inset of Fig. 6.7. The relative layer thicknesses are determined from the extinction ratio by means of the Beer-Lambert-law (Eq. 6.4)

$$E_i = \ln \frac{I_0}{I_i} = \epsilon \cdot d_i \quad (6.4)$$

with E being the extinction, ϵ the extinction coefficient and d_i (i =thick, medium, thin) the respective layer thicknesses. Using the extinction coefficient for D131 molecules determined by Howie et al.[89] and assuming it is valid for the layers a rough estimation of the absolute thickness is possible. The estimated mean layer thicknesses are about $d= 3$ nm for the thin layer, $d= 40$ nm in case of the medium layer and 100 nm for the thick layer, respectively. The thickness of the dye film on the mesoporous sample could not be evaluated this way due to the much stronger scattering of the porous material, Sakuragi et al. estimated 1.5 monolayer[174]. The PL transients at $T = 10$ K and RT

Table 6.3.: Charge transfer times and exciton recombination times for D131 using Eq. 6.3 (upper part) and exciton diffusion time determined with Eq. 6.6 (lower part). See text for detailed discussion. The accuracy of all values is $\pm 5\%$.

T = 290 K					T = 10 K			
D131 (<i>calc. with eq. 6.3</i>)	τ_{trans} [ps]	n_a [%]	τ_{exc} [ps]	n_b [%]	τ_{trans} [ps]	n_a [%]	τ_{exc} [ps]	n_b [%]
layer on SiO ₂ (0001)	110	59	550	41				
thick layer on ZnO(0001)	90	64	500	36	130	46	550	54
medium layer on ZnO(0001)	75	68	350	32	100	56	375	46
thin layer on ZnO(0001)	65	72	275	28	70	68	300	32
ZnO(meso)	23	95	175	5	37	88	275	12
D131 (<i>calc. with eq. 6.6</i>)	τ_D [ps]	n_a [%]	τ_{exc} [ps]	n_b [%]	τ_D [ps]	n_a [%]	τ_{exc} [ps]	n_b [%]
thick layer on ZnO(0001)	345	78	550	22	556	63	600	37
medium layer on ZnO(0001)	324	90	550	10	505	85	600	15
thin layer on ZnO(0001)	288	95	550	5	334	93	600	7
ZnO(meso)	83	99	550	1	149	97	600	3

are depicted in Fig. 6.7 a and b, respectively. It can be seen that the overall decay is slower the thicker the film is. This is caused by the increasing amount of excitons which recombine radiatively and do not reach the interface.

Again, we find the slowest decay for a D131 film prepared on silica. Using Eq. 6.3 we are able to fit the experimental curve at $T = 10$ K as well as at RT, as can be seen by the dashed lines using the parameters given in Table 6.3 (upper part). The times τ_{trans} and τ_{exc} increase with increasing layer thickness at RT as well as at 10 K. Both times are, however, effective parameters as the exciton mobility is not explicitly included in Eq. 6.3. The transfer time $\tau_{\text{trans}} = 23$ ps and $\tau_{\text{trans}} = 37$ ps for D131 on ZnO(meso) at RT and 10 K are most likely the correct values. For thicker layers τ_{trans} increases effectively due to the prior exciton diffusion. For the same reason, the effective exciton lifetime gets shorter, the stronger the charge transfer. The influence of energy migration on the PL transients, e.g., by hopping or diffusion [57, 223, 64, 22, 90], the mechanism of quenching [42], as well as the dimensionality of the system [29, 14] remain under discussion since several decades. Regardless, all analytical expressions describe the reality in most cases just approximately. Therefore, numerical procedures are used in some cases [113, 144]. To take into account the exciton diffusion we modify our model in the following way. The simplest approximation to include a diffusion process is given by the so called Smoluchowski model which assumes an instantaneous quenching of the PL if the fluorophore or excitation energy reaches the quencher by diffusion. By integration of the respective differential equation the intensity decay is given by Eq. 6.5 (see e.g. [113]).

$$I(t) = I_0 \exp\left(\frac{-t}{\tau} - 2b\sqrt{t}\right) \quad (6.5)$$

with $1/\tau = 1/\tau_{\text{exc}} + \alpha \cdot D$ and $b = \beta \cdot \sqrt{D}$, D is the diffusion parameter. α and β are parameters including the interaction radius and molar quencher concentration, which can be considered constant in our case. For the D131 films on ZnO the electron transfer rate is determined by the number of excitons reaching the interface by diffusion. We have to replace the Eq. 6.3 by Eq. 6.6.

$$n_{\text{exc}}(t) = n_a \cdot \exp\left(-\frac{t}{\tau} - 2b\sqrt{t}\right) + n_b \cdot \exp\left(-\frac{t}{\tau_{\text{exc}}}\right) \quad (6.6)$$

We define a mean diffusion time $\tau_D = 1/(\alpha \cdot D)$ to eliminate the unknown diffusion parameter, yielding $1/\tau = 1/\tau_{\text{exc}} + 1/\tau_D$ and $b = \beta' \cdot \sqrt{1/\tau_D}$. Applying Eq. 6.6 to the decay curves in Fig. 6.7 yields a perfect fit (full black lines). As already mentioned, the overall decay becomes slower with increasing layer thickness. This is attributed to the lengthy diffusion process of excitons towards the interface, which is given in the model by a diffusion time. As can be seen in Table 6.3 (lower part) the exciton lifetime $\tau_{\text{exc}} = 550$ ps at RT is now the same for all samples but the mean diffusion time increases from 83 ps for D131 on ZnO(meso) to about 345 ps for the thickest layer. It is particularly interesting to note that almost all the excitons suffer an electron loss by charge transfer in case of the ZnO(meso) structure. The value is reduced to about 78% for the thick layer at RT. The exciton lifetime at $T = 10$ K of the D131 layers $\tau_{\text{exc}} = 600$ ps is longer than the value at RT due to reduced radiationless losses. The longer lifetime should basically enhance the probability for charge transfer. As can be seen in table 6.2 and also in the upper part of table 6.3, the charge transfer is reduced in all cases. The explanation for this surprising behavior is now given in table 6.3 (lower part). The diffusion times are substantially longer at $T = 10$ K compared to RT, which obviously hints at a strongly reduced mobility at $T = 10$ K. This clearly reveals exciton hopping as the underlying mobility process.

6.1.4. Conclusion

In conclusion, we studied the charge transfer from excitons in indoline dye layers to the organic-inorganic interface. The external quantum efficiency of solar cells is the most important parameter for practical use. It is defined by the number of electrons flowing through the external circuit divided by the number of incident photons. The charge transfer, though very important, is only one step in others and used to be not known. We present here a method to determine independently the charge transfer time for dye semiconductor hybrids. The relevant processes, namely excitation, recombination, diffusion, and charge transfer are depicted schematically in Fig. 6.8.

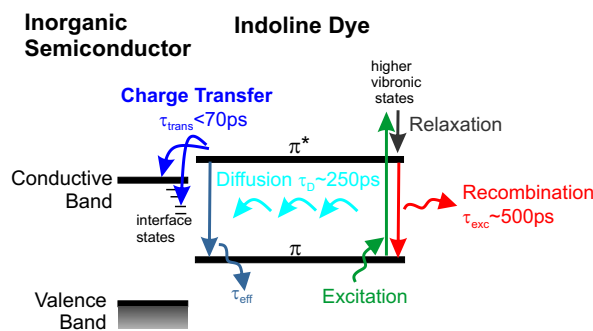


Fig. 6.8.: Schematic picture of the processes at the interface between the indoline layer and inorganic semiconductor.

Comparing D149 and DN91 reveals that the second COOH-anchor and expected enhanced bonding strength improves the charge transfer. Enhancing the distance between the chromophore and the interface by extending the anchor chain (DN91 \rightarrow DN216 \rightarrow DN285) reduces the transfer probability. The fastest transfer was found for the D131. This is ascribed to larger energy difference of the excited dye state and the conduction band minimum of the bulk semiconductor. The relevance of the level alignment is supported by the temperature dependence of the charge transfer manifested in the PL decay times: the transfer probability into the ZnO is reduced with lower temperature for all dyes. The reason is the increasing band gap of the semiconductor but decreasing $\pi \rightarrow \pi^*$ transition energies. This results in a reduced energetic difference between the excitonic states of the dyes with the semiconductor CBM.

Finally, we revealed the influence of the excitonic mobility on the charge transfer. Increasing dye layer thicknesses enhances the absorption and hence the total number of charge transfer electrons, but reduces the quantum efficiency due to the increasing number of excitons which do not reach the interface and cannot contribute to the charge transfer.

Analogue thickness dependent studies of D131 dropcasted on rutile TiO₂ can be found in the appendix C.2.1. Besides, the different indoline dyes were also prepared on mesoporous TiO₂, the results can be found in the appendix in C.2.2 and are further discussed in section 6.2.2.

6.2. Accessing the Level Alignment at the Interface

6.2.1. Optical Determination of Charge Transfer Times from Indoline Dyes to ZnO in Solid State Dye-Sensitized Solar Cells

We studied the electron transfer at the interface of organic-inorganic hybrids consisting of indoline derivatives (D149 and D131) on ZnO substrates using a new optical method. We revealed the electron transfer times from the excited dye, e.g. the excitons formed in the dye aggregates to the ZnO substrate by analyzing the photoluminescence transients

of the excitons after femtosecond excitation and applying kinetic model calculations. We reveal the changes of the electron transfer times by applying electrical bias. Pushing the Fermi energy of the ZnO substrate towards the excited dye level the transfer time gets longer and eventually the electron transfer is suppressed. The level alignment between the excited dye state and the ZnO Fermi-level is estimated. The excited state of D131 is about 100 meV higher than the respective state of D149 compared to the ZnO conduction band. This leads to shorter electron transfer times and eventually to higher quantum efficiencies of the solar cells.

Introduction

The functionalization of inorganic semiconductors with organic materials is a highly topical field of research in semiconductor physics. Organic molecules and layers on ZnO are promising functional hybrids for advanced optoelectronic devices. For example, dye-sensitized solar cells of the Grätzel type [148] are candidates for commercial photovoltaic applications. Despite the relatively low quantum efficiencies compared to silicon or perovskite based solar cells [120], there is continuous interest in Grätzel type solar cells, as they are low cost devices and thus provide short energy payback times. Especially, solid state dye-sensitized solar cells are a candidate for stable and sustainable photovoltaic devices since they avoid liquid components in the cell. Recently, their efficiency was shown to be greatly improved by starting from a liquid based solar cell and letting the solvent evaporate very slowly [59, 24]. An important process in high efficient dye-sensitized solar cells is an optimized electron transfer from the photoexcited dye into the conduction band of the semiconductor at the organic-inorganic interface [119, 71]. Efficient electron injection requires fast injection relative to the recombination time of the dye. Kinetic competition between these two processes strongly influences the quantum efficiency. Usually, techniques such as femtosecond transient absorption spectroscopy are used to determine the kinetics of the injection process by measuring the absorption changes. In a recent paper [131] we presented a way to study the electron transfer from the lowest excited exciton state by photoemission. We revealed a correlation between the transfer time and three parameters:(i) the number of anchoring groups, (ii) the distance between the dye and the organic-inorganic interface, which was varied by the length of an alkyl-chain between the carboxylate anchoring group and the dye, (iii) the thickness of the adsorbed dye layer. Another important parameter is the level alignment between the excited dye (π^* -level) and the conduction band minimum or the Fermi-level of the inorganic semiconductor. It is known, that due to different ionization energies of both hybrid materials substantial interface dipoles can occur [89, 170, 110]. Furthermore, the Fermi-level of the mesoporous semiconductor depends on the specific electrolyte used in the solar cell [109, 45, 141]. In the present paper we report about the influence of external applied bias on the charge transfer using fully operational solid state solar cells. By studying the photoluminescence (PL) and particularly time resolved photoluminescence (TRPL) of the dyes we are able to reveal differences in the level alignment of the indoline dyes D149 and D131.

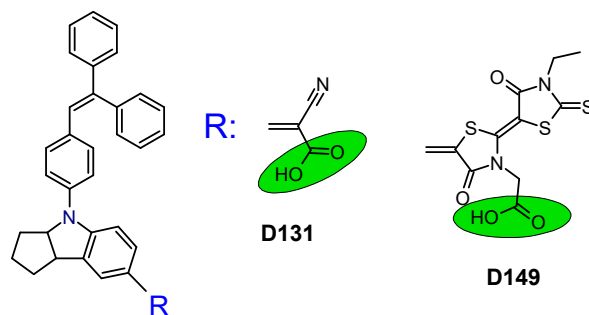


Fig. 6.9.: Schematic picture of the chemical structure of the indoline derivatives D131 and D149

Sample preparation and experimental Details

Unlike noted otherwise, all chemicals were purchased from Roth, Aldrich or Merck in ACS grade or higher and used without further purification. We studied two equally prepared solar cells either sensitized by D131 or D149. The schematic structure of the indoline derivatives is depicted in Fig.6.9. Both dyes have one carboxyl anchor group but differ in the size of the π electron system.

The porous ZnO substrates were prepared by electrodeposition as described in detail elsewhere [169]. In short, precleaned FTO coated glass substrates (Asahi glass, 10 Ohm/sq) were put in a three-electrode setup with Ag/AgCl as reference and a Pt wire as counter electrode in an aqueous solution of 0.1 M KCl and saturated with oxygen. At first, samples were pre-electrolysed by applying -1.05 V for 30 min. Afterwards, 5 mM ZnCl₂ were added to the solution and a potential of -1.05 V was applied for 10 min to deposit a compact layer of ZnO. For the deposition of the porous ZnO 300 μ M of EosinY were added and a potential of -0.75 V was applied for 20 min. The samples were stored overnight in an aqueous solution of KOH (pH 10.5) to remove the EosinY from the film. For the sensitization, the porous ZnO films were cleaned with water, dried at 100°C for 1 h and put in an UV/ozone cleaner for 30 min. Then the samples were immersed into a 0.5 mM solution of D131 (Chemicrea) or D149 (Chemicrea) in a 50:50 mixture of acetonitrile:tert-Butanol for 2 h and subsequently rinsed with ethanol and dried in air. Solar cells were prepared by attaching a pre-drilled ATO coated glass (Geomantec, 5 Ohm/sq) with sputtered Pt onto the sensitized electrode using a hot-melt Surlyn sealant with thickness of 30 μ m. An electrolyte with 1 M tetrapropylammonium iodide and 0.1 M iodine dissolved in 1:4 acetonitrile:ethylen carbonate was poured into the cell. To obtain solid state solar cells, the electrolyte was allowed to slowly evaporate.

We performed photoluminescence (PL) measurements by means of a standard setup with a high-resolution grating spectrometer. For the steady-state PL, a laser diode of 442 nm (2.8 eV) was used. For the electrooptical spectroscopy a computer-controllable power-supply was used with integrated measuring devices for voltage and current. This setup allowed recording of detailed voltage-dependent cw PL spectra in reflection geometry with excitation at 2.1 eV (514 nm) combined with a notch filter to suppress the reflected laser beam. The time-resolved PL experiments were performed using a standard streak-camera setup. Details are given for example in[7]. The 100-fs pulses

Table 6.4.: Fitting parameters for the calculated decay curves in Fig. 6.10 using Eq. 6.7 for D131 and D149 on mesoporous ZnO at room temperature under open circuit conditions.

ZnO (meso)	τ_{trans} [ps]	n_a [%]	τ_{exc} [ps]	n_b [%]
D131	23	95	175	5
D149	61	77	200	23

of the tunable Ti:Sapphire laser were frequency doubled to 2.8 eV (442nm) for most experiments; a 475 nm color-glass edge filter was used in the detection to suppress scattered laser light. Voltage dependent time-resolved PL measurements on processed dye sensitized solar cells have been performed with excitation at 3.06 eV (405nm) in combination with an edge filter at 2.76 eV (450 nm).

Results and Discussion - Level Alignment

In a recent paper we have shown, that the electron transfer times from the lowest excited dye state can be determined with high accuracy by studying the dye PL. A detailed discussion of the kinetic model is given in Ref.[131]. In what follows, we will apply this model to the solar cells under consideration.

The PL spectra of both indoline derivatives on mesoporous ZnO in air at room temperature are depicted in the inset of Fig. 6.10. The PL maximum of D149 is seen at about 650 nm, whereas the PL peak of D131 at about 540nm is clearly blue shifted compared to D149. This is typical for the smaller π electron system. In Fig. 6.10 the transients of the PL are depicted for D131 and D149 on mesoporous ZnO. Both curves exhibit the typical dependence with an initially fast decay and a slow tail at later times. The experimental curves can be well fitted by the biexponential function Eq. 6.7 (see full black lines in Fig. 6.10).

$$n_{\text{exc}}(t) = n_a \cdot \exp\left(-\frac{t}{\tau_{\text{eff}}}\right) + n_b \cdot \exp\left(-\frac{t}{\tau_{\text{exc}}}\right) \quad (6.7)$$

Accordingly to our kinetic model the long time τ_{exc} is the excitonic lifetime comprising the radiative and nonradiative recombination probability of the dye. The short time τ_{eff} is caused by the fast electron transfer to ZnO in competition with the exciton recombination. Describing the electron transfer probability to the ZnO by $w_{\text{trans}} = 1/\tau_{\text{trans}}$ the resulting lifetime for the dye excitons is given by Eq. 6.8.

$$1/\tau_{\text{eff}} = 1/\tau_{\text{exc}} + 1/\tau_{\text{trans}} \quad (6.8)$$

As discussed in detail in Ref.[131] only those excitons close enough to the interface can contribute to the charge transfer. Excitons which are too far away from the interface cannot dissociate. The annihilation of those excitons exhibit the time constant τ_{exc} yielding the weak but long living tail of the decay curve. The exciton lifetimes, the transfer times and the respective weighting factors are given in Table 6.4. The weighting

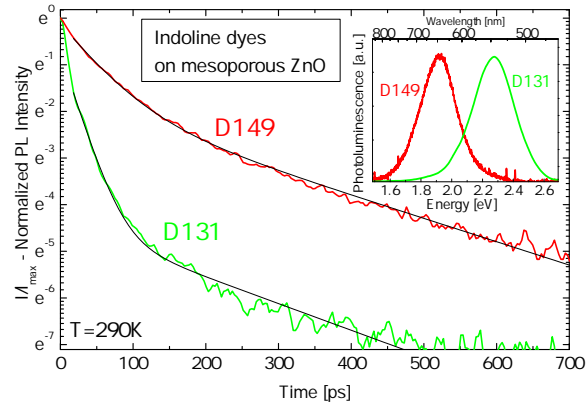


Fig. 6.10.: Photoluminescence transient of D131 and D149 on mesoporous ZnO. Inset: time integrated photoluminescence

factor n_a gives the amount of excitons which are created by absorption close enough to the interface and can perform either a charge transfer or recombine radiatively. The weighting factor n_b gives the number of excitons which are too far away from the interface and will therefore recombine radiatively or nonradiatively, respectively. In case of D131 about 95% of the excited molecules are able to transfer the electron to ZnO and only 5% of the dye molecules are too far away. Though, the solar cells have been prepared equally, the amount of transferred electrons is substantially smaller in case of D149. Note, the electron transfer time to ZnO of D131 is substantially shorter compared to D149, i.e. the transfer probability of D131 is higher. This is a first indication for a higher lying excited-state of D131 yielding a higher electron injection rate due to the higher number of unoccupied states for electron injection above the ZnO Fermi-level. We come back to this point later again.

It is known for a long time that an increase in PL intensity can be observed upon negative electrical bias to the semiconductor electrode [149, 99, 197]. Such an increase in PL intensity is typically attributed to the reduced electron injection process from the dye. In Fig. 6.11 the PL intensities of solid-state solar cells with D131 and D149 on ZnO are depicted as function of the applied bias voltage. A total suppression of the PL was achieved in reversed bias at about -600 mV, i.e. the positive potential at the ZnO electrode. It can be seen, that in forward bias, i.e. the Fermi-level in ZnO is now shifted upwards, the PL intensity increases. It is important to note, that the shape of the PL is independent of the applied voltage as can be seen in the inset of Fig. 6.11 for D131 as example. The intensity increase is caused by a decreasing probability of the electron transfer. The maximum PL intensity, in other words the total suppression of electron transfer, was found at $U_s = +750$ mV and $U_s = +850$ mV for D149 and D131, respectively.

To reveal the influence of the applied bias on the electron transfer in more detail, we now apply our kinetic model on the PL transients of the D131 solar cell. In Fig. 6.12 the PL decay transients of D131 are depicted for various applied voltages and compared with calculated curves. Between 0 mV and the open circuit voltage $V_{oc} = 508$ mV no significant changes of the decay curves could be found, although the integrated PL

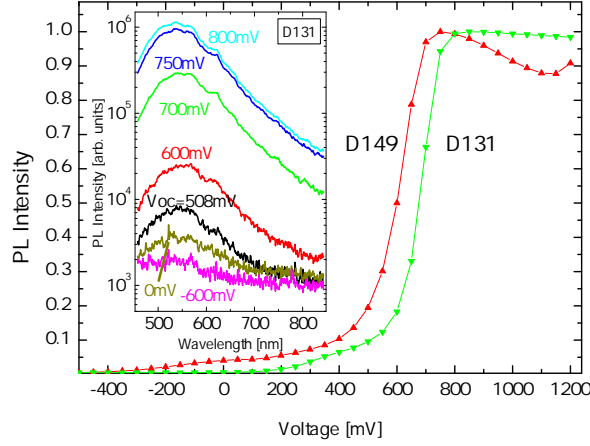


Fig. 6.11.: Photoluminescence intensity of D131 and D149 as function of the applied electrical bias.

intensity is already somewhat higher at 508 mV compared to 0 mV. A significant change of the transients was found however between 508 mV and 750 mV. The overall decay becomes significantly slower. Between 750 mV and 800 mV the remaining changes are weak. Above 800 mV we could not detect further changes within the experimental errors. At a first glance the changes can be explained by a reduced electron transfer and respective increasing amount of recombining excitons. Actually, the transfer times determined by means of Eq. 6.7 increase with increasing voltage and the respective weighting factors decline (see upper part of Tab. 6.5).

It should be noted, however, that the transients for bias voltages above 600 mV could no longer be fitted well by means of Eq. 6.7. A third exponential with increasing weighting factors was necessary at higher applied voltages. To make this clear, for $U=600$ mV and $U=700$ mV the best fits using Eq. 6.7 are depicted as dotted black lines in Fig. 6.12. It is obvious that for late decay a new slow decay component comes into play. Almost perfect fits could be achieved using a third exponential function using Eq. 6.9. All the respective parameters are given in the lower part of Tab. 6.5.

$$\begin{aligned}
 n_{\text{exc}}(t) = n_a \cdot \exp\left(-\frac{t}{\tau_{\text{eff}}}\right) + n_b \cdot \exp\left(-\frac{t}{\tau_{\text{exc}}}\right) \\
 + n_{\text{mol}} \cdot \exp\left(-\frac{t}{\tau_{\text{mol}}}\right)
 \end{aligned}
 \tag{6.9}$$

Interestingly, the third component with long decay time $\tau_{\text{mol}} = 500$ ps is the known lifetime of unbound dye molecules without any molecule-molecule interaction (see e.g. Ref.[131]). It is known, that a certain portion of unbound molecules can be found in dye sensitized solar cells. It is interesting to note, however, that the amount of unbound molecules increases drastically from very small amounts 2% at 508mV to about 31% at 800mV. The molecules adsorb again by reducing the applied voltage. It

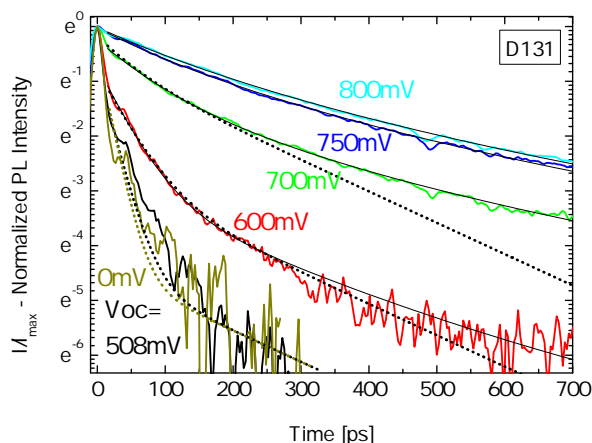


Fig. 6.12.: Photoluminescence transient of D131 for various applied voltages. A new long decay time component occurs due to non-transferring molecules, requiring a fit different from a biexponential fit. The dotted black lines indicate the biexponential fit results with equation 6.7.

is worth mentioning, that Lemon and Hupp [115] reported a similar result on the basis of electrochemical quartz crystal microbalance experiments. They observed reversible potential-induced dye desorption from nanocrystalline TiO_2 .

We now consider the variation of the transfer times by applying an increasing negative potential at the ZnO electrode, i.e. shifting the Fermi-level in ZnO upwards. It can be seen in Tab. 6.5, the number of transferred electrons declines tremendously with increasing voltage whereas the emission of excitons without electron transfer increases respectively. The decay curve measured at 800 mV is the first curve, which can be fitted without any electron transfer (parameters see lowest line in Tab. 6.5), i.e. the transfer would be completely suppressed. Unfortunately, the fit of the curve is not unique in this case. A complete suppression of the transfer is just a limiting case. An almost identical curve could be achieved assuming a weak remaining electron transfer (full black line in Fig. 6.12). The respective values are also given in Tab. 6.5. The electron transfer time $\tau_{\text{trans}} = 140 \text{ ps}$ approaches the radiative lifetime and the number of transferred electrons is reduced to 13%. Both limiting cases, no transfer on the one side and a remaining transfer of about 10% on the other side were applicable for all transients measured even at higher voltages. Actually, we can not exclude such remaining electron transfer at higher voltages. The reduction of the oxidized dye by electrons from ZnO or interface states is possible. This would provide a certain number of unoccupied states below the Fermi-level, which can be refilled either by electrons from π^* or by refilling from upper lying but filled electron states of ZnO.

The shorter electron transfer times from D131 to ZnO compared to D149 are caused by a different level alignment of the π^* to the quasi Fermi-level in ZnO as depicted in Fig. 6.13. Unfortunately, it is not possible to reveal the absolute offset directly from the electro-optical measurements. However, a relative consideration of the D131 and D149 solar cells is possible, as both cells have been prepared equally. We can assume therefore equal positions of the Fermi-energy in ZnO. In so far, the voltage difference needed to suppress the electron transfer can be used to estimate the difference of the

Table 6.5.: Voltage dependence of the fitting parameters using Eq. 6.8 (upper part) or Eq. 6.9 (lower part) for Indoline dye D131 solar cells based on mesoporous ZnO at temperatures of 290 K.

ZnO (meso)	τ_{trans} [ps]	n_a [%]	τ_{exc} [ps]	n_b [%]	τ_{mol} [ps]	n_{mol} [%]
D131 0mV	18	95	175	5		
D131 508mV	23	95	175	5		
D131 600mV	50	82	175	18		
D131 700mV	70	37	175	63		
D131 600mV	48	85	175	13	500	2
D131 700mV	104	50	175	36	500	14
D131 750mV	120	18	175	55	500	27
D131 800mV	140	13	175	56	500	31
D131 800mV			175	71	500	29

ZnO conduction band and the π^* energy of the dyes. The maximum of the dye PL is reached if the ZnO Fermi-energy reaches a level, where an electron transfer from the dye is no longer possible. It is important to note, that the binding energy due to the coulomb interaction must be taken into account to release electrons completely from ionized dye molecules. As discussed above, the intensity curves of D149 and D131 in Fig. 6.11 are shifted by 100 mV. We can conclude therefore, that the excited state π^* of D131 lies about 100 meV above the respective state of D149. The respective band alignments of D149 or D131 and the ZnO conduction band edge is depicted in Fig. 6.13.

Care needs to be taken comparing energy levels from the literature for analyses of the actual energetic situation. The values are often taken from measurements of the individual components, excluding effects due to adsorption of the dye and electrolyte species to the oxide surface. For example, Matsui et al. [127] determined by means of cyclic voltammetry for the energy difference between the ZnO conduction band and HOMO of D131 and D149 $E_{CB}^{ZnO} - E_{ox} = 1.42 eV$ and $E_{CB}^{ZnO} - E_{ox} = 1.35 eV$, respectively. However, in the here presented method a direct measure for the relative LUMO for two similar dyes position is presented when adsorbed to a porous semiconductor. Cyclic voltammetry measurements of dissolved D149 and D131 dyes reveal a LUMO difference of around 240 meV [127] which somewhat differs from the here obtained 100 meV highlighting the importance of in situ measured energy levels of adsorbed molecules.

Conclusion

In summary, we studied and compared the charge transfer from optically excited indoline dyes D131 and D149 into mesoporous ZnO by applying an external electrical bias. We were able to reveal the electron transfer times using time resolved photoluminescence in combination with electrical bias of solid state solar cells. The transfer probability of electrons from the excited dye to ZnO can be strongly reduced by shifting the Fermi-level of the ZnO to higher energies. In case of D131 the transfer time can be tuned from $\tau_{\text{trans}} = 18 ps$ to $\tau_{\text{trans}} = 140 ps$. The longer times are caused by the reduced number of unoccupied states available for electron injection. At open circuit

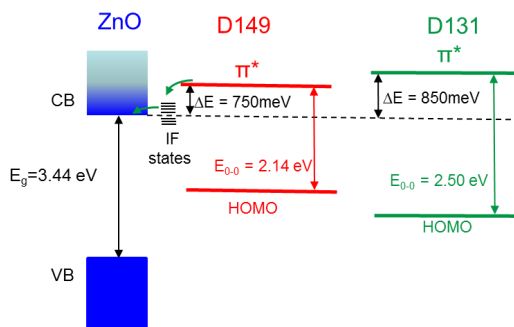


Fig. 6.13.: Level alignment of indoline dyes D131 and D149 with respect to the ZnO bands.

voltage, the transfer time of D131 is $\tau_{trans} = 23 ps$ and substantially faster than the transfer time of D149 with $\tau_{trans} = 61 ps$. This is due to the different level alignment. The excited state π^* of D131 is about 100 meV above the respective state of D149.

6.2.2. Variation of Substrates: Determining the Level Alignment of Substrates and Dyes relative to each other

If an organic material is prepared as a layer or soaked on different substrates it can be used to determine levels of substrates relative to each other. This can be done by exciting the organic material and detecting the time resolved photoluminescence on different substrates. A faster decay curve reveals accepting electronic states at lower energy relative to the electronic injection states of the organic material. Regarding substrates with slower decay curve the accepting electronic states show a higher energy level relative to the injection states. In consequence, the relative level alignment of different substrates to each other can be deduced. Isolators as glass can be used as a reference in order to show the decay of the organic material without charge transfer.

It has to be mentioned that great care has to be taken to prepare and localize a suitable thin and homogeneous layer which shows interaction with the substrate. This can be achieved for layers by OMBD, but also by drop casting and choosing a suitable sample region with a microscope in high magnification. Only decay curves on substrate with equal organic layer thickness should be compared due to strong influence of diffusion effects, see discussion in section 6.1.3 and fit equation 6.6. Here $TiO_2(meso)$ and $ZnO(meso)$ are chosen to discuss the relative level alignment since soaked mesoporous substrates without agglomerations of organic material should have a comparable homogeneous organic layer and about equal organic layer thickness.

CdS with D149 - excited by 517 nm below CdS bandgap

Fig. 6.14 and 6.15 show the visual similarity of ps-TRPL images if D149 is excited on glass and on CdS, respectively. 517nm with an energy below the bandgap of CdS are used in order to not excite CdS but only D149.

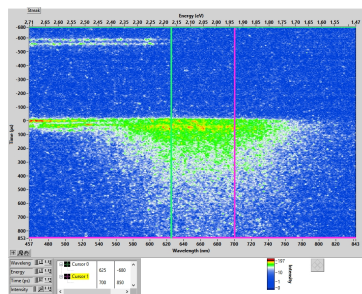


Fig. 6.14.: D149 on glass excited with 517nm. ps-stage image. resulting decay curve is shown in Fig. 6.16

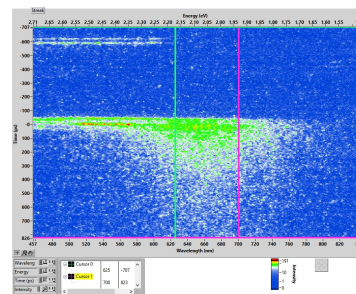


Fig. 6.15.: D149 on CdS excited with 517nm. ps-stage image. resulting decay curve is shown in Fig. 6.16.

The resulting TRPL curves in Fig. 6.16 show similar decay curves. Since no transfer from D149 to glass is expected due to isolator properties of glass, in consequence it can be deduced that also no charge transfer from D149 into CdS occurs and the accepting electronic states of CdS have a higher energy level than the electron injection states of D149.

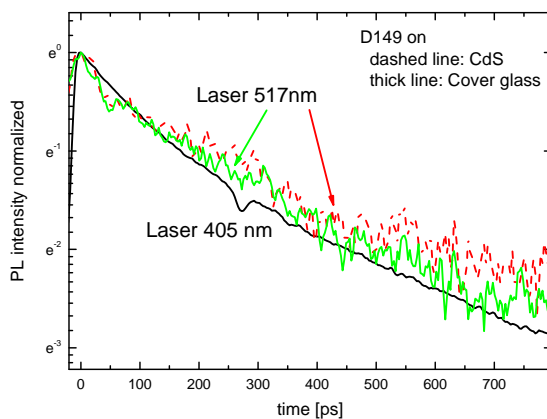


Fig. 6.16.: TRPL curve of D149 on CdS decays similar to the decay curves an isolating glass, both excited at 517nm. In consequence, no charge transfer occurs for D149 on CdS.

ZnSe with D149 - excited by 517 nm below ZnSe bandgap

The level alignment of the conductive band of ZnSe is about 1 eV higher than that of CdS (see Landolt-Börnstein New Series III/34C2 [98] Fig. 5.1.2). On CdS, no charge

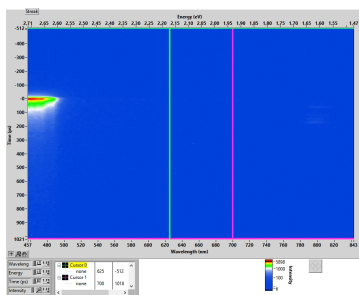


Fig. 6.17.: ps-stage image of CdS substrate TRPL, excited with 405 nm

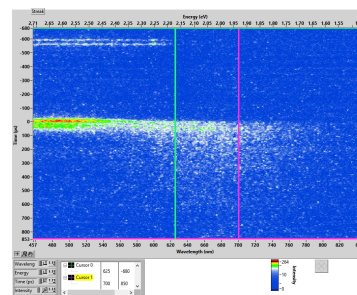


Fig. 6.18.: ps-stage TRPL image of CdS substrate with D149, excited with 515 nm

transfer from D149 to the substrate is revealed, see discussion in the upper paragraph. Therefore no transfer is expected for D149 on ZnSe.

ZnSe shows a blue coloured PL with fast decay if excited with a 405 nm laser, see Fig. 6.17. To avoid this ZnSe PL, the substrate is excited below the ZnSe bandgap with 515 nm.

Fig. 6.19 shows the decay curves of D149 on glass and on ZnSe.

A slightly faster curve on ZnSe at the begin of the decay curve can be seen. An even faster decay occurred for another sample of D149 on ZnSe (not shown here), the main difference to D149 on glass showing in the first 100 ps. This difference can be due to experimental stage influence in the first 100 ps (as can be also seen on glass excited by 517 nm in Fig. 6.14).

Another explanation for the difference of decay times at the begin might be a Förster energy transfer (see section 6.2.2) from excited states below bandgap of ZnSe into D149. Deeper lying states in the bandgap of ZnSe and its green luminescence at 500 nm are investigated for example in publications about ZnSe nanocrystals [136, 124] and might show a Förster transfer to D149. But since the green PL of lower lying states is not shown on flat ZnSe samples, the explanation with a disturbing PL due to stage properties is more probable.

As a result of the discussion, D149 dominates the long times of the decay curves both on ZnSe and on glass with a similar decay. Regarding the decay times at the begin, the difference between D149 on ZnSe and on glass can be explained either by stage induced PL or Förster transfer induced PL, both options would explain the faster decay on ZnSe. Therefore, the the decay on ZnSe is similar to the decay without charge transfer on glass. This indicates that no charge transfer occurs between D149 and ZnSe, as expected.

TiO₂ and ZnO with indoline dyes D131 and D149

The level alignment of the conductive band of TiO₂ (anatase) is revealed by cyclovoltammetry as slightly lower than for ZnO ([72], Fig. 3; [229]), this should lead to a faster decay on TiO₂. As can be seen in Fig. 6.3 and Tab. 6.1 for D149, this as-

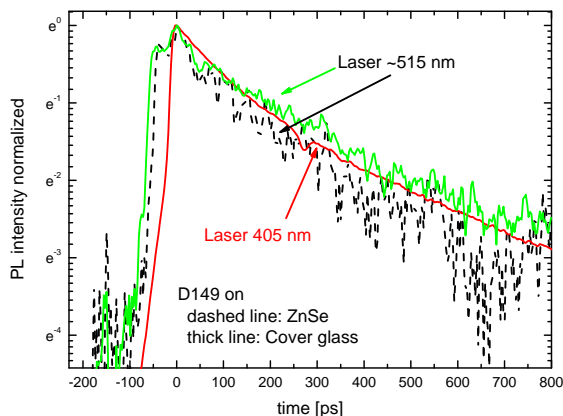


Fig. 6.19.: TRPL curve of D149 on ZnSe decays similar to the decay curves on isolating glass, both excited at about 515 nm. In consequence it can be deduced that no charge transfer occurs for D149 on ZnSe.

sumption can be confirmed, as the charge transfer time on $\text{TiO}_2(\text{meso})$ is faster than an $\text{ZnO}(\text{meso})$. This was also the result indicated in literature [193].

Comparing D131 decay times for room temperature on both substrates ZnO (Fig. 6.7b) and TiO_2 (Fig. C.12) fit results (Tab. C.1) show a slightly slower charge transfer time for D131 on $\text{TiO}_2(\text{meso})$ than on $\text{ZnO}(\text{meso})$, which is not as expected. An explanation for the unexpected discrepancy on $\text{TiO}_2(\text{meso})$ can be that the investigated diffusion time on $\text{TiO}_2(\text{meso})$ is with 222 ps more than double the time on $\text{ZnO}(\text{meso})$ (83 ps) and that the ratio of molecules which are not connected to the substrate are doubled on $\text{TiO}_2(\text{meso})$ in comparison to on ZnO (compare tables and 6.3 and C.1). This points to thicker and in parts agglomerated layer on $\text{TiO}_2(\text{meso})$, possibly due to the smaller molecule size of D131 in comparison to D149.

This contrary result is possibly due to the very fast charge transfer from D131 which does not reveal the expected slight level alignment differences of the substrates but points to other important mechanisms not included. Such Additional mechanisms which might have unexpected influence on the decay times may be trap filling in inorganic semiconductors or that the slower charge transfer of D149 allows the effect of level alignment to be more dominant.

Regarding the layers on flat substrates, a comparison of fit results shows faster injection and diffusion times on $\text{TiO}_2(100)$. The thickest layer on $\text{TiO}_2(100)$ is a bit thicker than the thickest layer on ZnO . Yet, the deduced transfer time is faster on TiO_2 (68 ps vs. 90 ps). For the medium layer, the extinction measurements indicate an about 30% smaller layer on TiO_2 than on ZnO , transfer times again would favor D131 on TiO_2 with 55 ps vs. 75 ps. For the thin layers the layer on ZnO is much thinner than the layer on TiO_2 . Yet the transfer time is faster on TiO_2 with 45 ps vs. 65 ps. The diffusion dynamic seems to be better for D131 on TiO_2 , which might be also driven by a faster charge transfer on TiO_2 than on ZnO .

A further question occurs comparing other indoline dyes on $\text{ZnO}(\text{meso})$ and on $\text{TiO}_2(\text{meso})$.

As shown in Fig. 6.5 on ZnO(meso) at room temperature, a second anchor leads to faster charge transfer, but the longer the second anchor, the slower the decay gets. For the longest second anchor of DN285, the charge transfer time is getting close to the slow charge transfer time of D149 with only one anchor. Comparing the same dyes on TiO₂(meso), the variance of charge transfer times is much less from D149 with one anchor to D285 with longest second anchor. It seems as if the second anchor is not as relevant on TiO₂(meso) as on ZnO(meso). This points out to the importance of binding mechanism at the interface between organic layer and inorganic substrate for the charge transfer times and questions the simple possibility of this level alignment detection method for example with organic molecule D149.

To sum up, more investigations with other organic materials, anchors and substrates must be performed in order to clarify this level alignment investigation method.

Deduced Level Alignment scheme for D149 and D131 and different substrates

Fig. 6.20 shows the level alignments of different substrates known from literature, including the substrates CdS and SiO₂ glass. D149 and D131 are shown in comparison to those substrate levels as a result from the experiments shown above. Since no charge transfer from D149 to CdS occurs, the electron donating level must have lower energy than the CdS accepting level and must have higher energy than the ZnO and TiO₂ levels. The relation between D149 and D131 is a rough estimation from own results which gave about 100 meV higher conductive band energy of the organic semiconductor for D131 compared to D149, see section 6.2.1; further estimation in literature can be found for example in [89], also resulting in a higher LUMO level of D131 in comparison to D149. The bandgaps are deduced from absorption measurements. D131 is shown with a slightly higher donating energy level, which explains the faster decay of the PL curves due to faster charge transfer into ZnO or TiO₂.

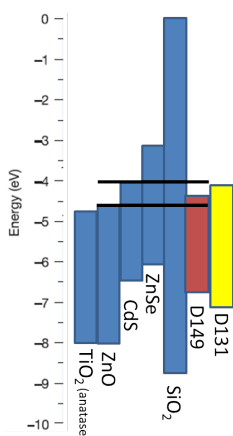


Fig. 6.20.: Rough estimation of level alignment of D149 and D131 and of several substrates. The measurements of D149 on CdS reveal the possible corridor for D149 LUMO shown by the black horizontal lines.

It has to be mentioned here that the levels here show only a rough scheme. This may

vary due to band building effects in organic semiconductors or different band formation in semiconductors.

Förster Transfer - CdS and ZnSe with indoline dye D149

Cds with D149 excited with 405 nm, above bandgap energy Another energy transfer effect can be used in order to determine a bandgap of a semiconducting substrate relative to an organic semiconductor. If the bandgap is larger than the bandgap of the organic semiconductor and the semiconductor is electronically excited, a Förster energy transfer occurs if the semiconductor is in interaction with the organic semiconductor layer at the interface between both materials. A Förster resonance energy transfer (FRET) is defined as a transfer of energy out of a excited state (donator) into a state nearby (acceptor)

After the Förster energy transfer, the recombination occurs on the organic semiconductor with the known decay on the given substrate. This back transfer can include again a re-injection of the electron into the inorganic substrate, if this is allowed by the level alignment of organic and inorganic semiconductor.

If known bandgaps of different substrates in interaction with the same organic semiconductor are excited, the bandgap of the organic semiconductor can also be deduced by this technique.

In Fig. 6.21 a 405 nm excitation of D149 on CdS leads to CdS and D149 PL, including Förster transfer to the layer of indoline dye D149, made by drop casting. This is revealed because the long substrate PL time shown in the left pictures is transferred to the D149 dye decay time shown in the right picture. While the upper right picture shows no visible elongation of D149 time either due to missing substrate to molecule interaction or to the little absolute excitation of the CdS substrate, the lower right picture shows a clear elongation of D149 time. This elongation is clear since after the measurement periode of several ns, characteristicly for the set ps-stage, the signal is still detected in the upper part of the lower right picture as a foothill. The resulting decay curves in Fig. 6.21 show the long lasting CdS substrate PL time, the faster D149 time, and the resulting TRPL curve if Förster transfer occurs, with a mixture of both times of D149 and CdS.

Further measurements with 405 nm excitation on CdS and glass are shown in appendix D.1 to explain difficulties which might occur during those interaction measurements and to show the PL decay time of D149 on an isolator, excited at 405 nm.

ZnSe with D149 - excited with 405 nm, above bandgap energy In the images of the ps structure 6.23 and 6.24, the substrate was also excited, which leads via Förster transfer to a PL spectrum blue-shifted to D149 on glass, with faster times than D149 on glass. The feeding of the D149 PL by Förster energy transfer acts like a laser that limits the temporal resolution. A Förster transfer can therefore be observed in that the TRPL of the organic layer adapts to the time of the substrate PL. The blue shift of the D149 PL in comparison to D149 on glass could be due to the fact that the electron

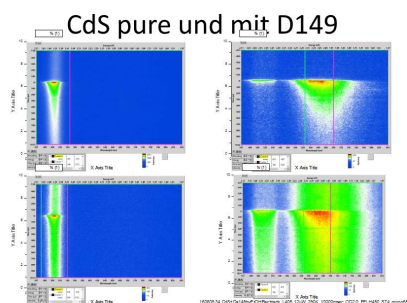


Fig. 6.21.: ps-images with and without Förster transfer: upper and lower left picture show pure CdS substrate PL, right pictures CdS with D149 layer. If little substrate interaction occurs, no elongation of D149 PL can be seen (upper right picture). With strong Förster transfer, the long substrate PL time is transferred to D149 PL time.

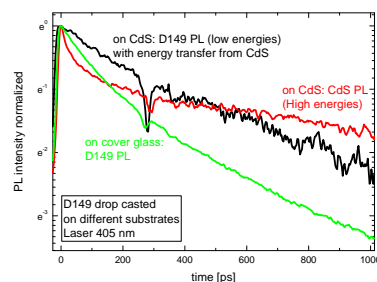


Fig. 6.22.: Resulting decay curves for ps TRPL measurements of CdS with D149. The red curve shows the decay of the CdS substrate PL at high energies around 510 nm, including the long decay time at longer times. This long PL time influences the PL decay of D149 on CdS and leads to a longer decay time at longer times (black curve) with a slower decay as for D149 on glass (green curve).

feed occurs with a longer feeding duration, allowing a higher density of population of higher energetic states. This phenomenon needs to be examined more closely.

To evaluate whether a charge transfer of the excited D149 back into the ZnSe occurs after the Förster energy transfer, the D149 PL would have to be measured without the influence of a Förster energy transfer. As with laser excitation, the evaluation of the decay times of the D149 TRPL is only possible after the laser, i.e. the Förster energy transfer, has decayed. Due to the slower decay of the Förster excitation compared to the laser, however, even after the Förster decay, there is an overlay by spectra from the broad time window of the Förster excitation, which leads to a blurring of the times in the TRPL curves. The long times of the D149 TRPL curves are again largely the right times of D149, the drop here is as fast as on glass or CdS, see Fig. 6.25. However, these long times are no longer as relevant for charge transfer as the TRPL in the first 100 ps. Measurements with excitations from D149 without excitation of the substrate are more effective in order to reveal charge transfer, see section 6.2.2.

6.3. Suitability for organic solar cells

In this chapter the newly developed method of ps-TRPL is used on different dyes in order to investigate charge transfer effects and suitability for organic solar cells. Also, level alignments can be deduced by this innovative method. The ps-TRPL method was introduced for indoline dyes in chapter 6. The test of suitability of a dye for a solar cell requires the preparation in solution and of layers on glass, on both no charge transfer is expected, and on mesoporous TiO_2 or ZnO, potentially with charge transfer

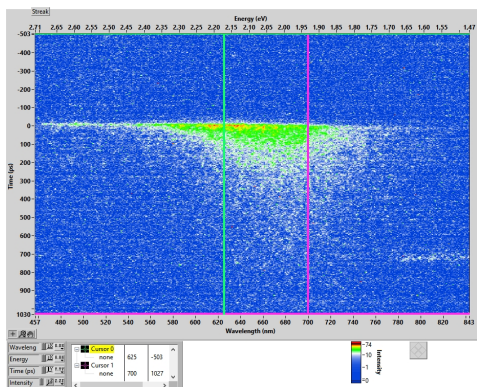


Fig. 6.23.: D149 drop casted on ZnSe by EtOH solvent evaporation. The shown ps-image results in the blue TRPL curve in Fig. 6.25.

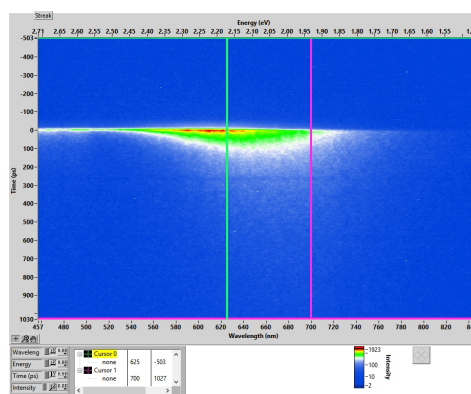


Fig. 6.24.: D149 drop casted on ZnSe by EtOH solvent evaporation. The shown ps-image results in the green TRPL curve with fastest decay time in Fig. 6.25. A blueshift in comparison to ps-image 6.23 occurs due to influence of Förster transfer from ZnSe substrate

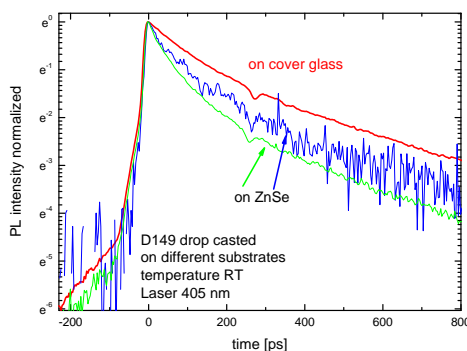


Fig. 6.25.: TRPL of D149 on glass and ZnSe excited by 405 nm. A blueshift of the PL spectrum seems to indicate a Förster transfer influence by excited traps of ZnSe substrate. The higher the influence of Förster transfer, the faster is the decay in the first part of TRPL in comparison to D149 without substrate interaction on glass.

and therefore with a faster decay curve of the PL.

If the dye photoluminescent spectra on glass and mesoporous semiconductor are qualitatively similar, a faster photoluminescence decay time on the mesoporous semiconductor in comparison with the non transferring system on glass reveals the dye loss of electrons by charge transfer (for explaining details see section 6.1.3). Analogously, thin layers on glass and flat crystalline semiconductor may show a charge transfer effect, if both spectra are congruent and the decay on the semiconductor is faster (see section 6.1.3).

Fully processed organic solar cells include an electrolyte which hinders clear ps-TRPL results, the dyes should be investigated without electrolyte or evaporated electrolyte in order to allow this measurement method to achieve results.

Some additional ps-TRPL investigations of Anthraquinone variations can be found in appendix B.2.

6.3.1. Variations of Phthalocyanine dyes

Besides metal-free organic dyes metallated porphyrin and phthalocyanine dyes are of interest to substitute the cost intensive ruthenium based dyes in DSSC[16]. Porphyrin dyes consist of a donor- π -acceptor sensitizer, where either the porphyrin chromophore constitutes the donor[121] or the π -bridge[16]. In the latter case YD2 has shown 11% efficiency [16] and further variations like YD2-o-C8 got 12.3% efficiency[222] (molecular structures see figure 6.26) and more (porphyrin panchromatic single molecules achieved 13% [126, 118]).

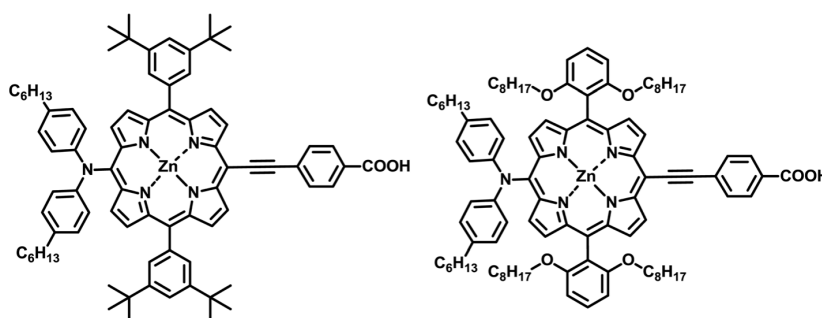


Fig. 6.26.: Structures of YD2 (left) with >11% and YD2-o-C8 (right) with 12.3% DSSC efficiency (figures taken from [222]; D- π -A sensitizer with porphyrin as π -bridge; slight changes in peripheral structure have influence on the DSSC efficiency)

In the former case, where the porphyrin acts as the donor, the record efficiency is only 5.14% [121].

A similar high molecular variety as for porphyrin DSSC can be synthesized with the group of phthalocyanines which is in consequence also in focus of interest for DSSC [61, 157]. Phthalocyanine based DSSC with the phthalocyanine acting as the donor achieve similar efficiencies as porphyrin based DSSC. For example PcS18 (see figure 6.28) gives a cell efficiency of 5.9% [105], the record dye PcS20 achieves 6.4% [92]. A molecule similar to the later investigated ZnPc*OH (see figure 6.33) is TT1 (see figure 6.27 and absorption spectra in 6.29) which achieved an efficiency of 3.52 percent [35]. A broadening of the absorption band in comparison with solution is visible due to the weak intermolecular coupling (van der Waals interaction). A chemical shift as the reason for the small redshift of 15 nm can be excluded since the chemical shift of ZnPc based dyes is negligible weak (for ZnPc in different solution [33] 668 nm to 673 nm occurs). The redshift and the new band in the red spectral region is probably due to

exciton formation (exciton formation for phthalocyanine molecules is discussed in detail in section 5.2).

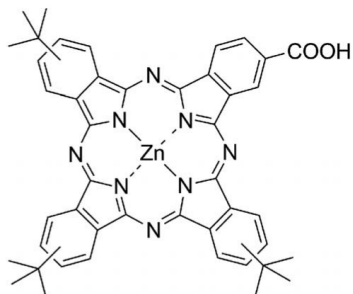


Fig. 6.27.: Carboxylate functionalized ZnPc* - TT1 with 3,52% DSSC efficiency (figure taken from [157])

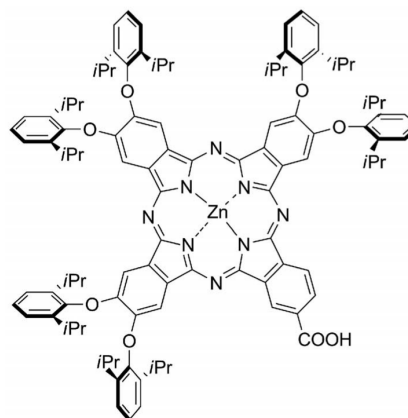


Fig. 6.28.: Molecular structure of PcS18 with 5.9% DSSC efficiency (figure taken from [157])

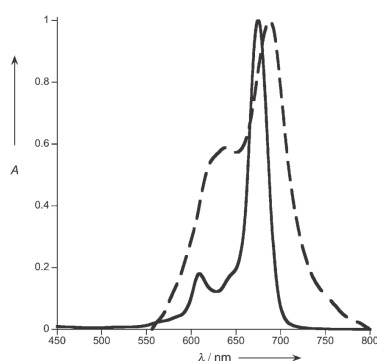


Fig. 6.29.: Visible absorption spectra of TT1 in ethanol (solid line) and adsorbed on a transparent 4-m-thick mesoporous TiO₂ film (dashed line). Graph and caption taken from [35]

From the variation of the two molecules TT1 and PcS18 one can conclude that the groups which cover around the planar π -conjugated ZnPc core are clearly important for the DSSC efficiency. Firstly, the peripheral surrounding substituents may influence the π -System and therefore shift the level-alignment of the dye-LUMO. Secondly, they are important regarding to the formation of molecular aggregates. Agglomerations are known leading to nonradiative deactivation of the excited state of the dye by formation of defect states [190]. For TT1 and its derivatives aggregation on mesoporous TiO₂ is suppressed and an adequate directionality of the excited states exists, which facilitates an efficient electron injection [61, 76, 34].

In addition to agglomeration issues, the structure of the anchor group is very important for an efficient charge transfer. A variation from dicarboxylic acid anchoring ligand (COOH) to catechol anchor (figure 6.30) leads to a drastic reduction of efficiency from 3.52% to 0.92% [176]. In detail discussed, both efficiencies are not comparable, because of different charge transfer systems: Looking at the absorption spectra of ZnPcOH-t-Bu on mesoporous TiO₂ (see figure 6.31, main peak at 750nm), a strong redshift of

170mV occurs in comparison to the solution (680nm). Sarker et al. explain this strong redshift by a formation of intense dye-to-TiO₂ charge-transfer (DTCT) bands, caused by the strong interaction between the catechol dye and TiO₂[176]. Different authors discuss such a DTCT band formation [199, 3, 146] which can be revealed by quantum efficiency measurements (see catechol discussion in section sec:TypeIIabsorptionRK1). While TT1 injects in the type I way, ZnPc-t-Bu-cat injects both in a type I and a type II way [199].

Agglomerations might be also the reason for such a strong redshift, this should be investigated by further experiments with layer preparation on planar interfaces. Additional ps-TRPL measurements can help to identify quenching mechanisms resulting of solid formation.

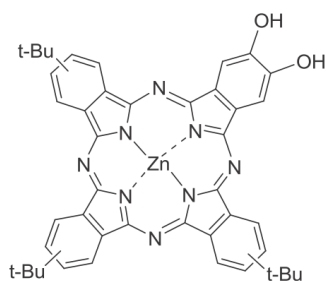


Fig. 6.30.: Catechol functionalized ZnPc-t-Bu with 0.92% DSSC efficiency taken from Sarker et al. [176]

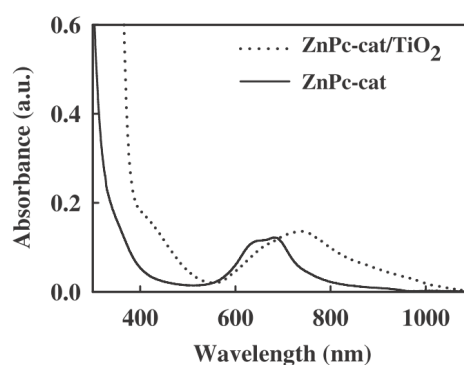


Fig. 6.31.: Absorption ZnPcOH-tBut taken from [176]; solid line: ZnPc-OH-tBut in 3% ethanol diluted in water, with a main peak around 685nm; dotted: after soaking on mesoporous TiO₂, a strong redshift occurs

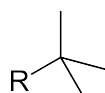


Fig. 6.32.: t-Bu: Tert-butyl group, R symbols the anchor point, at every end of the tree arms a CH₃ is situated.

It should be taken into account that the comparison of efficiencies of different groups may reveal preparation uncertainties and different results. Yet, regarding TT1 variations, record results of different groups generally documentate comparable values for slight variations of the anchor group (for example molecule PCH001[160] with 3.05%). In order to compare efficiencies reliably, the preparation conditions should be exactly equal. In consequence, when looking at the results of one specific group (García-Iglesias and Torres et al.) conclusions of the effect of anchor variation on the cell efficiency may be deduced. In case of the COOH anchor a longer spacer between COOH group and phthalocyanine results in lower efficiency. An anchor very close to the phthalocyanine is most efficient [61]. Two COOH anchors on one anchor chain result in a higher cell efficiency than for only one COOH anchor [61]. Normally, two separated but adjacent COOH anchors are resulting in a higher efficiency than one COOH anchor, if the influ-

ence of the anchors on the π -system is negligible [62]. But, if the influence of the anchor chains on the π -complex is inserting relevant electron density into the pi-complex (for example with a carboxyethyl anchor) and therefore a remarkable redshift in absorption spectrum occurs, worse efficiencies may appear due to a lower lying LUMO [156]. When using a phosphinic acid instead of COOH anchoring, similar cell efficiencies are documented [123].

In this chapter, starting from the promising efficiencies discussed above, newly synthesized phthalocyanine dye variations (AG Sundermeyer, Marburg, Martin Liebold) are examined and tested for suitability in DSSC. Therefore, samples on mesoporous ZnO or mesoporous TiO₂ are prepared by soaking and in addition layers on flat substrates including glass and a crystalline semiconductor are prepared by drop casting (further details regarding the preparation conditions and principles of measurement see Indoline section 6.1 and a shorter description in the introduction of section RK1 6.3.2).

Zinc- and H₂-Phthalocyanine*(OH)₂: catechol binding

Due to the similarity to the carboxyl functionalized ZnPc* (figure 6.27), which achieved 3.52% cell efficiency, a variation with promising molecular structures ZnPc*(OH)₂ and H₂Pc*(OH)₂ (see figure 6.33) were synthesized by Martin Liebold, AG Sundermeyer, chemistry department, university Marburg. The catechol group (OH)₂ is shortly written as OH in the following text and graphs. Detailed absorption and photoluminescence spectroscopy from solution (see figure 6.34) to solids (see appendix A.1) was performed as part of the Examensarbeit of Luise Rost, AG Heimbrodt.

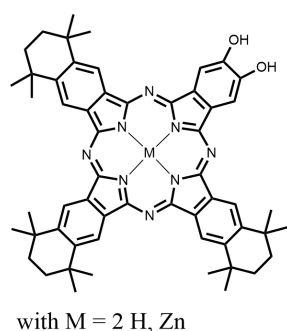


Fig. 6.33.: Molecular structure for the two phthalocyanine dyes ZnPc*OH and H₂Pc*OH. The two molecules differ only in the central position.

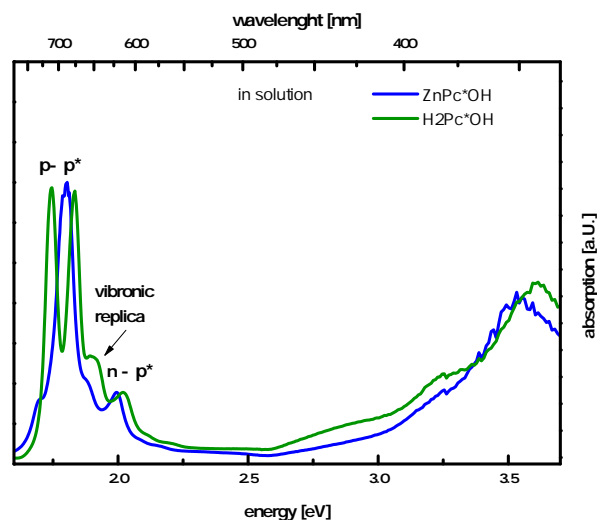


Fig. 6.34.: Absorptions of H₂Pc*OH and ZnPc*OH in solution. Taken from the Examensarbeit of Luise Rost, AG Heimbrodt

Solar cells based on mesoporous ZnO were built with both molecules (AG Schlettwein, Gießen, Jan Tinz) which achieved no efficiency (<0.03%). In order to understand this,

time resolved measurements of the dye luminescence on processed solar cells, soaked in mesoporous TiO_2 and of layers on glass were performed.

For $\text{H}_2\text{Pc}^*(\text{OH})$, figure 6.36 shows the decay curves on different substrates. While in solution the expected slowest decay curve can be seen, on glass (SiO_2), where no charge transfer is allowed, a stronger decay evolves due to quenching processes in the layer. The decay on mesoporous TiO_2 is not faster than on glass, no new loss channel and in consequence no charge transfer occurs from the dye into the semiconductor. In consequence, regarding the level alignment, the LUMO of $\text{H}_2\text{Pc}^*\text{OH}$ should be below the CB of the semiconductor.

The spectra in solution, on glass and on mesoporous TiO_2 are similar, the decay curves are comparable. This is not the case for the solar cell based on mesoporous ZnO . Here, a broadening and slight redshift occurs. A pronounced shoulder in the red wavelength region can be seen. The defect band (see figure 6.35) builds up by agglomerations due to a presumably too high dye concentration in the soaking solution. The stronger decay is a result of quenching by defects, an assumption supported by similar effects of the later discussed ZnPc^*OH on mesoporous ZnO (see figure 6.38).

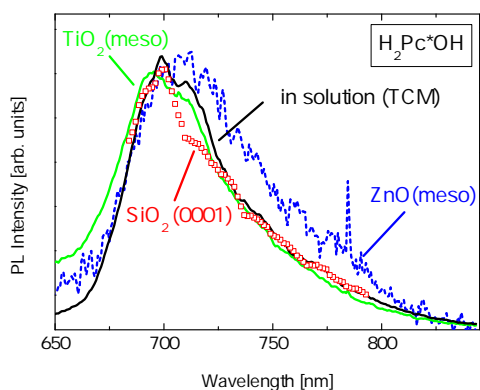


Fig. 6.35.: Comparison of $\text{H}_2\text{Pc}^*\text{OH}$ in solution and on different substrates. Clearly, the spectrum on mesoporous ZnO differs from the other due to defect band formation

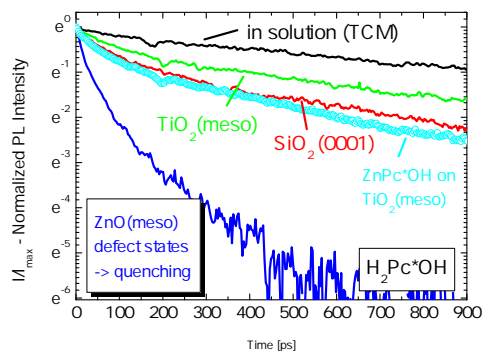


Fig. 6.36.: Time resolved photoluminescence spectroscopy decay curves: Comparison of $\text{H}_2\text{Pc}^*\text{OH}$ in solution and on different substrates. SiO_2 and $\text{TiO}_2(\text{meso})$ are comparable which indicates the absence of a charge transfer. On $\text{ZnO}(\text{meso})$ quenching occurs due to the formation of defect states. ZnPc^*OH on $\text{TiO}_2(\text{meso})$ is shown for comparison.

Now regarding the spectrum of ZnPc^*OH on mesoporous TiO_2 (see figure 6.37), it is comparable with the spectrum in solution. A quasimolecular structure is revealed with low influence of defect band formation. A comparison of the times of $\text{H}_2\text{Pc}^*\text{OH}$ and ZnPc^*OH on mesoporous TiO_2 reveals similar slow decay times (see figure 6.36). This can be interpreted in a way that also for ZnPc^*OH no charge transfer exists on mesoporous semiconductors.

Interestingly, there was no success in preparing a reference layer on glass with a quasimolecular spectrum, since strong defect band states appear like in the comparable spectrum on mesoporous ZnO (see figure 6.37). The spectra are redshifted and clearly

broadened compared with ZnPc^*OH on $\text{TiO}_2(\text{meso})$. While on mesoporous ZnO this is probably again (as also for $\text{H}_2\text{Pc}^*\text{OH}$ ZnO solar cell) the consequence of agglomerations induced by a too high concentrated solution used for the soaking process, the quenching in a layer on glass should be discussed further, since for $\text{H}_2\text{Pc}^*\text{OH}$ the formation of a thin layer with low quenching succeeded.

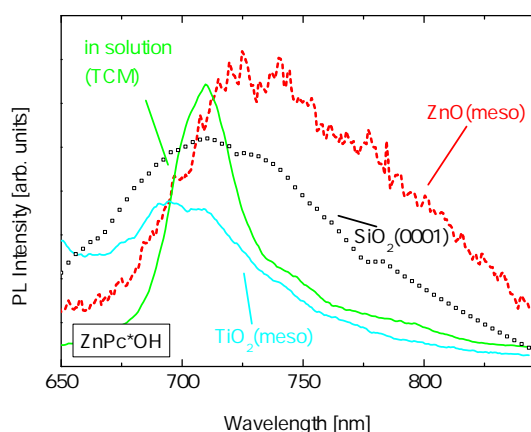


Fig. 6.37.: Comparison of ZnPc^*OH in solution and on different substrates. Clearly, the spectrum on ZnO(meso) differs due to defect band formation. Defect formation does not occur on $\text{TiO}_2(\text{meso})$ since the main peak position is comparable to the one in solution.

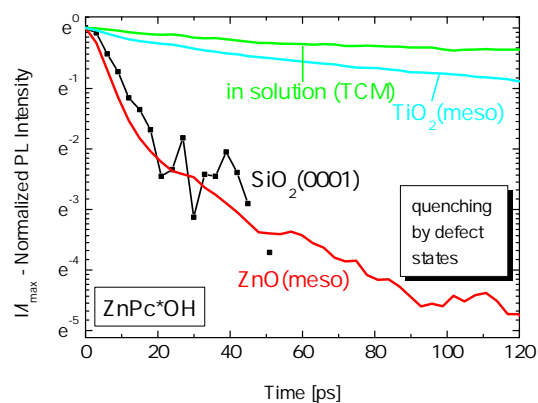


Fig. 6.38.: Time resolved photoluminescence spectroscopy decay curves: Comparison of ZnPc^*OH in solution and on different substrates. For ZnPc^*OH both on ZnO(meso) and SiO_2 even stronger quenching occurs than for $\text{H}_2\text{Pc}^*\text{OH}$. This is again due to the formation of defect states.

A quasimolecular spectrum of ZnPc^*OH on SiO_2 is missing, though the absence of a charge transfer can be concluded since ZnPc^*OH on $\text{TiO}_2(\text{meso})$ is comparably slow as $\text{H}_2\text{Pc}^*\text{OH}$ on SiO_2 . A clearly faster decay would have been expected if a charge transfer occurred.

It is known from literature [173] that the fluorescence quantum yields of the H_2 -phthalocyanine thin films are very low (2×10^{-4}) in comparison to in solution (0.7). The photoluminescence spectra shown by Sakakibara et al. show a hardly viewable quasimolecular spectral photoluminescence (quasimolecular region is the region where no luminescence out of trapped states occurs, i.e. where free molecules in solution would have their luminescence) whereas a strong formation of defect bands in the lower energy region appear. The authors conclude that nonradiative relaxation is dominant in the solid films and propose trapping processes, lattice defects and deformation or exciton scattering by lattice phonons as some possible reasons. For ZnPc , a low quantum yield of 0.3 in solution hints to even worse luminescence conditions in the quasimolecular region. In that way, the difficulties in the production of a quasimolecular layer on glass is congruent with expectations from literature.

It should be discussed why no charge transfer occurs with ZnPc^*OH while the similar

TT1-dye (figure 6.27) achieves an efficiency of over 3%. The changes compared to TT1 are the anchor group and a change of the peripheral substituents.

Regarding the anchor, a change of the anchor group of ZnPc from phosphonate group with ($\sim 679\text{nm}$) or without ($\sim 675\text{nm}$) vinyl chain to vinyl-COOH group ($\sim 683\text{nm}$) only shows little effect on the main spectral peak position of the according IPCE-spectra (Incident Photon to Charge Carrier Efficiency or Quantum Efficiency) and therefore to the expected absorption spectra (see further informations in appendix 6.3.1, figure 6.46 and IPCE results see figure 6.47 including the cell efficiencies in table 6.48; prepared and measured variation of ZnPc with different anchors by Jan Tinz, AG Schlettwein, Gießen; synthesized by Martin Liebold, AG Sundermeyer, Marburg). This suggests a rather small influence of such anchor groups on the absorption energy (up to $\sim 20\text{mV}$). In contrast, IPCE spectra shown of García-Iglesias et al. ([61], see fig. 5a in the paper) show, that a carboxylate anchor variation leads to differences of up to $\sim 50\text{meV}$. The anchor group might have a relevant influence on the absorption. Yet one cannot conclude that the influence on absorption is in a clear context to the level alignment between dye and semiconductor.

Regarding the peripheral substituents, a spectral shift of the absorption from pure ZnPcOH (673 nm , 1.842 eV , in TCM solution; since the OH anchor is known to have little influence on the absorption spectrum, this is concluded from ZnPc measurements [33]) to ZnPc*OH ($\sim 690\text{ nm}$, 1.80 eV ; measured in solution with TCM) is detected. A redshift of the main absorption peak of $\sim 40\text{ meV}$ occurs. A red-shift in spectrum seems to be correlated with the contribution of the outer substituents to the π -system, which may influence the LUMO level alignment and in consequence the solar cell efficiency. Furthermore the t-Butyl groups of TT1 do not have a relevant influence on the absorption spectrum, since solved in ethanol TT1 absorbs at $\sim 675\text{ nm}$ (1.84eV) and at $\sim 690\text{ nm}$ (1.8 eV) on mesoporous TiO_2 (see figure 6.29), which is comparable with the absorption of ZnPc anchor variations (i.e. TT1 without t-Butyl groups, only with changed anchors) absorbing around 680 nm (on ZnO(meso), see figure 6.47). If the absorption energy of a dye would be decisive for the efficiency, ZnPcOH should therefore have comparable efficiencies as TT1. But ZnPc with anchor variations (group Schlettwein, see appendix figure 6.48) achieved clearly lower efficiencies of $<0.6\%$ in DSSC. Again it can be concluded that the solar cell efficiencies do not only depend on the absorption energy. The amount of defect states resulting from agglomeration is also a critical point. In case of TT1 the agglomeration is effectively reduced by suitable peripheral groups, ZnPc with different anchors but without peripheral groups tends to agglomerate (further details in appendix figures 6.49 and 6.50).

In case of ZnPc*OH a quasimolecular soaking was successfully achieved which is not influenced by quenching and yet shows no charge transfer in TRPL (see figures 6.37 and 6.38). This none-efficiency might therefore be explained by a LUMO lying below the Fermi-level of the semiconductor, while TT1 would have a LUMO level just above the Fermi-level of the semiconductor. But this constellation is unlikely since only $\sim 40\text{ mV}$ redshift would lead to a lowering of efficiency from 3% to 0%.

Another point is possibly more relevant in this discussion: the none-efficiency might rather be the result of the catechol $(\text{OH})_2$ anchor which is known to inject worse than COOH or phosphonate anchors (results of AG Schlettwein: ZnPc*OH with nearly 0% 6.48; Ooyama et al. reveal a change of efficiency from 1.51% to 0.06% after replacing

the carboxyl anchor with an catechol anchor group [146]; a porphyrin variation with catechol anchor achieves 0.6% [1] - untypically low for porphyrin DSSC). Despite the low efficiencies an injection by a catechol anchor is at least possible, since ZnPcOH-t-Bu achieved 0.92% (c.f. figure 6.30). A more detailed discussion of the effects of a catechol anchor and the catechol binding can be found in the beginning of section B.2. Finally it can be concluded that a change of absorption energy due to molecular structure variations (peripheral groups, anchor) does not take into account the electron orbital overlap between dye and semiconductor which is strongly influenced by the anchor group. The carboxylate anchor seems to inject better than the catecholate anchor as a consequence of a intensified electron orbital overlap with the semiconductor, conversely a more suitable level alignment at the interface can be concluded. The COOH anchor is the main reason which leads to >3% efficiency for TT1 in comparison with 0% for ZnPc*OH.

In summary, ZnPc*OH and H₂Pc*OH are not suited for dye sensitized solar cells. Proven by TRPL measurements, either the level alignment is not suitable for a charge injection into the conductive band of the semiconductor or the catechol anchor is non-injecting or both arguments are true. In addition, in thin layers of Pc*OH strong defect formation occurs which traps the built excitons and may hinder exciton diffusion to the interface. A peripheral group which prevents agglomeration is relevant for a better efficiency of the processed solar cell, the used peripheral group for Pc*OH tends to agglomerate on mesoporous semiconductors when used for soaking in high concentrated solutions.

An interesting secondary result is a PL at higher energies not known from literature (to our knowledge), this is shown in appendix A.1.

SubPcBOH

BSubPcs (boron substituted phthalocyanines) are of high interest for functional materials like OLEDs and organic photovoltaics, see the review of Morse and Bender [138]. Only boron is able to template the formation of the SubPc ligand [139]. Solubility is examined for Cl-SubPcB and its derivatives [138, 139], a solubility range depending on the solvent from dye to pigment can be found. Layer formation and bulk material properties are discussed regarding to the use in solid state organic heterojunction solar cells for SubPcBCl [138, 103, 25], for example acting as a donor in combination with C₆₀ as an acceptor. The less discussed derivative OH-SubPcB is also of high interest for chemical synthesists, the crystal structure can be seen in Fig. 6.39 taken from [206]. The paper of Virido et al. discusses the influence of strong and weak hydrogen bonds on crystal formation for SubPcBOH and its derivatives. Yet there is little known about the optical properties of layers of SubPcBOH or their integration into organic solar cells. In order to examine this, samples were prepared on different inorganic substrates. In case of mesoporous TiO₂ as substrate this is done by soaking in a solution of SubPcBOH in toluene, in case of crystalline flat substrates it is performed by drop casting with toluene as solution. The photoluminescence is observed including time resolved pho-

toluminescence decay. A clear charge transfer is revealed when comparing the decay of SubPcBOH on isolating substrates like quartz and on semiconducting substrates like TiO_2 .

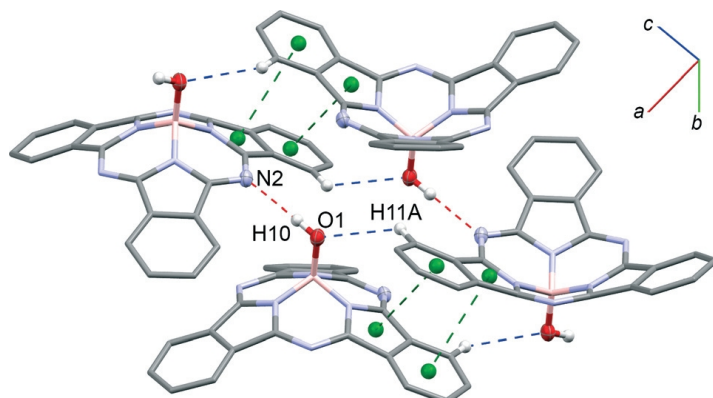


Fig. 6.39.: SubPcBOH molecular packing arrangement taken from Virido et al. [206], Fig. 2; citation of original caption: The molecular packing arrangement of 2 (HO-BsubPc), with strong hydrogen bonds depicted as red dotted lines and weak hydrogen bonds depicted as blue dotted lines. The centroids of rings participating in convex-convex π - π interactions are shown in green. Key: carbon = grey; nitrogen = light purple; oxygen = red; boron = pink; hydrogen = white. For clarity, non-hydrogen atoms involved in hydrogen bonds shown as 50% ellipsoids; interacting hydrogen atoms shown as balls; non-interacting hydrogen atoms omitted.

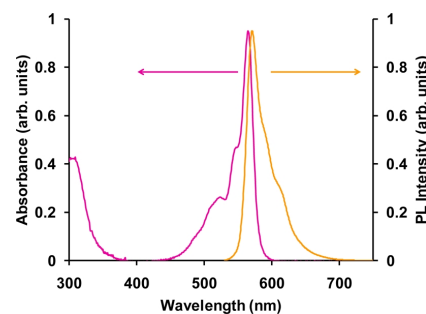


Fig. 6.40.: Figure taken from Morse and Bender [138], Fig. 3; citation of original caption: Absorption (magenta) and emission (orange) spectrum of Cl-BsubPc in toluene.

Regarding the spectral properties of both absorption and photoluminescence, BSubPc and its derivatives are generally spectrally blueshifted to phthalocyanine and its derivatives due to a smaller pi-complex (the absorption maximum for Cu-phthalocyanine is at around 670 nm, see Fig. 4.6). The molecular PL of BSubPcs is in a clear mirror symmetry to the absorption in solution, this is published exemplarily for SubPcBCl in toluene (taken from [138], shown here in Fig. 6.40). Regarding SubPcBOH the absorption of low concentrated SubPcBOH in acetonitrile is shown with a maximum at about 560 nm, see Fig. 6.41. While at low concentration the absorption and photoluminescence spectrum is purely molecular, the molecular PL of higher concentrated solution is broadened due to the stronger interaction of the molecules. In addition, for too high concentrations, a powder formation can be seen in photoluminescence at 725 nm for higher concentrations of SubPcBOH in acetonitril (see Fig. 6.41). In TRPL, a strong concentration quenching is revealed for this spectral region of the powder (not shown here due to not being of interest for the charge transfer discussion).

A broadened PL in comparison with a PL of low concentrated SubPcB derivatives in solution (see Fig. 6.40) results for SubPcBOH soaked in TiO_2 meso. This is again due to molecular-molecular interaction. No powder formation peak around 725 nm (Fig.

6.41) can be observed. The high energetic underground stems from the PL of the optical filter, this is revealed by the fact that for SubPcBOH in acetonitril the PL is of higher energy than the lowest energy absorption in solution. Except for the powder PL, the PL spectra around 600 nm of SubPcBOH high concentrated in acetonitril and soaked on TiO₂meso are similar. This reveals a successful binding of SubPcBOH on TiO₂meso without the formation of powder. Due to their PL similarity, the decay times of the molecular photoluminescence peaks of high concentrated SubPcBOH in solution and soaked on TiO₂meso can be compared. The comparison of the TRPL-times is shown in Fig. 6.42. For molecules on mesoporous TiO₂, the molecular PL decay is faster than on an amorphous layer in a substrate region without mesoporous TiO₂. This indicates a loss of excited electrons by charge transfer from the organic into the anorganic system. The molecular PL of SubPcBOH in solution (toluol, low concentration) is different from the PL on TiO₂(meso), it shows a mirror symmetry to the absorption in solution (not shown here). The resulting TRPL-time is shown in figure 6.42 (blue curve) with a slower decay than for an amorphous layer.

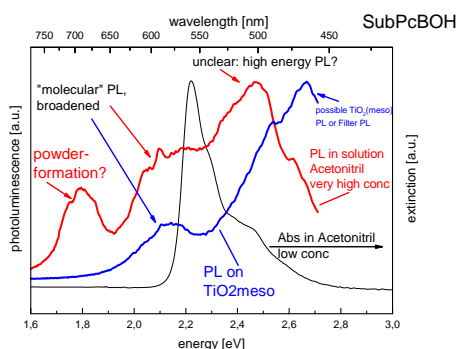


Fig. 6.41.: Absorption of SubPcBOH in solution (acetonitril, low concentration) and photoluminescence in solution (acetonitril, high concentration) and on TiO₂(meso) - PL on TiO₂(meso) is similar to in Acetonitril, but without powder formation.

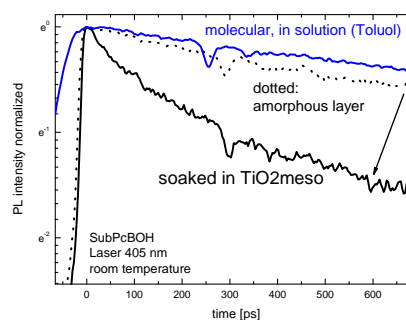


Fig. 6.42.: ps-TRPL times of SubPcBOH in solution (toluol, low concentration) and as an amorphous layer show similar slow decay times. The arrow indicates the faster decay due to charge transfer on mesoporous TiO₂(meso).

In Fig. 6.43 the PL spectra of layers on quartz and on crystalline TiO₂ are compared. The redshift on quartz in comparison to on TiO₂ is caused by powder PL forming up in the red part of the spectrum around 725 nm. This powder region was revealed by high concentrated SubPcBOH in solution, see Fig. 6.41. If compared with the PL on TiO₂(meso), a clear redshift occurs to the region indicated by the grey area. This is not due to powder formation but due to exciton formation in the layer.

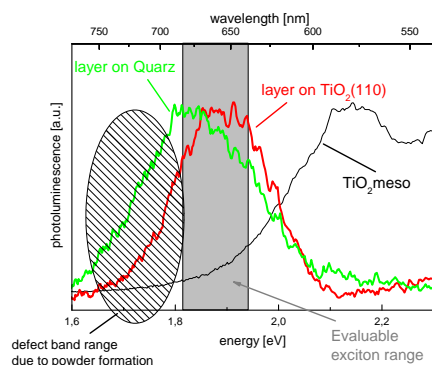


Fig. 6.43.: Comparison of SubPcBOH PL spectra of layer on flat crystalline substrates with soakings in mesoporous TiO_2 . A clear redshift occurs due to solid exciton formation and not due to deep trap photoluminescence.

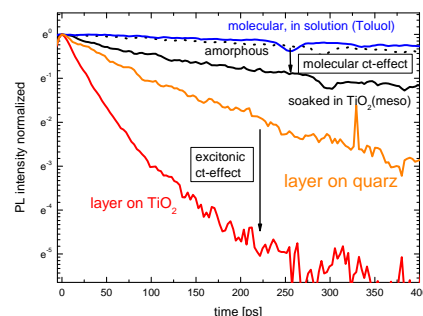


Fig. 6.44.: SubPcBOH ps-TRPL curves: Comparison of molecular charge transfer effect (see also Fig. 6.42) with layers shows lower charge transfer effect on $\text{TiO}_2(\text{meso})$ (small arrow) compared to the stronger excitonic charge transfer effect for layers (large arrow).

Regarding the decay times of Fig. 6.42 the faster decay for excitonic photoluminescence is obvious, also on quartz where no charge transfer is possible. Excitons have a larger delocalization than excited single molecules or agglomerated molecules, in that way it exists a higher probability that they reach the killer centers due to their high mobility. The exciton diffusion length of SubPcBCl formed in layers is known to be about 10 nm[138], therefore the quenching by killer centers competes with a possible charge transfer. This limits the active layer thickness in organic photovoltaics. For SubPcBOH a similar exciton diffusion length can be assumed. Thus, solid exciton formation in the solid state with the associated delocalization over several nm is necessary, so that the electron-hole pair diffuses to the interface and is separated there. This is revealed by the clearly faster decay on crystalline $\text{TiO}_2(110)$ in comparison to the decay on quartz. Regarding mesoporous TiO_2 , agglomeration is presumed to exist in the mesoporous network, but no particle formation with exciton formation like in a crystalline layer occurs. Hence a broadening of the spectrum compared to the otherwise finer structured molecular spectra occurs, but no redshift due to exciton formation in crystalline layers occurs. The agglomerated molecules show a rather slow PL decay, the molecules are not as delocalized as in a crystalline formation. The loss by charge transfer to the interface is therefore not high as for crystalline layers, it competes with the slow internal decay. Therefore, the charge-transfer is less visible on mesoporous TiO_2 .

The charge transfer time on TiO_2 can be calculated by a biexponential fit, see Fig. 6.45. At first, the long time component of the decay on quartz reveals the undisturbed exciton time in crystallized layers (325 ps). This exciton time can be used for the biexponential fit of the curve on TiO_2 in order to achieve the time component of the fast decay (33ps). From the biexponential model, the charge transfer time can be calculated to 37 ps.

Summarized, in SubPcBOH layers delocalized excitons exist which might be interesting for solar cell applications, although here attention must be paid to powder formation.

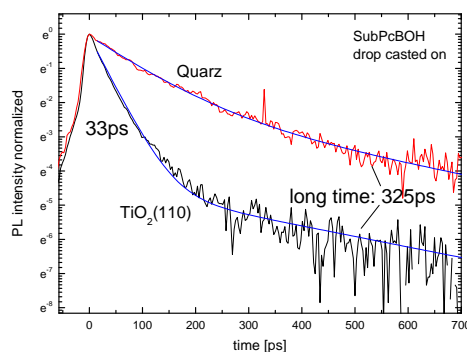


Fig. 6.45.: SpcBOH on quartz and $\text{TiO}_2(110)$. Usable areas are evaluated which are without the influence of powder PL. With the solid exciton time of 325 ps and the fast decay time of 33 ps the charge transfer time of 37 ps can be calculated

SubPcBOH in soakings on mesoporous TiO_2 forms agglomerated molecules with an existing but lower possibility of charge transfer.

Unsubstituted ZnPc - anchor variation - TRPL and IPCE results

ZnPc is modified by different peripheral anchors: phosphonic anchor without and with vinyl group (PA and vPA) and a carboxylate anchor including a vinyl group (vCA). Molecular structures can be seen in figure 6.46. The synthesization was performed by Martin Liebold, AG Sundermeyer, University of Marburg. Solar cells were processed based on electrochemically fabricated mesoporous ZnO (Jan Tinz, Ag Schlettwein, University of Gießen) and characterized (Jan Tinz) by IPCE/absorption spectroscopy (see figure 6.47) and electrical characterization including the resulting solar cell efficiencies 6.48. The anchor variation achieve low efficiencies $<0.6\%$ but yet this proves a working charge transfer for the three molecules.

The low efficiency in comparison to TT1 (figure 6.27, 3.52% efficiency) is discussed in section 6.3.1. With TRPL measurements (figure 6.50) we can conclude that the low efficiency is probably mainly a consequence of defect formation. While in IPCE/absorption spectra no defect formation can be seen, photoluminescence reveals defect formation: regarding ZnPc-vPA, a strong redshift on ZnO(meso) in comparison to on SiO_2 occurs (figure 6.49) which is a clear indicator of defect band formation. For ZnPc-vCA a similar red-shifted defect band formation can be deduced. As a consequence, either the soaking solution was too high concentrated and agglomerates therefore already built up in solution, or ZnPc variations without peripheral groups tend to agglomerate during layer formation and on mesoporous ZnO. Interestingly, for ZnPc-PA no such strong redshift occurs, yet a defect formation cannot be excluded.

Since the anchors PA/vPA and vCA are known for a good electron injection, the level alignment should be not the main problem for the low DSSC efficiencies. Without the defect band formation a comparable solar cell efficiency as for TT1 seems to be possible.

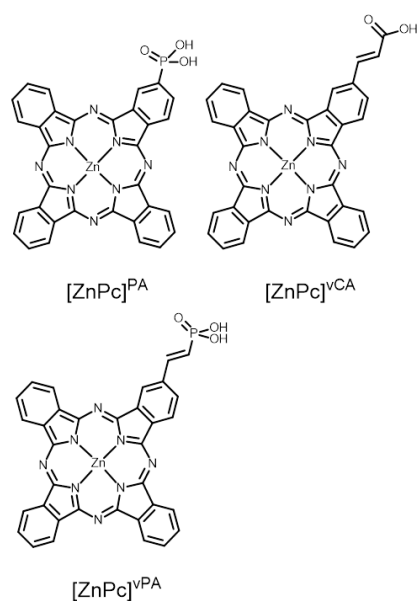


Fig. 6.46.: Molecular structures for ZnPc with a PA/vPA and a vCA anchor; structures provided by Martin Liebold, AG Sundermeyer, Marburg

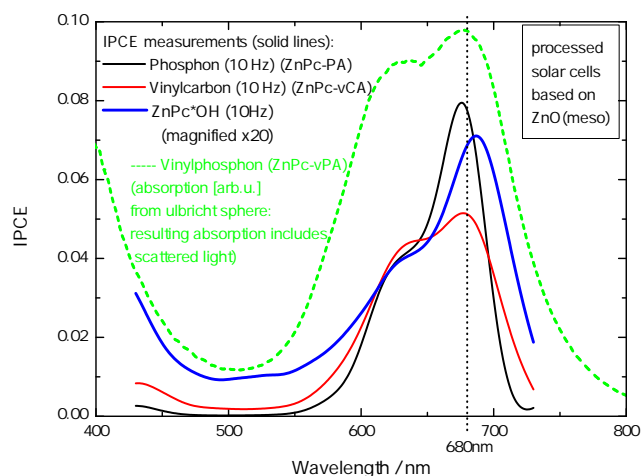


Fig. 6.47.: ZnPc with varied anchors were processed as solar cells. IPCE and absorbance data is provided by Jan Tinz, AG Schlettwein, Gießen. ZnPc*OH is slightly redshifted to the unsubstituted ZnPc variations. For ZnPc-vPA curve no IPCE curve is available, the absorbance is shown instead, but only for a qualitative comparison of peak positions.

Film	Area / cm ²	I _{sc} / mA/cm ²	V _{oc} / V	FF	Efficiency / %
[ZnPc] ^{PA}	0.450473	1.2882	0.45	0.73	0.42
[ZnPc] ^{vCA}	0.445246	0.6432	0.37	0.67	0.16
[ZnPc] ^{vPA}	0.445641	1.7417	0.49	0.65	0.55
[ZnPc] ^{*OH}	0.406794	0.0328	0.10	0.31	0.001056

Fig. 6.48.: Efficiencies of different anchor variations on ZnPc. ZnPc*OH has no efficiency; table provided by Jan Tinz, AG Schlettwein, Gießen

6.3.2. RK1 dye - reaching 10% efficiency with a fully organic dye

RK1 (bought from Sigma-Aldrich) is investigated in this work due to promising efficiency of 10.2% in solar cells [95] and to verify the ps-TRPL method developed in this thesis. RK1 is a fully organic dye and shows no measurable degradation after 2200 h of light exposure. For further details of RK1 see Joly et al. [95].

An absorption spectrum is shown in Fig. 6.51 in solution (ethanol), showing a low energy absorption at about 480 nm. Astonishingly, the efficiency of solar cells is nearly as high as for N719, although the red spectral part is not absorbed as it is for N719. This is due to a molar extinction coefficient at the lower energy peak of RK1 which is almost two times higher than the corresponding values for N719. The Indoline dye D149 (see Fig. 6.2) has similar absorption peaks as N719, therefore the main absorption of RK1 is at higher energies than for D149. The carboxylate group of RK1 is probably the anchoring group similar as with indoline dyes, therefore indoline dyes and RK1 have chemical structures allowing comparison also in regard to level alignment (see indoline structure in Fig. 6.9 and RK1 structure in Fig. 6.52). Deduced from the absorption at

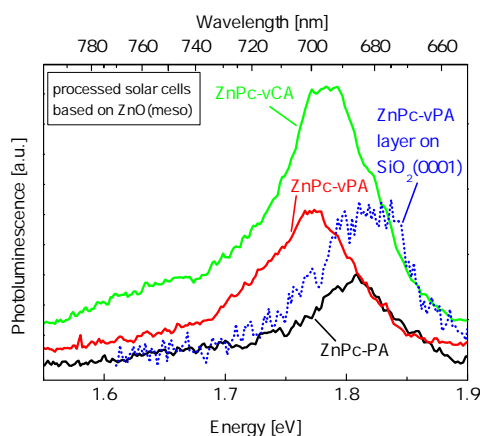


Fig. 6.49.: Spectra of ZnPc-PA/-vPA and -vCA. Defect formation can be identified by clear redshifts for ZnPc-vCA and ZnPc-vPA while ZnPc-PA seems to be quasi-molecular. A faster decay with stronger red-shift in PL is in good accordance to this, see Fig. 6.50. Yet PA shows low efficiency which indicates quenching by trap states not as clearly visible as for vPA and vCA anchors.

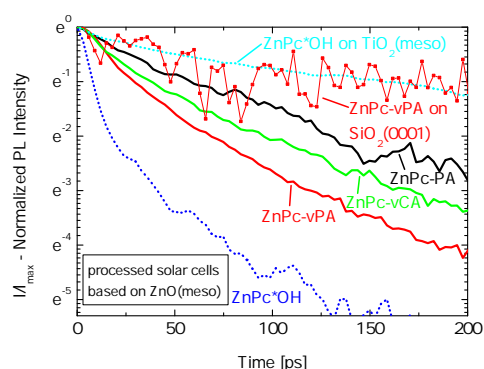


Fig. 6.50.: Transients of ZnPc with anchors vPA, vCA and PA. ZnPc*OH TRPL curves are shown for comparison. Efficiencies and short currents are not consistent with the relative decay - obviously, a combination of quenching and charge transfer occurs, a pure charge transfer time is therefore not determinable.

higher energy a higher level alignment of the organic conduction band can be expected for RK1 in comparison with D149. In consequence, a faster decay curve on mesoporous TiO₂(meso) is expected for RK1 in comparison to D149.

RK1 samples on mesoporous TiO₂ are prepared by soaking and in addition layers on flat substrates as glass and a crystalline semiconductor (ZnO(0001)) are prepared by drop casting (further details see section 6.1.1).

Time-Resolved Photoluminescence Spectroscopy In Fig. 6.53 the decay curves are shown as results of ps-TRPL measurements. While on isolator glass a long decay time occurs, on flat ZnO(0001) the curves decay faster with thinner layers. The long times on ZnO(0001) show the non transferring layer parts with equal times as on glass, the short times reveal a charge transfer component. The difference between a thinner and thicker layer is due to longer diffusion times of charge carriers to the interface for thicker layers, as discussed for indoline dyes in section 6.1.3 and described by equation 6.6. On TiO₂(meso) the decay is faster than on ZnO(0001) due to charge transfer excluding a dominant diffusion influence due to the molecular coupling.

The corresponding ps-TRPL images to the decay curves in Fig. 6.53 are shown in the following pictures. The PL-waterfalls clearly visualize the different charge transfer situations from RK1 on an isolator to a molecular binding on TiO₂(meso) without delay by diffusion or non transferring molecules. The long decay time for the thin RK1 layer on ZnO(0001) is the same time as the long decay time on glass, this reveals a proportion

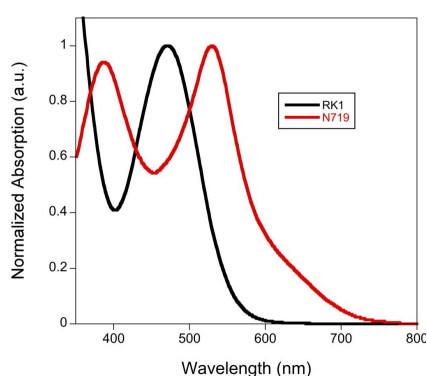


Figure 2 | UV-Visible absorption spectra of RK1 and N719 in ethanol solution.

Fig. 6.51.: Absorption spectra in solution (ethanol): Comparison of fully organic RK1 dye with Ruthenium dye N719. N719 is a standard dye used in Grätzel cells. Fig. taken from [95]

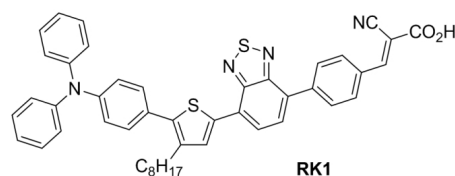


Fig. 6.52.: RK1 - chemical structure. Fig. taken from [95]

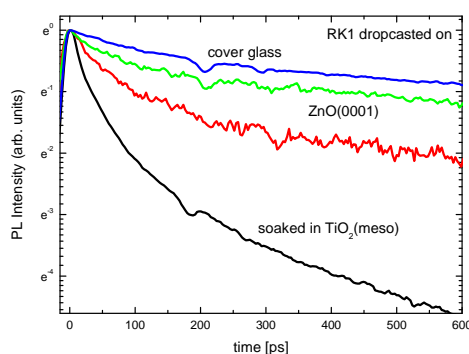


Fig. 6.53.: ps-TRPL decay curves for RK1 drop casted on cover glass, ZnO(0001) and TiO₂(meso). The slow decay on glass is due to non existing charge transfer, a faster decay with thinner layer on ZnO(0001) indicates charge transfer. On TiO₂(meso) molecular binding leads to fastest charge transfer.

of non transferring molecules on ZnO(0001).

The decay curves of RK1 dye as a fully organic dye can be compared to the decay curves of fully organic indoline dyes. Fig. 6.57 shows the comparison of RK1 on TiO₂(meso) with the decay curves of different indoline dyes on ZnO(meso). RK1 shows a faster decay than D149 on ZnO and about the same decay as for DN285 on ZnO. Although the level alignment of TiO₂(meso) (anatase TiO₂) is slightly lower than ZnO (see. Fig. 6.20), it can be concluded that the level alignment of RK1 LUMO conduction band is slightly higher than the D149 LUMO conduction band, as was supposed from absorption spectra. A higher LUMO band above the semiconductor conduction band level results in a faster transfer and in consequence in faster decay curves, as is shown here for RK1. Further assumptions can be made: DN285 should have a LUMO band slightly lower than RK1, from DN216 over DN91 to D131 the LUMO band is getting higher compared

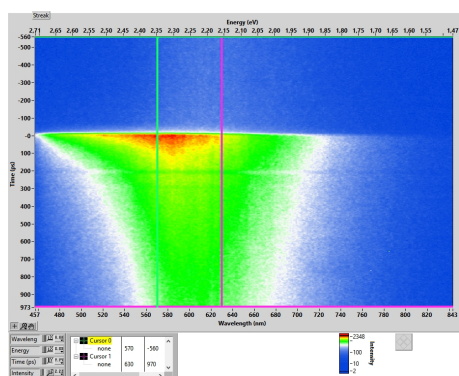


Fig. 6.54.: ps-TRPL image of RK1 on cover glass (isolator, no charge transfer expected). The foothill signal coming from top is 16 ns after excitation, this indicates a long luminescence of RK1 without charge transfer. Evaluation of this image results in the blue decay curve in Fig. 6.53.

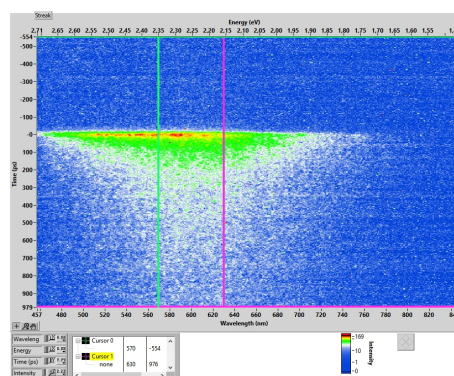


Fig. 6.55.: ps-TRPL image of a thin RK1 layer on flat ZnO(0001). The faster decay in comparison to the decay on glass reveals a charge transfer, the long time decay component has its origin in non transferring molecules. Evaluation of this image results in the red decay curve in Fig. 6.53.

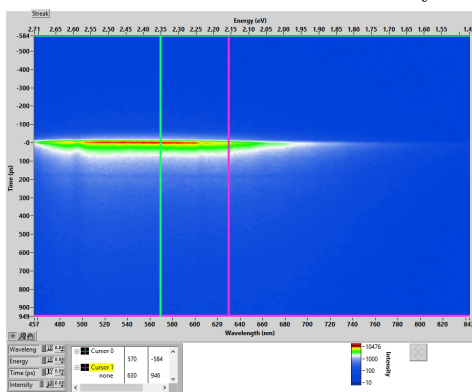


Fig. 6.56.: ps-TRPL image of a RK1 soaked in TiO₂(meso). The even faster decay in comparison to the decay on ZnO(0001) reveals a charge transfer without non transferring molecules and without delay by diffusion of charge carriers. Evaluation of this image results in the black decay curve in Fig. 6.53.

with RK1 LUMO band.

In Fig. 6.58 RK1 on TiO₂(meso) is compared with decay curves of indoline dyes on TiO₂(meso), in this comparison the small difference of levels between ZnO and anatase TiO₂ is not relevant. RK1 shows a slightly faster decay than D149 and a slower decay than RK1. This supports the level alignment assumption deduced from the comparison with indoline on ZnO(meso).

Joly et al. performed cyclic voltammetry (CV) measurements and IPCE measurements (see Fig. G.1) in order to determine the energy level positions of the RK1 bands, a more detailed discussion can be found in [95]. They indicated the LUMO band 0.4 eV above the TiO₂ conduction band edge.

By ps-TRPL measurements of this thesis shown in Fig. 6.57 and 6.58 it was revealed that RK1 has a LUMO band slightly higher than D149 in comparison to the TiO₂(meso)

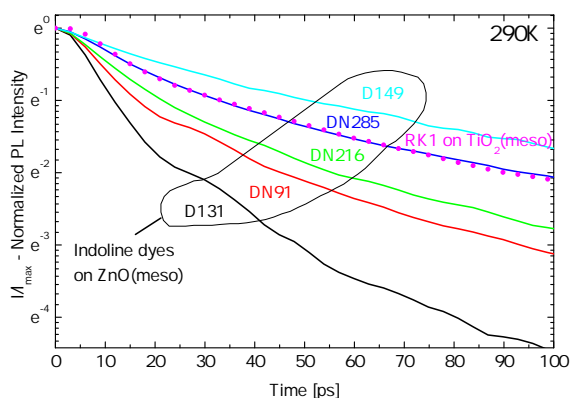


Fig. 6.57.: ps-TRPL curves of RK1 dye on $\text{TiO}_2(\text{meso})$ compared with indoline dyes on $\text{ZnO}(\text{meso})$ in the most relevant time region regarding charge transfer (first 100 ps). RK1 shows a faster decay than D149, as expected from absorption measurements with RK1 absorbing at higher energies than D149.

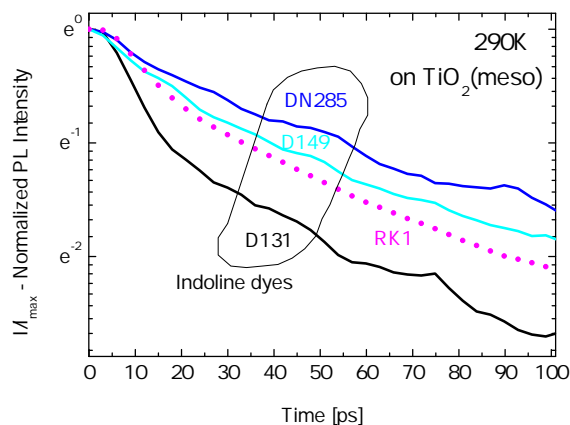


Fig. 6.58.: ps-TRPL curves of RK1 dye on $\text{TiO}_2(\text{meso})$ compared with indoline dyes on $\text{TiO}_2(\text{meso})$ in the most relevant time region regarding charge transfer (first 100 ps). RK1 shows a faster decay than D149, as expected from absorption measurements with RK1 absorbing at higher energies than D149. The LUMO band level of D149 is expected to lie slightly above the LUMO band level of D131 and clearly below the D131 LUMO band level.

conduction band edge. Therefore we can compare results of Joly et al. with the results of this work by comparing with D149 level results. The level alignment of D149 LUMO band is determined from the optical ps-TRPL measurements to be about 750 meV above the conduction band edge of ZnO, see 6.20, and roughly estimated to be about 400 meV higher deduced from the absorption measurements in combination with ps-TRPL measurements on different flat substrates, see 6.13. Both results would fit quite well to the result of Joly et al..

By the ps-TRPL optical measurement method it could be shown that RK1 exhibits charge transfer to $\text{TiO}_2(\text{meso})$, the level alignment could be roughly revealed and the suitability for DSSC is proven. A tandem cell with indoline dye D149 or N719 might achieve even higher efficiencies than DSSCs with single dyes. In section 7.0.1 it is discussed if further measurement methods can support the charge transfer discussion.

In appendix G the level alignment picture is supported by different other methods. A possible type II absorption visible from IPCE measurements is discussed in detail.

7. Conclusion

A more detailed understanding of processes and charge transfer at the interface is important for further optimization of hybrid systems. Regarding "Functionalization of Semiconductors" (Project Graduate School 1782) we investigated in detail organic molecules and solid formation of different organic materials (pentacene, phthalocyanine, anthraquinone) including solid exciton formation depending on molecular orientation and phase, see chapter 5. The results on pentacene should be emphasized because the results show the detailed relationships between physical influencing variables and atomic, microscopic and macroscopic structure. These findings can be transferred to the investigation of other organic materials. The conclusion of section 5.1.4 regarding the results of absorption spectroscopy of pentacene is therefore repeated as main conclusion in the following paragraph.

A clear interrelation between the herringbone angle of the molecules in the unit cell of pentacene crystals and the respective Davydov splitting in the linear optical absorption spectra is found. The variation of the peak height of the individual excitonic Davydov components with temperature is explained by a variation of this herringbone angle. An extraordinarily strong variation of the herringbone angle for C-phase pentacene samples grown on ZnO substrates is observed, whereas it remains essentially constant for freestanding bulk C-phase crystals. This is attributed to the microscopic interface structure between the pentacene film and the ZnO substrate where the more weakly coupled molecule in the unit cell is capable of an efficient rotation about its elongated axis. For the reliable analysis of optical spectra the microscopic structure has to be appropriately taken into account. This is particularly true, when interfacial strain and interface-induced effects are relevant, for example due to largely different thermal expansion coefficients of organic film and substrate. Hence, the exciton transition energies and microscopic interaction scenarios reported in this study for $T = 290$ K and $T = 10$ K may contribute to a detailed theoretical modelling of the different pentacene phases including interfacial strain.

Regarding "Structure and Dynamics of Internal Interfaces" (Project SFB 1083) charge transfer at the interface is investigated, see chapter 6. The electron transfer was successfully shown with ps-TRPL measurements including applied electrical bias, resulting in higher dynamics than seen before in literature and an innovative access to level alignment. This method can therefore be implemented in future organic inorganic interface research.

A type II recombination could not be detected, which would deliver more informations about the interface. The detection of type II PL or electroluminescence or a direct type II absorption should be investigated further in future projects.

In the following, the main conclusions regarding optical spectroscopy of charge transfer dynamics are presented, including a discussion and outlook.

7.0.1. Proof of innovative ps-TRPL method

ps-TRPL measurements on organic-inorganic interfaces including DSSCs (see experimental parts 4.2.2 and 4.5) are revealed as meaningful to investigate charge transfer and determine level alignment.

Three fit models were developed for this innovative ps-TRPL method. A biexponential one using charge transfer time and one long time, the latter a result of non transferring excitons and molecules, see equations used in indoline dye sections 6.3 and 6.7. And a triexponential fit addressing three individual time components, charge-transfer time and the two times by non-transferring components exciton and molecules, see equation 6.9; this three exponential fit allows to evaluate samples with a larger amount of non-transferring molecules, for example due to agglomerations in solar cells, when a simple biexponential fit is not fitting anymore. A third fit model considers diffusion times of charge carriers to the interface and is especially useful when evaluating the transfer of organic layers on flat semiconductors. The third fit model is a biexponential fit with a component of charge carriers which succeed to reach the interface after diffusion and the rest of charge-carriers which do not reach the interface, see equation 6.6. All three fits have their individual advantages regarding the different kind of samples, giving insights into charge transfer times and trends of decay times.

The ps-TRPL method allows to characterize the influence on charge transfer of different dyes, anchor variation of dyes, temperature, layer thickness and substrate material. DSSCs can be characterized regarding unwanted agglomerations and charge transfer and suitability of dyes, thus DSSC can be tested on functionality and compared with each other. From ps-TRPL measurements on DSSCs including applied bias the level alignment of dyes and substrates can be deduced. Furthermore, different excitonic behavior and concentration dependences can be identified, which helps to characterize solids and solutions in general.

See detailed conclusions for the two main sections of indoline dyes which were also published [131, 132] in sections 6.1.4 and 6.2.1.

Relevance of preparation conditions and sample properties The preparation conditions and sample properties are very important for interpretable results, for example soaking conditions are relevant for the optical properties of DSSCs as discussed in section B.2 and appendix C.2.2. The effect of applied electrical bias on DSSCs is dependent on sample choice and preparation. In general, a DSSC with with fast charge transfer and little amount of non transferring molecules is showing the best decay dynamics with different applied bias.

The influence of the electrolyte and the vaporization of it is relevant for the ps-TRPL

results, this should be investigated in future. Literature [197, 75] shows that measurements of complete cells including the electrolyte are evaluable, although our first measurements indicate that a dried electrolyte seems to be relevant for a correct comparison of samples, see appendix D.3 for a discussion. But Tachibana et al. showed clear effects on working solar cells with included different electrolytes at applied bias with TAS measurements.

The paper of Tachibana [197] discusses the influence of the electrolyte on the fermi level in the conduction band, according to this work the electrolyte is able to shift the flat band potential up to 1 V, further literature about the influence on the inorganic semiconductor conduction band properties can be found in [109, 45, 141]. Furthermore, the recombination rate is dependent on the electrolyte, since the electrolyte influences the density of states of the TiO_2 , see also TAS measurements of Haque et al. [75].

In order to understand in detail the effect of changed electrolyte or of different applied electrical bias the Marcus theory [149, 228, 197, 44, 108, 119] is an important theory.

7.0.2. DSSC optimization

ps-TRPL measurements should be performed with organic-inorganic interfaces with different new promising organic materials, for example with D131 variations or with the related D102 and its variations [41].

The influence of different electrolytes should be investigated, both in "freshly" prepared DSSC and in dried DSSC, preferably with a non clustering material with fast charge transfer as with D131. It has to be kept in mind that for an efficient DSSC it is more important that quantum efficiency is high than a fast charge transfer [71, 119].

In order to investigate not only organic-inorganic charge transfer but also organic-organic charge transfer, hetero-junctions with donor-acceptor pairs can be investigated. More application related, if efficiency optimization of solar cells and multistack-cells is needed, the ps-TRPL method should be taken and be affirmed as a working method for optimization.

7.0.3. Additional measurement methods in DSSCs

Electroluminescence As discussed in section 7.0.4 and shown in fig. 7.1 from Piersimoni et al. in 2015, electroluminescence of a organic-inorganic hybrid system is possible. This method should therefore be tested taking applied bias during IR PL detection. As a sample, a defined thin layer of a dye with fast charge transfer and with optical absorption at relatively high energy is suitable, as for exemple D131 on ZnO . In principle, D131 on mesoporous ZnO should also show a recombination electroluminescence.

TAS Transient absorption spectroscopy allows to analyze electron injection dynamics from ultrafast to longer timescales (fs-ns). Especially interesting is the ability to detect

ultrafast charge transfer in the fs range, which is not seeable in ps-TRPL. Furthermore, the forming of ionized states and recombination [71, 165, 164] processes are detected by this method. The experimental method using the pump-probe method laser as pump source and white light as a probe is explained and used on organic inorganic interfaces in multiple publications, for example for ruthenium dyes [197, 75] or for indoline dyes [150, 165, 164, 133]. It is shown for D149 on ZnO(meso) in TAS measurements that D149 very efficiently injects electrons on an ultrafast timescale (Oum et al. [150] <250 fs, Rohwer et al. [165] 150 fs), a more detailed investigation of different indolines with different anchor length followed by Rohwer et al. [164] resulting in times <260 fs, 230 fs for D149. Minda et al. show a direct injection from DN216 with 200 fs and propose different charge transfer states influenced of the ionic and neutral form of the dye [133].

From the fast times resulting from TAS for injection it can be deduced that the main electron injection is from hot states above the LUMO ground state, while the electron injection of ps-TRPL is due to the LUMO band emission. TAS is an important additional spectroscopic method in addition to ps-TRPL.

CV, IPCE, DFT, PES It can be stated that the results of cyclovoltammetry (CV), Incident Photon to Current efficiency (IPCE), electron density measurements and density functional theory calculations (DFT) can be implemented in future investigations and discussions in order to allow a more detailed level alignment and charge transfer discussion. Especially the IPCE measurements on fully processed solar cells can help to give insights into absorption processes, even if optical absorption spectra are not available or possible, see as an example appendix G. CV measurements should be performed in situ with the sensitizer absorbed on the oxide, also it has to be considered that the redox potentials are depending on measurement conditions (see Hagfeldt et al. for a discussion [71] and [227]).

PES measurements can support the level alignment and binding discussion, see measurements of ruthenium on TiO₂(meso) [94] and compared with on ZnO(meso) [18]. Schlesinger et al. [179] use PES for investigation of organic inorganic semiconductor hybrid structures. They reveal with PES the changed work functions in consequence of the implementation of an organometallic donor monolayer in the hybrid interface. Their PES results are consistent with TRPL measurements in the same paper, a lower LUMO band of the organic material in comparison to the conduction band of ZnO leads to a slower decay of the PL. Hagfeldt et al. discuss that with PES method valence level spectra from sensitized nanostructured TiO₂ can be derived and the energy level of the dye/oxide interface can be determined, but Eyer et al. [50] also point on insecurities in PES measurements depending on sample preparation.

In summary PES can contribute to a detailed level alignment picture.

7.0.4. Type II transition

Type II Absorption

In appendix G it is explained in detail why IPCE measurements show a type II absorption for the organic material catechol on $\text{TiO}_2(\text{meso})$. This dye-to- TiO_2 charge-transfer (DTCT) by a type II absorption is also visible in optical absorption spectra as a new absorption in the red part of the spectrum. If RK1 DTCT is confirmed by further measurements, it would be not a typical type II absorption as for catechol, since a carboxylate anchor instead of the catecholate anchor would be involved.

In literature, Haeldermans et al. [70] show for P3HT: MO_x on TiO_2 an increasing external quantum efficiency (EQE) in the red spectral part with increasing ratio of TiO_2 ; EQE is the same as IPCE, but without the conversion ratio into photovoltaic cell performance. Piersimoni et al. [153] show a type II absorption of the organic dye α -NPD layer on ZnO also by EQE measurements. They show the absorption of a new hybrid charge transfer state (HCTS) in the red part (see fig. 7.1). This HCTS has its origin in the same reason as for type II absorption (DTCT) revealed by IPCE method, namely a direct charge transfer from the dye into the inorganic semiconductor.

The EQE shows a CT absorption which is by orders of magnitude lower than the intrinsic dye absorption, this is due to the low absorption cross section [161].

Type II absorption gives insight to the level alignment between dye HOMO band and the inorganic semiconductor conduction band acceptor level.

Type II emission

A clear type II PL could not be found within this thesis, see IR-PL of D131 on inorganic semiconductors in sec C.2. The question arises, where the energy is distributed in this case, when not in recombination from inorganic semiconductor to the dye HOMO band. A possible way would be loss by heat processes in the inorganic semiconductor. It is not excluded by this thesis if in the steady decrease of the PL in the IR a type II recombination PL is overlaid. It should be confirmed by a non transferring material as $\text{ZrO}_2(\text{meso})$ with equivalent agglomeration and binding properties as $\text{TiO}_2(\text{meso})$ and $\text{ZnO}(\text{meso})$ if there is clearly no overlaid recombination PL in the IR spectrum of mesoporous samples (as used in Haeldermans [70]), D131 should be used due to the fast charge transfer and the little tendency to agglomerate. For type II detection of D131 on planar inorganic semiconductor, defined thin layers of D131 should be prepared with high quality of preparation.

Regarding literature, Bansal et al. [11] showed an electroluminescence of the charge transfer recombination from CdS conduction band to P3HT HOMO band in P3HT:CdS solar cells. Piersimoni et al. [153] were the first who could show a type II injection (as discussed above in "Type II absorption") and emission in one system, see fig. 7.1. They could show a type II recombination indirectly by electroluminescence measurements.

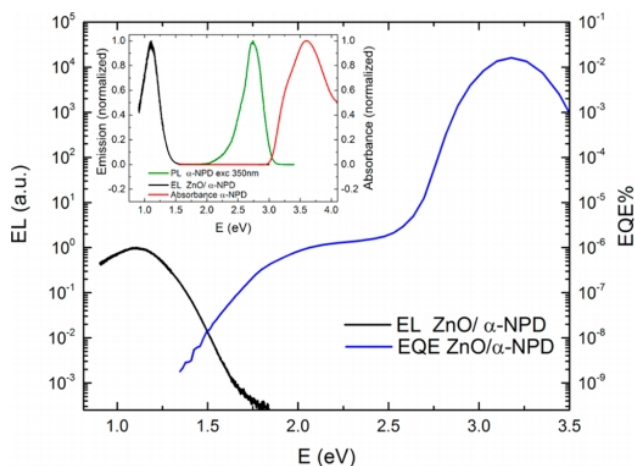


Fig. 7.1.: Electroluminescence (EL) intensity and external quantum efficiency for a planar bilayer device using α -NPD as the donor and ZnO as the acceptor (logarithmic scale). The inset shows the PL and absorption from a neat α -NPD thin film and EL of α -NPD deposited on ZnO (linear scale). Figure and caption taken from Piersimoni et al. [153], Fig. 1.

While the PL of the investigated dye α -NPD layer on ZnO is completely quenched due to complete charge transfer of the excited electrons into the ZnO, the recombination of the HCTS state can be seen clearly as an electroluminescence corresponding to the EQE curve.

Electroluminescence could be also shown in planar heterojunction solar cells: Panda et al. [151] detected the electroluminescence of hybrid charge transfer excitons (HCTEs) for a layer of CBP on ZnO in a heterojunction solar cell; Eyer et al. [50] could reveal an electroluminescence from a layer of P3HT on ZnO with a variation of the EL with Mangan content in the ZnO layer due to the higher bandgap with increasing Mn content. For a layer of SP6 on planar ZnMnO Blumstengel et al. [17] could show ps-TRPL decay curves varying with different SP6 layer thickness, but with less dynamics than for our measurements of indoline layers on ZnO. Yet, the system SP6/ZnMO might be useful for detection of type II PL or EL.

One paper by Wang et al. [209] indicates a proof of type II band alignment after exciting a P3HT/CdSe nanoscale heterostructure with a laser. A recombination PL from the inorganic semiconductor CdSe to the organic material P3HT can be detected.

Type II emission gives insight to the level alignment between the inorganic semiconductor conduction band fermi level and the HOMO band level of the organic semiconductor. Different systems should be investigated in electroluminescence and also in IR-PL. A type II photoluminescence is still not clearly shown in literature and should therefore be investigated thoroughly for samples showing electroluminescence.

Type II interface state

The building and the existence of interface states is presently controversially discussed ([161]) in many publications. This discussion should be implemented in further inves-

tigation of type II transfer properties. Those bound interface charge transfer states (ICT) are also addressed as hybrid charge transfer exciton states (HCTE) [152], bound charge pair states (BCP) [205] or surface bound states [5]. Delocalized interface states and localized interface states are in discussion [196]. The electron injection by different pathways including the injection into neutral charge transfer states and ionic charge transfer states is proposed by Minda et al. [133], both states are revealed by TAS method. Transfer of electrons, but also holes and energy transfer is discussed as charge transfer process in organic inorganic interfaces [36].

Appendices

A. Phthalocyanine

A.1. Pc*OH₂ - catechol anchor - PL results

Measurements with Phthalocyanine*OH were performed as part of the Examensarbeit of Luise Rost, AG Heimbrodt, university Marburg [168]. A high energy PL was detected which can be seen in Fig. A.1 for ZnPc*OH and in Fig. A.2 for H₂Pc*OH. The associated absorption is shown in Fig. 6.34. In addition, an absorption of a 11 nm thick layer of ZnPc*OH formed on SiO₂ is shown in Fig. A.3. The high energy PL with maximum at about 2.3 eV probably belongs to the high energy absorption increasing from 2.4 eV to a maximum at about 3.5 eV. This high energetic PL should be investigated in future experiments since it was not discussed in literature until now up to our knowledge.

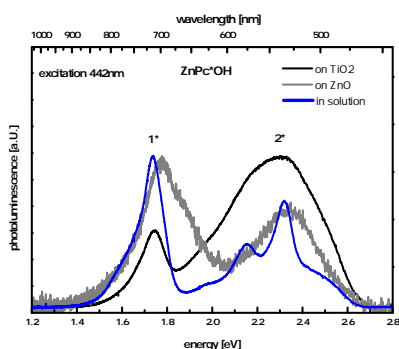


Fig. A.1.: ZnPc*OH PL in solution, soaked in TiO₂(meso) and in a processed solar cell with mesoporous ZnO

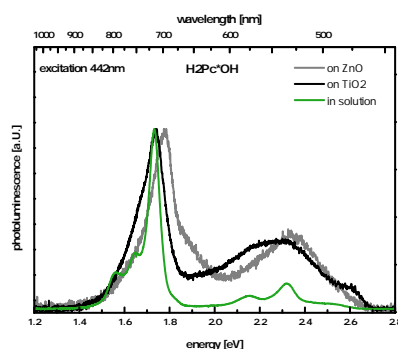


Fig. A.2.: H₂Pc*OH PL in solution, soaked in TiO₂(meso) and in a processed solar cell with mesoporous ZnO

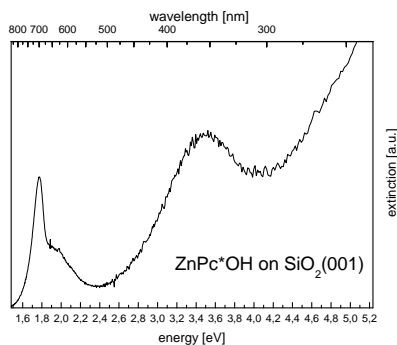


Fig. A.3.: Absorption of ZnPc*OH on planar substrate SiO₂(001) - 11 nm thickness. The sample was prepared by OMBD at 316 K by Michael Kothe, AG Witte, university Marburg.

B. Anthraquinone variations

B.1. Absorption and Photoluminescence Spectroscopy: Comparison of Alizarin, Phenoxazin, Anthraphen, Anthraphenol

Different Anthraquinone based dyes were investigated in the bachelor thesis of Benjamin Heidelmeier [79]. Fig. B.1 shows Phenoxazin, Anthraphen and Anthraphenol. Alizarin is shown in Fig. 5.53d with its two hydroxyl anchor groups building the catecholate with the unsaturated six-carbon ring, resulting in a bidentate anchoring to TiO_2 .

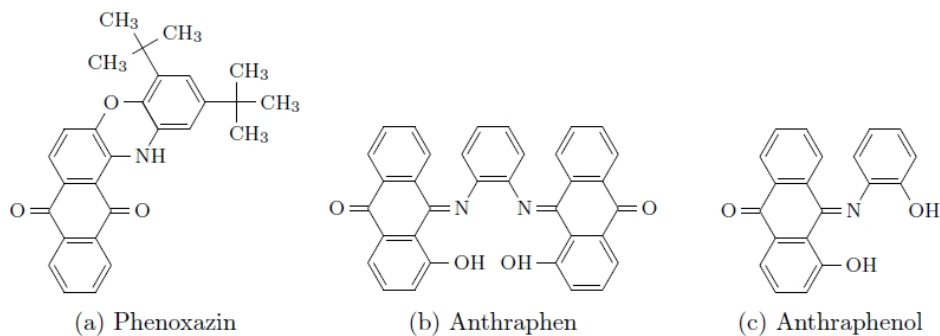


Fig. B.1.: Chemical Structure of Phenoxazine, Anthraphene and Anthraphenol. The picture is taken from bachelor thesis of Benjamin Heidelmeier [79].

Fig. B.2 shows absorption and Fig. B.3 PL of different Anthraquinones on $\text{TiO}_2(\text{meso})$. Comparing Anthraphen and Anthraphenol absorption spectra, due to the similarity of spectra it can be deduced that the main π -complex does not include the whole molecule but only the separated Anthraquinone parts, otherwise Anthraphen should have a larger red shift against Anthraphenol due to its larger molecular size. This is confirmed if the PL spectra are compared with the PL spectra of pre steps of Alizarin, including hydroxy-Anthrachinon, see Fig. 5.54. Both peaks around 2eV can also be found for hydroxy-Anthraquinone in solution, as expected.

The absorptions of Anthraphene and Anthraphenol are comparable and the PL shows two distinct peaks at same energy positions around 2eV, with Anthraphene showing a more dominant peak at lower energies. The lower energy part probably stems from Frenkel exciton formation, the higher energy part originates from the molecule PL (as discussed for Anthraphenol, see Fig. 5.57).

Phenoxazine on $\text{TiO}_2(\text{meso})$ exhibits a broadening into the red spectrum compared with the other Anthraquinone variations both in absorption and PL. Interestingly it shows two absorption regions, the higher energy peak at about 425 nm possibly due to the Anthraquinone part at about the same energy as for Anthraphene and Anthraphenol; the lower energy at about 525 nm (2.35 eV) and 675 nm (1.8 eV) are possibly due to solid formation effects, the latter possibly by Frenkel exciton formation.

Phenoxazine on $\text{TiO}_2(\text{meso})$ shows PL at about 1.7 eV (about 730 nm), possibly belonging to the absorption of solid crystalline Phenoxazin at around 550 nm, as can be seen in Fig. B.5 better than in Fig. B.3. The higher energetic PL part at about 550 nm (2.25 eV), better shown without filter influence in Fig. B.4, is possibly due to the anthraquinone part of the molecule, which seems to appear isolated on $\text{TiO}_2(\text{meso})$ (Fig. B.4) and in solution (see Fig. B.3), but interestingly not for crystalline Phenoxazine (see Fig. B.5).

From the spectra in Fig. B.4 it can be deduced that with its maximum at about 550 nm a blue shift of the high energetic Phenoxazine PL occurs in comparison to Anthraphene and Anthraphenol. The more pronounced high energy peak of the PL spectra in comparison to Fig. B.3 indicates a higher dominance of the isolated anthraquinone part, which indicates less crystallization.

The general question is why an isolated Anthraquinone part should occur, is the Phenoxazine molecule perhaps decomposed or is the absorption and PL in the Anthraquinone spectral region a consequence of a crystal formation? Since for Phenoxazine solids crystal formation does not show 550 nm PL (see Fig. B.4), a partial decomposition of Phenoxazine seems to be the right explanation.

In this context it has to be pointed out that in solution with Tri-Chlor-Methane (Chloroform) only a lower energy peak at 600 nm can be seen in absorption (see Fig. B.2), possibly belonging to the full π -complex of the whole molecule. In consequence, a PL of the phenoxazine solution with lower energies than 600 nm is expected, but astonishingly a high energy PL at around 550 nm in solution occurs (see Fig. B.4), the complete PL of the solution being very similar to the PL on $\text{TiO}_2(\text{meso})$. As discussed above, the 550 nm PL might occur to a decomposed Phenoxazine molecule.

In addition, PL in solution and on $\text{TiO}_2(\text{meso})$ at around 1.7 eV occurs, which was shown to be clearly related to solid formation (see Fig. B.4). This points to a solid formation with a crystalline structure not only on mesoporous TiO_2 as was already shown in absorption spectra (Fig. B.2), but also in the measured chloroform-solution. *It has to be verified if for the shown PL spectrum in Fig. B.4 perhaps a much higher concentration of Phenoxazine was chosen, where solid formation occurred.*

The molecular PL of Phenoxazine measured without decomposition is expected at lower energies than 600 nm. Interestingly, the ps-TRPL images of Phenoxazine in section B.2 can support the expectation. As can be seen in ps-TRPL image B.9, a PL with a maximum of about 680 nm occurs on $\text{TiO}_2(\text{meso})$. This sample was prepared and measured before the bachelor thesis of Benjamin Heidelmeier and showed a clear blue to violet

colouring, while later prepared $\text{TiO}_2(\text{meso})$ samples showed no such colouring anymore. A further ps-TRPL image B.8 of Phenoxazine in Acetonitrile shows the known spectrum including decomposition PL at 550 nm and solid formation PL at lower energies, not showing the real Phenoxazine PL at 680 nm.

To be investigated: It might depend on the solution concentration and solvent material, used spacers and on the size of TiO_2 nanoclusters in the mesoporous TiO_2 if a binding of Phenoxazine molecules occurs during soaking of mesoporous TiO_2 , without decomposition and solid formation and with clear colouring of the mesoporous sample. Some different concentrations were tried, but the molecular PL as in image B.9 could not be reproduced. Also, soaking in mesoporous ZnO should be tried out. This preparation investigation should be performed in further experiments.

Phenoxazine is discussed here in high detail in order to be able to discuss the detected fast TRPL of ps-TRPL image B.9 in section B.2.

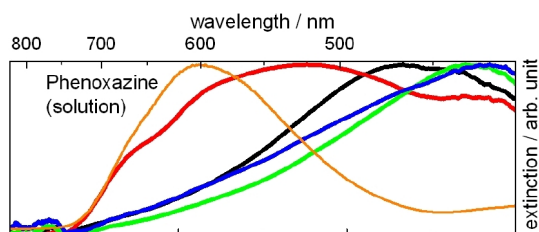


Fig. B.2.: Range of absorptions of Alizarin, Phenoxazin, Anthraphene and Anthraphenol soaked in mesoporous TiO_2 (orange curve: Phenoxazine in solution with chloroform). Figure and caption taken from bachelor thesis of Benjamin Heidelmeier [79].

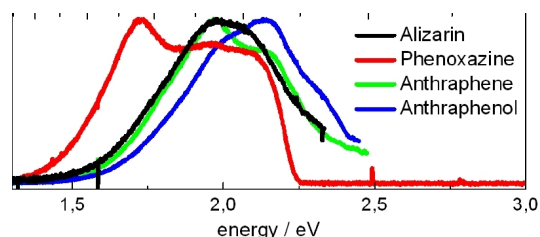


Fig. B.3.: Corresponding photoluminescences of the absorptions in Fig. B.2 of four different derivatives Alizarin, Phenoxazin, Anthraphene and Anthraphenol soaked in mesoporous TiO_2 . Figure taken from bachelor thesis of Benjamin Heidelmeier [79].

For each of the four molecules PL spectra in solution and on $\text{TiO}_2(\text{meso})$ are very similar, a comparison is exemplarily shown for Phenoxazine in Fig. B.4. Further spectra with such PL spectra comparisons can be seen for Alizarin, Anthraphen and Anthraphenol in [79]. Powder PL is always redshifted in comparison to PL in solution or on $\text{TiO}_2(\text{meso})$ due to deep trap formation, for example for Phenoxazine in Fig. B.4 it can be seen that powder is redshifted in PL to the PL peak of crystalline Phenoxazine at about 730 nm.

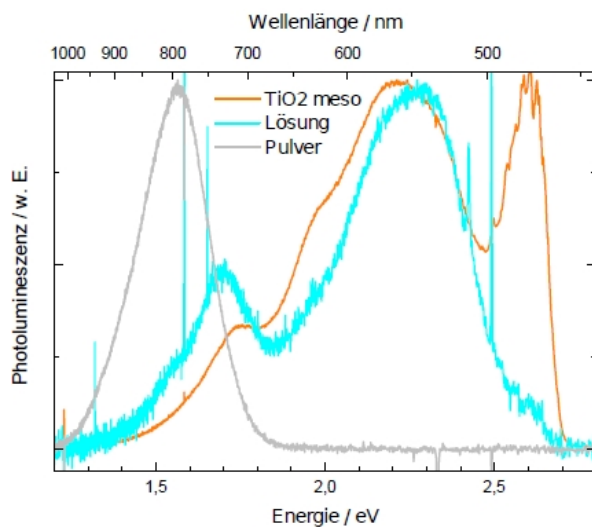


Fig. B.4.: Phenoxazine PL in solution (Lösung), on TiO_2 (meso) and as powder (Pulver), figure taken from bachelor thesis of Benjamin Heidelmeier [79]. Shown is the PL over the energy (lower x-scale) and wavelength in nm (upper x-scale). The PL peak with wavelengths smaller than 500 nm is due to TiO_2 (meso) and not from Phenoxazine.

Fig. B.5 shows absorption and PL spectra of Phenoxazine crystalline structures. Crystals were produced by drop casting. More rods lead to an increase in absorption at lower energy (675 nm) which was already shown on TiO_2 (meso) in Fig. B.2, this absorption is not shown in solution and might be an excitonic absorption of the crystalline structure.

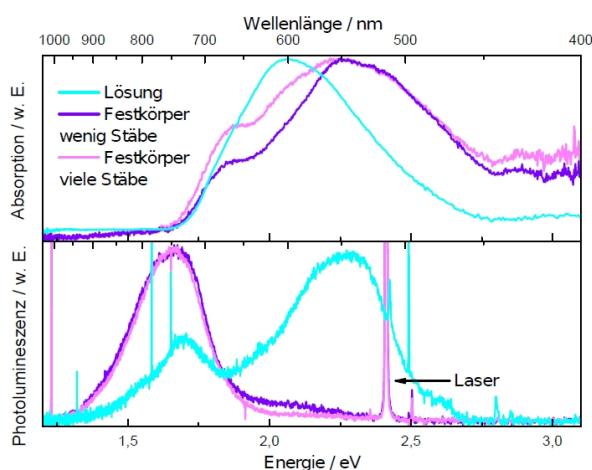


Fig. B.5.: Phenoxazine PL in solution with chloroform (Lösung), on TiO_2 (meso) and as powder (Pulver), figure taken from bachelor thesis of Benjamin Heidelmeier [79]. Shown is the PL over the energy (lower x-scale) and wavelength in nm (upper x-scale). The PL peak with wavelengths smaller than 500 nm is due to TiO_2 (meso) and not from Phenoxazine.

B.2. Charge Transfer: ps-TRPL measurements

Anthraquinones were introduced in section 5.3.1. Alizarin (Chemical structure shown in Fig. 5.53) shows about 2% DSSC efficiency [195] and was already discussed in 1993 on colloidal TiO_2 [140]. It has to be considered that Alizarin is absorbing only in the blue spectral range and has therefore naturally low efficiencies in DSSCs, yet it is suitable for harvesting in panchromatic DSSCs. Further variations of Anthraquinones could lead to improved efficiency.

An important property of Alizarin is the catechol anchor [146]. An et al. discuss the binding of the catechol anchor with varied molecules which achieve about 0.7% efficiency [3]. Interestingly only very low efficiencies near 0% were shown for other Anthraquinone variations [117] with a carboxyl anchor instead of a catechol anchor.

Regarding Phenoxazin, Anthraphen and Anthraphenol (Chemical structure see Fig. B.1), no catechol anchor is part of the molecule. Two ways of bidentate binding can occur with TiO_2 : chelating bidentate and bridging bidentate. While chelating bidentate binding occurs only with one TiO_2 complex, bridging bidentate binding occurs with two TiO_2 complex. Mech et al. [129] show different ways of chelating bidentate binding, but the binding of Anthraquinone which is also the possible anchoring part of Phenoxazin is not shown. Son et al. [194] discuss the functions of Benzoanthraquinone and only assign the 1,2-Benzoanthraquinone with neighbouring oxygen atoms a binding to TiO_2 , not for 1,4-Benzoanthraquinone with oxygen atoms towards each other. The binding of Phenoxazin and Anthraquinone to TiO_2 is therefore unclear: Since Hydroxyl groups are missing only the two O atoms of the quinone complex are possible as anchors, but those are not neighbours and therefore cannot show a bidentate binding to TiO_2 . This favours a pure molecular adhesion without anchoring.

Regarding Anthraphen and Anthraphenol, both molecules probably bind by its two hydroxyl groups, either with chelating or bridging bidentate binding. If a metal is included in Anthraphen and is bound in combination with the two hydroxyl anchors, no clear binding mechanism as for Anthraquinone and Phenoxazin is expected. Anthraphenol may show a stronger binding in comparison to Anthraphen due to the geometry which should allow a chelating bidentate binding.

An et al. [3] discuss a so-called Type II photoinjection (first introduced by Mulliken in 1952 [142]), an injection directly from the dye into the conductive band of the semiconductor, in particular for TiO_2 (see Fig. B.6). It is called dye-to- TiO_2 charge-transfer (DTCT). The Type II injection is described for bidentate catechol anchors to the TiO_2 and not for monodentate anchors [117]. Catechol anchors seem to favour the Type II injection [199], see more details and a revealed type II injection in discussion part 7.0.3 in Fig. G.5 and G.6. From absorption measurements of Alizarin on $\text{TiO}_2(\text{meso})$ (see Fig. B.2) no such distinct type II injection at lower energies can be seen for energies down to 1.25 eV (1000 nm); perhaps the binding to $\text{TiO}_2(\text{meso})$ is not correct as assumed from ps-TRPL results, further investigations should be done to verify and examine this interesting phenomenon.

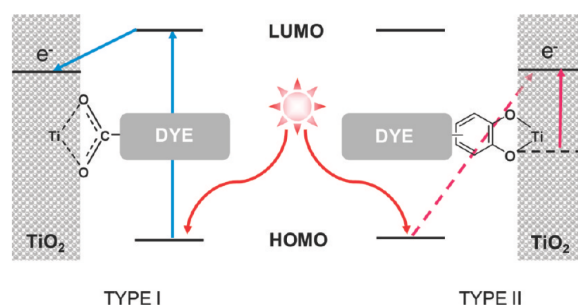


Fig. B.6.: Figure and caption taken from [3];

Schematic showing Type I and Type II photoinjection in a DSSC. Binding via a carboxylic acid such as in N3 [Ruthenium dye] allows Type I injection which occurs via the dye excited state. Binding via a bidentate catechol bridge yields Type II injection where excitation is a low energy charge transfer state of the dye-titania complex. The solid arrows in both cases indicate the actual pathway for excitation and photoinjection and the dashed arrow in the Type II case indicates “the apparent” pathway from the isolated dye ground state.

Time-Resolved Photoluminescence Spectroscopy

A suitability for solar cells was checked by means of time-resolved photoluminescence, a faster decay curve on $\text{TiO}_2(\text{meso})$ in comparison to the decay curve in solution indicates a charge transfer. The effect of the variation of the different anthraquinones on the charge transfer is of interest.

Based on the absorption measurements of Fig. B.2 one would expect comparable level alignments due to the similar absorptions and molecular composition. This should result in similar transfer times for Anthraphen, Anthraphenol and Alizarin. In the case of Phenoxazine, the high-energy part could also show similar times, while the low-energy part might not show a charge transfer due to lower level alignment.

However, the result of the transfer times in Fig. B.7 does not show these expected properties of the decay curves. While Alizarin and Anthraphen show a comparable but slight acceleration compared to the decay curves in solution, the anthraphenol shows no acceleration.

Interestingly, Phenoxazine shows the fastest transfer of all variations and is therefore usable in a dye solar cell, see the associated ps-TRPL image B.9. However, the spectrum of the PL decay does not match the other measured PL spectra on $\text{TiO}_2(\text{meso})$ and in solution measured by Benjamin Heidelmeier in his bachelor thesis [79]. In order to clarify this discrepancy, Phenoxazine spectra are discussed in detail in the Appendix B.1. It is shown there that the spectrum which shows the fast TRPL probably has its origin from Phenoxazine molecules without solid formation.

However, the phenoxazine result with successful molecular attachment could not be reproduced, although several tests were carried out and in solution the Phenoxazine spectrum did not change from previous spectra, see also comments in B.1.

The spectra including solid formation and the probably isolated anthraquinone PL, i.e. without a molecular spectrum, are similar in time to those in solution, revealing no

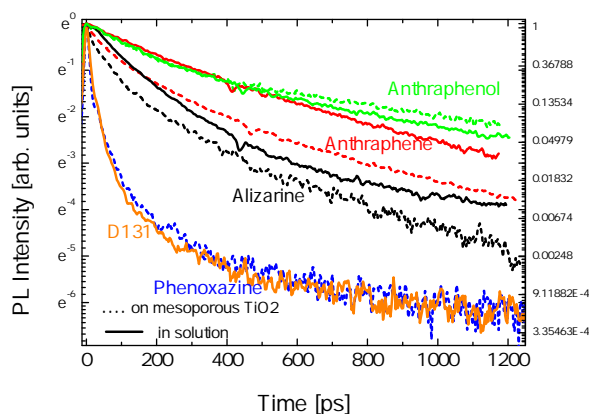


Fig. B.7.: Comparison of TRPL of different Anthraquinones in solution and on $\text{TiO}_2(\text{meso})$, D131 on $\text{TiO}_2(\text{meso})$ is shown for comparison.

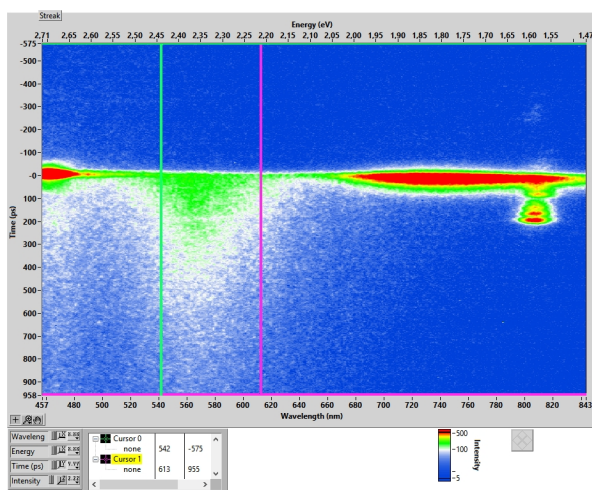


Fig. B.8.: Image of ps-TRPL of Phenoxazine in solution (Acetonitril), intensity is scaled in that way that the PL around 570 nm can be seen. That PL possibly belongs to isolated anthraquinone parts of decomposed Phenoxazine molecules.

charge transfer effect (see ps-TRPL image B.8 and the decay curve in solution in Fig. B.10).

Only the molecular absorption seems to allow charge transfer from the organic dye to $\text{TiO}_2(\text{meso})$. If this interpretation is correct, the level alignment of Phenoxazine conduction band would be above the conduction band of $\text{TiO}_2(\text{meso})$. All other higher-energy anthraquinone variations should therefore show charge transfer, but this cannot be seen from the decay curves. On $\text{TiO}_2(\text{meso})$ Anthraphenol does not show any faster decay and Alizarin and Anthraphenol show only slightly faster decay. This indicates that apart from molecular Phenoxazine, there was no successful connection to the substrate. The spectra are isolated solid-state spectra without showing a clear connection of Phenoxazine to the $\text{TiO}_2(\text{meso})$. The slightly faster decay in Alizarin and Anthraphene could either result from the concentration effect on $\text{TiO}_2(\text{meso})$ or from a small proportion of attached molecules that overlap the spectra and thus accelerate the decay

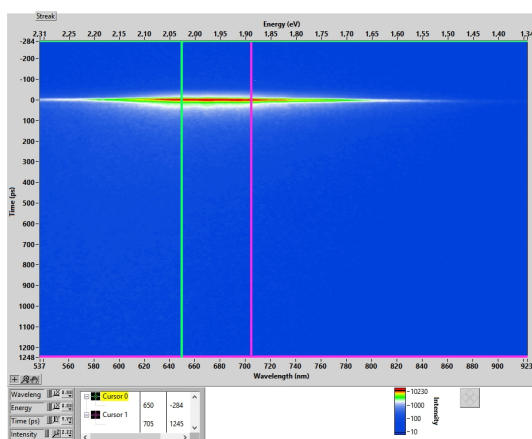


Fig. B.9.: ps-TRPL image of Phenoxazine soaked in $\text{TiO}_2(\text{meso})$. The PL indicates a molecular attachment without solid formation. Other prepared soakings in later times could not reproduce this molecular soaking but reveal solid formation effects and probably also decomposition of Phenoxazine.

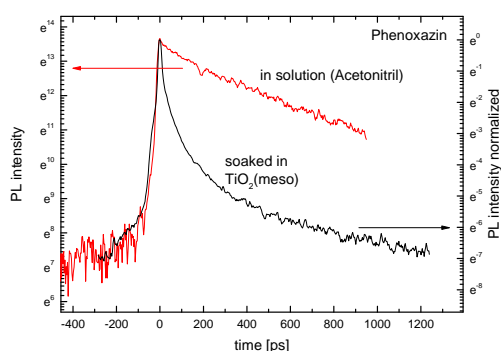


Fig. B.10.: Resulting Phenoxazine TRPL curves, comparison of possibly molecular Phenoxazine on $\text{TiO}_2(\text{meso})$ and in solution (high energy part, possibly due to Anthraquinone part of Phenoxazine)

curves at the beginning.

The following figures B.11 and B.12 support these theses. Co-Anthraphene (Cobalt) shows a faster decay on $\text{TiO}_2(\text{meso})$ compared to glass, which can be due to the better electronic coupling resulting from the included metal atom. The faster decay in the first 100 ps can thus actually be an indication of a charge transfer, while for Anthraphene the curves on glass and $\text{TiO}_2(\text{meso})$ remain the same in the beginning relevant for charge transfer, i.e. they show no charge transfer on $\text{TiO}_2(\text{meso})$. Regarding OH-Anthraquinone, the same PL was measured for hydroxyanthraquinone as amorphous crystal on the surface of the $\text{TiO}_2(\text{meso})$ (probably without visible substrate interaction) and on $\text{TiO}_2(\text{meso})$. There is a faster decay on $\text{TiO}_2(\text{meso})$ (see Fig. B.12), this might indicate charge transfer or at least an influence of a charge transfer component.

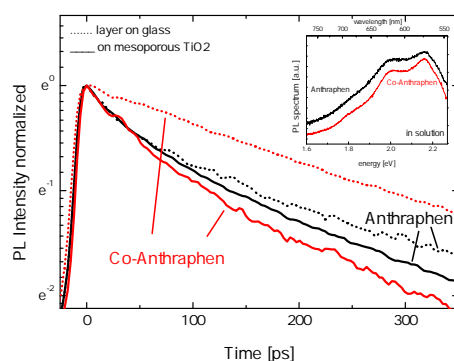


Fig. B.11.: ps-TRPL comparison of layer on glass and soakings on $\text{TiO}_2(\text{meso})$ for Anthraphene and Co-Anthraphene. Co-Anthraphene exhibits a faster decay on $\text{TiO}_2(\text{meso})$ in comparison to the decay on glass indicating a better charge transfer than for Anthraphene. The inset shows PL spectra in solution, the cobalt atom does not change the PL spectrum of Anthraphene.

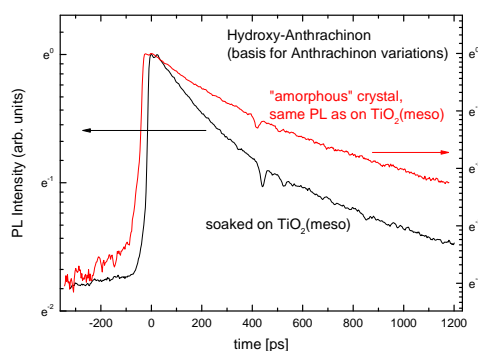


Fig. B.12.: ps-TRPL curves of Hydroxyanthraquinone on $\text{TiO}_2(\text{meso})$ and as amorphous crystal. A faster decay on $\text{TiO}_2(\text{meso})$ indicates a charge transfer from the organic material to the substrate.

Summary

- Phenoxazine reveals fast decay probably due to charge transfer, but problems with the reproduction of the layers indicate that Anthraquinones are not as easy to handle as indolines. Soaking procedures on $\text{TiO}_2(\text{meso})$ have to be improved and thoroughly understood before further investigations on Anthraquinone variations are performed.
- Anthraphene including metals might be interesting for future investigations
- TypeII injection of catecholate anchors directly from the organic material into the inorganic semiconductor should be investigated in future

C. Indoline dyes

C.1. Absorption and Photoluminescence of Indoline dyes in solution

Indoline dyes were measured in solution in absorption and PL, the result is shown in Fig. C.1. D131 was not measured in the same stage (UV-VIS device), the PL was measured in the ps-TRPL stage (absorption measurement is missing). These measurements are a supplement to the measurements in Fig. 6.3.

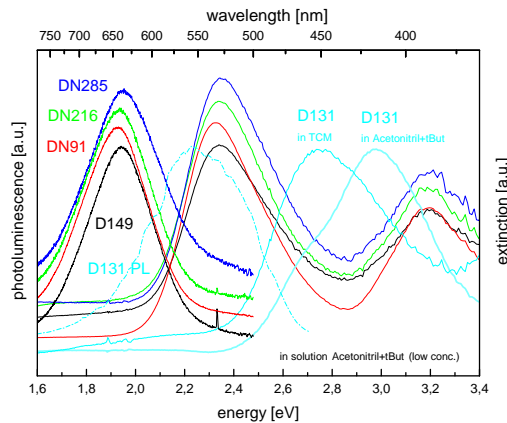


Fig. C.1.: Absorption and PL of indoline dyes in solution (Acetonitril+tBut) except for the absorption of D131 which was measured in TCM at low concentration. The PL of D131 was measured in ps-TRPL stage and shows therefore detector specific noise. Absorption is showing the same shifts as in PL.

The same shift can be seen in absorption and PL. The trend of the anchor length is reversed, the second anchor leads to a blue shift but longer second anchor leads back to a red shift, until DN285 with two anchors has nearly the same spectral characteristics as D149 with one anchor.

Further detailed investigations of D149 in solution can be found in literature [48].

C.2. Photoluminescence spectroscopy - Trap formation for solid Indoline dyes

The following pictures C.2 to C.6 are screenshots of the ns-TRPL measurement software Andor Solis, the purpose is to illustrate the effects of powder formation in ZnO(meso)

samples soaked with D131. The left part shows the spectrum measured at room temperature, the right part the spectrum measured at 10 K. The pictures C.2 to C.4 with center wavelength 625 nm show the low energy part of the main PL region; an optical filter OG550 cuts the spectrum at 550 nm, the maximum PL at 570 nm is not the real maximum.

It can be seen at starting point of the PL decay (picture C.2) a peak formation in the curve side occurs at 10K. This belongs to powder PL, see ps-TRPL image of D131 powder in picture C.5. While the molecular PL disappeared after 10 ns, the powder PL remains (picture C.3) with its long time. Even after 27 ns a powder PL peak remains, see picture C.4. An increase of PL from room temperature to 10 K can be observed due to less PL quenching.

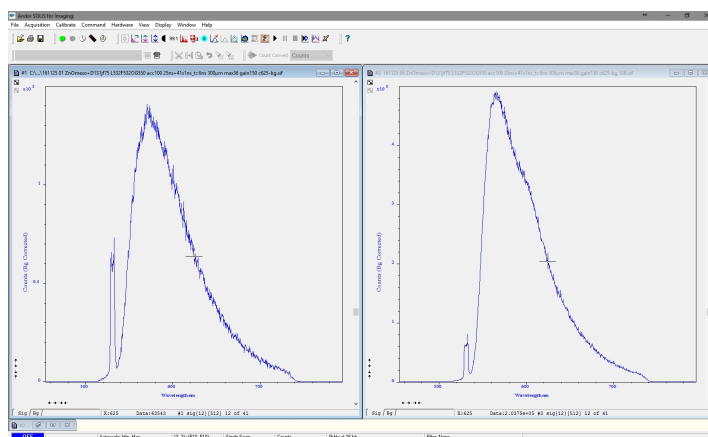


Fig. C.2.: D131 on ZnO(meso). Spectra of the first nanosecond of the TRPL begin are shown at room temperature (left) and at 10 K (right). Central wavelength is 625 nm, a spectral range from 570 nm to 740 nm shows the low energy part of the PL peak of D131 on ZnO(meso). At 10 K a band can be seen in the side of the curve which belongs to powder PL, the whole PL peak consists of a molecular PL part and a powder PL part.

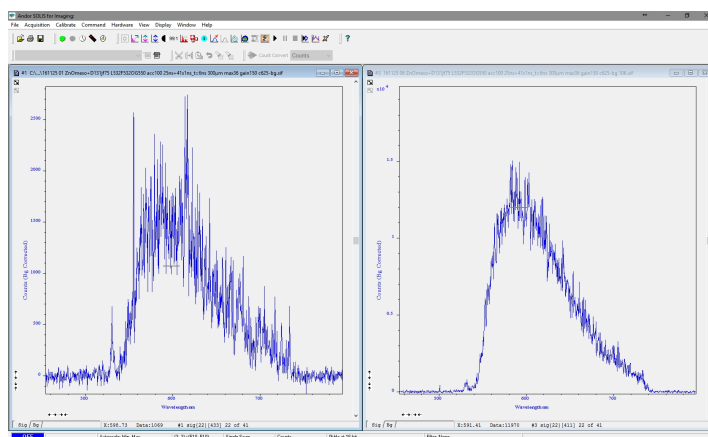


Fig. C.3.: Same conditions as in picture C.2, but the 10th ns of the ns-TRPL spectra is shown. While the molecular part disappeared at 10 ns, the powder PL peak is still existent.

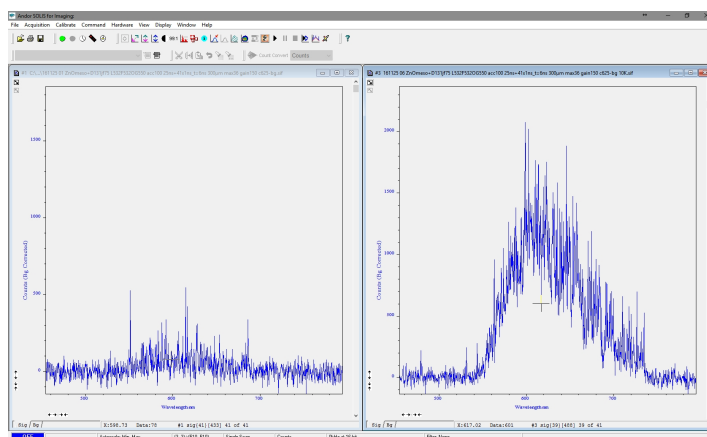


Fig. C.4.: Same conditions as in picture C.2, but here the 27th ns after PL begin is shown. Even after 27 ns the powder PL can be observed.

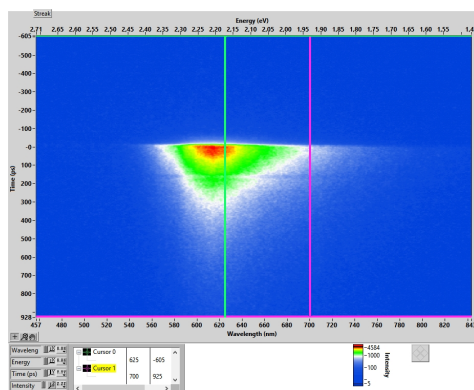


Fig. C.5.: ps-TRPL image of D131 powder - clear red shifted to the molecular PL of D131 in solution or on ZnO(meso) with a maximum at about 620 nm.

Picture C.6 shows the NIR-spectral region with center 835 nm wavelength, the upper part showing spectra at room temperature and the lower part spectra at 10 K. The integral over 1 microsecond of the PL evolving 6 ns after the start of the PL decay is shown. At 10 K a band formation at about 830 nm can be observed. This deep PL has a long lifetime and cannot belong to molecular PL. This deep PL is correlated with the powder PL around 617 nm, meaning an increase of powder PL leads to an increase of the deep PL.

The possibility is yet not excluded that the deep PL is arising from type II charge transfer from ZnO(meso) back to D131. In order clarify this, TRPL of a D131 agglomeration on SiO₂ was measured at cold temperature, which also shows the powder PL at 617 nm, see picture C.7. No charge transfer can occur on this isolator. A slight band at 830 nm indicates again the correlation of the deep PL at 830 nm and the powder PL at 617 nm. In consequence it is shown that the band forming at 830 nm does not belong to a type II recombination.

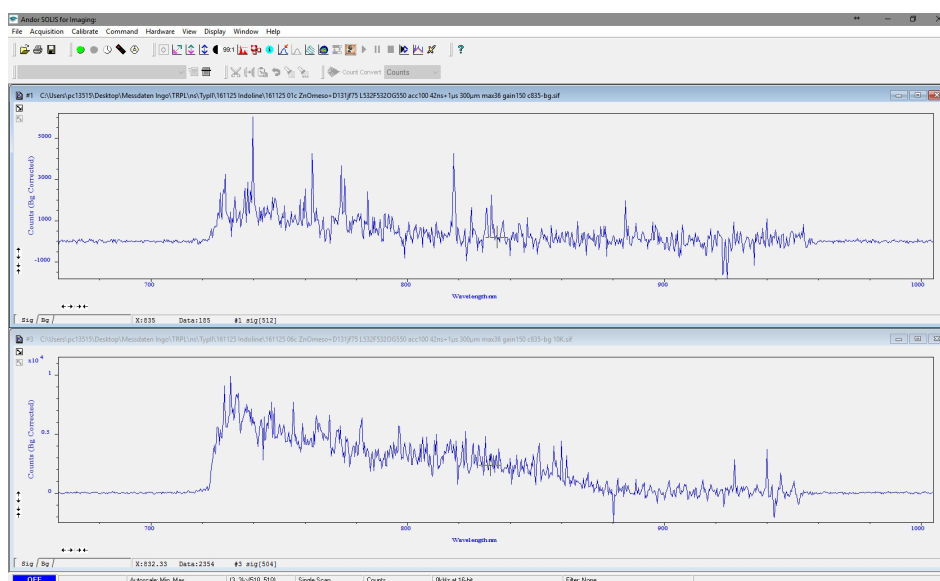


Fig. C.6.: D131 on ZnO(meso). Spectra of the first microsecond integrated with starting point at 6 ns after TRPL begin are shown at room temperature (top) and at 10 K (bottom). Central wavelength is 835 nm, a spectral range from 730 nm to 950 nm shows the NIR region of the low energy part of the PL peak of D131 on ZnO(meso). As shown in the upper pictures, only the powder PL remains at 6 ns and no molecular PL of D131 is existent. At 10 K a band formation can be seen in the side of the powder PL curve.

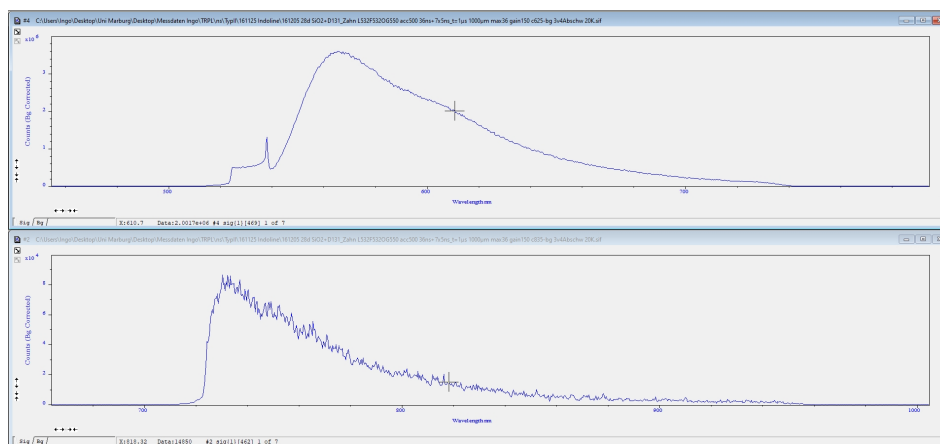


Fig. C.7.: D131 agglomeration on SiO₂ showing D131 powder PL. Spectra of the first 5 nanoseconds of the TRPL are shown at central wavelength of 625 nm (top) and at central wavelength of 835 nm 10 K (bottom), temperature is 20 K. At 830 nm a slight band formation can be seen in the curve side. This deep PL is therefore correlated with the powder PL, possibly forming by deep traps of powder.

Further investigations with cw-PL stages including IR-detector confirm the NIR band forming at 10 K, see figures C.8 and C.9. The shown measurements were performed on a solar cell which was prepared by Jane Falgenhauer, university Gießen.

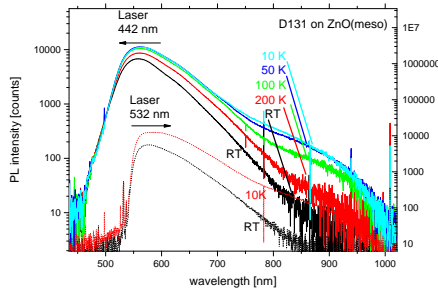


Fig. C.8.: PL of D131 on ZnO(meso) measured in cw at different temperatures. The logarithmic scale clearly shows the evolution of the deep trap PL of D131. A stronger effect occurs with 442 nm laser excitation.

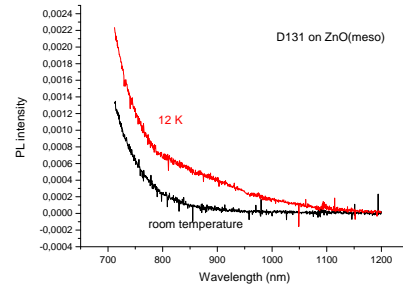


Fig. C.9.: At 442 nm laser excitation the deep trap PL formation at 10 K is shown, measured with IR-PL stage.

Is a type II recombination existent? After Hagfeldt et al. [71] it is not possible to investigate fully processed DSSCs in regard to type II recombination, because the electrolyte in working DSSCs would reduce the oxidized dyes faster than a recombination from the oxide. Therefore, the IR part of the spectrum of D149 and D131 on ZnO(meso) was investigated in order to reveal a possible type II PL resulting from electrons recombining from ZnO(meso) to the organic dye. The spectral region up to 1700 nm was investigated, but no peaks or bands were found at room temperature. In future, the measurements should be performed again at 10 K in order to avoid PL quenching. First measurements at 10 K with 532 nm laser did not achieve a signal in IR (not shown here), but this might be due to a wrong signal optimisation.

It is probable that most of the electrons which transferred to ZnO(meso) lose energy by internal loss processes in the ZnO(meso). To ensure that the IR PL is not influenced by recombination processes, a mesoporous material which does not allow charge transfer should be investigated in future as a reference, as for example mesoporous ZrO_2 .

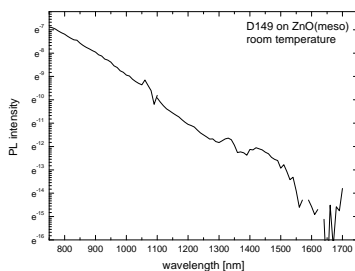


Fig. C.10.: IR-PL at room temperature of D149 on ZnO(meso) in IR region down to low energies as 0.73 eV (1700 nm). No explicit band which might indicate a type II recombination can be found on ZnO(meso) at room temperature.

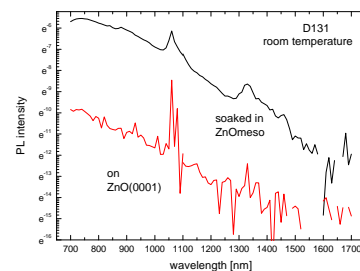


Fig. C.11.: IR-PL at room temperature of D131 on ZnO(meso) and on ZnO(0001) in IR region down to low energies as 0.73 eV (1700 nm). No explicit band which might indicate a type II recombination can be found on ZnO(meso) at room temperature.

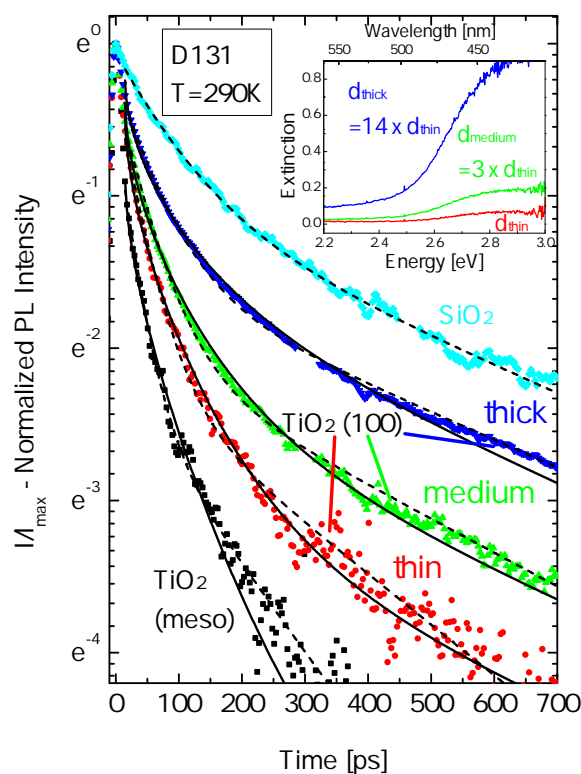


Fig. C.12.: Photoluminescence decay of D131 on TiO_2 at 290 K. Dashed line: Fit using Eq. 6.3; full lines: Fit using Eq. 6.6 (see text for details). Inset: Extinction of different layers on $\text{TiO}_2(100)$.

C.2.1. Charge Transfer Dependence of Layer Thickness - D131 on TiO_2

The same fit model including diffusion model as for D131 on ZnO can be applied with D131 on $\text{TiO}_2(100)$. This confirms the applicability of the diffusion model also on different substrates.

C.2.2. Influence of anatase Mesoporous TiO_2 on Charge Transfer of different Indoline dyes

Ps-TRPL measurements at room temperature for indoline dyes soaked in $\text{TiO}_2(\text{meso})$ show slower decay compared to measurements on $\text{ZnO}(\text{meso})$ (see Fig. 6.5) for all shown dyes except for D149. This slower decay is due to the higher proportion of non-transferring molecules: the long decay times caused by non-transferring molecules are comparably long as on $\text{TiO}_2(\text{meso})$, but the amount of non-transferring molecules is highly increased, except for D149 and DN285. In consequence it can be observed that the different indolines are visibly much more similar in their decay behavior in the first 100 ps than on $\text{ZnO}(\text{meso})$. The visibly faster decay of D131 compared to the other dyes persists as on $\text{ZnO}(\text{meso})$, but also D131 shows a much higher amount of non-transferring molecules.

Table C.1.: Charge transfer times and exciton recombination times for D131 using Eq. 6.3 (upper part) and Eq. 6.6 (lower part)

D131 (<i>calc. with Eq. 6.3</i>)	τ_{trans} [ps]	n_a [%]	τ_{exc} [ps]	n_b [%]
in solution			575	
layer on SiO ₂ (0001)	110	59	550	41
thick layer on TiO ₂ (100)	68	68	550	32
medium layer on TiO ₂ (100)	55	77	450	23
thin layer on TiO ₂ (100)	45	79	300	21
TiO ₂ (meso)	28	75	175	25
D131 (<i>calc. with Eq. 6.6</i>)	τ_D [ps]	n_a [%]	τ_{exc} [ps]	n_b [%]
thick layer on TiO ₂ (100)	313	76	550	24
medium layer on TiO ₂ (100)	270	87	550	13
thin layer on TiO ₂ (100)	238	93	550	7
TiO ₂ (meso)	222	98	550	2

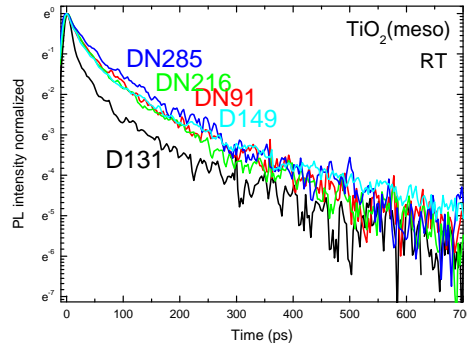


Fig. C.13.: Photoluminescence decay of indoline dyes on mesoporous TiO₂ at 290 K.

The decay in the first 100 ps should nevertheless show stronger differences than shown here. The soaking procedure on TiO₂(meso) should be examined further in order to clarify this question. If the more similar times of the different anchors of D149 and the DN-indolines would be confirmed, then an explanation would be that the second anchor on TiO₂(meso) is not dominantly binding as on ZnO(meso). The consequence would be that the decay curves decay similar to D149, only steric effects would remain as differences between D149 and the DN-indolines.

D. Accessing the level alignment at the interface

D.1. Variation of Substrates

D.1.1. CdS and glass + D149 - reaching PL without substrate influence

As revealed in image with substrate interaction D.1, a strong Förster transfer can be detected if the right sample preparation and measurement is performed. The following discussion reveals that it is important to measure at the interface between organic material and substrate with the right focus and a homogeneous layer on it.

With no substrate interaction from CdS to D149 layer no hillfoot can be seen in the TRPL image D.2 after one measurement period of the ps-TRPL stage, that means no signal enters the image from upper side. Increasing substrate interaction leads to an increasing hillfoot in the TRPL images D.4 and D.3. The measurements should be performed very carefully on different sample locations and with altering focus in order to not miss the interaction.

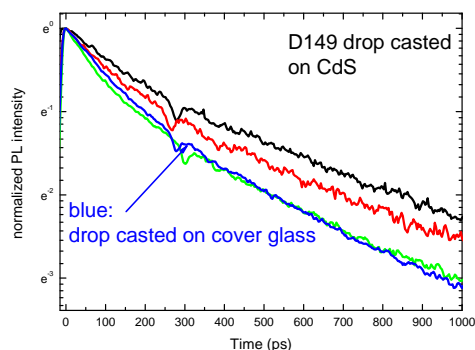


Fig. D.1.: The TRPL decay curves of D149 on CdS and on glass are shown. It is possible to measure the PL of D149 uninfluenced from the substrate PL, see green curve. The slower decay of the red and black curve indicate increasing influence of the Förster transfer.

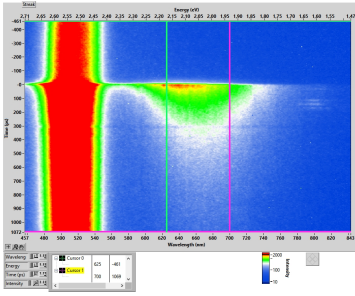


Fig. D.2.: Strong substrate PL revealed on high energy side (left). The image was scaled on the D149 PL (broad PL in centrum). The evaluated TRPL is the green curve in Fig. D.1 and shows about the same decay properties as on glass. No interaction between D149 and CdS substrate revealed here, possibly due to focus on CdS instead of the interface between D149 and CdS.

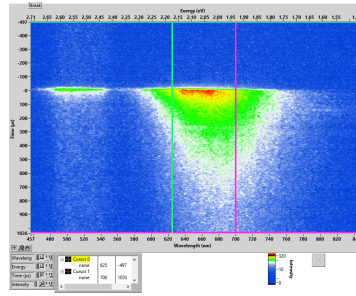


Fig. D.3.: CdS PL is small and indicates a good focus on the interface between D149 and CdS. A small redshift of the D149 PL indicates that an agglomeration of molecules or powder was measured, but the spectrum should still be evaluable. The red curve in D.1 shows a slower decay than on glass which indicates that a small amount of Förster transfer occurred from CdS to D149.

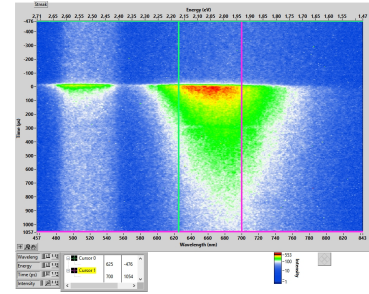


Fig. D.4.: This image shows the same spectral properties as Fig. D.3 with a bit more D149-substrate interaction. This can be seen in Fig. 6.21 where it is shown that a small hill-foot of D149 is entering the picture in the upper part of the image, this means that the long lasting PL decay of CdS transferred some of its energy to D149.

D.2. Electrooptical Characterization of D149 DSSC

D149 solar cells were investigated with voltage dependent ps-TRPL spectroscopy in analogy to D131 solar cells, see section 6.2.1, for example Fig. 6.11. With increasing applied electrical bias an increase of PL occurs, see Fig. D.5 (the cell is prepared from Melanie Rudolph (MR)). An increase of an order of magnitude can be seen in PL intensity, which is less dynamic than seen for the D131 cells.

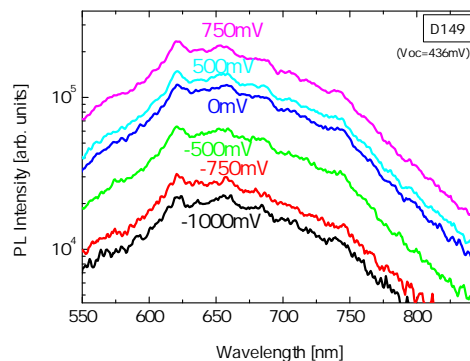


Fig. D.5.: D149 soaked on ZnO(meso) and processed to a solar cell (Melanie Rudolph, group Schlettwein, university Gießen) are investigated in ps-TRPL with applied electrical bias. Resulting spectra are shown. An increase in PL amplitude occurs with increasing applied bias.

The resulting ps-TRPL curves from the spectra in Fig. D.5 are shown in Fig. D.6, with increased applied bias a slower decay occurs.

Another D149 DSSC is evaluated which was prepared by Jane Falgenhauer (JF), group Schlettwein, university Gießen. Strong differences in charge transfer times occur with biexponential fits, the fit results are indicated in the graphs, see Fig. D.6 and D.8. This points to a problem of this ps-TRPL method applied on "flat" curves. If the charge transfer times are similar to the effective exciton times or the amount of non transferring excitons is so dominant that the charge transfer times are not dominant in the first relevant decay part (which is mostly the first 100 ps), an evaluation of charge transfer times is not possible with a free fit. A triexponential model allows to achieve similar charge transfer times for both cells, but also not as a result of a free fit, see Fig. D.7 and D.9. The trend of slower decay with increased applied bias is yet revealed in every fit constellation, biexponential and triexponential.

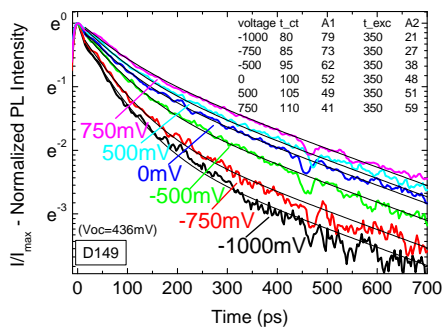


Fig. D.6.: D149 on ZnO(meso) processed to a solar cell (Melanie Rudolph, group Schlettwein, university Gießen). Applied electrical bias varied from -1000 mV to 750 mV. The fit curves are performed by biexponential fits.

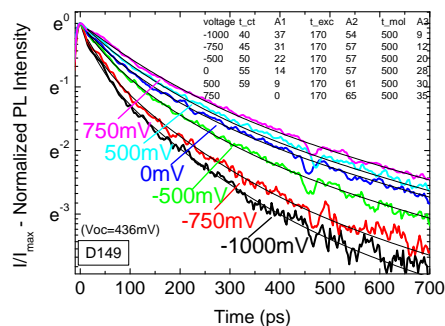


Fig. D.7.: Same conditions and curves as in Fig. D.6, fitted with triexponential fit

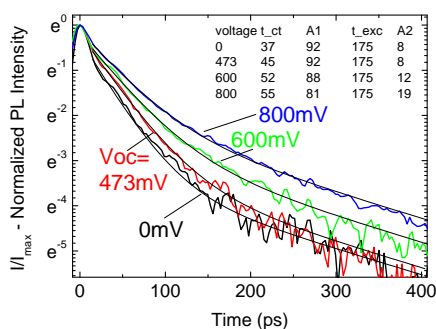


Fig. D.8.: D149 on ZnO(meso) processed to a solar cell (Jane Falgenhauer, group Schlettwein, university Gießen). Applied electrical bias varied from 0 mV to 800 mV. The fit curves are performed by biexponential fits.

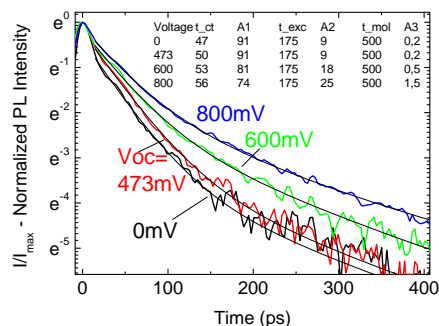


Fig. D.9.: Same conditions and curves as in Fig. D.8, fitted with triexp fit

The cell of JF is better evaluable than the cell of MR since the exciton part is less dominant, which is due to less agglomerations in the cell. Agglomeration depends on soaking parameters: the cell of JF was soaked 1 min while the cell of MR was soaked 15 min in solution, in combination with the other soaking parameters as concentration of dye and spacers this has lead to a stronger agglomeration in the MR cell. The effective exciton time and amount of non-transferring molecules is therefore longer for the MR cell than for the JF cell.

D.3. Influence of Electrolyte on Level Alignment

DN216 DSSC with Iodide and Cobalt electrolyte were produced by Raffael Ruess, group Schlettwein, university Giessen. Both samples show a similar large amount of clusters and are therefore comparable, even though the samples are not as suitable as DSSCs with low amount of clusters. D131 cells would also have the advantage of a faster charge transfer and therefore a higher possible dynamic of decay times. The result is a slower decay for the DSSC with iodide electrolyte. This is expected since a lower V_{OC} for cobalt indicates a lower Fermi-level in the conduction band of the inorganic semiconductor during illumination, which should result in a faster charge transfer from the dye LUMO band.

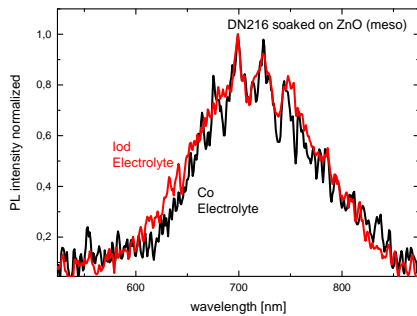


Fig. D.10.: Spectra of DN216 DSSCs with Iodide and Cobalt electrolyte. Due to the similarity of the spectra, the TRPL decay curves are comparable.

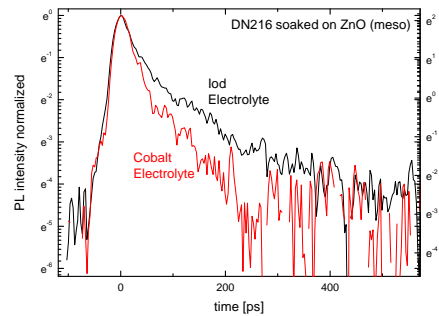


Fig. D.11.: ps-TRPL decay curves of the spectra in left figure. The PL of the DSSC with cobalt electrolyte decays faster than the cell with iodide electrolyte.

The influence of the electrolyte on charge transfer is discussed for example in [119]. It should be further investigated, which influence different electrolytes of DSSCs show in ps-TRPL in following experiments.

E. ps-TRPL method applied in processed solar cells

E.0.1. Monochromatic Sensitized Solar Cells

In the following, solar cell measurements are compared with those on mesoporous layers without processing to the solar cell. Although the spectra have general similarities, the resulting times are clearly different (see Fig. E.1). When examining processed solar cells with the ps-TRPL measurement method, a systematic error must be taken into account that results from drying out to different degrees. The ps-TRPL measurement method only allows a reliable comparison of measurements with one another for completely dried electrolyte, i.e. for cells or soakings in which the electrolyte has completely evaporated. If the electrolyte is still present, the comparisons with one another are difficult since the same degree of evaporation would have to be present. This question is investigated in the succeeding phd work of Nico Hofeditz, AG Koch, university Marburg.

However, PL spectra and ps-TRPL measurements can identify agglomerates and in particular non-transferring agglomerates, which have to be avoided because the efficiency of the solar cells decreases due to non-transferring agglomerates. Comparisons of degrees of non-transferring agglomerates between the different solar cells are possible with ps-TRPL in case of dried cells. Both spectroscopic methods, PL and ps-TRPL, can be helpful in the preparation and optimization of solar cells.

In Fig. E.2 some spectra of D149 on ZnO(meso) and TiO₂(meso) are shown. It often applies that the more intense the cells are coloured, the more agglomerated the dye and in consequence the more red-shifted the PL and the slower the decrease of the PL. For example, Fig. E.1 shows very different decay curves for two prepared cells on ZnO(meso). The cell prepared by Jane Falgenhauer (JF, group Schlettwein, Gießen) has fewer agglomerations than the cell prepared by Melanie Rudolph (MR, group Schlettwein, Gießen), see redshift for MR cell in Fig. E.2. There may also be a residual electrolyte in the MR cell, which slows down the decay.

The concentration of the spacers and the concentration of the dye solution during soaking as well as the soaking conditions are decisive for whether agglomerations occur more often. The speeds of the slow solar cells of JF-TiO₂ and MR-ZnO are comparable to those of the thin layers on TiO₂ or ZnO, so in addition to the undesired agglomeration, the diffusion to the interface is increased by thicker layers. The TiO₂ solar cell in particular is probably very agglomerated, which can also be seen from the spectrum that is strongly red-shifted from the normal TiO₂(meso). With these measurement methods it is therefore possible to conclude if the cell preparation is not optimal.

The ZnO-SC from JF decays the fastest. Although the spectrum is blue shifted against

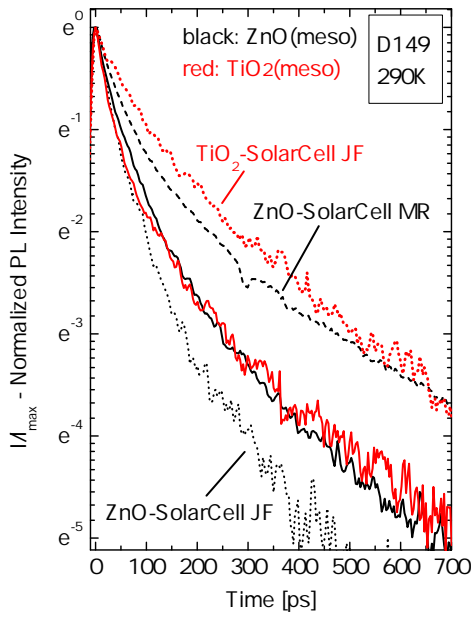


Fig. E.1.: Comparison of ps-TRPL of D149 solar cells and simple soakings in $\text{TiO}_2(\text{meso})$ and $\text{ZnO}(\text{meso})$. JF=Jane Falgenhauer, MR=Melanie Rudolph, both of university of Gießen, Group Schlettwein.

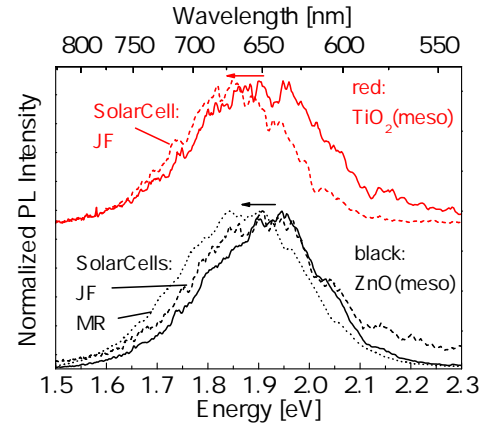


Fig. E.2.: PL spectra of D149 soakings and complete solar cells from ps-TRPL stage, the corresponding times shown in Fig. E.1. Due to detector properties the spectra are noisy, yet the shift are unambiguously. Spectra without noise are shown in Fig. E.3

the much slower cell of MR, the simple soaking without solar cell processing is still more blue shifted, so the even faster PL drop compared to the soakings in $\text{ZnO}(\text{meso})$ is not to be expected. The long times of the $\text{ZnO}(\text{meso})$ cell indicate less agglomerations than $\text{ZnO}(\text{meso})$ soaking. Assumption: more agglomerations than for the simple soaking are existent in the solar cell, but in the cell they may still be small enough that charge transfer can still take place, while agglomerations that do not transfer are more present on $\text{ZnO}(\text{meso})$ soakings.

A test was made for monochromatic cells stacked in tandem cells, one sensitized with D131 and the other with D149. Fig. E.4 illustrates the principle: the two curves in the upper part show D149 and D131 PL, respectively. The 3rd curve shows the two cells individually electrically connected, the curve on 4th position shows the PL of a serial connection of an electrically connected D149 and D131 cell. Laser illumination leads to V_{oc} of 433 mV for D131 and 340 mV for D149 in individual cells, the electrically connected "Schottky" series stack would let expect 773 meV; 812 meV is measured, which is close. Those measurements show the possibility of measure tandem cells with optical spectroscopy, by this measurement it can be tested if the residual laser light passes into the next cell and if absorption occurs in the bottom cell.

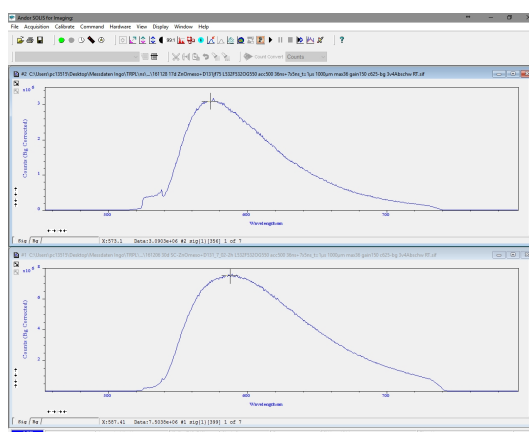


Fig. E.3.: PL of ns-TRPL stage, comparison of D149 on ZnOmeso (top) and processed solar cell by Melanie Rudolph (bottom), group Schlettwein, university Gießen. A broadening of PL occurs with the red part due to agglomerations.

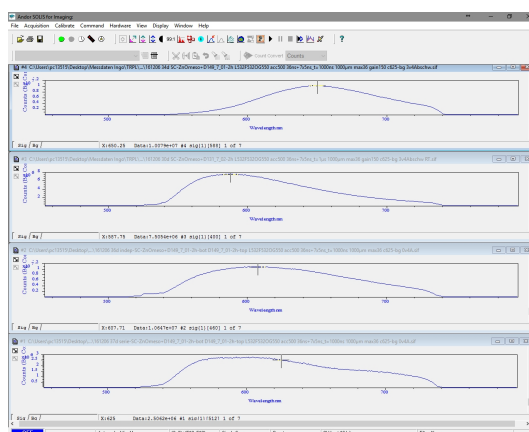


Fig. E.4.: Independent and serial tandem of monochromatic solar cells D131 and D149 shown in 3rd and 4th curve, respectively. The first two curves show D131 solar cell and D149 solar cell measured without tandem stack. The spectra of the individual cells add to each other in the tandem spectra

E.0.2. Panchromatic Sensitized Solar Cells

Panchromatic Sensitized Solar Cells with Indoline dyes - TRPL

Adding dyes during soaking of one mesoporous layer as done with D149 and D131 leads to panchromatic DSSC. The ps-TRPL images show the different single junctions in Fig. E.5 and the resulting panchromatic ps-TRPL image E.6. The spectral properties of the single junctions are added in the panchromatic cell to a combined spectrum. The resulting ps-TRPL curves of D131 and D149 stay the same for single junctions and panchromatic junctions, no influence of charge transfer occurs due to a panchromatic connection.

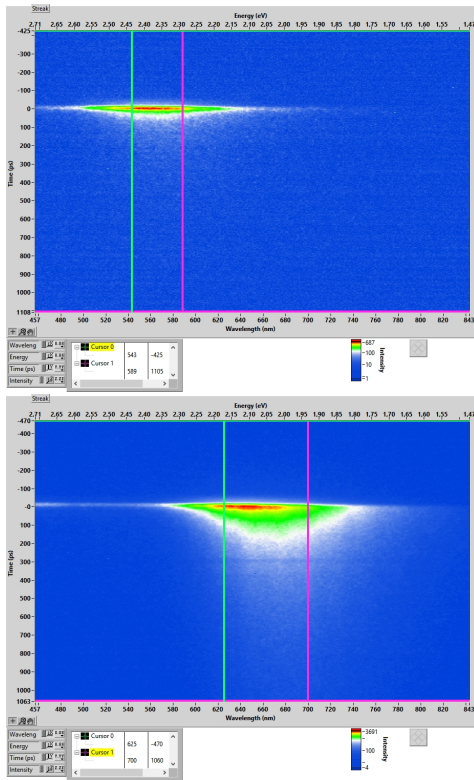


Fig. E.5.: ps-TRPL image of single junction DSSCs sensitized with D131 (top) and D149 (bottom)

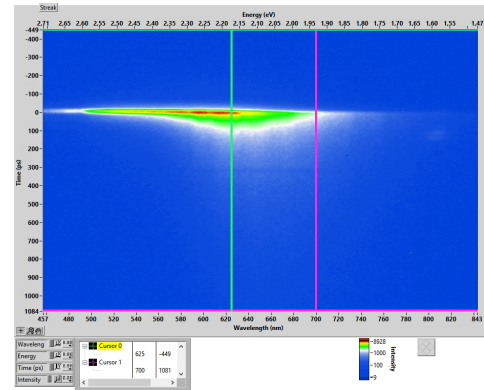


Fig. E.6.: ps-TRPL image of panchromatic junction DSSC sensitized with D131 and D149, resulting in a combination of the single junction cells.

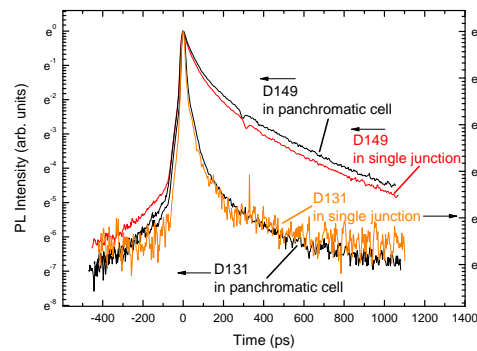


Fig. E.7.: ps-TRPL curves of panchromatic junction DSSC sensitized with D131 and D149, compared with decay curves of the single junction DSSCs. A panchromatic addition of dyes does not change the CT behavior. (All samples were taken from one preparation row of Melanie Rudolph, group Schlettwein, university Gießen)

Side result: spacer CA seems to space D149 further away from $TiO_2(meso)$ than OA, this can be concluded from the slower charge transfer time in Fig. E.5 compared with E.10.

Panchromatic Sensitized Solar Cells with Indoline dyes and SQ2 - TRPL

The goal for all panchromatic dyes is efficient charge transfer, i.e. connection to the semiconductor. The order of the soaking, the selected dyes and the spacers used in the soaking are relevant for a good solar cell. A detailed study of the combination of three dyes in a panchromatic solar, namely the dyes D131, D149 and the dye SQ2, was performed (not shown here). The result is that the dye SQ2 is not an easy partner with both indoline dyes, especially with D149.

- If SQ2 is adsorbed prior to D149 with spacer CA, no D149 can be absorbed afterwards and no charge transfer of the quasimolecular SQ2 occurs.
- If SQ2 is adsorbed without spacer CA, agglomerations and possibly exciton formation occurs; if D149 is then added, no absorption of D149 occurs, but the binding of agglomerated SQ2 is much better, the D149 seems to remove unbound agglomerations of SQ2 and in consequence to improve the charge transfer of the agglomerated SQ2, see Fig. E.8. Exciton PL at longer times show the TRPL for agglomerations which do not have charge transfer, while the short time in the begin is the consequence of charge transfer of excitons.

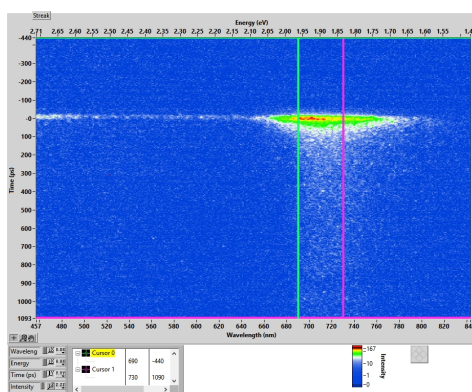


Fig. E.8.: ps-TRPL image shows the PL spectral region of agglomerated SQ2, redshifted to the quasimolecular PL forming up when spacer CA is used during soaking (see Fig. E.9) which is possibly formed by solid exciton PL of SQ2. A charge transfer is shown by the fast times at the begin, the long times indicate the exciton times without charge transfer.

Investigating the effect of added D131 and D149 to SQ2, only specific preparation conditions lead to a useful panchromatic cell.

- If SQ2 is added after soaking of D131+D149, the SQ2 molecules do not agglomerate, but show now charge transfer. Therefore SQ2 should not be added after soaking of D131 and D149.
- If SQ2 is soaked first before adding D131+D149 without spacers, D131 is absorbed without agglomeration forming up and a panchromatic cell of SQ2 and D131 with fast charge transfers is created, but D149 is not absorbed, see ps-image E.9.
- If spacers are added during soaking with performing first SQ2+CA soaking and then

D131+D149+OA soaking, the charge transfer of D131 and SQ2 is less fast as without spacers. Interestingly, in this case D149 is also absorbed. This soaking and spacer combination leads to the best absorption of all three dyes, but SQ2 does not show charge transfer, see ps-image E.10. D149 shows charge transfer and is therefore bound to $\text{TiO}_2(\text{meso})$, see bottom of Fig. E.5 as a reference for D149 charge transfer, when a spacer is used.

- interestingly, the soaking of SQ2+D131 was improved with added D149, although D149 was not absorbed. This confirms the observation that D149 seems to remove unbound agglomerations of SQ2, see above.
- Without adding D131 to SQ2, SQ2 shows no charge transfer in quasimolecular PL.

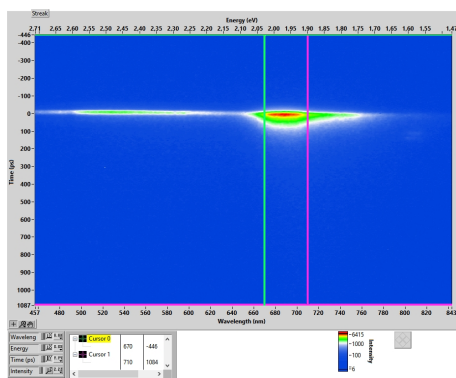


Fig. E.9.: ps-TRPL image of 5 minutes soakings of SQ2+D131 and then added soaking of a mixture of D131+D149. D149 is not absorbed, but the soaking of SQ2+D131 was improved by D149 soaking. Both absorbed dyes D131 and quasimolecular SQ2 show charge transfer to $\text{TiO}_2(\text{meso})$ proven by the fast TRPL times.

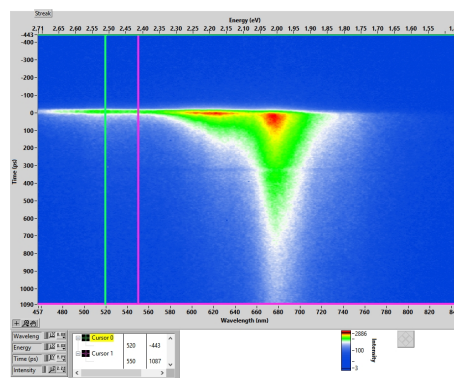


Fig. E.10.: ps-TRPL image showing all three dyes D131, D149 and SQ2 absorbed. The long times indicate no or poor charge transfer from SQ2 and D149 to $\text{TiO}_2(\text{meso})$, probably the connection to $\text{TiO}_2(\text{meso})$ is not effective. Solar cells should be produced to ensure no charge transfer of D149 and SQ2, which should show worse efficiency than cells made in configuration of Fig. E.9.

To sum up, only D131 is a suitable absorbing partner together with SQ2. D131 supports the molecular binding of SQ2. D149 can be useful to remove agglomerated SQ2, but was not successfully charge transferring when absorbed together with SQ2 and D131. The reason of this should be investigated in future.

This example proves that soaking processes needs a lot of optimization in order to achieve the most efficient solar cell. Not every dye is suitable with every other dye and special dye combinations can improve the adhesion of another dye.

Panchromatic cells can help to improve solar cell efficiencies compared to single junctions. The advantage over stacked multi junction cells with different single absorbers at each cell part might be less light loss through the electrodes and interfaces. But the optimization procedures are better scalable with isolated single junctions stacked into a multi junction, also due to the possibility to use the perfect suiting thicknesses of absorber layers for each junction.

F. Ruthenium dyes

F.1. Ruthenium dyes

Ruthenium-based dyes are very well known for its use in DSSC. Grätzel et al. had been investigated Ruthenium for a long time (year 1979 [112]) before O'Regan and Grätzel found out the ability in connection with nanocrystalline TiO_2 films in DSSC, DSSC are therefore also called Grätzel cells (year 1991 [148]). Further investigations with ruthenium as sensitizer in DSSCs followed, including the use of different anchors than carboxyl anchors for ruthenium dyes (for example catechol anchors, year 2000 [162] or added sulfonyl groups [49]) or using a polymer gel electrolyte instead of a liquid electrolyte resulting in a quasi-solid state DSSC (year 2003 [210]). Very high efficiencies were achieved for a ruthenium single junction (for example in year 1993 [145] 10%, year 2008 [60] 10.53%, year 2009 [27] 11.5%), thus also investigating the influence of co-absorbents (year 2012 [74] 11.4%).

Phil Rosenow, Group Roling, University of Marburg, gives a good overview of the use of ruthenium dyes in Grätzel solar cells and the independent construction of complete Grätzel cells in his bachelor thesis ([167]).

First, an investigation of the solid state effects is important, this is shown below with N719. In the section F.2 on time-resolved photoluminescence measurements on ruthenium (N3 and N719) the PL decay behavior, which is significantly slower than that of indolines, is explained.

The ruthenium dyes investigations presented in this work are for N3 and N719, see the chemical structure in Fig. F.1. More ruthenium dyes (N3, N719, N712, N749) were investigated in solution, dropcasted on different substrates and on mesoporous TiO_2 in the framework of a student project work, some results are explained here in the following list.

- the lowest absorption peaks of N3 and 719 in ethanol solution result in 535nm and 526 nm and the photoluminescence is 782 nm and 754 nm, respectively. From these results it can be deduced that the deprotonation of the N3 molecule leads to a blue shift.
- Comparing solution to layer absorption spectra, a broadening of absorption spectra occurs which might be due to agglomerations.
- In photoluminescence, a variance of Peak maxima occurs with redshifts probably due to agglomerations; the more agglomerations, the more redshifted is the PL.

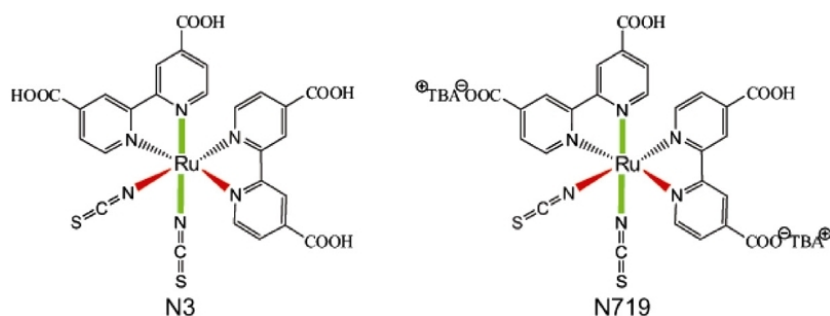


Fig. F.1.: Chemical structure of N3 and N719 taken from Chen et al.[28]. The difference between N719 and N3 is the deprotonation bei tert-Butyl alcohol (TBA) which leads to a slight blueshift in absorption and PL for N719.

Another effect has to be kept in mind when comparing solution and solid spectra. A chemical shift was detected for N719 in different solvents, see more explanations about chemical shift in section 4.1.1.

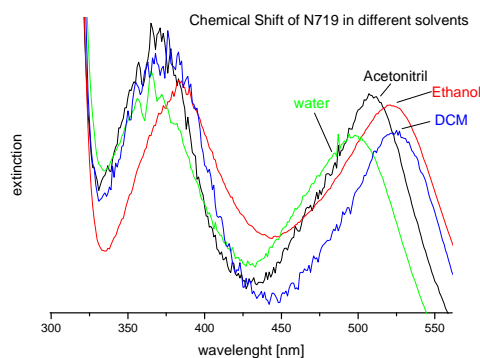


Fig. F.2.: Chemical Shift of N719 absorption in different solvents. The position of the lowest energy peak is between 495 nm (2.51 eV) and 530 nm (2.34 eV), resulting in a chemical shift of about 170 meV.

F.1.1. Solid formation for Ruthenium dye N719

Fig. F.3 shows the absorption and photoluminescence of ruthenium dye N719 in solution and drop casted on glass. Furthermore, the photoluminescence of soaked N719 in TiO₂(meso) is shown. When drop casted on flat rutile TiO₂(110), besides the known photoluminescence a sharp peak occurs at higher energies.

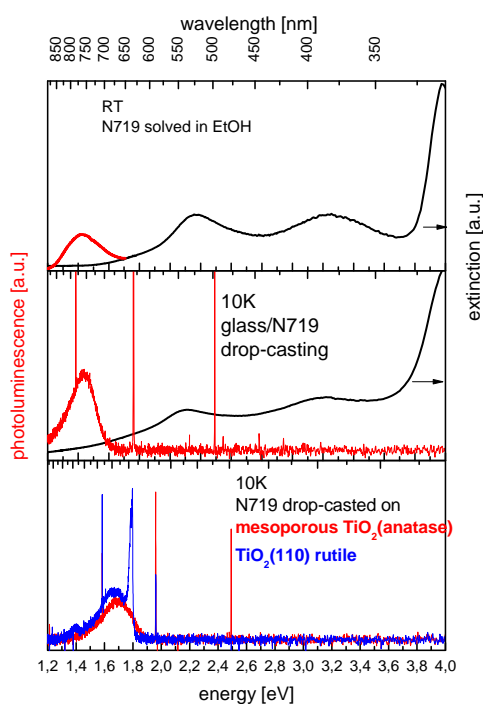


Fig. F.3.: N179 PL and absorption spectra in solution and drop casted on flat substrate cover glass. PL of soaking in $\text{TiO}_2(\text{meso})$ and drop casting on rutile $\text{TiO}_2(110)$ are also shown.

In the following Fig. F.4 the photoluminescences are shown in one graph for a better comparability. The PL of solid layers on flat substrates as glass or $\text{TiO}_2(110)$ are slightly red shifted compared with the PL on mesoporous TiO_2 . This indicates a molecular PL on $\text{TiO}_2(\text{meso})$ and an influence of solid formation for PL on solids. The sharp peak at higher energy on $\text{TiO}_2(110)$ is clearly added to the PL on glass, without showing this sharp peak on glass.

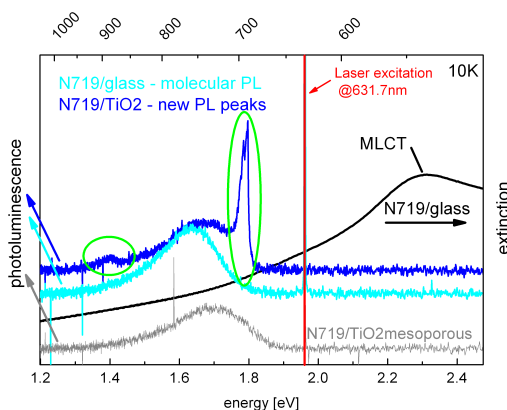


Fig. F.4.: For a better comparability of N179 PL spectra the PL of N719 in solution and drop casted on flat substrates cover glass and $\text{TiO}_2(110)$ is shown in one single graph. The occurring sharp PL peak at about 690 nm is probably due to crystal formation.

The $\text{TiO}_2(110)$ sample is investigated thoroughly in order to solve the PL differences. As can be seen in Fig. F.5 the sharp PL at about 690 nm might be due to exciton formation at 660 nm. This sharp PL is occurring only in crystalline solid and not amorphous structures, therefore the PL only exists on the more crystalline solid layer on flat $\text{TiO}_2(110)$.

In order to prove that the sharp PL peak belongs to crystalline N719, various positions on the $\text{TiO}_2(110)$ sample were investigated in absorption and PL. Fig. F.5 shows different absorptions with different positions on the sample, revealing a new band formation probably due to exciton formation in crystalline N719. Fig. F.6 shows the PL results, interestingly a PL spectrum without molecular PL could be found. The deep PL at about 870 nm (1.42 eV) is only occurring together with the sharp PL peak at 690 nm (1.8 eV), therefore the deeper PL peak is probably also due to crystal formation (see also D131 on ZnO(meso), where the deep trap PL is correlated with powder PL, see appendix C.2). Yet, it should be verified in further experiments on samples not allowing charge transfer (for example on flat SiO_2) if the deep trap forming 380 meV below the sharp excitonic PL is due to a solid PL or to a type II recombination from $\text{TiO}_2(110)$ to N719.

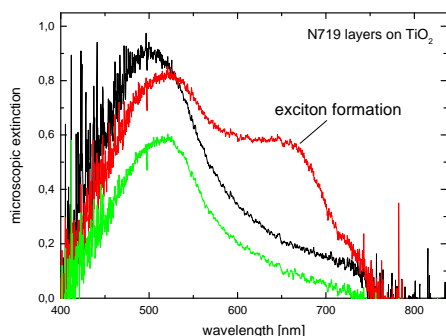


Fig. F.5.: Absorption of N719 on $\text{TiO}_2(110)$. Different positions on the layer produced by drop casting are investigated. If a crystal spot is hit, excitonic solid PL occurs.

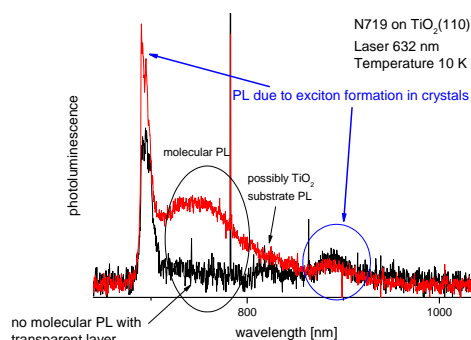


Fig. F.6.: PL of N719 layers on $\text{TiO}_2(110)$. The blue marked deep PL is probably not a type II recombination, but a PL due to exciton formation in crystals, because this deep PL is only occurring together with the sharp high energetic PL peak on crystals.

In consequence it can be deduced that two solid PL exist, the amorphous PL and the crystalline PL. Fig. F.7 summarizes the PL results. While the PL of N719 powder is red shifted to the solid PL on glass due to higher trap formation, the PL on $\text{TiO}_2(\text{meso})$ probably shows dominantly molecular PL, chemical shift and molecular PL lead to a blue shift. The PL on flat substrate $\text{TiO}_2(110)$ shows the crystalline PL in combination with amorphous layer PL. A small crystalline PL peak is also detected for N719 powder revealing a small proportion of crystals also in N719 powder.

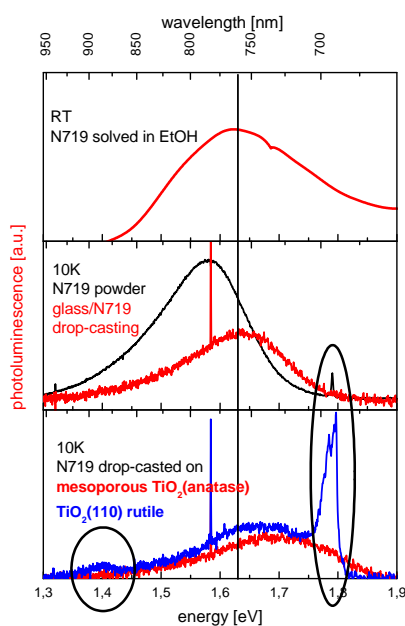


Fig. F.7.: Comparison of photoluminescence of ruthenium dye N719 in solution, as powder and drop casted on different substrates. The sharp peak at about 690 nm on $\text{TiO}_2(110)$ can also be seen as a tiny peak in the powder PL, its origin are N719 crystals.

In Fig. F.8 the diffusive reflection spectra of N719 is shown together with the PL of a combination of crystal and amorphous layer. New absorption band formation can be seen precisely at energies suiting to the crystalline sharp peak, see marked rectangle.

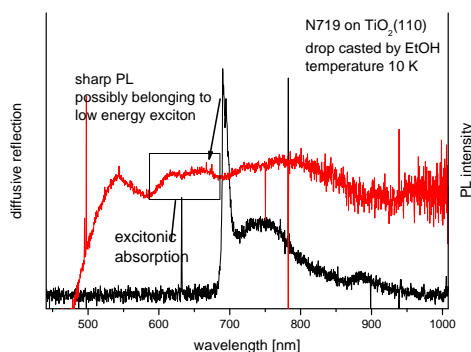


Fig. F.8.: Diffusive reflection of N719 on $\text{TiO}_2(110)$ indicates new absorption bands possibly due to exciton formation in solids.

It has to be mentioned that the crystalline PL seems to be very sensitive to laser power. In one experiment the crystalline PL could not be reproduced after the switching from 632 nm laser to 532 nm laser, possibly through warming effects. 632 nm laser seems to efficiently excite the excitonic absorption, while 532 nm is absorbed from the amorphous

or molecular N719. A use of 632 nm laser from start on and generally low laser power is recommended in further experiments with crystalline N719. For better spectral results new defined and more homogeneous layers of crystalline N719 should be prepared, if possible by OMBD, and investigated by 632 nm laser only at the beginning.

F.2. Ruthenium dyes in DSSC - TRPL

The ruthenium dyes N719 and N3 were investigated in TRPL. Theoretical basics for transfer processes of ruthenium dyes are explained for example in Listorti et al. [119]. In contrast to a purely organic dye the metal ruthenium atom allows a "intersystem crossing from the singlet to the triplet excited states on ultrafast time scales" (100 fs or faster) [119].

The simple injection of a singlet state which is explained for example in Listorti et al. [119], see Fig. 2.3, cannot be taken for ruthenium dyes due to this inter system crossing. Fig. 11 in [119] gives more insights into the details of processes between N719 and TiO_2 acceptor states. The following scheme F.9 illustrates the processes, taken from [109]. Triplet recombination times without injection are indicated as 10 ns in scheme F.9. 50 ns are indicated in degassed solvent [145] and 3-25 ns when absorbed on an inert substrate as ZrO_2 [198], such long times are revealed also by own ns-TRPL measurements (not shown here) of N3 and N719 in solution (EtOH) as about 33 ns.

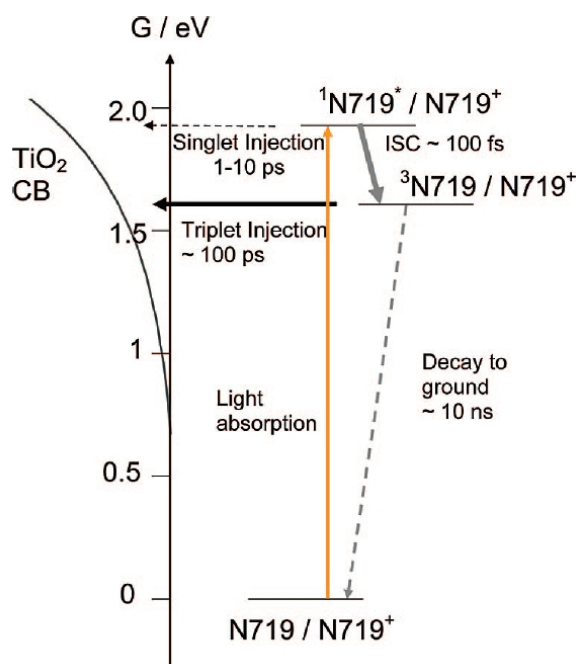


Fig. F.9.: Energetics and Kinetics of Electron Injection in a "Standard" DSSC, Focusing in Particular upon Comparison of Triplet versus Singlet Injection. Figure and caption taken from Koops et al. [109]

Injection times from singlet-state of ruthenium dyes into TiO_2 are in the time region of fs

to ps, this time range is too fast for the available ps-TRPL stage in this work. Transient absorption measurements reveal this time range for N719 [119] and N3 [13, 8]. Another loss channel for singlet PL is the conversion from singlet to triplet states, with faster conversion times than the injection times. This leads to triplet states as main injection states in N719 sensitized solar cells [119]. As triplet injection times are in the time region of 100 ps (150 ps from Haque et al. [75], indicated are half times $t_{50\%}$ which is close to $1/e$), those times should be measurable by the ps-TRPL stage used in this thesis. TRPL results can be found in literature, for example Koops et al. [109, 108]. Triplet injection times of N719 in complete solar cells with changing additive concentrations yield injection times between <60 ps and >500 ps (table 1 in [109], indicated are $t_{50\%}$).

First ps-TRPL measurements of N719 and N3 are shown in the following graphs, the evaluated spectra in Fig. F.10 and resulting ps-TRPL in Fig. F.11. The results should be verified in further measurements in future, yet some conclusions can be deduced also from the present measurements.

The times for N3 and N719 in solutions are very slow (approx. 33 ns measured in ns-TRPL measurements, not shown here), but the long times on the $\text{TiO}_2(\text{meso})$ are more of the order of 1 ns for the decay curves shown here and thus significantly faster than the decay in solution (see Fig. F.11). The reason might be not optimal soaking which leads to layer forming up also on $\text{TiO}_2(\text{meso})$, this results in a similar decay behavior to that on the cover glass for longer times (for times of approx. 300 ps and more, a parallel decay in the curves on the cover glass and on $\text{TiO}_2(\text{meso})$ can be seen). This assumption is supported by the fact that the PL spectra on $\text{TiO}_2(\text{meso})$ in Fig. F.10 also apparently have parts of the PL on cover glass. As shown in section F.1.1 for N719, the PL on cover glass with lower-energy than the PL on $\text{TiO}_2(\text{meso})$ is probably due to an amorphous layer that no longer shows pure molecular PL, but solid-state PL as a result of agglomerations. N3 on cover glass is slower than soaked in $\text{TiO}_2(\text{meso})$ in the first 300 ps, but declines almost as quickly in the first 50 ps as on $\text{TiO}_2(\text{meso})$. This is a result of concentration quenching, since on cover glass the fast decay cannot be a due to charge transfer. The visible faster decay on $\text{TiO}_2(\text{meso})$ in the first 150 ps is only partially the result of concentration quenching, since the spectra clearly show a strong part of molecular PL possibly without agglomerations. It is therefore mainly due to the charge transfer. The order of magnitude from the literature is confirmed with 100 to 150 ps injection time.

The spectra on $\text{TiO}_2(\text{meso})$ show that N3 is slightly red shifted against N719, this was expected from cw-measurements, see section F.1. The lower level alignment of N3 is reflected in the slightly slower decay on $\text{TiO}_2(\text{meso})$. Interestingly, Haque et al. [75] indicate a faster transfer for N3 in comparison with N719 regarding the ultrafast transfer measured by TAS measurements, which would be contrary to the ps-TRPL results; this should be investigated and discussed in a further more detailed measurement row.

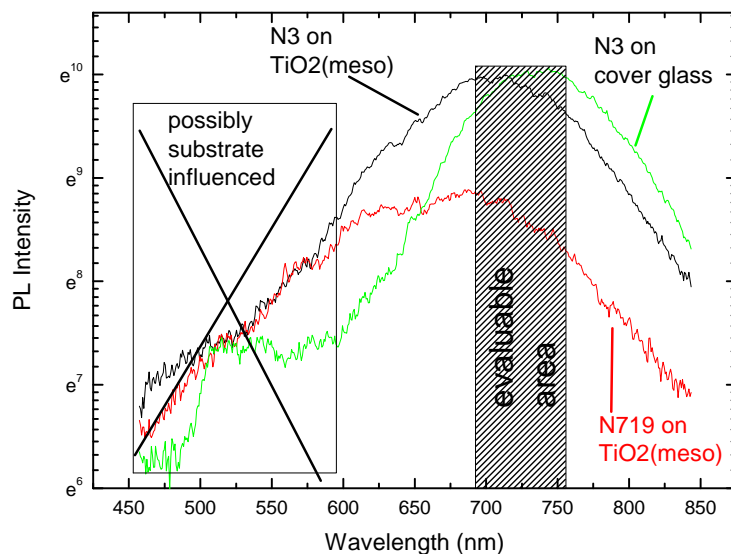


Fig. F.10.: PL spectra from ps-stage. Comparison of N3 with N719 on $\text{TiO}_2(\text{meso})$. N3 is slightly red shifted against N719, as expected from literature.

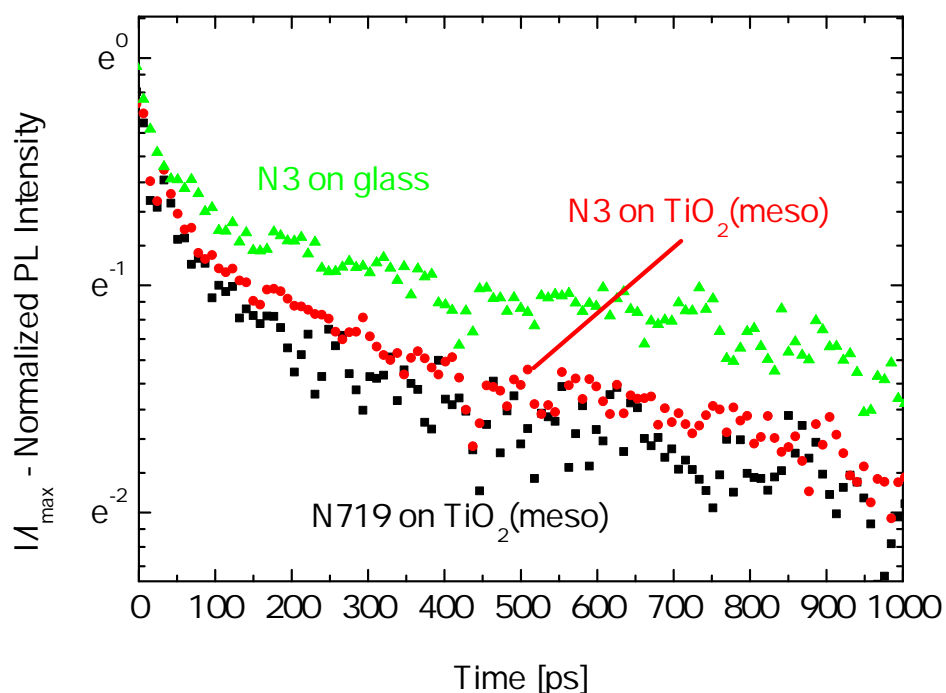


Fig. F.11.: Resulting PL decay of N3 and N719 from spectra in Fig. F.10. The long times are influenced by layer formation or agglomerations. Interestingly, the long decay times both on cover glass and $\text{TiO}_2(\text{meso})$ are equal which is possibly due to an amount of agglomerations forming up also on $\text{TiO}_2(\text{meso})$. The visible faster decay in the first 150 ps indicates a charge transfer on $\text{TiO}_2(\text{meso})$.

Discussion Transfer from triplet states should not be slower towards the semiconductor conduction band than from singlet states. According to that the transfer from the triplet state of ruthenium dyes is actually rather slow with decay times of 100 to 150 ps. In literature this is discussed regarding the yet very efficient ruthenium sensitized DSSC, see [75]. Slow times don't have to be an indicator of bad cells, there just has to be a big difference between injection time and internal decay: "We conclude that optimum DSSC device performance is obtained when the charge separation kinetics are just fast enough to compete successfully with the dye excited-state decay [75]".

Further investigations of Ruthenium based charge transfer processes should include a systematic optimization of layer preparation and soaking procedures. A detailed literature research should be performed in order to be able to discuss in detail the effects at the interface between ruthenium dye and inorganic semiconductor, see for example [28]. Voltage dependant TRPL measurements should be performed on processed solar cells, some results can already be found in literature [149, 109, 185] as a starting point; the dynamics are relatively modest, see [109], here a preparation with dried electrolyte should be tested in own experiments.

Interestingly, regarding ruthenium dyes, is the occurrence of different TRPL behavior for different distance chains. The PL of the ruthenium dye Z907 with added chains decays extremely much slower than without added chains at N719 [108], presumably because the transfer is more difficult due to the distance (less electronic coupling), see also [9] or the performed investigations on Indoline dyes with different anchor lengths in chapter 6.1 and resulting publication [131].

G. Type II Absorption for Catechol on TiO₂(meso) revealed by IPCE - also for RK1?

Further methods are meaningful for a better understanding of processes at the interface and in order to clarify and confirm the level alignment between organic material and semiconductor.

Regarding RK1 discussed in section 6.3.2, in addition to cyclic voltammetry measurements and IPCE measurements, Joly et al. performed DFT calculations, the resulting molecular orbital energy diagram and iso density plots of HOMO and LUMO are shown in picture G.2. The calculated HOMO-LUMO bandgap of RK1 is about 2 eV (620 nm), this fits quite well to the absorption in solution beginning at about 620 nm (see Fig. 6.51). On mesoporous TiO₂ only a slight broadening of the absorption spectrum in comparison to in solution is expected, this is assumed from the behavior of indoline dyes.

This raises the question why a current is produced down to 700 nm where no optical absorption exists. Interestingly, the calculated absorption from RK1 HOMO into the conduction band of TiO₂(meso) by DFT would be 1.78 eV (about 700 nm), see picture G.2, which would suit to the 700 nm absorption. It has to be mentioned also that a new shoulder peak occurs at 600 nm in the IPCE spectrum which is not visible in the absorption spectrum in solution. Both facts, the new low energy absorption and the new shoulder, point to the assumption that a Type II injection might occur in the red part between 550 and 700 nm. This would imply a charge transfer directly from RK1 HOMO into TiO₂ as also discussed for Alizarin in appendix B.2, Fig. B.6. Such a dye-to-TiO₂ charge-transfer (DTCT) by a type II absorption should be visible also in optical absorption spectra of RK1 on TiO₂(meso) as shown in Fig. G.5 and G.6 for the chemical structures G.3 and G.4, respectively (Fig. taken from [199]). Absorption on TiO₂(meso) and IPCE spectrum resemble each other [199]. Further molecules with catecholate anchors are investigated in [199] and all investigated molecules show type II injection on TiO₂(meso), revealed by absorption and IPCE measurements.

The type II absorption for RK1 has to be verified and investigated in future measurements. If a type II injection is revealed here for RK1 with its carboxylate anchoring, this would be different from the shown type II injection of catecholate anchoring of Tae et al. [199].

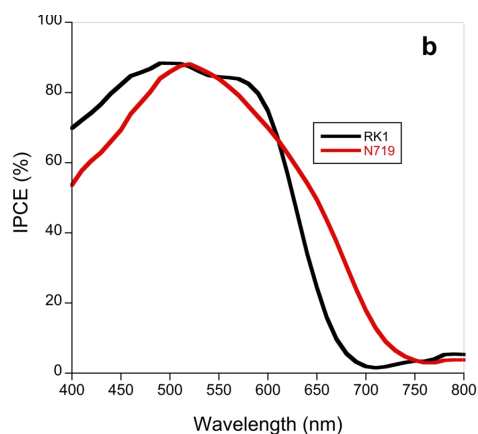


Fig. G.1.: IPCE (incident photon conversion efficiency) spectrum of RK1 und N719. In comparison to absorption spectra (Fig. 6.51) a clear new red absorption occurs for RK1 below 2 eV (620 nm), without this new absorption no current could be produced at lower energies than the optical absorption at 620 nm. For N719 the absorption band gap stays the same in solution and for IPCE measurements (750 nm). Figure taken from Joly et al. [95]. It has to be clarified if this indicates a Type II injection from RK1 directly into the conduction band of $\text{TiO}_2(\text{meso})$.

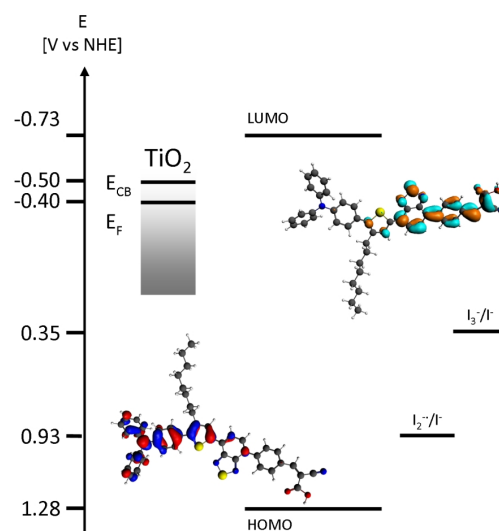
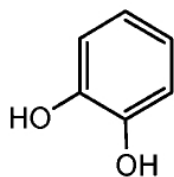


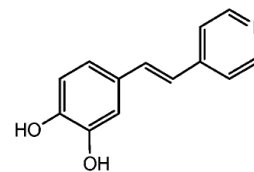
Fig. G.2.: The calculated molecular orbital energy diagram for RK1, along with iso density plots of the HOMO and LUMO. Figure taken from [95].

Joly et al. also measured the electron density in the conduction band of $\text{TiO}_2(\text{meso})$ during illumination of the solar cells and revealed a higher electron density if RK1 is the injecting dye in comparison to N719. In general, for a similar IPCE spectrum of two dyes excluding type II injection, a faster charge transfer should lead to higher electron density in the conduction band of $\text{TiO}_2(\text{meso})$. This method can therefore deliver additional information about how fast the charge transfer occurs, in this case RK1 would have a faster charge transfer than N719. The measured TRPL curves support this result (see Fig. F.11 and 6.57).



Catechol (Cat)

Fig. G.3.: Chemical structure of Catechol (Cat), taken from [199].



Cat-v-P

Fig. G.4.: Chemical structure of Catechol-v-P (Cat-v-P), taken from [199].

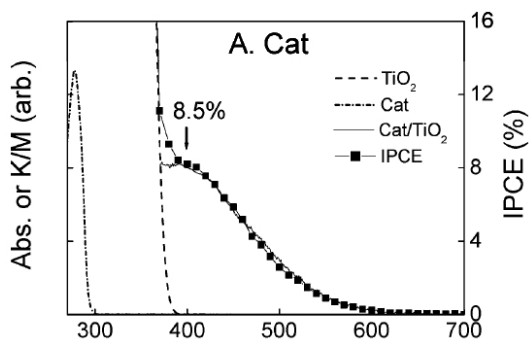


Fig. G.5.: IPCE (incident photon conversion efficiency) and absorption spectrum of Cat on TiO₂(meso) compared with absorption of Cat in solution (Acetonitril). TiO₂(meso) is measured in diffusive reflection. In the soaking in TiO₂(meso) a clear new absorption occurs at lower energies for Cat below TiO₂(meso) absorption which cannot be due to the molecular absorption but has its origin in a direct type II injection from dye to semiconductor. IPCE measurements of the processed solar cell (0.6% efficiency) confirm this absorption. Fig. taken from Tae et al. [199].

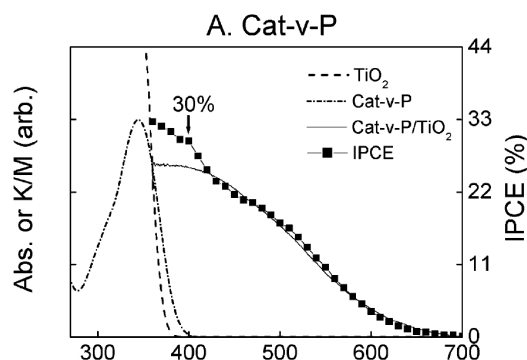


Fig. G.6.: IPCE (incident photon conversion efficiency) and absorption spectrum of Cat-v-P on TiO₂(meso) compared with absorption of Cat-v-P in solution (Acetonitril). TiO₂(meso) is measured in diffusive reflection. In the soaking in TiO₂(meso) a clear new absorption occurs at lower energies for Cat-v-P below TiO₂(meso) absorption which cannot be due to the molecular absorption but has its origin in a direct type II injection from dye to semiconductor. IPCE measurements of the processed solar cell (1.1% efficiency) confirm this absorption. Fig. taken from Tae et al. [199].

Bibliography

- [1] M. Adineh, P. Tahay, A. Shahrjerdi, S. S. H. Davarani, and N. Safari. Dye-sensitized solar cells, based on electrochemically functionalized porphyrins. *Journal of the Iranian Chemical Society*, 13(7):1357–1365, 2016.
- [2] C. Ambrosch-Draxl, D. Nabok, P. Puschnig, and C. Meisenbichler. The role of polymorphism in organic thin films: oligoacenes investigated from first principles. *New J. Phys.*, 11(12):125010, 2009.
- [3] B.-K. An, W. Hu, P. L. Burn, and P. Meredith. New type ii catechol-thiophene sensitizers for dye-sensitized solar cells. *The Journal of Physical Chemistry C*, 114(41):17964–17974, 2010.
- [4] F. Anger, J. Ossó, U. Heinemeyer, K. Broch, R. Scholz, A. Gerlach, and F. Schreiber. Photoluminescence spectroscopy of pure pentacene, perfluoropentacene, and mixed thin films. *The Journal of chemical physics*, 136(5):054701, 2012.
- [5] J. A. Anta, E. Guillén, and R. Tena-Zaera. Zno-based dye-sensitized solar cells. *The Journal of Physical Chemistry C*, 116(21):11413–11425, 2012.
- [6] J. E. Anthony. The larger acenes: versatile organic semiconductors. *Angew. Chem. Int. Ed.*, 47(3):452–483, 2008.
- [7] J. Arbiol, C. Magen, P. Becker, G. Jacopin, A. Chernikov, S. Schäfer, F. Furtmayr, M. Tchernycheva, L. Rigutti, J. Teubert, et al. Self-assembled gan quantum wires on gan/aln nanowire templates. *Nanoscale*, 4(23):7517–7524, 2012.
- [8] J. B. Asbury, R. J. Ellingson, H. N. Ghosh, S. Ferrere, A. J. Nozik, and T. Lian. Femtosecond ir study of excited-state relaxation and electron-injection dynamics of ru (dcbpy) 2 (ncs) 2 in solution and on nanocrystalline tio2 and al2o3 thin films. *The Journal of Physical Chemistry B*, 103(16):3110–3119, 1999.
- [9] J. B. Asbury, E. Hao, Y. Wang, and T. Lian. Bridge length-dependent ultrafast electron transfer from re polypyridyl complexes to nanocrystalline tio2 thin films studied by femtosecond infrared spectroscopy. *The Journal of Physical Chemistry B*, 104(50):11957–11964, 2000.
- [10] A. A. Bakulin, A. Rao, V. G. Pavelyev, P. H. van Loosdrecht, M. S. Pshenichnikov, D. Niedzialek, J. Cornil, D. Beljonne, and R. H. Friend. The role of driving energy and delocalized states for charge separation in organic semiconductors. *Science*, 335(6074):1340–1344, 2012.
- [11] N. Bansal, L. X. Reynolds, A. MacLachlan, T. Lutz, R. S. Ashraf, W. Zhang, C. B. Nielsen, I. McCulloch, D. G. Rebois, T. Kirchartz, et al. Influence of crystallinity and energetics on charge separation in polymer–inorganic nanocomposite films for

- solar cells. *Scientific reports*, 3:1531, 2013.
- [12] V. Belova, P. Beyer, E. Meister, T. Linderl, M.-U. Halbich, M. Gerhard, S. Schmidt, T. Zechel, T. Meisel, A. V. Generalov, et al. Evidence for anisotropic electronic coupling of charge transfer states in weakly interacting organic semiconductor mixtures. *Journal of the American Chemical Society*, 139(25):8474–8486, 2017.
- [13] G. Benkő, J. Kallioinen, J. E. Korppi-Tommola, A. P. Yartsev, and V. Sundström. Photoinduced ultrafast dye-to-semiconductor electron injection from nonthermalized and thermalized donor states. *Journal of the American Chemical Society*, 124(3):489–493, 2002.
- [14] P. Berdowski, R. Van Mens, and G. Blasse. Energy migration in a quasi-two-dimensional system: Eu₂O₂SO₄. *J. Lumin.*, 33(2):147–158, 1985.
- [15] T. C. Berkelbach, M. S. Hybertsen, and D. R. Reichman. Microscopic theory of singlet exciton fission. iii. crystalline pentacene. *J. Chem. Phys.*, 141(7):074705, 2014.
- [16] T. Bessho, S. M. Zakeeruddin, C.-Y. Yeh, E. W.-G. Diau, and M. Grätzel. Highly efficient mesoscopic dye-sensitized solar cells based on donor–acceptor-substituted porphyrins. *Angewandte Chemie*, 122(37):6796–6799, 2010.
- [17] S. Blumstengel, S. Sadofev, C. Xu, J. Puls, R. Johnson, H. Glowatzki, N. Koch, and F. Henneberger. Electronic coupling in organic-inorganic semiconductor hybrid structures with type-ii energy level alignment. *Physical Review B*, 77(8):085323, 2008.
- [18] M. Borgwardt, M. Wilke, T. Kampen, S. Mähl, M. Xiao, L. Spiccia, K. M. Lange, I. Y. Kiyan, and E. F. Aziz. Charge transfer dynamics at dye-sensitized zno and tio₂ interfaces studied by ultrafast xuv photoelectron spectroscopy. *Scientific reports*, 6:24422, 2016.
- [19] I. P. M. Bouchoms, W. A. Schoonveld, J. Vrijmoeth, and T. M. Klapwijk. Morphology identification of the thin film phases of vacuum evaporated pentacene on SiO₂ substrates. *Synth. Met.*, 104(3):175, 1999.
- [20] K. Broch, M. Gerhard, M. Halbich, S. Lippert, V. Belova, M. Koch, and F. Schreiber. Time-resolved photoluminescence spectroscopy of charge transfer states in blends of pentacene and perfluoropentacene. *physica status solidi (RRL)–Rapid Research Letters*, 11(7):1700064, 2017.
- [21] W. Brütting. Introduction to the physics of organic semiconductors. *Physics of Organic Semiconductors*, pages 1–14, 2005.
- [22] A. Burshtein. Energy transfer kinetics in disordered systems. *J. Lumin.*, 34(4):167–188, 1985.
- [23] R. Campbell, J. M. Robertson, and J. Trotter. The crystal structure of hexacene, and a revision of the crystallographic data for tetracene. *Acta Crystallogr.*, 15(3):289–290, 1962.
- [24] Y. Cao, Y. Saygili, A. Ummadisingu, J. Teuscher, J. Luo, N. Pellet, F. Giordano, S. M. Zakeeruddin, J.-E. Moser, M. Freitag, et al. 11% efficiency solid-state

- dye-sensitized solar cells with copper (ii/i) hole transport materials. *Nature Communications*, 8:15390, 2017.
- [25] J. S. Castrucci, M. G. Helander, G. E. Morse, Z.-H. Lu, C. M. Yip, and T. P. Bender. Charge carrier mobility in fluorinated phenoxy boron subphthalocyanines: Role of solid state packing. *Crystal Growth & Design*, 12(3):1095–1100, 2012.
- [26] W.-L. Chan, M. Ligges, A. Jailaubekov, L. Kaake, L. Miaja-Avila, and X.-Y. Zhu. Observing the multiexciton state in singlet fission and ensuing ultrafast multielectron transfer. *Science*, 334(6062):1541–1545, 2011.
- [27] C.-Y. Chen, M. Wang, J.-Y. Li, N. Pootrakulchote, L. Alibabaei, C.-h. Ngoc-le, J.-D. Decoppet, J.-H. Tsai, C. Graetzel, C.-G. Wu, et al. Highly efficient light-harvesting ruthenium sensitizer for thin-film dye-sensitized solar cells. *ACS nano*, 3(10):3103–3109, 2009.
- [28] J. Chen, J. Wang, F.-Q. Bai, L. Hao, Q.-J. Pan, and H.-X. Zhang. Connection style and spectroscopic properties: theoretical understanding of the interface between n749 and tio2 in dsscs. *Dyes and Pigments*, 99(1):201–208, 2013.
- [29] L. Chen, T. Niebling, W. Heimbrodt, D. Stichtenoth, C. Ronning, and P. Klar. Dimensional dependence of the dynamics of the mn 3 d 5 luminescence in (zn, mn) s nanowires and nanobelts. *Phys. Rev. B*, 76(11):115325, 2007.
- [30] H.-L. Cheng, X.-W. Liang, W.-Y. Chou, Y.-S. Mai, C.-Y. Yang, L.-R. Chang, and F.-C. Tang. Raman spectroscopy applied to reveal polycrystalline grain structures and carrier transport properties of organic semiconductor films: Application to pentacene-based organic transistors. *Organic Electronics*, 10(2):289–298, 2009.
- [31] H.-M. Cheng and W.-F. Hsieh. Electron transfer properties of organic dye-sensitized solar cells based on indoline sensitizers with zno nanoparticles. *Nanotechnology*, 21(48):485202, 2010.
- [32] A. A. Chernikov. *Time-resolved photoluminescence spectroscopy of semiconductors for optical applications beyond the visible spectral range*. PhD dissertation, 2012.
- [33] W. Chidawanyika, A. Ogunsipe, and T. Nyokong. Syntheses and photophysics of new phthalocyanine derivatives of zinc, cadmium and mercury. *New Journal of Chemistry*, 31(3):377–384, 2007.
- [34] J.-J. Cid, M. García-Iglesias, J.-H. Yum, A. Forneli, J. Albero, E. Martínez-Ferrero, P. Vazquez, M. Grätzel, M. K. Nazeeruddin, E. Palomares, et al. Structure–function relationships in unsymmetrical zinc phthalocyanines for dye-sensitized solar cells. *Chemistry–A European Journal*, 15(20):5130–5137, 2009.
- [35] J.-J. Cid, J.-H. Yum, S.-R. Jang, M. K. Nazeeruddin, E. Martínez-Ferrero, E. Palomares, J. Ko, M. Grätzel, and T. Torres. Molecular cosensitization for efficient panchromatic dye-sensitized solar cells. *Angewandte Chemie*, 119(44):8510–8514, 2007.
- [36] A. E. Colbert, E. M. Janke, S. T. Hsieh, S. Subramaniyan, C. W. Schlenker, S. A. Jenekhe, and D. S. Ginger. Hole transfer from low band gap quantum dots to conjugated polymers in organic/inorganic hybrid photovoltaics. *The Journal of*

- Physical Chemistry Letters*, 4(2):280–284, 2013.
- [37] N. Coppedè, E. Bonnini, F. Mezzadri, G. Tarabella, P. Ranzieri, L. Barba, G. Arrighetti, L. Lutterotti, and S. Iannotta. Structural and morphological phase control by supersonic beams on titanyle phthalocyanine: An investigation on the growth. *Organic Electronics*, 32:15–20, 2016.
- [38] P. Cudazzo, M. Gatti, and A. Rubio. Excitons in molecular crystals from first-principles many-body perturbation theory: Picene versus pentacene. *Phys. Rev. B*, 86(19):195307, 2012.
- [39] A. S. Davydov. The theory of molecular excitons. *Phys.-Usp.*, 7(2):145, 1964.
- [40] T. Del Cano, V. Parra, M. Rodriguez-Mendez, R. Aroca, and J. De Saja. Characterization of evaporated trivalent and tetravalent phthalocyanines thin films: Different degree of organization. *Applied surface science*, 246(4):327–333, 2005.
- [41] T. Dentani, Y. Kubota, K. Funabiki, J. Jin, T. Yoshida, H. Minoura, H. Miura, and M. Matsui. Novel thiophene-conjugated indoline dyes for zinc oxide solar cells. *New Journal of Chemistry*, 33(1):93–101, 2009.
- [42] D. L. Dexter. A theory of sensitized luminescence in solids. *J. Chem. Phys.*, 21(5):836–850, 1953.
- [43] M. Dressel, B. Gompf, D. Faltermeier, A. Tripathi, J. Pflaum, and M. Schubert. Kramers-kronig-consistent optical functions of anisotropic crystals: generalized spectroscopic ellipsometry on pentacene. *Opt. Express*, 16(24):19770–19778, 2008.
- [44] J. R. Durrant. Modulating interfacial electron transfer dynamics in dye sensitised nanocrystalline metal oxide films. *Journal of Photochemistry and Photobiology A: Chemistry*, 148(1-3):5–10, 2002.
- [45] J. R. Durrant, S. A. Haque, and E. Palomares. Towards optimisation of electron transfer processes in dye sensitised solar cells. *Coordination Chemistry Reviews*, 248(13-14):1247–1257, 2004.
- [46] R. Eiermann, G. Parkinson, H. Bässler, and J. Thomas. Structural investigations of amorphous tetracene and pentacene by low-temperature electron diffraction. *J. Phys. Chem.*, 87(4):544–551, 1983.
- [47] M. El-Nahass, H. Zeyada, M. Aziz, and N. El-Ghamaz. Structural and optical properties of thermally evaporated zinc phthalocyanine thin films. *Optical Materials*, 27(3):491–498, 2004.
- [48] A. El-Zohry, A. Orthaber, and B. Zietz. Isomerization and aggregation of the solar cell dye d149. *J. Phys. Chem. C*, 116(50):26144–26153, 2012.
- [49] S. Erten-Ela and K. Ocakoglu. Fabrication of thin film nanocrystalline tio2 solar cells using ruthenium complexes with carboxyl and sulfonyl groups. *Journal of Industrial and Engineering Chemistry*, 20(2):474–479, 2014.
- [50] M. Eyer, S. Sadofev, J. Puls, and S. Blumstengel. Charge transfer excitons at zn-mgo/p3ht heterojunctions: Relation to photovoltaic performance. *Applied Physics Letters*, 107(22):221602, 2015.
- [51] A. Facchetti. π -conjugated polymers for organic electronics and photovoltaic cell

- applications. *Chem. Mater.*, 23(3):733–758, 2010.
- [52] M. Fakis, P. Hrobárik, E. Stathatos, V. Giannetas, and P. Persephonis. A time resolved fluorescence and quantum chemical study of the solar cell sensitizer d149. *Dyes Pigm.*, 96(1):304–312, 2013.
- [53] M. Fakis, E. Stathatos, G. Tsigaridas, V. Giannetas, and P. Persephonis. Femtosecond decay and electron transfer dynamics of the organic sensitizer d149 and photovoltaic performance in quasi-solid-state dye-sensitized solar cells. *J. Phys. Chem. C*, 115(27):13429–13437, 2011.
- [54] J. Falgenhauer, C. Richter, H. Miura, and D. Schlottwein. Stable sensitization of zno by improved anchoring of indoline dyes. *ChemPhysChem*, 13(12):2893–2897, 2012.
- [55] D. Faltermeier, B. Gompf, M. Dressel, A. K. Tripathi, and J. Pflaum. Optical properties of pentacene thin films and single crystals. *Phys. Rev. B*, 74(12):125416, 2006.
- [56] A. Fattori, L. M. Peter, H. Wang, H. Miura, and F. Marken. Fast hole surface conduction observed for indoline sensitizer dyes immobilized at fluorine-doped tin oxide- tio2 surfaces. *J. Phys. Chem. C*, 114(27):11822–11828, 2010.
- [57] L. R. Faulkner. Effects of diffusion on resonance energy transfer. comparison of theory and experiment. *Chem. Phys. Lett.*, 43(3):552–556, 1976.
- [58] M. Fox. *Optical properties of solids*. AAPT, 2002.
- [59] M. Freitag, Q. Daniel, M. Pazoki, K. Sveinbjörnsson, J. Zhang, L. Sun, A. Hagfeldt, and G. Boschloo. High-efficiency dye-sensitized solar cells with molecular copper phenanthroline as solid hole conductor. *Energy & Environmental Science*, 8(9):2634–2637, 2015.
- [60] F. Gao, Y. Wang, J. Zhang, D. Shi, M. Wang, R. Humphry-Baker, P. Wang, S. M. Zakeeruddin, and M. Grätzel. A new heteroleptic ruthenium sensitizer enhances the absorptivity of mesoporous titania film for a high efficiency dye-sensitized solar cell. *Chemical communications*, (23):2635–2637, 2008.
- [61] M. García-Iglesias, J.-J. Cid, J.-H. Yum, A. Forneli, P. Vázquez, M. K. Nazeeruddin, E. Palomares, M. Grätzel, and T. Torres. Increasing the efficiency of zinc-phthalocyanine based solar cells through modification of the anchoring ligand. *Energy & Environmental Science*, 4(1):189–194, 2011.
- [62] M. García-Iglesias, J.-H. Yum, R. Humphry-Baker, S. M. Zakeeruddin, P. Péchy, P. Vázquez, E. Palomares, M. Grätzel, M. K. Nazeeruddin, and T. Torres. Effect of anchoring groups in zinc phthalocyanine on the dye-sensitized solar cell performance and stability. *Chemical Science*, 2(6):1145–1150, 2011.
- [63] M. Gerhard, A. P. Arndt, I. A. Howard, A. Rahimi-Iman, U. Lemmer, and M. Koch. Temperature-and energy-dependent separation of charge-transfer states in ptb7-based organic solar cells. *The Journal of Physical Chemistry C*, 119(51):28309–28318, 2015.
- [64] K. Ghosh, J. Hegarty, and D. Huber. Theory of donor fluorescence in the diffusion limit. *Phys. Rev. B*, 22(6):2837, 1980.

- [65] J. Götzen and G. Witte. Rapid preparation of highly ordered ultraflat ZnO surfaces. *Appl. Surf. Sci.*, 258(24):10144–10147, 2012.
- [66] M. Grätzel. Photoelectrochemical cells. *Nature*, 414:338344, 2001.
- [67] M. Grätzel. Solar energy conversion by dye-sensitized photovoltaic cells. *Inorg. Chem.*, 44(20):6841–6851, 2005.
- [68] M. Grätzel and A. Hagfeldt. Molecular photovoltaics. *Acc. Chem. Res.*, 33(5):269–277, 2000.
- [69] S. Haas, B. Batlogg, C. Besnard, M. Schiltz, C. Kloc, and T. Siegrist. Large uniaxial negative thermal expansion in pentacene due to steric hindrance. *Phys. Rev. B*, 76(20):205203, 2007.
- [70] I. Haeldermans, K. Vandewal, W. Oosterbaan, A. Gadisa, J. Dhaen, M. Van Bael, J. Manca, and J. Mullens. Ground-state charge-transfer complex formation in hybrid poly (3-hexyl thiophene): titanium dioxide solar cells. *Applied Physics Letters*, 93(22):431, 2008.
- [71] A. Hagfeldt, G. Boschloo, L. Sun, L. Kloo, and H. Pettersson. Dye-sensitized solar cells. *Chemical reviews*, 110(11):6595–6663, 2010.
- [72] A. Hagfeldt and M. Grätzel. Light-induced redox reactions in nanocrystalline systems. *Chemical reviews*, 95(1):49–68, 1995.
- [73] H. Haken and H. C. Wolf. *Atomic and quantum physics: an introduction to the fundamentals of experiment and theory*. Springer Science & Business Media, 2012.
- [74] L. Han, A. Islam, H. Chen, C. Malapaka, B. Chiranjeevi, S. Zhang, X. Yang, and M. Yanagida. High-efficiency dye-sensitized solar cell with a novel co-adsorbent. *Energy & Environmental Science*, 5(3):6057–6060, 2012.
- [75] S. A. Haque, E. Palomares, B. M. Cho, A. N. Green, N. Hirata, D. R. Klug, and J. R. Durrant. Charge separation versus recombination in dye-sensitized nanocrystalline solar cells: the minimization of kinetic redundancy. *Journal of the American Chemical Society*, 127(10):3456–3462, 2005.
- [76] J. He, G. Benkő, F. Korodi, T. Polívka, R. Lomoth, B. Åkermark, L. Sun, A. Hagfeldt, and V. Sundström. Modified phthalocyanines for efficient near-ir sensitization of nanostructured tio2 electrode. *Journal of the American Chemical Society*, 124(17):4922–4932, 2002.
- [77] R. He, X. Chi, A. Pinczuk, D. Lang, and A. Ramirez. Extrinsic optical recombination in pentacene single crystals: Evidence of gap states. *Applied Physics Letters*, 87(21):211117, 2005.
- [78] X. He, G. Zhu, J. Yang, H. Chang, Q. Meng, H. Zhao, X. Zhou, S. Yue, Z. Wang, J. Shi, et al. Photogenerated intrinsic free carriers in small-molecule organic semiconductors visualized by ultrafast spectroscopy. *Scientific reports*, 5:17076, 2015.
- [79] B. Heidelmeier. Optische spektroskopie an anthrachinon-derivaten. Master’s thesis, 2015.
- [80] J. Helzel. *Wechselwirkungen im organisch anorganischen Halbleiterhybridsystem*

- Pentacen Zinkoxid*. Diploma thesis, University Marburg, 2011.
- [81] J. Helzel, S. Jankowski, M. El Helou, G. Witte, and W. Heimbrodt. Temperature dependent optical properties of pentacene films on zinc oxide. *Appl. Phys. Lett.*, 99(21):211102, 2011.
- [82] N. J. Hestand, H. Yamagata, B. Xu, D. Sun, Y. Zhong, A. R. Harutyunyan, G. Chen, H.-L. Dai, Y. Rao, and F. C. Spano. Polarized absorption in crystalline pentacene: Theory vs experiment. *J. Phys. Chem. C*, 119(38):22137–22147, 2015.
- [83] A. Hinderhofer, U. Heinemeyer, A. Gerlach, S. Kowarik, R. M. Jacobs, Y. Sakamoto, T. Suzuki, and F. Schreiber. Optical properties of pentacene and perfluoropentacene thin films. *J. Chem. Phys.*, 127(19):194705, 2007.
- [84] N. Hofeditz. Electrooptical investigation of dye sensitized solar cells. Bachelor thesis, University Marburg, 2016.
- [85] D. Holmes, S. Kumaraswamy, A. J. Matzger, and K. P. C. Vollhardt. On the nature of nonplanarity in the [n] phenylenes. *Chem. Eur. J.*, 5(11):3399–3412, 1999.
- [86] T. Horiuchi, H. Miura, K. Sumioka, and S. Uchida. High efficiency of dye-sensitized solar cells based on metal-free indoline dyes. *J. Am. Chem. Soc.*, 126(39):12218–12219, 2004.
- [87] A. Hoshino, Y. Takenaka, and H. Miyaji. Redetermination of the crystal structure of α -copper phthalocyanine grown on kcl. *Acta Crystallographica Section B: Structural Science*, 59(3):393–403, 2003.
- [88] Y. Hosoi, D. M. Deyra, K. Nakajima, and Y. Furukawa. Micro-raman spectroscopy on pentacene thin-film transistors. *Molecular Crystals and Liquid Crystals*, 491(1):317–323, 2008.
- [89] W. H. Howie, F. Claeysens, H. Miura, and L. M. Peter. Characterization of solid-state dye-sensitized solar cells utilizing high absorption coefficient metal-free organic dyes. *J. Am. Chem. Soc.*, 130(4):1367–1375, 2008.
- [90] D. Huber. Fluorescence in the presence of traps. *Phys. Rev. B*, 20(6):2307, 1979.
- [91] K. Hümmer. Interband magnetoreflexion of zno. *Phys. Status Solidi B*, 56(1):249–260, 1973.
- [92] T. Ikeuchi, H. Nomoto, N. Masaki, M. J. Griffith, S. Mori, and M. Kimura. Molecular engineering of zinc phthalocyanine sensitizers for efficient dye-sensitized solar cells. *Chemical Communications*, 50(16):1941–1943, 2014.
- [93] S. Ito, S. M. Zakeeruddin, R. Humphry-Baker, P. Liska, R. Charvet, P. Comte, M. K. Nazeeruddin, P. Péchy, M. Takata, H. Miura, S. Uchida, and M. Grätzel. High-efficiency organic-dye-sensitized solar cells controlled by nanocrystalline-tio2 electrode thickness. *Adv. Mater.*, 18(9):1202–1205, 2006.
- [94] E. M. Johansson, M. Hedlund, H. Siegbahn, and H. Rensmo. Electronic and molecular surface structure of ru (tcterpy)(ncs) 3 and ru (dcbpy) 2 (ncs) 2 adsorbed from solution onto nanostructured tio2: a photoelectron spectroscopy study. *The Journal of Physical Chemistry B*, 109(47):22256–22263, 2005.

- [95] D. Joly, L. Pellejà, S. Narbey, F. Oswald, J. Chiron, J. N. Clifford, E. Palomares, and R. Demadrille. A robust organic dye for dye sensitized solar cells based on iodine/iodide electrolytes combining high efficiency and outstanding stability. *Scientific reports*, 4:4033, 2014.
- [96] R. Jose, A. Kumar, V. Thavasi, and S. Ramakrishna. Conversion efficiency versus sensitizer for electrospun tio2 nanorod electrodes in dye-sensitized solar cells. *Nanotechnology*, 19(42):424004, 2008.
- [97] C. Jundt, G. Klein, B. Sipp, J. Le Moigne, M. Joucla, and A. Villaeys. Exciton dynamics in pentacene thin films studied by pump-probe spectroscopy. *Chem. Phys. Lett.*, 241(1):84–88, 1995.
- [98] H. Kalt. General properties. In *Optical Properties. Part 2*, pages 1–5. Springer, 2004.
- [99] P. V. Kamat, I. Bedja, S. Hotchandani, and L. K. Patterson. Photosensitization of nanocrystalline semiconductor films. modulation of electron transfer between excited ruthenium complex and sno2 nanocrystallites with an externally applied bias. *J. Phys. Chem.*, 100(12):4900–4908, 1996.
- [100] N. Karl. Charge carrier transport in organic semiconductors. *Synth. Met.*, 133:649–657, 2003.
- [101] N. Karl and J. Marktanner. Electron and hole mobilities in high purity anthracene single crystals. *Molecular Crystals and Liquid Crystals Science and Technology. Section A. Molecular Crystals and Liquid Crystals*, 355(1):149–173, 2001.
- [102] H. E. Katz and J. Huang. Thin-film organic electronic devices. *Annu. Rev. Mater. Res.*, 39:71–92, 2009.
- [103] J. Kim and S. Yim. Influence of surface morphology evolution of subpc layers on the performance of subpc/c60 organic photovoltaic cells. *Applied Physics Letters*, 99(19):248, 2011.
- [104] J. Y. Kim, Y. H. Kim, and Y. S. Kim. Indoline dyes with various acceptors for dye-sensitized solar cells. *Curr. Appl. Phys.*, 11(1):S117–S121, 2011.
- [105] M. Kimura, H. Nomoto, H. Suzuki, T. Ikeuchi, H. Matsuzaki, T. N. Murakami, A. Furube, N. Masaki, M. J. Griffith, and S. Mori. Molecular design rule of phthalocyanine dyes for highly efficient near-ir performance in dye-sensitized solar cells. *Chemistry—A European Journal*, 19(23):7496–7502, 2013.
- [106] N. Koch, A. Vollmer, I. Salzmann, B. Nickel, H. Weiss, and J. P. Rabe. Evidence for temperature-dependent electron band dispersion in pentacene. *Phys. Rev. Lett.*, 96:156803, Apr 2006.
- [107] K. Kolata, T. Breuer, G. Witte, and S. Chatterjee. Molecular packing determines singlet exciton fission in organic semiconductors. *ACS Nano*, 8(7):7377–7383, 2014.
- [108] S. E. Koops and J. R. Durrant. Transient emission studies of electron injection in dye sensitised solar cells. *Inorganica Chimica Acta*, 361(3):663–670, 2008.
- [109] S. E. Koops, B. C. ORegan, P. R. Barnes, and J. R. Durrant. Parameters influ-

- encing the efficiency of electron injection in dye-sensitized solar cells. *Journal of the American Chemical Society*, 131(13):4808–4818, 2009.
- [110] J. Krüger, U. Bach, and M. Grätzel. Modification of tio₂ heterojunctions with benzoic acid derivatives in hybrid molecular solid-state devices. *Advanced Materials*, 12(6):447–451, 2000.
- [111] J. Kuhnert, M. Kothe, W. Heimbrodtt, and G. Witte. Orientation controlled growth of metal phthalocyanines and their optical characterization. *Poster contribution at DPG conference, Regensburg*, 2016.
- [112] U. Lachish, P. P. Infelta, and M. Grätzel. Optical absorption spectrum of excited ruthenium tris-bipyridyl (ru (bpy) 2+ 3). *Chemical Physics Letters*, 62(2):317–319, 1979.
- [113] J. R. Lakowicz, J. Kuśba, H. Szmactinski, M. L. Johnson, and I. Gryczynski. Distance-dependent fluorescence quenching observed by frequency-domain fluorometry. *Chem. Phys. Lett.*, 206(5-6):455–463, 1993.
- [114] H. Laurs and G. Heiland. Electrical and optical properties of phthalocyanine films. *Thin Solid Films*, 149(2):129–142, 1987.
- [115] B. I. Lemon and J. T. Hupp. Eqcm investigations of dye-functionalized nanocrystalline titanium dioxide electrode/solution interfaces: Does luminescence report directly on interfacial electron transfer kinetics? *J. Phys. Chem. B*, 103(19):3797–3799, 1999.
- [116] C. C. Leznoff. Phthalocyanines. *Properties and Applications*, 1989.
- [117] C. Li, X. Yang, R. Chen, J. Pan, H. Tian, H. Zhu, X. Wang, A. Hagfeldt, and L. Sun. Anthraquinone dyes as photosensitizers for dye-sensitized solar cells. *Solar Energy Materials and Solar Cells*, 91(19):1863–1871, 2007.
- [118] X.-Y. Li, C.-R. Zhang, L.-H. Yuan, M.-L. Zhang, Y.-H. Chen, and Z.-J. Liu. A comparative study of porphyrin dye sensitizers yd2-o-c8, sm315 and sm371 for solar cells: the electronic structures and excitation-related properties. *The European Physical Journal D*, 70(10):211, 2016.
- [119] A. Listorti, B. O’Regan, and J. R. Durrant. Electron transfer dynamics in dye-sensitized solar cells. *Chem. Mater.*, 23(15):3381–3399, 2011.
- [120] M. Liu, M. B. Johnston, and H. J. Snaith. Efficient planar heterojunction perovskite solar cells by vapour deposition. *Nature*, 501(7467):395–398, 2013.
- [121] Y. Liu, N. Xiang, X. Feng, P. Shen, W. Zhou, C. Weng, B. Zhao, and S. Tan. Thiophene-linked porphyrin derivatives for dye-sensitized solar cells. *Chemical Communications*, (18):2499–2501, 2009.
- [122] P. W. Lohse, J. Kuhnt, S. I. Druzhinin, M. Scholz, M. Ekimova, T. Oekermann, T. Lenzer, and K. Oum. Ultrafast photoinduced relaxation dynamics of the indoline dye d149 in organic solvents. *Phys. Chem. Chem. Phys.*, 13(43):19632–19640, 2011.
- [123] I. López-Duarte, M. Wang, R. Humphry-Baker, M. Ince, M. Martínez-Díaz, M. K. Nazeeruddin, T. Torres, and M. Grätzel. Molecular engineering of zinc

- phthalocyanines with phosphinic acid anchoring groups. *Angewandte Chemie*, 124(8):1931–1934, 2012.
- [124] B. T. Luong, E. Hyeong, S. Yoon, J. Choi, and N. Kim. Facile synthesis of uv-white light emission znse/zns: Mn core/(doped) shell nanocrystals in aqueous phase. *RSC Advances*, 3(45):23395–23401, 2013.
- [125] J. Mack and M. J. Stillman. Assignment of the optical spectra of metal phthalocyanine anions. *Inorganic Chemistry*, 36(3):413–425, 1997.
- [126] S. Mathew, A. Yella, P. Gao, R. Humphry-Baker, B. F. Curchod, N. Ashari-Astani, I. Tavernelli, U. Rothlisberger, M. K. Nazeeruddin, and M. Grätzel. Dye-sensitized solar cells with 13% efficiency achieved through the molecular engineering of porphyrin sensitizers. *Nature chemistry*, 6(3):242–247, 2014.
- [127] M. Matsui, M. Kotani, Y. Kubota, K. Funabiki, J. Jin, T. Yoshida, S. Higashijima, and H. Miura. Comparison of performance between benzoindoline and indoline dyes in zinc oxide dye-sensitized solar cell. *Dyes Pigm.*, 91(2):145–152, 2011.
- [128] C. C. Mattheus, A. B. Dros, J. Baas, A. Meetsma, J. L. de Boer, and T. T. Palstra. Polymorphism in pentacene. *Acta Crystallogr., Sect. C: Cryst. Struct. Commun.*, 57(8):939–941, 2001.
- [129] J. Mech, K. Mech, and K. Szaciłowski. Tio 2–anthraquinone hybrids: from quantum-chemical design to functional materials. *Journal of Materials Chemistry C*, 3(16):4148–4155, 2015.
- [130] I. Meyenburg, T. Breuer, A. Karthäuser, S. Chatterjee, G. Witte, and W. Heimbrot. Temperature-resolved optical spectroscopy of pentacene polymorphs: variation of herringbone angles in single-crystals and interface-controlled thin films. *Physical Chemistry Chemical Physics*, 18(5):3825–3831, 2016.
- [131] I. Meyenburg, J. Falgenhauer, N. Rosemann, S. Chatterjee, D. Schlettwein, and W. Heimbrot. Charge transfer at organic-inorganic interfaces indoline layers on semiconductor substrates. *J. Appl. Phys.*, 120(21):215502, 2016.
- [132] I. Meyenburg, N. Hofeditz, R. Ruess, M. Rudolph, D. Schlettwein, and W. Heimbrot. Optical determination of charge transfer times from indoline dyes to zno in solid state dye-sensitized solar cells. *AIP Advances*, 8(5):055218, 2018.
- [133] I. Minda, E. Ahmed, V. Sleziona, C. Richter, M. Beu, J. Falgenhauer, H. Miura, D. Schlettwein, and H. Schworer. Identification of different pathways of electron injection in dye-sensitized solar cells of electrodeposited zno using an indoline sensitizer. *Physical Chemistry Chemical Physics*, 18(13):8938–8944, 2016.
- [134] T. Mino, Y. Saito, H. Yoshida, S. Kawata, and P. Verma. Molecular orientation analysis of organic thin films by z-polarization raman microscope. *Journal of Raman Spectroscopy*, 43(12):2029–2034, 2012.
- [135] J. Mizuguchi, G. Rihs, and H. Karfunkel. Solid-state spectra of titanylphthalocyanine as viewed from molecular distortion. *The Journal of Physical Chemistry*, 99(44):16217–16227, 1995.
- [136] M. Molaei, A. Bahador, and M. Karimipour. Green synthesis of znse and core-shell znse@ zns nanocrystals (ncs) using a new, rapid and room temperature

- photochemical approach. *Journal of Luminescence*, 166:101–105, 2015.
- [137] R. Mondal, C. Tönshoff, D. Khon, D. C. Neckers, and H. F. Bettinger. Synthesis, stability, and photochemistry of pentacene, hexacene, and heptacene: a matrix isolation study. *J. Am. Chem. Soc.*, 131(40):14281–14289, 2009.
- [138] G. E. Morse and T. P. Bender. Boron subphthalocyanines as organic electronic materials. *ACS applied materials & interfaces*, 4(10):5055–5068, 2012.
- [139] G. E. Morse, A. S. Paton, A. Lough, and T. P. Bender. Chloro boron subphthalocyanine and its derivatives: dyes, pigments or somewhere in between? *Dalton Transactions*, 39(16):3915–3922, 2010.
- [140] J. E. Moser and M. Grätzel. Observation of temperature independent heterogeneous electron transfer reactions in the inverted marcus region. *Chemical physics*, 176(2-3):493–500, 1993.
- [141] A. J. Mozer, P. Wagner, D. L. Officer, G. G. Wallace, W. M. Campbell, M. Miyashita, K. Sunahara, and S. Mori. The origin of open circuit voltage of porphyrin-sensitized tio 2 solar cells. *Chemical communications*, (39):4741–4743, 2008.
- [142] R. S. Mulliken. Molecular compounds and their spectra. iii. the interaction of electron donors and acceptors. *The Journal of Physical Chemistry*, 56(7):801–822, 1952.
- [143] D. Nabok, P. Puschnig, C. Ambrosch-Draxl, O. Werzer, R. Resel, and D.-M. Smilgies. Crystal and electronic structures of pentacene thin films from grazing-incidence x-ray diffraction and first-principles calculations. *Phys. Rev. B*, 76(23):235322, 2007.
- [144] W. Naumann. Reversible fluorescence quenching: Generalized stern–volmer equations on the basis of self-consistent quenching constant relations. *J. Chem. Phys.*, 112(16):7152–7157, 2000.
- [145] M. K. Nazeeruddin, A. Kay, I. Rodicio, R. Humphry-Baker, E. Müller, P. Liska, N. Vlachopoulos, and M. Grätzel. Conversion of light to electricity by cis-x2bis (2, 2'-bipyridyl-4, 4'-dicarboxylate) ruthenium (ii) charge-transfer sensitizers (x= cl-, br-, i-, cn-, and scn-) on nanocrystalline titanium dioxide electrodes. *Journal of the American Chemical Society*, 115(14):6382–6390, 1993.
- [146] Y. Ooyama, K. Furue, T. Enoki, M. Kanda, Y. Adachi, and J. Ohshita. Development of type-i/type-ii hybrid dye sensitizer with both pyridyl group and catechol unit as anchoring group for type-i/type-ii dye-sensitized solar cell. *Physical Chemistry Chemical Physics*, 18(44):30662–30676, 2016.
- [147] Y. Ooyama and Y. Harima. Photophysical and electrochemical properties, and molecular structures of organic dyes for dye-sensitized solar cells. *ChemPhysChem*, 13(18):4032–4080, 2012.
- [148] B. O'Regan and M. Grätzel. A low-cost, high-efficiency solar cell based on dye-sensitized. *Nature*, 353(6346):737–740, 1991.
- [149] B. O'Regan, J. Moser, M. Anderson, and M. Graetzel. Vectorial electron injection into transparent semiconductor membranes and electric field effects on the

- dynamics of light-induced charge separation. *J. Phys. Chem.*, 94(24):8720–8726, 1990.
- [150] K. Oum, P. W. Lohse, O. Flender, J. R. Klein, M. Scholz, T. Lenzer, J. Du, and T. Oekermann. Ultrafast dynamics of the indoline dye d149 on electrodeposited zno and sintered zno₂ and tio₂ thin films. *Phys. Chem. Chem. Phys.*, 14(44):15429–15437, 2012.
- [151] A. Panda, K. Ding, X. Liu, and S. R. Forrest. Free and trapped hybrid charge transfer excitons at a zno/small-molecule heterojunction. *Physical Review B*, 94(12):125429, 2016.
- [152] A. Panda, C. K. Renshaw, A. Oskooi, K. Lee, and S. R. Forrest. Excited state and charge dynamics of hybrid organic/inorganic heterojunctions. ii. experiment. *Physical Review B*, 90(4):045303, 2014.
- [153] F. Piersimoni, R. Schlesinger, J. Benduhn, D. Spoltore, S. Reiter, I. Lange, N. Koch, K. Vandewal, and D. Neher. Charge transfer absorption and emission at zno/organic interfaces. *The journal of physical chemistry letters*, 6(3):500–504, 2015.
- [154] M. Pope and C. Swenberg. *Electronic Processes in 23. NIST Standard Reference Database 124. Organic Crystals, New York*. Oxford: Clarendon Stopping-Power and Range Tables for Press, 1982.
- [155] C. Prinzisky, I. Meyenburg, A. Jacob, B. Heidelmeier, F. Schröder, W. Heimbrodt, and J. Sundermeyer. Optical and electrochemical properties of anthraquinone imine based dyes for dye-sensitized solar cells. *European Journal of Organic Chemistry*, 2016(4):756–767, 2016.
- [156] M.-E. Ragoussi, J.-J. Cid, J.-H. Yum, G. de la Torre, D. Di Censo, M. Grätzel, M. K. Nazeeruddin, and T. Torres. Carboxyethynyl anchoring ligands: A means to improving the efficiency of phthalocyanine-sensitized solar cells. *Angewandte Chemie International Edition*, 51(18):4375–4378, 2012.
- [157] M.-E. Ragoussi, M. Ince, and T. Torres. Recent advances in phthalocyanine-based sensitizers for dye-sensitized solar cells. *European Journal of Organic Chemistry*, 2013(29):6475–6489, 2013.
- [158] C. V. Raman and K. S. Krishnan. A new type of secondary radiation. *Nature*, 121(3048):501–502, 1928.
- [159] B. P. Rand, J. Genoe, P. Heremans, and J. Poortmans. Solar cells utilizing small molecular weight organic semiconductors. *Prog. Photovoltaics Res. Appl.*, 15(8):659–676, 2007.
- [160] P. Y. Reddy, L. Giribabu, C. Lyness, H. J. Snaith, C. Vijaykumar, M. Chandrasekharam, M. Lakshmikantam, J.-H. Yum, K. Kalyanasundaram, M. Grätzel, et al. Efficient sensitization of nanocrystalline tio₂ films by a near-ir-absorbing unsymmetrical zinc phthalocyanine. *Angewandte Chemie*, 119(3):377–380, 2007.
- [161] C. K. Renshaw and S. R. Forrest. Excited state and charge dynamics of hybrid organic/inorganic heterojunctions. i. theory. *Physical Review B*, 90(4):045302, 2014.

- [162] C. R. Rice, M. D. Ward, M. K. Nazeeruddin, and M. Grätzel. Catechol as an efficient anchoring group for attachment of ruthenium–polypyridine photosensitisers to solar cells based on nanocrystalline tio 2 films. *New Journal of Chemistry*, 24(9):651–652, 2000.
- [163] C. Richter, M. Beu, and D. Schlettwein. Influence of counter-anions during electrochemical deposition of zno on the charge transport dynamics in dye-sensitized solar cells. *Phys. Chem. Chem. Phys.*, 17(3):1883–1890, 2015.
- [164] E. Rohwer, I. Minda, G. Tauscher, C. Richter, H. Miura, D. Schlettwein, and H. Schworer. Ultrafast charge-transfer reactions of indoline dyes with anchoring alkyl chains of varying length in mesoporous zno solar cells. *ChemPhysChem*, 16(5):943–948, 2015.
- [165] E. Rohwer, C. Richter, N. Heming, K. Strauch, C. Litwinski, T. Nyokong, D. Schlettwein, and H. Schworer. Ultrafast photodynamics of the indoline dye d149 adsorbed to porous zno in dye-sensitized solar cells. *ChemPhysChem*, 14(1):132–139, 2013.
- [166] N. W. Rosemann. *Funktionalization of inorganic semiconductors by advanced nanostructures*. PhD dissertation, University Marburg, 2016.
- [167] P. Rosenow. Aufbau einer farbstoffsolarzelle, ermittlung der kennlinie und impedanzspektroskopische untersuchungen. Master’s thesis, 2010.
- [168] L. Rost. *Optische Spektroskopie an organischen Molekülen und organisch-anorganischen Hybridstrukturen*. Examensarbeit lehramt, University Marburg, 2016.
- [169] M. Rudolph, T. Yoshida, and D. Schlettwein. Influence of indoline dye and coadsorbate molecules on photovoltaic performance and recombination in dye-sensitized solar cells based on electrodeposited zno. *J. Electroanal. Chem.*, 709:10–18, 2013.
- [170] S. Rühle, M. Greenshtein, S.-G. Chen, A. Merson, H. Pizem, C. S. Sukenik, D. Cahen, and A. Zaban. Molecular adjustment of the electronic properties of nanoporous electrodes in dye-sensitized solar cells. *The Journal of Physical Chemistry B*, 109(40):18907–18913, 2005.
- [171] R. Ruiz, D. Choudhary, B. Nickel, T. Toccoli, K.-C. Chang, A. C. Mayer, P. Clancy, J. M. Blakely, R. L. Headrick, S. Iannotta, and G. G. Malliaras. Pentacene thin film growth. *Chem. Mater.*, 16(23):4497–4508, 2004.
- [172] T. Saito, Y. Iwakabe, T. Kobayashi, S. Suzuki, and T. Iwayanagi. Thermochromism of specific crystal form oxotitanium phthalocyanines studied by electroabsorption and x-ray diffraction measurements. *The Journal of Physical Chemistry*, 98(11):2726–2728, 1994.
- [173] Y. Sakakibara, R. N. Bera, T. Mizutani, K. Ishida, M. Tokumoto, and T. Tani. Photoluminescence properties of magnesium, chloroaluminum, bromoaluminum, and metal-free phthalocyanine solid films. *The Journal of Physical Chemistry B*, 105(8):1547–1553, 2001.
- [174] Y. Sakuragi, X.-F. Wang, H. Miura, M. Matsui, and T. Yoshida. Aggregation

- of indoline dyes as sensitizers for zno solar cells. *J. Photochem. Photobiol., A*, 216(1):1–7, 2010.
- [175] T. D. Santos, A. Morandeira, S. Koops, A. J. Mozer, G. Tsekouras, Y. Dong, P. Wagner, G. Wallace, J. C. Earles, K. C. Gordon, et al. Injection limitations in a series of porphyrin dye-sensitized solar cells. *J. Phys. Chem. C*, 114(7):3276–3279, 2010.
- [176] A. K. Sarker, M. G. Kang, and J.-D. Hong. A near-infrared dye for dye-sensitized solar cell: catecholate-functionalized zinc phthalocyanine. *Dyes and Pigments*, 92(3):1160–1165, 2012.
- [177] H. Sasabe and J. Kido. Multifunctional materials in high-performance oleds: Challenges for solid-state lighting. *Chem. Mater.*, 23(3):621–630, 2010.
- [178] S. Schiefer, M. Huth, A. Dobrinevski, and B. Nickel. Determination of the crystal structure of substrate-induced pentacene polymorphs in fiber structured thin films. *J. Am. Chem. Soc.*, 129(34):10316–10317, 2007.
- [179] R. Schlesinger, F. Bianchi, S. Blumstengel, C. Christodoulou, R. Ovsyannikov, B. Kobin, K. Moudgil, S. Barlow, S. Hecht, S. Marder, et al. Efficient light emission from inorganic and organic semiconductor hybrid structures by energy-level tuning. *Nature communications*, 6(1):1–7, 2015.
- [180] A. Schneider. *Ortsaufgeloste Raman- und Photolumineszenzspektroskopie*. Diploma thesis, University Marburg, 2009.
- [181] B.-E. Schuster, T. V. Basova, H. Peisert, and T. Chassé. Electric field assisted effects on molecular orientation and surface morphology of thin titanyl (iv) phthalocyanine films. *ChemPhysChem*, 10(11):1874–1881, 2009.
- [182] J. Schwaben, N. Münster, M. Klues, T. Breuer, P. Hofmann, K. Harms, G. Witte, and U. Koert. Efficient syntheses of novel fluoro-substituted pentacenes and azapentacenes: Molecular and solid-state properties. *Chem. Eur. J.*, 21(39):13758–13771, 2015.
- [183] M. Schwoerer and H. C. Wolf. *Organic molecular solids*. John Wiley & Sons, 2007.
- [184] K. Seto and Y. Furukawa. Study on solid structure of pentacene thin films using raman imaging. *Journal of Raman Spectroscopy*, 43(12):2015–2019, 2012.
- [185] J. Shao, T. Sun, S. Ji, H. Li, S. Lan, and W. Li. Electrochemically-tuned luminescence of a [ru (bpy) 2 (tatp)] 2+-sensitized tio2 anode and its applications to photo-stimulated guanine/h2o2 fuel cells. *Journal of Power Sources*, 196(23):10511–10517, 2011.
- [186] S. Sharifzadeh, A. Biller, L. Kronik, and J. B. Neaton. Quasiparticle and optical spectroscopy of the organic semiconductors pentacene and ptcda from first principles. *Phys. Rev. B*, 85:125307, Mar 2012.
- [187] C. She, J. Guo, S. Irle, K. Morokuma, D. L. Mohler, H. Zabri, F. Odobel, K.-T. Youm, F. Liu, J. T. Hupp, et al. Comparison of interfacial electron transfer through carboxylate and phosphonate anchoring groups. *J. Phys. Chem. A*, 111(29):6832–6842, 2007.

- [188] J. Shinar and R. Shinar. Organic light-emitting devices (oleds) and oled-based chemical and biological sensors: an overview. *J. Phys. D: Appl. Phys.*, 41(13):133001, 2008.
- [189] T. Siegrist, C. Kloc, J. H. Schön, B. Batlogg, R. C. Haddon, S. Berg, and G. A. Thomas. Enhanced physical properties in a pentacene polymorph. *Angew. Chem. Int. Ed.*, 40(9):1732–1736, 2001.
- [190] V. K. Singh, R. K. Kanaparthi, and L. Giribabu. Emerging molecular design strategies of unsymmetrical phthalocyanines for dye-sensitized solar cell applications. *RSC Advances*, 4(14):6970–6984, 2014.
- [191] M. B. Smith and J. Michl. Singlet fission. *Chem. Rev.*, 110(11):6891–6936, 2010.
- [192] H. J. Snaith, A. Petrozza, S. Ito, H. Miura, and M. Grätzel. Charge generation and photovoltaic operation of solid-state dye-sensitized solar cells incorporating a high extinction coefficient indolene-based sensitizer. *Adv. Funct. Mater.*, 19(11):1810–1818, 2009.
- [193] J. Sobuś, G. Burdziński, J. Karolczak, J. Idígoras, J. A. Anta, and M. Ziołek. Comparison of tio2 and zno solar cells sensitized with an indoline dye: time-resolved laser spectroscopy studies of partial charge separation processes. *Langmuir*, 30(9):2505–2512, 2014.
- [194] E. J. Son, J. H. Kim, K. Kim, and C. B. Park. Quinone and its derivatives for energy harvesting and storage materials. *Journal of Materials Chemistry A*, 4(29):11179–11202, 2016.
- [195] S. Sönmezoğlu, C. Akyürek, and S. Akin. High-efficiency dye-sensitized solar cells using ferrocene-based electrolytes and natural photosensitizers. *Journal of Physics D: Applied Physics*, 45(42):425101, 2012.
- [196] C. Strothkaemper, A. Bartelt, P. Sippel, T. Hannappel, R. Schütze, and R. Eichberger. Delayed electron transfer through interface states in hybrid zno/organic-dye nanostructures. *The Journal of Physical Chemistry C*, 117(35):17901–17908, 2013.
- [197] Y. Tachibana, S. A. Haque, I. P. Mercer, J. E. Moser, D. R. Klug, and J. R. Durrant. Modulation of the rate of electron injection in dye-sensitized nanocrystalline tio2 films by externally applied bias. *J. Phys. Chem. B*, 105(31):7424–7431, 2001.
- [198] Y. Tachibana, J. E. Moser, M. Grätzel, D. R. Klug, and J. R. Durrant. Subpicosecond interfacial charge separation in dye-sensitized nanocrystalline titanium dioxide films. *The Journal of Physical Chemistry*, 100(51):20056–20062, 1996.
- [199] E. L. Tae, S. H. Lee, J. K. Lee, S. S. Yoo, E. J. Kang, and K. B. Yoon. A strategy to increase the efficiency of the dye-sensitized tio2 solar cells operated by photoexcitation of dye-to-tio2 charge-transfer bands. *The Journal of Physical Chemistry B*, 109(47):22513–22522, 2005.
- [200] Y. Takeyama, S. Maruyama, and Y. Matsumoto. Growth of single-crystal phase pentacene in ionic liquids by vacuum deposition. *Cryst. Growth Des.*, 11(6):2273–2278, 2011.
- [201] M. L. Tiago, J. E. Northrup, and S. G. Louie. Ab initio calculation of the electronic

- and optical properties of solid pentacene. *Phys. Rev. B*, 67:115212, Mar 2003.
- [202] J. Tomm, B. Ullrich, X. Qiu, Y. Segawa, A. Ohtomo, M. Kawasaki, and H. Koinuma. Optical and photoelectrical properties of oriented zno films. *J. Appl. Phys.*, 87(4):1844–1848, 2000.
- [203] W. Tong, H. Chen, A. Djurišić, A. Ng, H. Wang, S. Gwo, and W. Chan. Infrared photoluminescence from α - and β -copper phthalocyanine nanostructures. *Optical materials*, 32(9):924–927, 2010.
- [204] T. Tsuzuki, Y. Kuwabara, N. Noma, Y. Shirota, and M. R. Willis. Effect of morphology on photovoltaic properties of titanyl phthalocyanine. *Japanese journal of applied physics*, 35(4A):L447, 1996.
- [205] Y. Vaynzof, A. A. Bakulin, S. Gélinas, and R. H. Friend. Direct observation of photoinduced bound charge-pair states at an organic-inorganic semiconductor interface. *Physical review letters*, 108(24):246605, 2012.
- [206] J. D. Virdo, L. Crandall, J. D. Dang, M. V. Fulford, A. J. Lough, W. S. Durfee, and T. P. Bender. The influence of strong and weak hydrogen bonds on the solid state arrangement of hydroxy-containing boron subphthalocyanines. *CrystEngComm*, 15(42):8578–8586, 2013.
- [207] K. P. C. Vollhardt and N. E. Schore. *Organische chemie. VCH*. Verlag, Weinheim, 1990.
- [208] M. G. Walter, A. B. Rudine, and C. C. Wamser. Porphyrins and phthalocyanines in solar photovoltaic cells. *Journal of Porphyrins and Phthalocyanines*, 14(09):759–792, 2010.
- [209] C. H. Wang, C. W. Chen, Y. T. Chen, C. T. Chen, Y. F. Chen, S. W. Chou, and C. C. Chen. Direct evidence of type ii band alignment in nanoscale p3ht/cdse heterostructures. *Nanotechnology*, 22(6):065202, 2011.
- [210] P. Wang, S. M. Zakeeruddin, J. E. Moser, M. K. Nazeeruddin, T. Sekiguchi, and M. Grätzel. A stable quasi-solid-state dye-sensitized solar cell with an amphiphilic ruthenium sensitizer and polymer gel electrolyte. *Nature materials*, 2(6):402–407, 2003.
- [211] M. Weber. *Raman- und Reflexionsspektroskopie an organisch-anorganischen Hybridssystemen*. Bachelor thesis, University Marburg, 2015.
- [212] M. Wilhelm. *Ramanspektroskopie an organisch-anorganischen Hybrid-Systemen*. Bachelor thesis, University Marburg, 2013.
- [213] M. WILLIS et al. *Structural and polymorphic considerations on the effects of copper phthalocyanine pigment on polypropylene nucleation*. PhD thesis, University of Cincinnati, 2007.
- [214] M. W. Wilson, A. Rao, B. Ehrler, and R. H. Friend. Singlet exciton fission in polycrystalline pentacene: From photophysics toward devices. *Acc. Chem. Res.*, 46(6):1330–1338, 2013.
- [215] D. Wöhrle, G. Schnurpfeil, S. Makarov, and O. Suvora. Phthalocyanine: Von farbmitteln zu materialien für optik und photoelektronik. *Chemie in unserer*

- Zeit*, 46(1):12–24, 2012.
- [216] M. Wojdyła, W. Bała, B. Derkowska, Z. Łukasiak, R. Czaplicki, Z. Sofiani, S. Dabos-Seignon, and B. Sahraoui. Photoluminescence and third harmonic generation in znpc thin films. *Nonlinear Optics Quantum Optics*, 35(1/3):103, 2006.
- [217] M. Wojdyła, B. Derkowska, Z. Łukasiak, and W. Bała. Absorption and photoreflectance spectroscopy of zinc phthalocyanine (znpc) thin films grown by thermal evaporation. *Materials Letters*, 60(29):3441–3446, 2006.
- [218] S. Wood, J. R. Hollis, and J.-S. Kim. Raman spectroscopy as an advanced structural nanoprobe for conjugated molecular semiconductors. *Journal of Physics D: Applied Physics*, 50(7):073001, 2017.
- [219] S. Yamaguchi and Y. Sasaki. Primary process of photocarrier generation in y-form titanyl phthalocyanine studied by electric-field-modulated picosecond time-resolved fluorescence spectroscopy. *The Journal of Physical Chemistry B*, 103(33):6835–6838, 1999.
- [220] Y. Yamakita, J. Kimura, and K. Ohno. Molecular vibrations of [n] oligoacenes (n= 2- 5 and 10) and phonon dispersion relations of polyacene. *The Journal of chemical physics*, 126(6):064904, 2007.
- [221] H. Yanagi, S. Chen, P. A. Lee, K. W. Nebesny, N. R. Armstrong, and A. Fujishima. Dye-sensitizing effect of tiopc thin film on n-tio2 (001) surface. *The Journal of Physical Chemistry*, 100(13):5447–5451, 1996.
- [222] A. Yella, H.-W. Lee, H. N. Tsao, C. Yi, A. K. Chandiran, M. K. Nazeeruddin, E. W.-G. Diau, C.-Y. Yeh, S. M. Zakeeruddin, and M. Grätzel. Porphyrin-sensitized solar cells with cobalt (ii/iii)-based redox electrolyte exceed 12 percent efficiency. *science*, 334(6056):629–634, 2011.
- [223] M. Yokota and O. Tanimoto. Effects of diffusion on energy transfer by resonance. *J. Phys. Soc. Jpn.*, 22(3):779–784, 1967.
- [224] H. Yonehara, H. Etori, M. Engel, M. Tsushima, N. Ikeda, T. Ohno, and C. Pac. Fabrication of various ordered films of oxotitanium (iv) phthalocyanine by vacuum deposition and their spectroscopic behavior. *Chemistry of materials*, 13(3):1015–1022, 2001.
- [225] P. Y. Yu and M. Cardona. *Fundamentals of semiconductors: physics and materials properties*. Springer, 2010.
- [226] S. Yu, S. Ahmadi, P. Palmgren, F. Hennies, M. Zuleta, and M. Gothelid. Modification of charge transfer and energy level alignment at organic/tio2 interfaces. *The Journal of Physical Chemistry C*, 113(31):13765–13771, 2009.
- [227] A. Zaban, S. Ferrere, and B. A. Gregg. Relative energetics at the semiconductor/sensitizing dye/electrolyte interface. *The Journal of Physical Chemistry B*, 102(2):452–460, 1998.
- [228] C.-R. Zhang, L. Liu, J.-W. Zhe, N.-Z. Jin, L.-H. Yuan, Y.-H. Chen, Z.-Q. Wei, Y.-Z. Wu, Z.-J. Liu, and H.-S. Chen. Comparative study on electronic structures and optical properties of indoline and triphenylamine dye sensitizers for solar cells. *J. Mol. Model.*, 19(4):1553–1563, 2013.

- [229] Q. Zhang, C. S. Dandeneau, X. Zhou, and G. Cao. ZnO nanostructures for dye-sensitized solar cells. *Advanced Materials*, 21(41):4087–4108, 2009.

List of Figures

2.1. Pentacene exciton is splitted into E+ and E-, scheme	4
2.2. Schematic of a liquid electrolyte dye-sensitized solar cell	5
2.3. Energetics of operation of DSSCs	6
2.4. Best Research Cell Efficiencies (taken from NREL) for organic-based solar cells	8
3.1. Isosurfaces illustration of s and p orbitals, so that an electron with a probability of 90% is in the enclosed volume	9
3.2. Upper: Ethylene illustrated with its σ and π bonds. Lower: illustrated with the π bonds in a clearer planar view	9
3.3. The benzene molecule (C_6H_6) with its two bond types. Visualization of the $2sp^2$ and $2p_z$ orbitals	10
3.4. Alternating multiple and single bonds for organic molecules, here benzene (C_6H_6)	10
3.5. Simplified description of Benzene with the ring inside instead of the varying multiple and single bonds	10
3.6. Relationship between Acene size and absorption bandgap	11
3.7. With increasing acene size the absorption spectra redshift, benzene to pentacene	11
3.8. Energy levels of a π -conjugated molecule	11
3.9. Energy level scheme of an organic molecule (left: singlet manifold, right: triplet manifold)	13
3.10. Mirror symmetry when comparing the absorbance with the photoluminescence spectrum of Titanyl-Phthalocyanine (TiOPc) in solution	14
3.11. Energy-level diagram for the ground state and an excited state of a simple diatomic molecule, as a function of the separation r between the two nuclei	15
3.12. Configuration diagram for two electronic states in a molecule including schematic representation of the absorption and emission spectra	15
3.13. Franck–Condon principle energy diagram	15
3.14. Excitons with different radii: diagram of a Frenkel exciton, a Wannier exciton, and a charge-transfer (CT) exciton	17
3.15. Comparison of absorption of TiOPc in solution (black curve) with TiOPc as crystalline structure	18
3.16. Comparison of TiOPc in solution, in powder form and as crystal regarding absorbance and photoluminescence spectra	19
3.17. Connection between ps-TRPL curves and organic material state for Anthracene (non transferring on shown substrates)	19
4.1. Schematic drawing of Agilent 8453 UV-VIS spectroscopy system	20

4.2. Schematic drawing of Agilent 8453 UV-VIS spectroscopy system	21
4.3. Pentacene in solution: π - π^* absorbance spectra. Chemical shift due to changed solvents	23
4.4. Pentacene in solution: Energy of the main π - π^* absorption peak in dependence of the solvent permittivity	23
4.5. Cu-phthalocyanine in solution: π - π^* absorbance spectra. Chemical shift due to changed solvents	24
4.6. Cu-phthalocyanine in solution: Energy of the main π - π^* absorption peak in dependence of the solvent permittivity	24
4.7. Absorbance measurements of thin film phase pentacene on sapphire. Short and long axis absorptions are indicated	24
4.8. Comparison of absorption of pentacene in solution (red curve) with pentacene as crystalline structure on KCl. The long axis absorption is much stronger viewable in solution	25
4.9. Schematic structure of a photoluminescence measuring station	26
4.10. Schematic drawing of the confocal ps-TRPL setup	27
4.11. Example for ps-Stage software HPDTA result which is used to evaluate the decay times	29
4.12. Laser decay of laser at 443 nm	29
4.13. The similarity between transmission and reflection is shown for thin layers of ZnPc on quartz	32
4.14. Refractive index n and extinction coefficient k as a function of wavelength	32
4.15. Comparison of Absorption and Reflection for monocrystalline pentacene Siegrist phase crystals	32
4.16. Microscopic pictures of standing CuPc on glass and lying CuPc on KCl	33
4.17. KCl+CuPc - comparison of diffusive reflection and absorbance identifies stray effects	33
4.18. Diagram comparing energy level transitions for Rayleigh and Raman scattering with respect to the ground and first excited electronic states (S_0 and S_1), and vibrational energy levels	35
4.19. Representation of two A_g and B_{3g} vibrational modes of pentacene as determined by a DFT/B3LYP at 6-31G(d) calculation of an isolated pentacene	36
4.20. Choice of an orthogonal coordinate system to specify the Raman tensors of the pentacene molecule	36
4.21. Raman spectra of pentacene: powder, ThinFilm, Campbell	37
4.22. Representation of the tilt angle of the different pentacene phases Campbell, Siegrist and ThinFilm	38
4.23. Scheme of the experimental setup for Raman spectroscopy	39
4.24. PL of D149 in DSSC of a shortcut cell (at 0 V) and without connected electrodes at open circuit voltage V_{OC}	40
4.25. ps-TRPL of D149 in DSSC of a shortcut cell (at 0 V) and without connected electrodes at open circuit voltage V_{OC}	40
4.26. Applied electrical bias on DSSC sensitized with indoline dye D131 under laser light at different bias voltages	41

4.27. Resulting ps-TRPL decay curve for the ps-TRPL images of Fig. 4.26 in linear scale	41
5.1. a) XRD data of different pentacene phases in upright orientation showing first and second order reflexes of the (00 <i>l</i>) plane; b) Schematic representation of the resulting different phases	45
5.2. Microscopic images of thin pentacene crystals grown by the liquid mediated growth using ionic liquids	46
5.3. Absorption of sample Fig. 5.2 (a) measured polarization dependent . . .	47
5.4. Polarization dependent absorption of Campbell bulk crystal (see Fig. 5.2 (c)) at room temperature	47
5.5. Siegrist a) and Campbell b) bulk crystals measured in polarization dependent absorption at room temperature and 10K	48
5.6. AFM images: with increasing substrate temperature during crystal growth from amorphous phase (nanocrystalline) to Campbell phase	49
5.7. Polarized transmission microscope images: The polarizer is turned by 90 deg, the effect is like a negative image	50
5.8. Finding equally aligned crystal surfaces by absorption mapping with fixed polarization	51
5.9. Absorption line scan with fixed polarization.	51
5.10. Microscopic polarized absorption spectra at room temperature with the polarizer parallel to the two maximal excitonic transition dipole moments which are perpendicular polarized to each other	53
5.11. Optical extinction spectra of pentacene in the visible range with different packing structure (bulk Siegrist- and Campbell-phase and thin-film-phase and Campbell-phase on ZnO substrates) at different temperatures	54
5.12. Absorption spectra of S-pentacene using linearly polarized light parallel to \mathbf{b} and perpendicularly to \mathbf{b} direction at $T = 10$ K and 290 K, see detailed explanation of crystallographic axes and dimer moments \vec{D}_{\pm} in Fig. 5.17.	56
5.13. In addition to Fig. 5.12 the unpolarized absorption is added. The 1s and 2s excitonic state areas and the band gap region are indicated.	56
5.14. Absorption of sample Fig. 5.2 (a) measured polarization dependent. The similar trends with turned polarizer are indicated including the postulated 2s states and the energy gap, both Davydov splitted	56
5.15. Absorption of sample Fig. 5.2 (c) measured polarization dependent. The similar trends with turned polarizer are indicated including the postulated 2s states and the energy gap, both Davydov splitted	56
5.16. Optical absorption spectra (unpolarized) of pentacene in different polymorphs (S-phase (bulk), C-phase (bulk), C-phase (on ZnO) and TF-phase (on ZnO)) at $T = 290$ K and $T = 10$ K, the two lowest exciton transitions E^+ and E^- are shown	58
5.17. a) Top view on pentacene molecules, $\vec{D}_{1,2}$ indicating the transition dipole moments; (b) Schematic representation of orientation of both molecules in the unit cell and the herringbone angle Φ ; (c) Schematic vector summation of the monomer dipole moments forming the dimer moments . . .	59

5.18. Absorption spectra (unpolarized) showing the region of 1.75eV to 2.03eV of pentacene films grown on ZnO in the (a) TF- and (b) C- phase at various temperatures.	60
5.19. Evaluated values for the herringbone angle as function of temperature for pentacene films crystallized in the C-phase (on ZnO) and TF-phase .	61
5.20. (a) The herringbone angle for the crystalline phases of pentacene and (b) the Davydov splitting at $T = 290$ K and $T = 10$ K, experimental and calculated data	62
5.21. Detailed view of the arrangement of both molecules in the unit cell at $T = 290$ K for a) C-phase (bulk) and b) TF-phase on amorphous silicon oxide	64
5.22. Reflection spectra of Siegrist-pentacene using linearly polarized light parallel to \mathbf{b} (blue) up to perpendicularly to \mathbf{b} direction (red) at $T=290$ K .	66
5.23. Comparison of reflection spectra of pentacene bulk crystals of Siegrist and Campbell phase at room temperature. Polarisation dependent measurement	67
5.24. Comparison of polarization dependent reflection spectra of standing and lying Siegrist-pentacene. For lying pentacene no Davydov splitting is viewable	68
5.25. Raman peaks for the different pentacene crystal phases Campbell and Siegrist	68
5.26. Raman spectra: On graphite pentacene can grow in lying Siegrist phase .	68
5.27. Raman spectra of a pentacene layer in ThinFilm phase grown on ZnO-O	69
5.28. Raman spectra of a pentacene layer in ThinFilm phase grown on ZnO-O with underground adapted	69
5.29. Pentacene photoluminescence and absorption in solution	71
5.30. Photoluminescence of layers of 10, 20 and 100 nm pentacene ThinFilm on crystalline ZnO measured at 10 K. The strain is reduced with increasing thickness, leading to lower energy of the free exciton PL	71
5.31. Photoluminescence of a pentacene powder at 8 K. No free exciton PL can be seen	72
5.32. Photoluminescence of a pentacene Siegrist crystal at 10 K. The tiny free exciton PL is indicated at 690 nm.	72
5.33. Chemical structure of phthalocyanine	73
5.34. Chemical structure of metal phthalocyanine indicating axial and equatorial anchors; outer colour appearance of phthalocyanine layers on glass and KCl; XRD measurements showing standing and lying alignment of CuPc layer depending on substrate	74
5.35. Comparison of 100 nm and 65 nm CuPc on glass prepared at different temperature conditions.	75
5.36. Molecular arrangements in α - and β -CuPc	75
5.37. Comparison of extinction spectra of 50 nm CuPc on glass and 40 nm on KCl	76
5.38. Comparison of lying CuPc on KCl and standing CuPc on glass at temperature of 10 K	76

5.39. Molecular structure of oxotitanium(IV) phthalocyanine (TiOPc) and molecular orientation models for (a) α -standing, (b) α -lying, and (c) β -lying	77
5.40. Representation of the molecular arrangement of TiOPc with respect to the substrate in the α -phase and β -phase	78
5.41. Absorption spectra of TiOPc in solution and as solid	79
5.42. Absorption measurements: Comparison of TiOPc layer on glass @500 K with 50 nm thickness, 25nm amorph layer on glass @<200 K and 53 nm layer on KCl @500 K	80
5.43. Investigation of TiOPc samples on glass and KCL with different measurement stages including Ulbricht sphere. This helps to identify straying phenomena and real absorption peaks	80
5.44. Absorption spectra of TiOPc from literature	81
5.45. Comparison of the PL of TiOPc in solution with on potassium chloride, showing mirror symmetry	83
5.46. Fluorescence spectra of (a) α (phase II)-Standing on Pt/glass and (b) β (phase II)-Lying on Au/glass	84
5.47. Photoluminescence spectra and absorption spectra are illustrated for TiOPc in solution and for layer on planar substrates	85
5.48. Photoluminescence spectra of TiOPc on different substrates and as powder	85
5.49. ns-TRPL results for TiOPc in solution at room temperature and for powder at 10 K	86
5.50. TiOPc on KCl: temperature dependent diffusive reflection measurements at varying temperatures with added photoluminescence at 10 K	87
5.51. TiOPc powder: temperature dependent diffusive reflection measurements at varying temperatures with added photoluminescence at 10 K	87
5.52. Specular reflection of TiOPc on KCl	87
5.54. PL of Anthracene, Anthraquinone, Hydroxy-Anthraquinone, Alicarine in solution	88
5.53. Chemical Structure of pre steps of Alizarin. Anthrachinon is the starting point of synthesis of all Anthraquinone modifications	88
5.55. 9-(2-Hydroxyphenylamino)-1,10-anthraquinone with trivial name Anthraphenol	89
5.56. Microscopic picture of an anthraquinone imine Anthraphenol single crystal grown on a quartz substrate	89
5.57. Luminescence spectra at room temperature of anthraquinone imine Anthraphenol in solution excited by different laser energies	90
5.58. Extinction and luminescence spectra at room temperature of (a) anthraquinone imine Anthraphenol in solution and on mesoporous TiO ₂ sensitized by soaking, and (b) for single crystals	91
5.59. Contribution of Anthraphenol mono-crystalline and amorphous layer to crystal absorption and PL spectra	92
6.1. Schematic picture of the chemical structure of the various indoline derivatives	93

6.2.	(a) Photoluminescence of indoline derivatives and extinction spectra of D149 in solution at room temperature. (b) Photoluminescence of D149 and D131 and extinction of D149 on mesoporous ZnO at room temperature	96
6.3.	Photoluminescence transients of D149 in solution and on various substrates on a logarithmic scale	97
6.4.	TRPL of indoline D149 in solution, measured concentration dependant. The lower the concentration, the slower is the decay of the photoluminescence	97
6.5.	Photoluminescence decay of indoline dyes on mesoporous ZnO at temperatures of 10 K and 290 K on a logarithmic scale. The respective curves on a linear scale can be found in the SI.	100
6.6.	Photoluminescence of various dyes on ZnO(meso) at room temperature and $T = 10$ K	100
6.7.	Photoluminescence decay of D131 on ZnO on a logarithmic scale. Inset: Extinction of different layers on ZnO(0001)	102
6.8.	Schematic picture of the processes at the interface between the indoline layer and inorganic semiconductor	105
6.9.	Schematic picture of the chemical structure of the indoline derivatives D131 and D149	107
6.10.	Photoluminescence transient of D131 and D149 on mesoporous ZnO. Inset: time integrated photoluminescence	109
6.11.	Photoluminescence intensity of D131 and D149 on mesoporous ZnO as function of the applied electrical bias	110
6.12.	Photoluminescence transient of D131 on mesoporous ZnO for various applied voltages. A fit different from a biexponential fit is required	111
6.13.	Level alignment of indoline dyes D131 and D149 with respect to the ZnO bands	113
6.14.	ps-stage image of D149 on glass excited with 517 nm	114
6.15.	ps-stage image of D149 on CdS excited with 517 nm	114
6.16.	No charge transfer of D149 on CdS: TRPL curve of D149 on CdS decays similar to the decay curves an isolating glass, both excited at 517 nm	114
6.17.	ps-stage image of CdS substrate TRPL, excited with 405 nm	115
6.18.	ps-stage TRPL image of CdS substrate with D149, excited with 515 nm	115
6.19.	No charge transfer of D149 on ZnSe: TRPL curve of D149 on ZnSe decays similar to the decay curves an isolating glass, both excited at about 515 nm	116
6.20.	Rough estimation of level alignment of D149 and D131 and of several substrates	117
6.21.	ps-images of CdS+D149 with and without Förster transfer	119
6.22.	Resulting decay curves for ps TRPL measurements of CdS+D149	119
6.23.	ps-image of D149 drop casted on ZnSe by EtOH solvent evaporation	120
6.24.	ps-image of D149 drop casted on ZnSe by EtOH solvent evaporation with fastest decay time	120
6.25.	TRPL of D149 on glass and ZnSe excited by 405 nm. Förster transfer by excited traps of ZnSe substrate indicated by blueshift of the PL spectrum	120
6.26.	Structures of YD2 with $>11\%$ and YD2-o-C8 with 12.3% DSSC efficiency	121
6.27.	Carboxylate functionalized ZnPc* - TT1 with 3,52% DSSC efficiency	122

6.28. Molecular structure of PcS18 with 5.9% DSSC efficiency	122
6.29. Visible absorption spectra of TT1 in ethanol and adsorbed on a transparent 4-m-thick mesoporous TiO ₂ film	122
6.30. Catecholite functionalized ZnPc-t-Bu with 0.92% DSSC efficiency	123
6.31. Absorption ZnPcOH-tBut in 3% ethanol diluted in water and after soaking on mesoporous TiO ₂ - a strong redshift occurs	123
6.32. Scheme of t-Bu (Tert-butyl group)	123
6.33. Molecular structure for phthalocyanine dyes ZnPc*OH and H ₂ Pc*OH	124
6.34. Absorptions of H ₂ Pc*OH and ZnPc*OH in solution	124
6.35. Comparison of H ₂ Pc*OH in solution and on different substrates. Defect band formation on mesoporous ZnO	125
6.36. ps-TRPL decay curves: Comparison of H ₂ Pc*OH in solution and on different substrates. No charge transfer revealed, formation of defect states	125
6.37. Comparison of ZnPc*OH in solution and on different substrates. Defect band formation on ZnOmeso, but not on TiO ₂ (meso)	126
6.38. ps-TRPL decay curves: Comparison of ZnPc*OH in solution and on different substrates - absence of charge transfer can be concluded	126
6.39. SubPcBOH molecular packing arrangement	129
6.40. Absorption and emission spectrum of Cl-BsubPc in toluene	129
6.41. Absorption and photoluminescence of SubPcBOH in solution and on TiO ₂ (meso) - PL on TiO ₂ (meso) without powder formation	130
6.42. ps-TRPL times of SubPcBOH in solution and as an amorphous layer with similar slow decay times - charge transfer on mesoporous TiO ₂ (meso) revealed	130
6.43. Comparison of SubPcBOH PL spectra of layer on flat crystalline substrates with soakings in mesoporous TiO ₂ - redshift due to solid exciton formation	131
6.44. SubPcBOH ps-TRPL curves of molecular charge transfer effect and layers - lower charge transfer effect on TiO ₂ (meso) compared to the stronger excitonic charge transfer effect for layers	131
6.45. ps-TRPL curves of SpcBOH on quartz and TiO ₂ (110). Charge transfer time is shown as calculation of fit results	132
6.46. Molecular structures for ZnPc with a PA/vPA and a vCA anchor	133
6.47. ZnPc with varied anchors were processed as solar cells. IPCE and absorbance data shown	133
6.48. DSSC Efficiencies of different anchor variations on ZnPc	133
6.49. Spectra of ZnPc-PA/-vPA and -vCA. Defect formation can be identified for ZnPc-vCA and ZnPc-vPA while ZnPc-PA seems to be quasimolecular	134
6.50. Transients of ZnPc with anchors vPA, vCA and PA - a combination of quenching and charge transfer occurs	134
6.51. Absorption spectra in solution: Comparison of fully organic RK1 dye with Ruthenium dye N719	135
6.52. RK1 - chemical structure. Fig. taken from [95]	135
6.53. ps-TRPL decay curves for RK1 drop casted on cover glass, ZnO(0001) and TiO ₂ (meso) - charge transfer is shown	135
6.54. ps-TRPL image of RK1 on cover glass - no charge transfer	136

6.55. ps-TRPL image of a thin RK1 layer on flat ZnO(0001) - charge transfer .	136
6.56. ps-TRPL image of a RK1 soaked in TiO ₂ (meso) - efficient charge transfer without non transferring molecules or diffusion	136
6.57. ps-TRPL decay curves of RK1 dye on TiO ₂ (meso) compared with indoline dyes on ZnO(meso)	137
6.58. ps-TRPL decay curves of RK1 dye on TiO ₂ (meso) compared with indoline dyes on TiO ₂ (meso)	137
7.1. Electroluminescence intensity and external quantum efficiency for a planar bilayer device using α -NPD as the donor and ZnO as the acceptor. Inset with PL and absorption of α -NPD	143
A.1. Spectra: ZnPc*OH PL in solution, soaked in TiO ₂ (meso) and in a processed solar cell with mesoporous ZnO	146
A.2. Spectra: H ₂ Pc*OH PL in solution, soaked in TiO ₂ (meso) and in a processed solar cell with mesoporous ZnO	146
A.3. Absorption of ZnPc*OH on planar substrate SiO ₂ (001)	146
B.1. Chemical Structure of Phenoxazine, Anthraphene and Anthraphenol . . .	147
B.2. Range of absorptions of Alizarin, Phenoxazin, Anthraphene and Anthraphenol soaked in mesoporous TiO ₂	149
B.3. Photoluminescences of four different derivates Alizarin, Phenoxazin, Anthraphene and Anthraphenol soaked in mesoporous TiO ₂	149
B.4. Phenoxazine PL in solution, on TiO ₂ (meso) and as powder	150
B.5. Phenoxazine PL in solution, on TiO ₂ (meso) and as powder	150
B.6. Schematic showing Type I and Type II photoinjection in a DSSC	152
B.7. Comparison of TRPL of different Anthraquinones in solution and on TiO ₂ (meso)	153
B.8. Image of ps-TRPL of Phenoxazine in solution	153
B.9. ps-TRPL image of Phenoxazine soaked in TiO ₂ (meso). The PL indicates a molecular attachment without solid formation	154
B.10. Resulting Phenoxazine ps-TRPL decay curves, comparison of possibly molecular Phenoxazine on TiO ₂ (meso) and in solution	154
B.11. ps-TRPL comparison of layer on glass and soakings on TiO ₂ (meso) for Anthraphene and Co-Anthraphene	155
B.12. ps-TRPL curves of Hydroxyanthraquinone on TiO ₂ (meso) and as amorphous crystal. Charge transfer revealed	155
C.1. Absorption and PL of indoline dyes in solution	156
C.2. ns-TRPL of D131 on ZnO(meso). Spectra of the first nanosecond of the TRPL begin are shown at room temperature and at 10 K	157
C.3. ns-TRPL of D131 on ZnO(meso). Spectra of the the 10th ns of the ns-TRPL spectra are shown at room temperature and at 10 K - molecular part disappeared	157
C.4. ns-TRPL of D131 on ZnO(meso). Spectra of the the 27th ns after PL begin are shown at room temperature and at 10 K - powder PL is still existent	158

C.5.	ps-TRPL image of D131 powder	158
C.6.	D131 on ZnO(meso). Spectra of the first microsecond integrated with starting point at 6 ns after TRPL begin are shown at room temperature and at 10 K - band formation can be seen in the side of the powder PL at 10 K	159
C.7.	D131 agglomeration on SiO ₂ showing D131 powder PL. Spectra of the first 5 nanoseconds of the ns-TRPL are shown - At 830 nm a slight band formation can be seen in the curve side	159
C.8.	PL of D131 on ZnO(meso) measured in cw at different temperatures. Evolution of the deep trap PL of D131	160
C.9.	PL of D131 on ZnO(meso) measured in cw - At 442 nm laser excitation the deep trap PL formation at 10 K is shown	160
C.10.	IR-PL at room temperature of D149 on ZnO(meso) in IR region down to low energies as 0.73 eV (1700 nm) - no type II recombination found . .	160
C.11.	IR-PL at room temperature of D131 on ZnO(meso) in IR region down to low energies as 0.73 eV (1700 nm) - no type II recombination found . .	160
C.12.	ps-TRPL decay curve of D131 on TiO ₂ at 290 K. Inset: Extinction of different layers on TiO ₂ (100)	161
C.13.	ps-TRPL decay curves of indoline dyes on mesoporous TiO ₂ at 290 K . .	162
D.1.	ps-TRPL decay curves of D149 on CdS and on glass - D149 measured uninfluenced of substrate and with Förster transfer	163
D.2.	ps-image of D149 on CdS: here with strong substrate PL	164
D.3.	ps-image of D149 on CdS: here with very small substrate PL	164
D.4.	ps-image of D149 on CdS: here with slight substrate PL	164
D.5.	ps-TRPL with applied electrical bias of D149 soaked on ZnO(meso) and processed to a solar cell	164
D.6.	ps-TRPL with applied electrical bias from -1000 mV to 750 mV of D149 DSSC based on ZnO(meso) (by Rudolph) - biexponential fit	165
D.7.	ps-TRPL with applied electrical bias from -1000 mV to 750 mV of D149 DSSC based on ZnO(meso) (by Rudolph) - triexponential fit	165
D.8.	ps-TRPL with applied electrical bias from 0 mV to 800 mV of D149 DSSC based on ZnO(meso) (by Falgenhauer) - biexponential fit	165
D.9.	ps-TRPL with applied electrical bias from 0 mV to 800 mV of D149 DSSC based on ZnO(meso) (by Falgenhauer) - triexponential fit	165
D.10.	Spectra of DN216 DSSCs with Iodide and Cobalt electrolyte	166
D.11.	ps-TRPL decay curves of DN216 DSSCs with Iodide and Cobalt electrolyte. The decay of the PL with cobalt electrolyte is faster	166
E.1.	Comparison of ps-TRPL of D149 solar cells and simple soakings in TiO ₂ (meso) and ZnO(meso)	168
E.2.	PL spectra of D149 soakings and complete solar cells from ps-TRPL stage	168
E.3.	Comparison of PL of D149 on ZnOmeso and processed solar cell by Melanie Rudolph, ns-TRPL stage PL shown	169
E.4.	PL of independent and serial tandem of monochromatic solar cells D131 and D149 is shown, PL of ns-TRPL-stage	169
E.5.	ps-TRPL image of single junction DSSCs sensitized with D131 and D149	170

E.6.	ps-TRPL image of panchromatic junction DSSC sensitized with D131 and D149, resulting in a combination of the single junction cells	170
E.7.	ps-TRPL curves of panchromatic junction DSSC sensitized with D131 and D149, compared with decay curves of the single junction DSSCs . . .	170
E.8.	ps-TRPL image shows the PL spectral region of agglomerated SQ2. A charge transfer is shown by the fast times at the begin	171
E.9.	ps-TRPL image of 5 minutes soakings of SQ2+D131 and then added soaking of a mixture of D131+D149	172
E.10.	ps-TRPL image showing all three dyes D131, D149 and SQ2 absorbed . .	172
F.1.	Chemical structure of N3 and N719	174
F.2.	Chemical Shift of N719 absorption in different solvents	174
F.3.	N179 PL and absorption spectra in solution and drop casted on flat substrate cover glass. PL of soaking in TiO ₂ (meso) and drop casting on rutile TiO ₂ (110)	175
F.4.	PL of N719 in solution and drop casted on flat substrates cover glass and TiO ₂ (110)	175
F.5.	Absorption of N719 on TiO ₂ (110) with different positions on a drop casted layer	176
F.6.	PL of N719 layers on TiO ₂ (110)	176
F.7.	Comparison of photoluminescence of ruthenium dye N719 in solution, as powder and drop casted on different substrates	177
F.8.	Diffusive reflection of N719 on TiO ₂ (110) indicates possible exciton formation in solids	177
F.9.	Energetics and Kinetics of Electron Injection in a “Standard” DSSC. Comparison of Triplet versus Singlet Injection	178
F.10.	Comparison of PL spectra of N3 and N719 on TiO ₂ (meso)	180
F.11.	Comparison of ns-TRPL decay curves of N3 and N719 on TiO ₂ (meso) and N3 on glass	180
G.1.	IPCE (incident photon conversion efficiency) spectrum of RK1 und N719. A clear new red absorption occurs for RK1	183
G.2.	The calculated molecular orbital energy diagram for RK1 and iso density plots of the HOMO and LUMO	183
G.3.	Chemical structure of Catecholate (Cat)	184
G.4.	Chemical structure of Catecholate-v-P (Cat-v-P)	184
G.5.	IPCE and absorption spectrum of Cat on TiO ₂ (meso) compared with absorption of Cat in solution. A clear new absorption occurs at lower energies for Cat	184
G.6.	IPCE and absorption spectrum of Cat-v-P on TiO ₂ (meso) compared with absorption of Cat-v-P in solution. A clear new absorption occurs at lower energies for Cat-v-P	184

List of Tables

4.1. Raman tensors of pentacene	35
5.1. Energy positions of exciton Davydov components E^+ and E^- of different pentacene phases at $T = 290$ K and $T = 10$ K	57
5.2. Overview of the determined peak ratios of the modes 1178 cm^{-1} (A_g -symmetry) and 1596 cm^{-1} (B_{3g} -symmetry). Determination of the phase of pentacene crystals.	69
6.1. Photoluminescence decay times and weighting factors of D149 determined by means of Eq. 6.3 (see text for details). The accuracy of all values is $\pm 5\%$	99
6.2. Indoline dyes on mesoporous ZnO at temperatures of 290 K and 10 K. The accuracy of all values is $\pm 5\%$	101
6.3. Charge transfer times and exciton recombination times for D131 using Eq. 6.3 (upper part) and exciton diffusion time determined with Eq. 6.6 (lower part). See text for detailed discussion. The accuracy of all values is $\pm 5\%$	103
6.4. Fitting parameters for the calculated decay curves in Fig. 6.10 using Eq. 6.7 for D131 and D149 on mesoporous ZnO at room temperature under open circuit conditions.	108
6.5. Voltage dependence of the fitting parameters using Eq. 6.8 (upper part) or Eq. 6.9 (lower part) for Indoline dye D131 solar cells based on mesoporous ZnO at temperatures of 290 K.	112
C.1. Charge transfer times and exciton recombination times for D131 using Eq. 6.3 (upper part) and Eq. 6.6 (lower part)	162

Scientific Contributions

Publications

- I. Meyenburg, N. Hofeditz, R. Ruess, D. Schlettwein, W. Heimbrodtt. *Optical determination of charge transfer times from indoline dyes to ZnO in solid state dye-sensitized solar cells*. American Institute of Physics, AIP Advances 8, 055218 (2018);
- I. Meyenburg, J. Falgenhauer, N.W. Rosemann, S. Chatterjee, D. Schlettwein, and W. Heimbrodtt, (2016). *Charge transfer at organic - inorganic interfaces - Indoline layers on semiconductor substrates*. Journal of Applied Physics 120(21) (2016): 215502
- Meyenburg, I., Breuer, T., Karthäuser, A., Chatterjee, S., Witte, G., and Heimbrodtt, W. (2016). *Temperature-resolved optical spectroscopy of pentacene polymorphs: variation of herringbone angles in single-crystals and interface-controlled thin films*. Physical Chemistry Chemical Physics, 18(5), 3825-3831.
- Prinzisky, C., Meyenburg, I., Jacob, A., Heidelmeier, B., Schröder, F., Heimbrodtt, W., and Sundermeyer, J. (2016). *Optical and Electrochemical Properties of Anthraquinone Imine Based Dyes for Dye-Sensitized Solar Cells*. European Journal of Organic Chemistry, 2016(4), 756-767.
- Not content part of this thesis, publication from my Diploma work:
Harhausen, J., Meyenburg, I., Ohl, A., and Foest, R. (2011). *Characterization of the plasma plume of a PIAD plasma source by means of optical emission spectroscopy*. Surface and Coatings Technology, 205, S407-S410.

Conferences and Seminars

1 Department of Physics and Material Sciences Centre, Philipps-Universität Marburg, Germany

2 Department of Chemistry, Philipps-Universität Marburg, Germany

3 Institute of Applied Physics, Justus-Liebig-Universität Gießen, Germany

- International Conference on Internal Interfaces 2016, Marburg:
Ingo Meyenburg¹, Benjamin Heidelmeier¹, Nils Rosemann¹, Christian Prinzisky², Martin Liebold², Jan Tinz³, Jane Falgenhauer³, Jörg Sundermeyer², Derck Schlettwein³, Wolfram Heimbrodtt¹,

Optical Spectroscopy on Organic-Inorganic Hybrids – Charge Transfer in Type-II Level Systems

- DPG Frühjahrstagung – Sektion Kondensierte Materie 2016, Regensburg:
Ingo Meyenburg¹, Benjamin Heidelmeier¹, Nils Rosemann¹, Christian Prinzisky², Martin Liebold², Jane Falgenhauer³, Jörg Sundermeyer², Derck Schlettwein³, Wolfram Heimbrod¹,
Optical Spectroscopy on Organic-Inorganic Hybrid Structures - Charge Transfer in Type-II Level Systems
- Materialforschungstag Mittelhessen, 2015, Marburg:
Ingo Meyenburg¹, Benjamin Heidelmeier¹, Matthias Weber¹, Christian Prinzisky², Nils Rosemann¹, Andrea Karthäuser¹, Tobias Breuer¹, Jane Falgenhauer³, Derck Schlettwein³, Jörg Sundermeyer², Gregor Witte¹, Wolfram Heimbrod¹,
Optical Spectroscopy on Organic-Inorganic Hybrids - Charge Transfer in Type-II Systems/Accessing the interface
- DPG Frühjahrstagung – Sektion Kondensierte Materie, 2015, Berlin:
Ingo Meyenburg¹, Benjamin Heidelmeier¹, Matthias Weber¹, Christian Prinzisky², Nils Rosemann¹, Andrea Karthäuser¹, Tobias Breuer¹, Jane Falgenhauer³, Derck Schlettwein³, Jörg Sundermeyer², Gregor Witte¹, Wolfram Heimbrod¹,
Optical Spectroscopy on Organic-Inorganic Hybrids - Charge Transfer in Type-II Systems/Accessing the interface
- International Summer School 'Semiconductor Interfaces' – Methods and Model Systems, 2014, San Sebastián, Spanien:
Ingo Meyenburg¹, Michael Kothe¹, Andrea Karthäuser¹, Jane Falgenhauer³, Tobias Breuer¹, Derck Schlettwein³, Gregor Witte¹, Wolfram Heimbrod¹,
Optical Spectroscopy on Organic-Inorganic Hybrid Structures
- Materialforschungstag Mittelhessen, 2014, Gießen:
Ingo Meyenburg¹, Michael Kothe¹, Andrea Karthäuser¹, Martin Liebold², Tobias Breuer¹, Gregor Witte¹, Wolfram Heimbrod¹,
Optical Spectroscopy on Organic-Inorganic Hybrid Structures
- Seminar Graduiertenkolleg 'Funktionalisierung von Halbleitern' (GRK 1782), 2013, Schloss Bettenburg in Hofheim
Ingo Meyenburg¹, Jonatan Helzel¹, Mira El Helou¹, Tobias Breuer¹, Gregor Witte¹, Wolfram Heimbrod¹
Optical Spectroscopy on planar ZnO/Pentacene Hybrids
- DPG Frühjahrstagung – Sektion Kondensierte Materie, 2013, Regensburg:
Ingo Meyenburg¹, Jonatan Helzel¹, Mira El Helou¹, Tobias Breuer¹, Gregor Witte¹, Wolfram Heimbrod¹
Optical Spectroscopy on planar ZnO/Pentacene Hybrids

Supervised Theses

- Thesis (Examensarbeit, Lehramt Physik) Janek Bernzen (2017)
Optische Spektroskopie an hybriden Polymer-Halbleiter-System - Untersuchung auf Ladungstransfer von LPPP zum ZnO
- Bachelor Thesis Manuel Lohoff (2017)
Spektroskopie an Perovskitmaterialien für Solarzellenanwendungen
- Bachelor Thesis Sandra Krämer (2017)
Optische Spektroskopie an Farbstoffsolarzellen
- Bachelor Thesis Nico Hofeditz (2016)
Elektro-optische Charakterisierung von Farbstoffsolarzellen
- Thesis (Examensarbeit, Lehramt Physik) Luise Rost (2016)
Optische Spektroskopie an organischen Molekülen und organisch-anorganischen Hybridstrukturen
- Bachelor Thesis Benjamin Heidelmeier (2015)
Optische Spektroskopie an Anthrachinon-Derivaten
- Bachelor Thesis Matthias Weber (2015)
Raman- und Reflexionsspektroskopie an organisch-anorganischen Hybridsystemen

Danksagung

Ich möchte all jenen danken, die am erfolgreichen Gelingen dieser Arbeit beteiligt waren. Danke für die konstruktive und erfolgreiche Zusammenarbeit mit Prof. Heimbrodt bei den Veröffentlichungen, ich danke auch allen Mitautoren der Veröffentlichungen. Vor dem Schreiben von Veröffentlichungen müssen sinnvolle Proben hergestellt werden und Experimente durchgeführt werden. bei der Probenbereitstellung wurde ich exzellent durch Kontakte des GrK und SfB aus Marburg unterstützt, auch Arbeitsgruppen aus Gießen und Potsdam waren bereit, mir Proben zur Verfügung zu stellen. Bei den wichtigen ps-TRPL Experimenten konnte ich mich auf meine Kollegen aus den Arbeitsgruppen Chatterjee und Koch stützen, generell bekam ich sehr konstruktive Mithilfe bei Fragen zu Aufbauten und Auswertungen sowohl an der Universität Marburg als auch in Gießen.

Danke für die Bildungsmöglichkeiten in Deutschland, die mir diesen Weg ermöglicht haben. Danke für das Vertrauen in meine Person bei der Einstellung, was mir die Möglichkeit der universitären Promotion eröffnet hat. Die Einbindung als Doktorand in das Graduiertenkolleg und den Sonderforschungsbereich hat mir Einblicke in die verschiedenen Forschungsbereiche gegeben und ein Netzwerk ermöglicht, vielen Dank den Organisatoren um Prof. Kerstin Volz und Prof. Ulrich Höfer. Insbesondere die summer school in San Sebastian war ein sehr wertvolles Erlebnis.

Ich bin dankbar über die verschiedenen Probenbereitstellungen und Projektzusammenarbeiten, die ich im Folgenden im Einzelnen aufführen möchte.

- Ich habe von den Vorarbeiten von Jonathan Helzel und Maria El Helou im Bereich Pentacen sehr profitiert, auch von den vorhandenen und neu erstellten Proben durch die Arbeitsgruppe Witte, insbesondere auch die gewachsenen Kristalle von Andrea Karthäuser, ich danke auch die Unterstützung durch Michael Klues. Bei der Veröffentlichung danke ich Prof. Witte und Dr. Tobias Breuer für die intensive und konstruktive Zusammenarbeit.
- Sehr wichtig war generell die Unterstützung durch die Arbeitsgruppe Witte. Ich möchte Michael Kothe besonders für die Zusammenarbeit danken. Leider resultierte die Vielzahl der in hoher Qualität von ihm hergestellte Proben insbesondere im Phthalocyanin-Bereich nicht in einer gemeinsamen Publikation.
- Proben und Messunterstützung von der Arbeitsgruppe Schlettwein, insbesondere von Jane Falgenhauer und Raffael Ruess. Der Kontakt zur Arbeitsgruppe Schlettwein in Gießen ergab sich durch das Kennenlernen von Jane Falgenhauer an ihrem Poster auf einem Materialwissenschaftstag. Dieser Kontakt war sehr wichtig für diese Dissertation, da er den Bereich der organischen Solarzellen erschloss. Danke auch an die wichtigen Proben von Melanie Rudolph und die Zuarbeit von Jan Tinz. Danke

an Professor Derck Schlettwein aus Gießen für die Besuche in Marburg inklusive der fachlichen Diskussionen und die konstruktive Unterstützung bei den Publikationen.

- Die Zusammenarbeit mit der Arbeitsgruppe Sundermeyer war von hohem Vertrauen und selbstständiger Zusammenarbeit geprägt, ich danke Michael Lieboldt, Christian Prinzisky, Marius Klein und Prof. Jörg Sundermeyer sehr für die Möglichkeiten, die sich aus der Zusammenarbeit mit dem Fachbereich Chemie ergeben haben. Während bei Christian Prinzisky ein Beitrag in seiner Publikation über Anthrachinone eingebracht werden konnte, war das bei Martin Lieboldt und Marius Klein leider nicht der Fall, was aber nicht an der hervorragenden Unterstützung von Martin und Marius lag.
- Die Unterstützung der Arbeitsgruppe Chatterjee im Bereich Experimente war außerordentlich. Sie haben mir den ps-TRPL Aufbau nicht nur erklärt und gezeigt, sondern sogar die Labview basierte Software für eine schnelle Auswertung in Origin zur Verfügung gestellt. Ganz vielen Dank an Nils Rosemann, Robin Döring und Andre Rinn dafür! Jan Kuhnert danke ich für die Bereitstellung und Programmierung des Messplatzes für den mikroskopischen Absorptionsscan. Danke auch an Prof. Sangam Chatterjee für die Bereitstellung von Messzeit und Messaufbauten im Labor und für seine Mitwirkung bei den Publikationen.

Auch der Arbeitsgruppe von Prof. Martin Koch, insbesondere Maximilian Schneider und Christian Kriso, danke ich für ihre Unterstützung.

Die Nutzung des Chemie-Labors der Arbeitsgruppe Biophotonik von Prof. Wolfgang Parak war wichtig für die Probenpräparation, die Mitarbeiter waren hilfsbereit. Das UV-VIS Spektrometer hat mir viele Messreihen mit hoher Reproduzierbarkeit ermöglicht, geholfen hat dabei auch die optimierte Software von Raimo Hartmann.

- Danke an Stefan Zeiske von der Universität Potsdam, Arbeitsgruppe von Prof. D. Neher, für die Bereitstellung der Solgel-ZnO-Polymer Proben, die im Rahmen eines Vertiefungsbericht von Janek Bernzen untersucht werden konnten. Die Verbindung zu Stefan hatte sich 2017 im Rahmen einer Frühjahrstagung der DPG an einem Poster ergeben. Das Potential der Zusammenarbeit mit anderen Universitäten ist vorhanden und nutzbar, erfreulich.
- Ich durfte einige studentische Arbeiten begleiten und möchte mich dafür bedanken, dass die Studenten mein Interesse für die Themen mit großem Einsatz geteilt und die Themen mit vorangebracht haben. Nico und ich konnten zusammen mit der immer hilfsbereiten Elektronikwerkstatt sogar den Aufbau einer Spannungsquelle umsetzen, die interessante automatisierte Messungen bei der Untersuchung von Solarzellen ermöglicht.

Danke Matthias Weber, Benjamin Heidelmeier, Luise Rost, Nico Hofeditz, Sandra Krämer...

Danke an meine Arbeitsgruppe: Manuel Demper, Uwe Kaiser, Mikko Wilhelm, Robert Malinowski, Carsten Kruska, Sebastian Gies, Jan Kuhnert, Johannes Röder, Luise Rost, Benjamin Heidelmeier, Nico Hofeditz, Simon Schmitt... Ich danke für die Unterstützung während der Einarbeitung in mein Thema, Hilfe bei Fragen zu den verschiedenen experimentellen Aufbauten und für die Diskussionen in den Gruppentreffen. Dank an Uwe für die L^AT_EX-Vorlage. Dankeschön auch für die gute Gemeinschaft. Zuletzt geht noch ein Dank an Herrn Heimbrodt für die großzügigen Weihnachtsessen und die Förderung der schönen Gruppenausflüge rund um Marburg.